Fundamental Properties of Solar-Type Eclipsing Binary Stars, and Kinematic Biases of Exoplanet Host Stars

Richard J. Hutcheon

Submitted in accordance with the requirements for the degree of Doctor of Philosophy.

Research Institute:

School of Environmental and Physical Sciences and Applied Mathematics.

University of Keele

June 2015

Keele University

Declaration Part 1. To be bound in the thesis

SUBMISSION OF THESIS FOR A RESEARCH DEGREE

Part I. DECLARATION by the candidate for a research degree. To be bound in the thesis

Degree for which thesis being submitted: Ph. D.

Title of thesis: Fundamental Properties of Solar-Type Eclipsing Binary Stars, and Kinematic Biases of Exoplanet Host Stars.

This thesis contains confidential information and is subject to the protocol set down for the submission and examination of such a thesis.

NO

Date of submission: June 2015
(Date of submission must comply with Regulation 2D)

Original registration date: 1 August 2008

Name of candidate: Dr. R.J. HUTCHEON

Research Institute: EPSAM

Name of Lead Supervisor: Dr. P.F.L. Maxted

I certify that:

(a) The thesis being submitted for examination is my own account of my own research
(b) My research has been conducted ethically. Where relevant a letter from the approving body confirming that ethical approval has been given has been bound in the thesis as an Annex
(c) The data and results presented are the genuine data and results actually obtained by me during the conduct of the research
(d) Where I have drawn on the work, ideas and results of others this has been appropriately acknowledged in the thesis
(e) Where any collaboration has taken place with one or more other researchers, I have included within an 'Acknowledgments' section in the thesis a clear statement of their contributions, in line with the relevant statement in the Code of Practice (see Note overleaf).
(f) The greater portion of the work described in the thesis has been undertaken subsequent to my registration for the higher degree for which I am submitting for examination
(g) Where part of the work described in the thesis has previously been incorporated in another thesis submitted by me for a higher degree (if any), this has been identified and acknowledged in the thesis
(h) The thesis submitted is within the required word limit as specified in the Regulations

Total words in submitted thesis (including text and footnotes, but excluding references and appendices) About 60 000.....

Signature of candidate R.J. Hutcheon.....Date April 2015

Note

Extract from Code of Practice: If the research degree is set within a broader programme of work involving a group of investigators – particularly if this programme of work predates the candidate's registration – the candidate should provide an explicit statement (in an 'Acknowledgments' section) of the respective roles of the candidate and these other individuals in relevant aspects of the work reported in the thesis. For example, it should make clear, where relevant, the candidate's role in designing the study, developing data collection instruments, collecting primary data, analysing such data, and formulating conclusions from the analysis. Others involved in these aspects of the research should be named, and their contributions relative to that of the candidate should be specified (*this does not apply to the ordinary supervision, only if the supervisor or supervisory team has had greater than usual involvement*).

Abstract

This thesis is in three parts: 1) a kinematical study of exoplanet host stars, 2) a study of the detached eclipsing binary V1094 Tau and 3) and observations of other eclipsing binaries.

Part I investigates kinematical biases between two methods of detecting exoplanets; the ground based transit and radial velocity methods. Distances of the host stars from each method lie in almost non-overlapping groups. Samples of host stars from each group are selected. They are compared by means of matching comparison samples of stars not known to have exoplanets. The detection methods are found to introduce a negligible bias into the metallicities of the host stars but the ground based transit method introduces a median age bias of about -2 Gyr.

Part II describes a detailed analysis of V1094 Tau. Spectra were analysed by the cross-correlation software TODCOR to obtain radial velocities, and *uvby* photometric light curves were analysed by the JKTEBOP software. Precise measurements obtained were: Improved ephemeris - T(min,prim) = HJD 2 454 555.51836(25) + 8.98854775(102) days. Absolute masses: M_1= 1.0969 ± 0.0037 $M_\odot$, M_2 = 1.0127 ± 0.0027 $M_\odot$. Absolute radii are R_1 = 1.406 ± 0.010 $R_\odot$ and R_2 = 1.099 ± 0.017 $R_\odot$. The apsidal period is (14.5 ± 3.7) × 10^3 years. The primary is somewhat evolved. The binary lies in an important region of the mass/radius/period grid for studying tidal interactions. These may introduce an important uncertainty when using eclipsing binaries to determine fundamental stellar parameters.

Part III describes an observing run at SAAO Sutherland, aimed to survey detached eclipsing binaries. Light curves and two spectra each from two binaries were analysed, to determine masses and radii to the 10 to 30% level. This is a proof in principle that runs on 2-metre class telescopes can identify targets for detailed follow-up observations.

General Acknowledgements

I would like to thank Dr. Pierre Maxted for all his help as a supervisor and for his prompt and detailed response to queries when I was working away from the University as a mature student. I would also like to thank other members of the Astrophysics Department, particularly Dr. John Taylor and Dr. Barry Smalley for their assistance.

Technical acknowledgements appear at the end of the main text.

Contents

Aims and layout of thesis

List of Figures

Figures in Appendices.

List of Tables

Tables in Appendices

List of Appendices

FUNDAMENTAL PROPERTIES OF SOLAR-TYPE ECLIPSING BINARY STARS, AND KINEMATIC BIASES OF EXOPLANET HOST STARS

AIMS AND LAYOUT OF THESIS

Two current major areas of interest in astrophysics are a) the discovery and analysis of exoplanet systems and b) the mass/radius relation in stars. This relation or an equivalent stellar model is required for a detailed analysis of exoplanet systems.

This thesis is in three distinct parts, all of which relate to issues in these areas.

I. Exoplanet systems have been discovered mainly by two methods, the transit method and the radial velocity method. Part I examines whether there are any significant observational biases between the two methods.

II. There is a long standing discrepancy between theoretical models and observations for the mass/radius relation in low mass stars. Eclipsing binaries provide the main method to determine stellar masses and radii. However tidal interactions between the members of binary systems are significant for many known systems and a consequence is that the mass/radius relation for binary stars may differ from that for single stars. Part II describes a detailed study of the detached eclipsing binary V1094Tau. The properties of this system, in particular the period, are suitable for testing tidal interaction theories.

III. Part III describes an observational program aimed to select binaries which may then be studied in greater detail with the ultimate aim of testing tidal interaction theories and to assess the importance of tidal effects.

The subjects of the second and third parts of this thesis were defined during the course of my project. The work in Part III was carried out before that of Part II, but is described afterwards so that concepts are introduced in a more logical order.

The abbreviations $M_\odot$ and $R_\odot$ are used throughout this thesis to denote the mass and radius of the Sun. Standardised nominal values of these parameters have been recommended by Harmanec and Prša (2011) as $M_\odot = 1.988416 \times 10^{30}$ kg and $R_\odot = 6.95508 \times 10^8$ m; these authors also recommend $\log g_\odot = 4.438307$ log(cm s^{-2}).

This thesis refers to websites. These are indicated as such in the text and the web reference listed in a separate section of the Reference list.

PART I KINEMATIC AND TEMPERATURE BIASES IN GROUND BASED SURVEYS OF EXOPLANETS.

CHAPTER 1. INTRODUCTION

An exoplanet is a planet orbiting a star other than the Sun. The first to be discovered was PSR 1257 12b reported by Wolszczan and Frail in 1992, and orbits a pulsar. The first planet discovered orbiting a solar type star (51 Pegasi) was reported by Mayor and Queloz (1995) by the radial velocity method (Sect. 2.2). As of 16 March 2015, the Extrasolar Planets Encyclopaedia (www.exoplanet.eu) has listed 1897 exoplanets from 1195 planetary systems and 478 multiple systems.

Basic questions in understanding the nature of exoplanets include the following.

- How common are exoplanets?
- What types of stars are most likely to possess planets?
- What theories can be proposed for the formation of planets (e.g. Fischer and Valenti (2005), Johnson (2009))?
- What correlations if any exist between the properties of a host star and its planets?
- What are the most likely values of planetary properties and in particular how common are Earth-like planets?
- What correlations exist between the different properties of exoplanets?
- To what extent are the lifetime of exoplanets limited by tidal interactions between the planet and its star?
- To what extent do the orbits of exoplanets migrate?

Answers to these questions are important to guide the efficient operation of the forthcoming exoplanet missions TESS and PLATO (Sect. 10.4).

Statistical analyses are needed to answer these questions. A prior requirement is to determine whether all the known systems can be regarded as a single group or instead whether the method of discovery introduces selection effects and hence biases in the properties of the host stars.

Most of the known exoplanets have been discovered either by the transit method, where the apparent brightness of a star is dimmed by a planet passing in front of it (Sect. 2.2) or by the radial velocity method, where the orbital motion of the planet causes a periodic reflex motion of the star, and hence a minute but measurable Doppler shift in the stellar spectral lines (Sect. 2.3). Part I of this thesis explores the question: Do the two main methods for discovering exoplanets introduce any selection biases in the observational data? There can in principle be inherent temperature and kinematic biases between them, which can lead to biases in the metallicity and age distributions of these stars, parameters thought to be associated with the frequency of exoplanets. This point does not appear to have been considered in detail to date. If an observational bias exists, discussions of the distribution of exoplanet and host star properties should consider how the exoplanets were discovered. It would be unsafe without further consideration to regard exoplanets as a single group regardless of how the planet was discovered.

At the time this thesis project part was undertaken (late 2008 to late 2010), the numbers of exoplanets discovered by these two methods were already large enough to form distinct data sets for a statistical analysis comparison. Possible biases were investigated as follows.

a) Define the two sample groups of exoplanet host stars discovered by these methods.

b) Compare the two samples statistically i.e. answer the question: Can the two groups of host stars be regarded as belonging to the same population?

c) Discuss possible reasons why these differences exist.

d) Test candidate observational reasons for these differences by constructing comparison calibration data sets formed from stars with no known exoplanets. These are matched as closely as possible to the real samples.

e) Investigate whether there is any significant difference between the metallicity and age distributions of the comparison samples. The appropriate kinematic parameter for this investigation is discussed in some detail.

It is found that there is a small but negligible difference in the metallicities of the stars in the two groups, but there is a statistically significant bias towards transit method host stars being younger.

CHAPTER 2. MAIN FEATURES OF DETECTION METHODS.

2.1 Main features of exoplanets

2.1.1 General description

This chapter briefly surveys the main features of exoplanets and detection methods, broadly insofar as they are relevant to the aims of this thesis. It is not intended as a comprehensive review of the subject.

Details in this chapter about the total number of exoplanets, the properties of a particular exoplanet, or the number of exoplanets discovered by each method or mission, have been obtained from the Extrasolar Planets Encyclopaedia (www.exoplanet.eu) maintained by Jean Schneider of the Observatory of Paris. They are correct as at 16 March 2015.

Exoplanets are common; the three nearest known exoplanet host stars which are confirmed are GJ 674, distance 4.54 ± 0.03 pc; GJ 876, distance 4.7 ± 0.01 pc, and, GJ 832, distance 4.94 ± 0.025 pc. (The inconsistencies between the number of decimal places in the distance itself and its uncertainty are as quoted). These distances may be compared with 1.301 pc for the nearest star, Proxima Centauri. The probability of a star hosting a planet has been discussed in detail by e.g. Howard at al., (2011) and Mayor et al. (2011); the latter state that more than half of solar type stars host at least one planet of any mass or orbital period. Masses of planets extend up to 13 M_J where M_J is the mass of Jupiter. The solar mass is ~ 1048M_J and 1 M_J is ~318 earth masses. According to the position statement of the International Astronomical Union (2003) any object with mass below 13M_J is to be regarded as a planet and any object which is heavier than this is regarded as a substellar brown dwarf (one not massive enough to ignite hydrogen fusion at

its core). Although the cores of substellar objects are not sufficiently hot to fuse hydrogen they can fuse deuterium. In contrast to exoplanets they therefore do emit their own radiation but are faint and have low surface temperatures. (The deuterium-deuterium reaction also takes place in the early evolutionary stages of a protostar sufficiently massive to start hydrogen fusion later, as explained in Sect.7.1). There does not appear to be a well defined physical mass boundary between planets and brown dwarfs (Bodenheimer at al., (2013, particularly their Sect. 1)). These authors describe numerical simulations of core nucleated accretion of giant planets and calculate, for a range of initial conditions, the final masses for which 50% of the initial deuterium is burned and find that these masses depend slightly on these conditions and lie in the range 11.6 to13.6 M_J. The Extrasolar Planets Encyclopaedia lists exoplanets up to masses of 19.4 M_J.

The mass of the lightest known exoplanet is set by detection technology. The lightest known exoplanet discovered by any method is the pulsar companion PSR 1257 12b mentioned earlier, which has a mass of about 0.00007 M_J i.e. about 0.022 Earth masses. The lightest discovered by the dedicated space borne *Kepler* transit survey mission is Kepler-70c (0.0021 M_J, i.e. 0.67 Earth masses, discovered by reflected light from the host star) followed by Kepler-42d (< 0.003 M_J, i.e. <0.95 Earth masses, discovered by the transit method). Thus the masses of these two *Kepler* planets are comparable with that of the Earth, a discovery which underlines the importance of exoplanet research. A particular class of exoplanets are "Hot Jupiters" which have masses of the order M_J and orbit very close to their host stars, typically closer than 0.1 A.U, with periods shorter than 10 days, for example WASP-1b (Collier Cameron et al. 2007) and WASP-12b (Hebb et al. 2009). A detailed discussion of the formation and growth of exoplanets has been given by Ida and Lin (2004)

2.1.2 Distribution of exoplanets

The Extrasolar Planets Encyclopaedia provides a wide choice of options for displaying the distribution of exoplanet properties. Four distributions are shown in Figs.2.1 and 2.2, namely 2.1a) a scatter plot of radius versus mass up to $20M_J$, 2.1b) the same distribution up to $4M_J$, 2.2a) a logarithmic histogram by mass from $0.002M_J$ to $20M_J$ and 2.2b) a logarithmic distribution by radius from $0.02R_J$ to $2R_J$. Here R_J is the mean radius of Jupiter i.e. $(6.9911 \pm 0.0006) \times 10^4$ km i.e.10.973 mean Earth radii. The figures c) and d) show the distribution in ten logarithmic steps. The upper mass limit in Fig. 2.1a corresponds closely to the mass limit adopted by the Encyclopaedia. Because this figure is crowded towards lower masses, an expanded version of the section between 0 and 4 M_J is shown in Fig. 2.1b.

It will be seen from the Figs. 2.2 that the most populated mass bins are in the region of $1M_J$, whereas the most populated radius bins are in the region 0.1 to $0.3R_J$

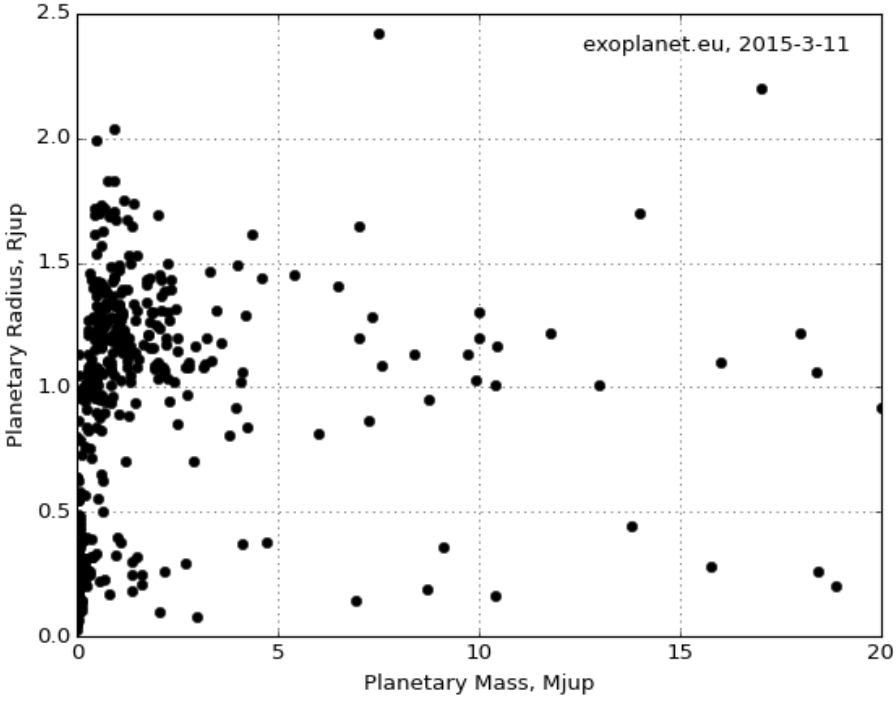

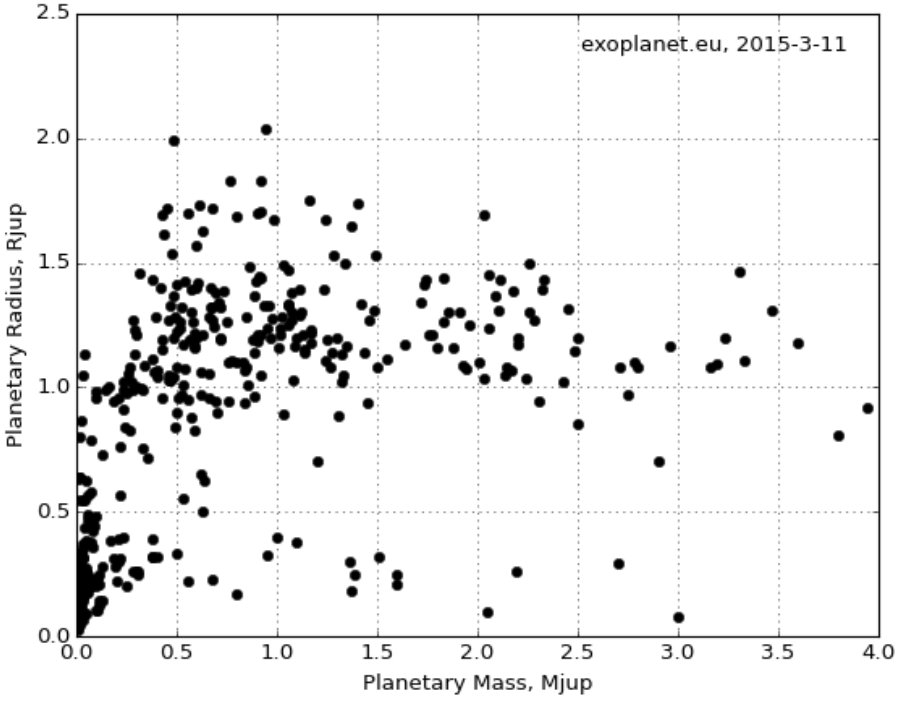

Figs 2.1a and 2.1b. Mass/radius scatter plot for exoplanets shown up to 20MJ (Fig. 2.1a), and expanded version of portion between 0 and 4 MJ (Fig. 2.1b). Obtained from the Extrasolar Planets Encyclopaedia.

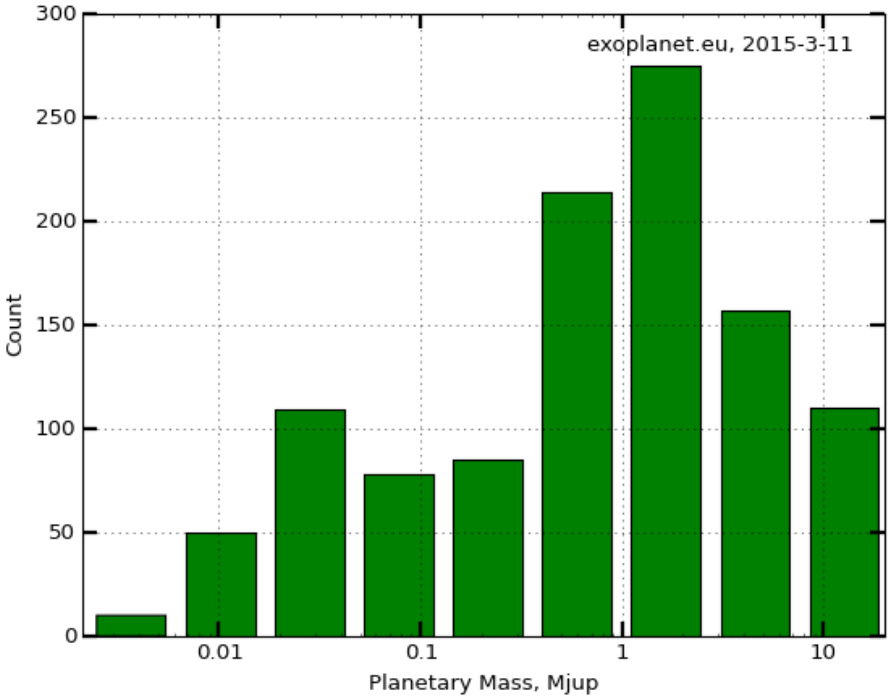

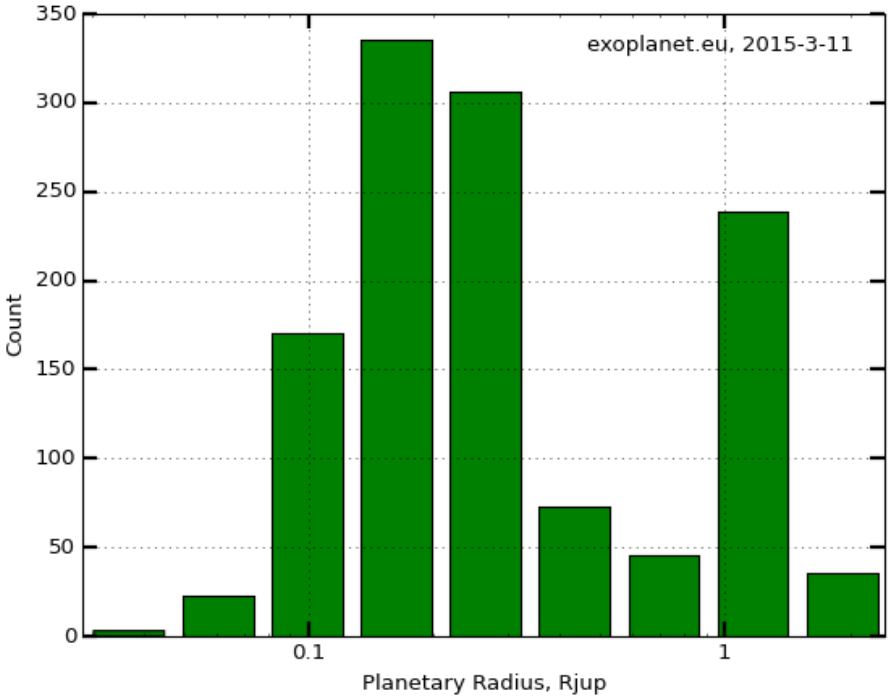

Figs. 2.2a and b. Logarithmic histograms of the distributions of exoplanet masses (Fig. 2.2a) and radii (Fig. 2.2b).
Obtained from the Extrasolar Planets Encyclopaedia.

2.2 The transit method.

2.2.1 Main features

If the orbit of an exoplanet is sufficiently well aligned with the line of sight from the Earth, it passes in front of the stellar disc i.e. transits it. The consequent apparent periodic dimming of the star reveals the presence of the exoplanet. The detection method has been described in detail by e.g. Collier Cameron et al. (2007a,b).

The alignment restriction is severe since the probability of a transit being observed is the ratio of the radii of the host star and the planet's orbit, which in general is small although it varies greatly from planet to planet. For known transiting planets the median radius r_{med} of the host stars is $1.01R_{\odot}$ and the median semi-axis radius a_{med} of the orbit is 0.056A.U. Since 1 A.U ~ $215.1R_{\odot}$, r_{med}/a_{med} is approximately 1/12. The planets most likely to be detected by the transit method are a) those which cause the greatest decrease in brightness i.e. those with large radii and b) those with orbits close to their parent star, because they have a shorter orbital period, and so make more frequent transits.

Data are obtained in the form of photometric light curves which are analysed to search for periodic intensity dips. Thus the telescope observing the transit need only have a large enough aperture to measure the depth of the intensity dip to sufficient accuracy. Some ground based transit survey facilities use arrays of moderate sized wide angle telescopes which survey a wide area of the sky simultaneously and so increase the detection rate e.g. WASP (Wide Angle Search for Planets - Pollacco et al. 2006, also www.superwasp.org) and HATNet (Hungarian Automated Telescope Network - Bakos et al. 2007). The apertures of the lenses are SuperWASP – 11.1 cm, HATNet – 11 cm and HATNet (Southern hemisphere network) – 18 cm. The WASP facilities comprise an array of 8 telescopes and cover an area of over 22 degrees square per pointing. In order to

illustrate the modest size of the instrumentation required, a photograph of the WASP South array at the South African Astronomical Observatory at Sutherland is shown in. 2.3a and its housing in Fig. 2.3b. The photographs were taken by the author.

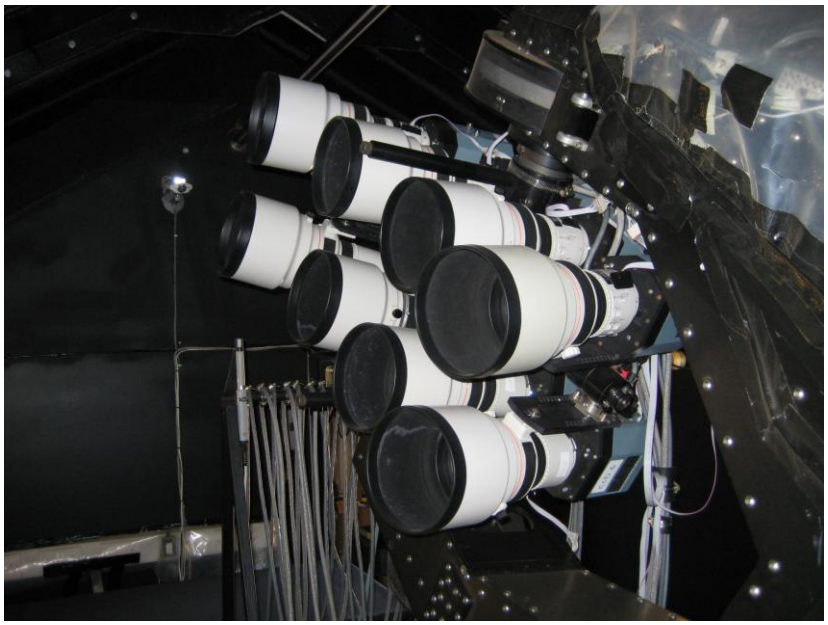

The WASP South telescope array at the South African Astronomical Observatory at Sutherland (Fig. 2.3a) and its housing (Fig. 2.3b). The photographs were taken by the author.

2.2.2 Basic principles of analysis.

In principle, the star and planet parameters can be derived by combining a geometrical analysis from the profile of the photometric light curve, Kepler's Third Law and an assumption from stellar properties.

The geometrical analysis has been described in detail by Seager and Mallén-Ornelas (2003), and by Collier Cameron et al. (2007b). The ratio $(R_P/R_S)^2$, where R_P and R_S are the radii of the planet and star, is simply the relative reduction ΔF of the observed stellar flux when the whole planet obscures the star. The other parameters which may be obtained purely from the profile of the light curves are a) the ratio of the planet's orbital radius to the stellar radius and b) inclination of the orbit to the line of sight. It is clear even without detailed analysis that the ratio a) is related to the ratio of the period to duration of the transit, and that for item b) the profile where the planet passes over the centre of the stellar disk will differ from that when the planet grazes it. This is illustrated further in Fig 2.4. Both these two articles point out that their analysis can be refined to include limb darkening.

The analysis to this stage leads to only the relative dimension of the planet to host star, the relative dimension of the host star radius to the orbital radius, and the ratio of the mean stellar density to that of the Sun. The first step to obtain the actual masses of the star and planet is to introduce Kepler's Third Law i.e.

$$(M_S + M_P) = \frac{4\pi^2 a^3}{GP^2} \qquad 2.1$$

where

M_S and M_P are the masses of the star and planet
a is the radius of the planetary orbit
P the planetary orbital period, and G is the gravitational constant.

In practice $M_P \ll M_S$ i.e. the relation between the orbital radius and the period is effectively independent of the mass of the planet. The dependence of the gravitational force on the planet due to its mass cancels the dependence on the inertia of the planet. Combining Eqn. 2.1 with the geometrical analysis gives the average stellar density relative to the Sun which is (Seager and Mallén-Ornelas, 2003, Eqn. 9):

$$\frac{\rho_S}{\rho_\odot} \equiv \frac{\frac{M_S}{M_\odot}}{\left(\frac{R_S}{R_\odot}\right)^3} = \left[\frac{4\pi^2}{P^2 G}\right]\left[\frac{\left(1+\sqrt{\Delta F}\right)^2 - b^2\left(1 - sin^2\left(\frac{t_T\,\pi}{P}\right)\right)}{sin^2\left(\frac{t_T\,\pi}{P}\right)}\right]^{\frac{3}{2}} \qquad 2.2$$

In this expression:

ρ_S and $\rho_\odot$	are the average densities of the host star and the Sun
b	is the impact parameter (a/R_S) cos i where i is the inclination of the planetary orbit as observed from the Earth (i = 90° if the orbit is edge on). This is the projected distance between the centre of the host star and the exoplanet in units of R_S.
t_T	The total transit duration i.e. the period between the time the exoplanet just starts to obscure the stellar disk to the time when the exoplanet finally clears it completely.

Other quantities have been defined previously.

These and other parameters which are needed for the analysis of transit light curves are illustrated in Fig. 2.4, taken from Fig. 1 of Seager and Mallén-Ornelas (2003). This shows the disc of the host star marked as radius R_*, and that of the exoplanet, marked as R_P. Schematic light curves are shown as a full line for i = 90° i.e. b = 0 and as a dotted line for a representative value with i < 90°. The Figure also illustrates t_F, the "flat" part of the light curve, which is the time during which the whole of the exoplanet disc obscures of the host star surface.

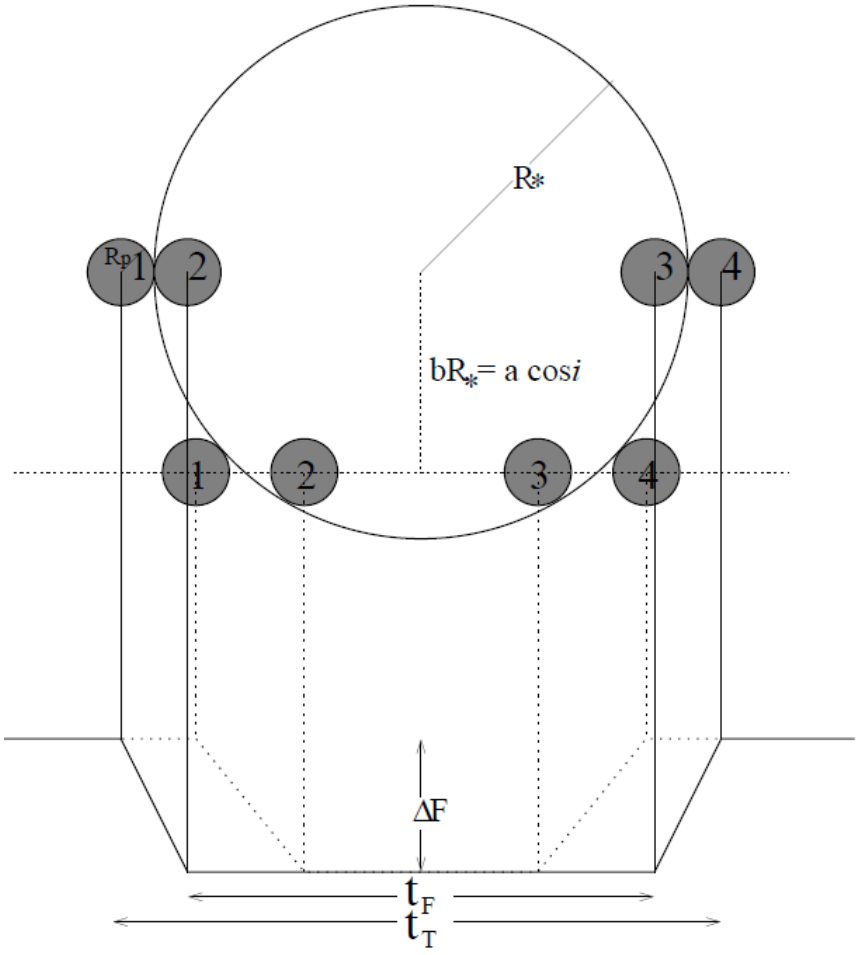

Fig. 2.4 Illustration of parameters defining light curves from transiting exoplanets.. Further explanation is given in the text. Taken from Fig.1 of Seager and Mallén-Ornelas (2003).

An example of an actual light curve is shown in Fig. 2.5, which is the light curve obtained by Southworth at al. (2011) for the WASP 7 system.

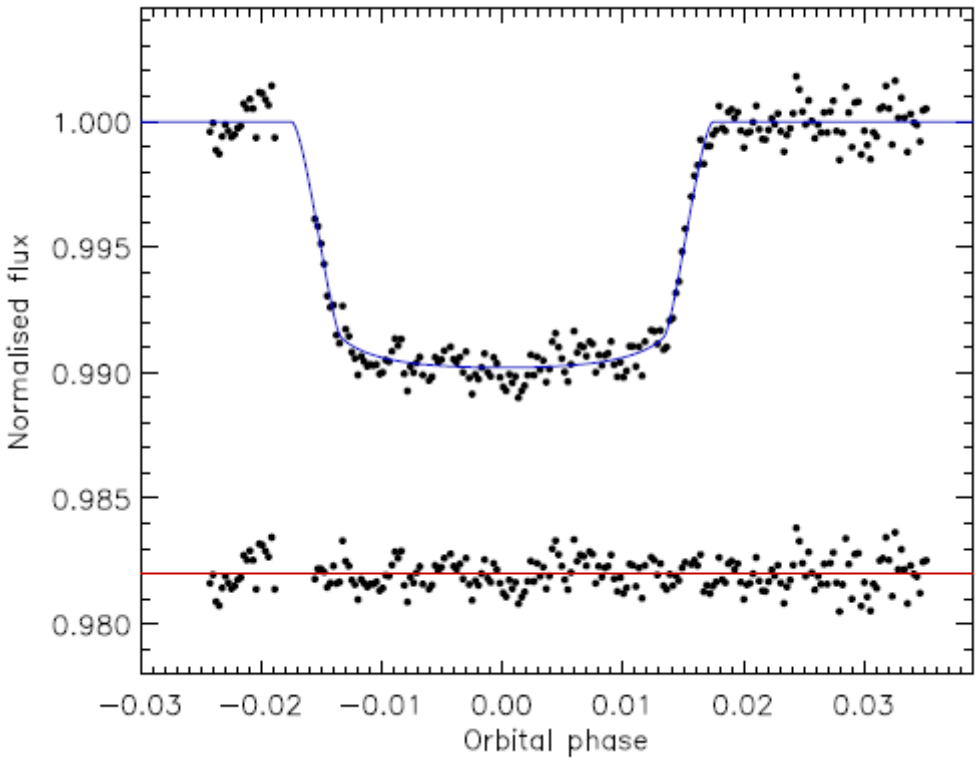

Fig. 2.5 Photometric light curve for WASP 7, taken from Fig. 1 of Southworth at al. (2011). The upper series of dots show the flux measurements during a single transit, normalised to unity when there is no transit. The blue solid line is the best fit found by JKTEBOP (Appendix F). The lower series of dots show the fitting residuals, offset for clarity.

Since Eqn. 2.2 gives only the (mean) density, the task of determining the actual mass and radius of the host star still needs some relation between these quantities, in other words an additional assumption about stellar properties (Torres et al. 2008). Various approaches towards this have been described in the literature. Seager and Mallén-Ornelas (2003) impose a power law dependence of the stellar radius upon mass, and use the simple empirical mass/radius relation ($R_S \sim M_S^{0.8}$). Observations with the ultimate aim of improving understanding of the mass/radius relation are the subject of Parts II and III of this thesis. Collier Cameron et al. (2007b) derive the stellar mass from the J-H colour

index, obtainable from the 2MASS point source catalogue of Skrutskie et al. (2006), and then use the relation $R_S \sim M_S^{0.8}$. Southworth (2008) and Torres et al. (2008) use detailed stellar evolution models; Southworth compares results from a series of models and so can estimate the systematic uncertainty due to the choice of model. As also pointed out by Southworth, it is possible to avoid relying on stellar evolution theory if the host star is near enough for accurate values of the necessary stellar parameters to be determined directly, either stellar distances by the parallax method e.g. from the Hipparcos mission (van Leeuwen, 2007), or angular diameter e.g. from interferometric measurements such as those of Baines et al. (2009). However most exoplanet host stars discovered by the transit method are too far away for this to be possible at present. This situation will improve when results from the *Gaia* astrometric mission launched in December 2013 (Sect. 10.3.1) become available. Eyer et al. (2012) present a diagram (their Fig. 1) showing how the precision of a parallax measurement with *Gaia* varies with the magnitude of the host star. The median V-band magnitude of a host star observed by the *Kepler* mission is about 14.1, for which the precision of a parallax measured by *Gaia* is expected to be ~ 0.02 milliarcseconds.

In practice a MCMC (Monte Carlo Markov Chain) method is used instead of the geometrical relations by themselves. The principles by which a MCMC method was applied to the analysis of the WASP-1 and -2 systems have been described by Collier Cameron et al. (2007b) and are summarised very briefly as follows. First, a set of six "proposal parameters" are chosen, five of them describe the light curve and the sixth is the mass of the host star. A set of four "physical parameters", the radii of the host star, planet and exoplanet orbit and inclination angle of the orbit are derived from the proposal parameters. The fluxes from each observation point in the light curve are then calculated from the algorithm of Mandel and Agol (2002). A set of flux deficits is obtained from the

differences between the calculated and observed fluxes and a χ^2 value calculated. One proposal parameter is perturbed randomly and another χ^2 value calculated. The new set of proposal parameters is accepted or rejected by a criterion related to the new χ^2 value. Plots are generated from pairs of system parameters with a "cloud" of data points. Each point in this cloud corresponds to an accepted set of proposal parameters. An example of one such plot is shown in Fig. 2.6, which is a mass/radius correlation diagram for the host star of the WASP-1 b exoplanet. It is interpreted so that the stated error bars contain the data points within 1σ of the centroid i.e.a fraction 68.3% of all the points. Thus for this particular case the error bars $M_S/M_\odot$ = 1.24 +0.12/-0.17 and $R_S/R_\odot$ = 1.382 + 0.047/-0.116 are narrower than a cursory look at the cloud would suggest.

Further detailed descriptions of the application of the MCMC method to the analysis of an exoplanet system have been given Holman et al. (2007) for the exoplanet XO-1b and Burke et al. (2007) for XO-2b. In many discovery papers the light curve fitting has been carried out simultaneously with stellar parameters obtained from the radial velocity method described in the next subsection, as is standard practice with exoplanets discoved by the SuperWASP survey cited above.

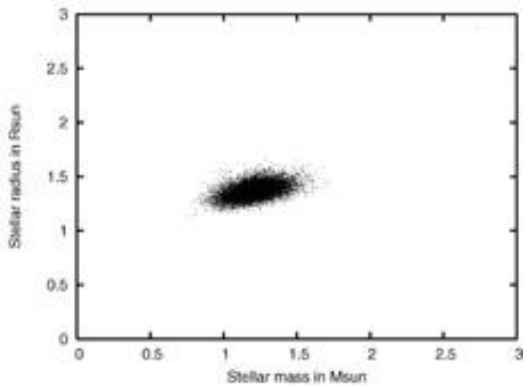

Fig. 2.6 Data point cloud for stellar radius versus mass derived from an MCMC analysis of WASP-2. Taken from one of the Figs. 5 of Collier Cameron et al. (2007b).

2.2.3 Spin-orbit alignment

The alignment of the planetary orbit with the rotational axis of the host star can be investigated by the Rossiter-McLaughlin effect. One of the two observable quadrants of the photosphere of a star will be approaching the observer and the other will be moving away. If a stellar disc is unobstructed the associated blue and red shifts in a spectral line will cancel. If an exoplanet or binary component transits the stellar disc, the cancellation is incomplete and the line profile becomes asymmetrical. The centroid (flux weighted mean wavelength) of the profile will be displaced from the unperturbed value first in one spectral direction and then to the other. This will introduce a shift in the apparent radial velocity. This may be used to determine the spin-orbit alignment angle λ between the rotational axis of the host star and the orbital plane of the exoplanet; this in turn can in principle provide an insight into the dynamical origin of the exoplanet. The theory of the radial velocity profiles has been described in detail by Ohta et al. (2006), and the application to the transit method assessed by Gaudi and Winn (2007). These latter authors present the temporal profile of the calculated shifts in the wavelength centroid for an exoplanet system similar to HD 209458 for the cases of an impact parameter $b = 0.5$ and inclination angles $i = 0$, 30 and 60. These are reproduced as Fig. 2.7 below.

Triaud et al. (2010) have described how the Rossiter-McLaughlin effect has been used to determine the spin-orbit angle λ of six exoplanets diecovered by the Super WASP survey. Their results show a degeneracy between λ and $v \sin i$, the projected rotation velocity of the star; since these authors used an MCMC analysis their results are shown (e.g. their Fig. 3) as a data point cloud similar to Fig. 2.6.

The observations require the high precision spectroscopic instrumentation used for the radial velocity method described later (Sect. 2.3.2).

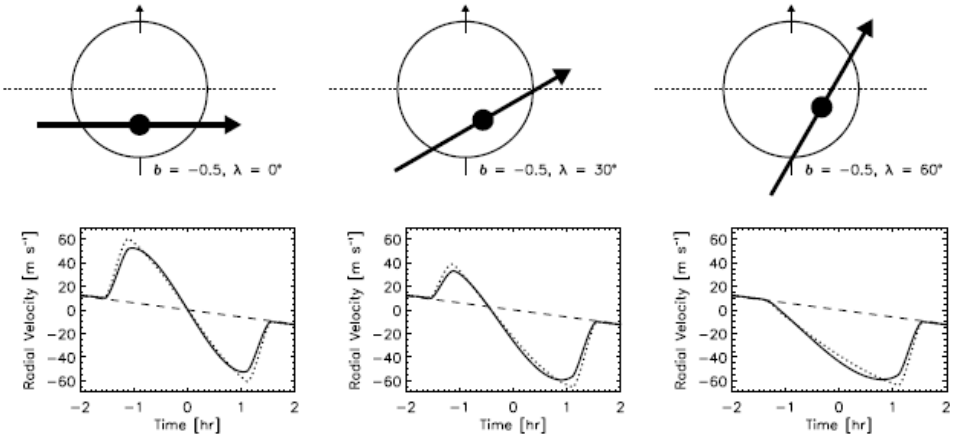

Fig.2.7 Temporal profile of the wavelength shift due to the Rossiter-McLaughlin effect for a series of spin-orbit angles explained in the text. Taken from Fig. 2 of Gaudi and Winn (2007).

2.2.4 Experimental details

The era of exoplanet discovery by the transit method opened with surveys by ground based telescope arrays with only modest apertures, of order 100 mm. These were sufficient to show a periodic ~1 % dip in intensity, i.e. radii down to order one tenth of the stellar radius, or roughly the size of Jupiter for a main sequence star. Two major ground based surveys are SuperWASP and HATNet referenced earlier. These surveys have discovered 88 and 56 exoplanets respectively by 31 July 2014 (two exoplanets have been discovered independently by both surveys). Other ground based surveys are TrES (Alonso et al. 2004), and XO (McCullough et al. 2006). Constraints on telescope and detector design have been discussed by Latham et al. (2009). Progress up to 2009 was reviewed by Mazeh (2009) who gave references to the survey programmes and details of the observing systems, and quoted magnitude ranges. The OGLE (Optical Gravitational Lensing Experiment) project (Udalski et al. 2002, Udalski 2007), was set up to detect dark matter by microlensing and uses a ground based 1.3 metre telescope in Chile. It has also descovered 8 exoplanets by the transit method and 16 by microlensing (Sect. 2.4). The first

space based exoplanet mission was COROT (Bordé et al., 2003, Barge et al. 2008, Auvergne at al., 2009), launched in December 2006. It was equipped with a 27 cm telescope and had discovered 27 exoplanets before a computer failure in November 2012, and a decision in June 2013 to decommission it.

A major recent space based survey is the *Kepler* mission (Basri et al., 2005; Borucki et al., 2010a,b). This was launched in March 2009, and has a 0.95 metre aperture telescope. It carried out a detailed survey of an area mainly in parts of the constellations Cygnus and Lyra and also a small section of the constellation Draco. It orbits the Sun with a period of 372 days in an orbit where it gradually lags further behind the Earth. *Kepler* has major advantages. Since it is space-based the observing platform is more stable and the observed intensities are free from fluctuations induced by the atmosphere. The telescope aperture is an order of magnitude larger than for the ground based surveys and so *Kepler* can detect exoplanets with radii an order of magnitude smaller i.e. down to the size of the Earth. *Kepler* has detected 982 exoplanets (including 5 detected independently) from 392 systems. The host stars lie in the magnitude range V = 11 to 16. The collection of science data ceased in May 2013 after the failure of a second gyroscope reaction wheel. It is now proposed to use the *Kepler* satellite in a modified manner to continue operating it as the K2 mission.

An advantage of the transit method is that follow-up studies can analyse the light from the star which passes through the atmosphere of the planet and so provide information about atmospheric composition (e.g. Charbonneau et al. 2002). The exoplanet system may also be observed at secondary eclipse (when the planet is hidden by its host star), and the intensity subtracted from the value before or after the eclipse; this isolates the radiation emitted by the planet itself so its effective temperature can be estimated (e.g. Charbonneau et al. 2005, Deming et al. 2005). These issues are outside the range of this

thesis and so are not described further. A disadvantage is that periodic variations in the photometric light curve may also be due to eclipsing binaries and variable stars. A rough indication that intensity variations are due to an eclipsing binary, instead of an exoplanet, is that both members of the system are luminous and that in general the photometric light curve will have two different dips with alternating profiles.

2.3 The Radial Velocity Method

2.3.1. Main features

The gravitational pull from an orbiting exoplanet causes the host star to wobble in a periodic reflex action about the system's centre of mass. This causes a minute periodic Doppler shift in the radiation from the star. This was the method used to discover the first known exoplanet orbiting a solar type star i.e. 51 Pegasi b on 5 October 1995 (Mayor & Queloz 1995) and as at 16 March 2015, 593 further exoplanets. Radial velocity surveys concentrate on bright stars nearer than 100 pc because a high signal to noise ratio is essential for the analysis of the spectra; however the radial velocity method can nevertheless also be used to confirm more distant planets.

The best fits to the observed shifts leads to values for a) the projected amplitude of the reflex velocity, b) the period and eccentricity of the planet's orbit and c) the angle of periastron (Sect. 12.4). The minimum values for the mass and semi-major axis of the planet's orbit can then be calculated from Kepler's Third Law (Eqn. 2.1). The second part of this thesis describes an analogous analysis of the radial velocity observations of V1094 Tau. The observed shift is the projected component of the gravitational wobble along the line of sight; this is why only the minimum values of the mass and semi-major axis can be determined. These are the values these quantities would have if the angle of inclination

were i = 90°. Combining Kepler's Third Law with the requirement that there is no net force on the centre of mass shows that the reflex velocity amplitude scales as $P^{-⅓} M_P M_S^{-⅔}$, or alternatively $a^{-½} M_P M_S^{-⅔}$, where P and a are the period and semi-major radius of the (elliptical) orbit of the exoplanet, and M_P and M_S the masses of the exoplanet and host star. These dependences show that radial velocity surveys are biased towards massive exoplanets, as may be expected intuitively, and towards short orbital periods. In this respect they are similar to the transit surveys.

Radial velocity surveys have been carried out at the Keck Observatory at Hawaii, the Lick Observatory, the Anglo-Australian Telescope and the HARPS (High Accuracy Radial velocity Planet Searcher) facility. The HARPS facility (www.eso.org/sci/facilities/lasilla/instruments/harps.html) is representative and consists of a fibre-fed high resolution echelle spectrograph mounted on the ESO (European Southern Observatory) La Silla telescope in Chile with a spectral resolution $\lambda/\delta\lambda$ = 120 000. It can measure radial velocities to a precision of 0.97 m s^{-1}. A sister HARPS-N facility (N for Northern Hemisphere) with effectively the same instrumentation was installed at La Palma in 2012. Exoplanets discovered by the HARPS facilities have been reported in a series of papers by Mayor of the Geneva Observatory and collaborating institutions; as of 12 March 2015 36 papers have been published.

A typical radial velocity curve is that obtained for the star HD 72659 by Moutou et al. (2011) on the HARPS La Silla facility and Keck telescopes, and shown in Fig. 2.8. This Figure shows typical values of the radial velocity amplitudes and the precision of radial velocity measurements. It is an example of how a radial velocity curve departs from being sinusoidal because the exoplanet orbit is eccentric.

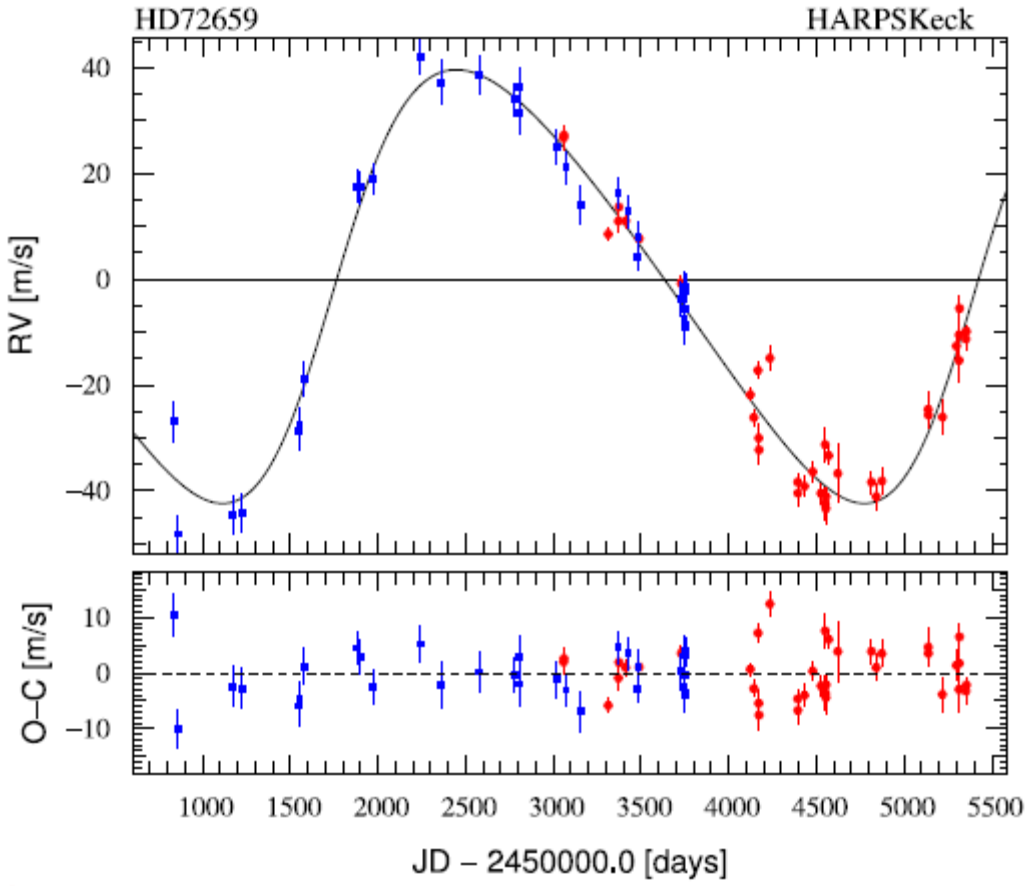

Fig. 2.8 Radial velocity curve for HD 72659. The radial velocity amplitude of the star is 41.0 ± 1.3 km s^{-1}. The curve departs from sinusoidal because the orbit of the exoplanet is eccentric (e = 0.22 ± 0.03). The lower panel shows the fitting residuals. The points marked in blue and red were measured by the HARPS and Keck telescopes respectively. Taken from Fig. 4 of Moutou et al. (2011).

2.3.2 Experimental Difficulties and Limitations

The amplitude of the reflex velocity oscillation of the host star is extremely small. From Kepler's Third Law it may be seen that if an exoplanet has an orbital radius of 1 A.U, the planetary mass of about $10M_{Earth}$ is required to induce a radial velocity amplitude even as large as 1 m s^{-1}, the precision achieved by the HARPS facility. Thus effective detection techniques require the measurement of minute Doppler shifts since a radial velocity of 1 m s^{-1} corresponds to a wavelength shift $\Delta\lambda/\lambda$ of $1/(3\times10^8)$. The

dispersed echelle spectrographs normally used have resolutions of only some tens of thousands, e.g. 120 000 for HARPS, hence it is necessary to measure Doppler shifts three orders of magnitude smaller than the resolution, which is typically equivalent to order one thousandth of a pixel of a CCD detector on a spectrograph. The techniques employed to meet the formidable challenge of measuring such small shifts have been described briefly by Butler et al. (1996) and in detail by Baranne et al. (1996) and particularly clearly by Johnson et al. (2006). Essentially a reference spectrum containing very many lines is taken at the same time as the stellar spectrum and the cross-correlation between these two large groups of lines is analysed. In one method the target star is observed through an iodine cell which provides the reference spectrum superimposed on to the target spectrum so problems introduced by flexure of the instrument are eliminated. The cell is maintained at a pressure of about 0.001 atmospheres and a temperature of 50 °C so that the iodine exists as a molecular gas and imposes many thousands of very sharp lines on to the stellar spectrum. An alternative, used on the HARPS facility, is that the target spectrum and a reference thorium spectrum are observed simultaneously with two identical optic fibre feeds.

Before radial velocity variations can be ascribed to a planet, alternative explanations must be considered. The main ones are a) surface inhomogeneities (starspots), b) stellar pulsations and c) an eclipsing binary. A discussion of this is outside the scope of this thesis but an important technique is to observe the shape and centroid of spectral lines. A true radial velocity oscillation will shift a spectral line uniformly; in contrast the rotational modulation due to inhomogeneities will not do so (Queloz et al. 2001, Santos et al. 2002 and references cited in these papers), and will have a different period. Spectral shifts due to stellar pulsations typically have much shorter periods (typically 1 hour for Sun-like stars) than genuine radial velocity shifts. The presence of an eclipsing binary is

often betrayed because the secondary star is much more massive than a putative exoplanet and so induces a much greater wavelength shift.

2.4 Combination of methods

Neither of these two methods can provide a complete analysis of an exoplanet system by itself. The transit method does not provide the mass of the the planet and the radial velocity provides only values of the planet mass and semi-major axis corresponding to the projected radial velocity. A complete solution can be obtained if both methods are used, essentially because the transit method provides the angle of inclination and hence the true planet mass and semi-major axis. Candidate transiting exoplanets are therefore frequently observed with the larger telescopes needed to obtain the good signal to noise ratio necessary to apply the radial velocity method. Ideally best values should be determined by obtaining a simultaneous best fit to data sets from both methods. The follow-up observations can also discriminate between periodic intensity dips due to an exoplanet and those due to eclipsing binaries and variable stars. A major difficulty however for candidate exoplanets discovered by deep sky transit surveys is that the host stars are fainter and observations typically require significant time on 8 metre class telescopes (Bayliss et al., 2009).

Given the mass and radius of the exoplanet, the mean density and surface gravity are known. The composition of the planet can then be inferred. Further properties of the planet then follow. Given the surface temperature of the host star, and a value for the albedo of the planet, the effective temperature of the planet can be calculated. Thus the thermal velocity of any gases which may exist in the planetary atmosphere can be calculated and compared with the escape velocity. The physical parameters of the planets

can be compared with theories of planetary structure and evolution (e.g. Sato et al. 2005: Guillot et al. 2006; Fortney et al. 2007).

Some of the facilities and missions for the two exoplanet methods discussed above are also used to study stars by asteroseismology; this field is briefly described later (Sect. 7.1.3).

2.5 Other detection methods

A few exoplanets have been discovered by other methods e.g. namely gravitational microlensing (Udalski et al. 2002), and direct imaging (Kalas et al. 2009). These methods are outside the range of this thesis and are not described further. All the detection methods, except direct imaging, are indirect in that what is observed is the effect of the exoplanet, not the planet itself.

CHAPTER 3 COMPOSITION AND COMPARISON OF EXOPLANET HOST STAR SAMPLE

3.1 Definition of Samples

The starting point of this investigation of biases between the two main methods for detecting exoplanets is to define samples of host stars discovered by each method i.e. as follows.

- The "Bright Transit Sample", hereafter called the BTS, contains all eligible host stars where the planet has been discovered by the transit method in a wide angle, ground based survey.
- The "Radial Velocity Sample", hereafter called the RVS, contains all eligible host stars where the planet has been discovered by the radial velocity method, and which lie on the main sequence and where the kinematics data are known.

The nature of this investigation requires that the BTS sample is defined as the complete sample of bright stars with exoplanets discovered by transit detection. Thus it excludes exoplanets discovered by the radial velocity method and later found to be transiting, for example those from the host stars HD 209458. The BTS is confined to wide-angle ground-based surveys because it is only for these surveys that the kinematic data are available for most or all of the stars. The exoplanet host stars detected by the space borne missions tend to be much further away and so the distances and proper motions are frequently not available. A comparison of the just two distances of host stars detected by the main ground based surveys and the distances measured by the *Hipparcos* space survey is given in Table 3.4.

The samples were intended to include all suitable host stars known to the author during the first stage of his project. Thus the samples are restricted to stars where the data has been published or has become otherwise publicly available by the cutoff date of 31

January 2011. If the samples had been prepared at the time of final writing, July 2014, they would have been much larger.

3.2 Restrictions on samples

These samples were aimed to include as many stars as possible from the Extrasolar Planets Encyclopaedia (www.exoplanet.eu) before the January 2011 cutoff, but some groups were excluded.

The first group is stars where the required data are unknown, generally radial velocity, metallicity or age.

The next group is the close binaries since interactions between the stars may affect their evolution and hence the processes whereby an exoplanet may form; such interactions are a major theme of Parts II and III of this thesis. The criterion for a star to be a binary is taken as a separation less than 500 A.U. This criterion follows that of the catalogue of Holmberg et al. (2009) which does not flag stars known to be binaries e.g. from the list of Raghavan et al. (2006) but where the projected separation is wider than 500 A.U. The catalogue of Holmberg et al. is the one used later as the source of the calibration samples. The samples do include stars flagged as binaries by Holmberg et al. where there is no evidence in the literature that the star actually is one. They also include widely separated binaries with separations exceeding 500 A.U. These are WASP-2 (Daemgen et al. 2009), HAT-P-1 (Bakos et al. 2007), TrES 2 and 4 (Daemgen et al. 2009) and XO-2. (Burke et al. 2007).

Thirdly, the samples are confined to stars with surface temperatures of 5400K or more because catalogues for calibration stars for lower temperatures are incomplete, again

because they do not list all the necessary stellar or kinematic parameters. A convenient source for available catalogues is the VizieR catalogue service (Ochsenbein et al., 2000). Listings for these parameters and age for these fainter stars are fragmentary. For example the catalogue by Kharchenko et al. (2007) gives radial velocities for many K- and fainter type stars, but not the surface temperature T_{eff} nor the metallicity *[Fe/H]*. The restriction to stars with T_{eff} hotter than 5400 K corresponds to F-, G- and just four K-type stars, all four of which are in the RVS, and also means that for both samples about 20% of otherwise eligible host stars are excluded.

Fourthly the samples exclude red giants. The transit method cannot be used for red giants because these stars have much larger radii, hence the ratio of exoplanet and stellar diameters is much smaller, thus the intensity dip due to the transit is too shallow to detect by current surveys. Since this analysis relies on treating each group equally, and there are no red giants in the BTS, they must also be excluded from the RVS. The criterion used for a star to be a red giant is that of Aumer and Binney (2009), where Fig.1 is an HR diagram showing the boundary between the Main Sequence and red giants. This figure plots the Hipparcos magnitude Hp versus the B-V colour index, and shows a boundary between the Main Sequence and Red Giants which is the lines joining the points in Table 3.1.

Table 3.1 Criterion for regarding a star as a red giant.

B-V	H_p
-0.3	-6
0.5	0
0.8	4 ⅔
1.5	7 ⅔

This criterion is shown diagrammatically in Fig. 3.1, which shows for comparison the ZAMS (Zero Age Main Sequence), for which values are taken from Table 3.9 of Binney and Merrifield (1998). That table adopts the V-band magnitude as the independent variable and the necessary transformation from this magnitude scale to the Hipparcos magnitude Hp is taken from Table 1 of Bessell (2000).

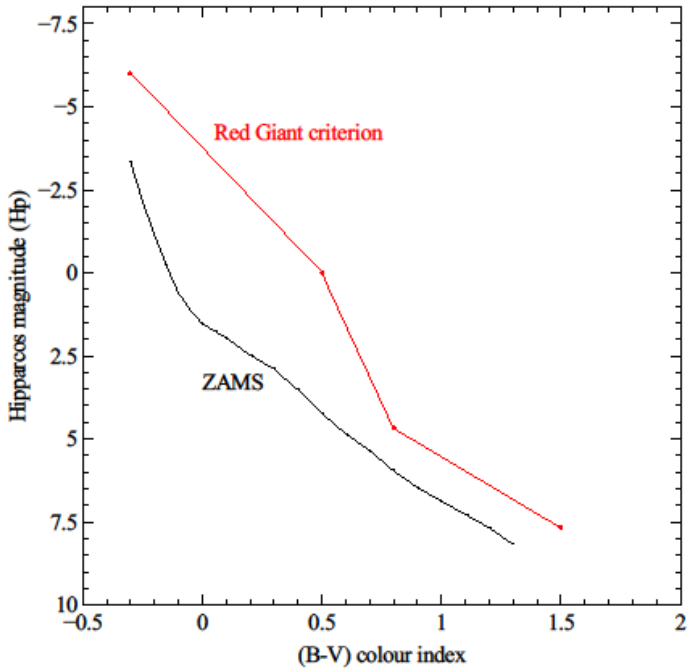

Fig. 3.1 Criterion for regarding a star as a red giant. The black line shows the ZAMS and the red line the red giant criterion.
The ZAMS data is taken from Table 3.9 of Binney and Merrifield (1998).

If a star has a Hipparcos magnitude H_p lower than this boundary for its B-V index i.e. higher up on the H-R diagram as conventionally plotted, it is regarded as a red giant.

Other particular exclusions are a) the host star of the previously reported exoplanet WASP-9b, now retracted (Extrasolar Planets Encyclopaedia) and excluded from the BTS and b) the two globular cluster stars NGC 2423-3 and NGC 4349-127 (Lovis and Mayor, 2007), excluded from the RVS for reasons which will become obvious when the analysis procedure is explained.

The exoplanet host stars which are finally included in the BTS and RVS are listed below.

3.3 List of sample stars

A table of all the data used in Part I of this thesis would be extremely large and unwieldy. Tables 3.2a and 3.2b therefore simply lists the stars themselves; the sources of the relevant stellar data are indicated in later sections as appropriate.

Table 3.2a List of BTS stars

HAT-P-1,2,4,5,6,7,8,9,13,14,15,16,21,23,24,25

TrES-3,4

WASP-1,3,4,5,6,7,8,12,13,14,15,16,17,18,21,24,26,28,31,34,37,41.

XO-1,3,4

Table 3.2b List of RVS stars

For stars with identifiers in both the Flamsteed/Bayer systems and a HD catalogue number, this list follows the usage of the Extrasolar Planets Encyclopaedia (Website Reference List).

Upsilon Andromedae, Mu Arae, 30 Arietis B, 51 Pegasi, 47 Ursae Majoris, 61 and 70 Virginis.

HD 1461, 2039, 4113, 4203, 4208, 4308, 5388, 6434, 6718, 8535, 8574, 9578, 10180, 10647, 10697, 12661, 13931, 16175, 16417, 20367, 20782, 23079, 23127, 23596, 25171, 28185, 30562, 31253, 33283, 33564, 34445, 37124, 37605, 39091, 40979, 43691, 44219, 45350, 49674, 50499, 50554, 52265, 60532, 63765, 66428, 68988, 69830, 70642, 72659, 73526, 74156, 75289, 75898, 76700, 81040, 82943, 83443, 86264, 89307, 89744, 90156, 92788, 102117, 102365, 106252, 107148, 108147, 108874, 109749, 111232, 117207, 117618, 118203, 121504, 125612A, 129445, 134987, 141937, 142022A, 142415, 145377, 147018, 147513, 148516, 149026, 152079, 153950, 154345, 154857, 155358, 156411, 159868, 168443, 168746, 170649, 171028, 178911B, 181720, 183263, 185269, 187123, 188015, 190360, 190984, 196050, 204313, 205739, 208487, 209458, 210277, 212301A, 213240, 216435, 216437, 217786, 219828, 221287, 222582, 224693, 330075.

HR810.

3.4 Source and calculation of stellar parameters

This kinematics study requires four stellar parameters, those being compared i.e. metallicity and age, and those used to form the calibration sample i.e. T_{eff} and Z_{max}. The parameter Z_{max} and the reasons for adopting it are explained later (Sect. 4.5.1). Values of metallicity, age and T_{eff} can be obtained from the literature for the actual sample stars with the adjustments explained in Section 3.9. Values of these parameters for the calibration stars are available in the Geneva-Copenhagen Survey (GCS) catalogue of Holmberg et al. (2009), hereafter H09.

The remaining parameter required is Z_{max}. Values of Z_{max} are given by GCS for the calibration and most of the RVS stars, but they are not adopted but instead are calculated afresh. This is because GCS includes only a very few BTS stars, and it is essential for the purposes of this study to calculate all Z_{max} values by a consistent method. The method used here is quite lengthy, and proceeds in the following steps.

- Obtain the distance of the star. (Section 3.5).
- Obtain the position and velocity in the Local Standard of Rest (LSR) (Section 3.6).
- Transform the LSR positions and velocities to absolute Galactic coordinates (Section 3.7)
- Use these values to calculate Z_{max} (Section 3.8).

3.5 Distance of star

Distances for the RVS stars can be obtained from the parallaxes from the *Hipparcos* astrometric mission (Perryman et. al. 1997). In contrast all but two of the BTS stars are too distant to be listed there; these two stars are the host stars for WASP-18 and HAT-P-2 stars (where the Hipparcos parallaxes have relatively wide error bars). Nevertheless, distances of the BTS stars can still be determined by the following consistent method since absolute

values of stellar masses and radii follow directly from the analysis of the exoplanet system. The starting point is the simple geometrical relation for the distance *D*

$$D = \frac{2R_S}{\theta_{LD}} \qquad 3.1$$

where

R_S is the absolute radius of the star

θ_{LD} the limb darkened (LD) angular diameter

Values of R_S were obtained either from the discovery papers or from later papers which present refined or homogeneously derived data, mainly from Southworth (2010) but also Ammler et al. (2009), and Torres et al. (2008). If a stellar radius appears in more than one of these three papers the most recent paper was used.

The limb darkened (LD) angular diameter θ_{LD} of a star can be calculated from T_{eff} and the K band magnitude by the empirical relation given by Kervella et al. (2004) i.e.

$$Log\ \theta_{LD} = 0.8470\,x^2 + 7.0790\,x + 15.2731 - 0.2K \qquad 3.2$$

where: x = log T_{eff}

K is the K band magnitude.

Kervella et al. derive nine relations in this form, one for each of the nine standard spectral bands in the visible and infrared regions. They consider measurements of T_{eff} and θ_{LD} for a suitable sample of nearby stars and derive the best fit relation. Nearby stars were used because the angular diameters can be measured directly and independently from interferometry. The reasons for choosing the K band relation for this study are in two steps. First, Kervella et al. find that the best fit i.e. smallest total residuals between the

measurement points and fitted curves are obtained for the infra-red K and L bands, since there are few spectral features in the infrared and so the properties of the stellar atmosphere such as composition, surface gravity, and rotation have only a weak effect on the surface brightness as a function of T_{eff}. For both these bands the dispersion of the residuals is so small that it is undetectable from the data. The second step is that of these two bands accurate values are available only for the K band magnitudes, namely from the 2MASS catalogue (Cutri et al., 2003). The K band magnitude required by Eqn. 3.2 was obtained from the 2MASS value of K_S by the transformation given by Bessell (2005, Sect 5.5), i.e. $K = K_S + 0.044$.

The reason why a semi-empirical relation between angular diameter, T_{eff} and magnitude is possible at all, and the reason for the form of this relation, can be understood because stars are approximate black bodies. For a true black body the surface temperature gives a total power radiated per unit area. The K-band magnitude gives the total luminosity. A simple form is possible because the logarithm of the surface brightness is proportional to $log\ T_{eff}$ (from the Stefan-Boltzmann law). The $(log(T_{eff}))^2$ term is an adequate representation of i) stars are not ideal black bodies and ii) the colour index is not a linear function of T_{eff} (although the relation is roughly linear for some colour bands and temperature ranges)

Uncertainty in derived stellar distance

In order to consider the uncertainties in the derived distance in detail the basic equation (3.1) needs to be rewritten in terms of directly observable quantities T_{eff}, the mean stellar density ρ_S and the K_S band magnitude. In this formalism the stellar radius R_S is written as

$$R_S{}^3 = \frac{M\left(T_{eff}, \rho_s\right)}{\rho_s} \qquad 3.3$$

where the mass M is written as a function of T_{eff} and the mean stellar density ρ_S.

Combining Eqns. 3.1, 3.2 and 3.3 gives

$$d = 2 \times \sqrt[3]{\frac{M\left(T_{eff}, \rho_s\right)}{\rho_s}} \times 10^{-F\left(\log T_{eff}\right)} \times 10^{0.2K_s} \qquad 3.4$$

where $F(\log T_{eff})$ represents the first three RHS terms of Eqn. 3.2.

This equation, considered from broadly right to left for ease of description, shows that the sources of uncertainty ΔD in the derived stellar distance D are:

- Uncertainty in the K_S band magnitude
- Uncertainty ΔT_{eff} in the input value of T_{eff} used in Eqn. 3.2
- The fitting residual Δs from Eqn. 3.2
- A contribution from the stellar radius (cube root) term in Eqn 3.4, as discussed below.

The partial combined uncertainty ΔD_{part} in the derived stellar distance, due to the first three items is obtained by adding them in quadrature i.e.

$$\Delta D_{part}{}^2 = \Delta D(K_S)^2 + \Delta D\left(T_{eff}\right)^2 + \Delta D(\Delta s)^2 \qquad 3.5$$

At first sight the final contribution, from the uncertainty in the stellar radius R_S, can be included as an independent fourth term $\Delta D(R_S)^2$ in Eqn.3.5 . This is strictly incorrect because, as shown from Eqn. 3.4, the stellar parameter directly obtained from the observational data is the mean stellar density ρ_S. The stellar mass and hence radius R_S are then calculated from stellar evolution models e.g. Southworth (2009), but since one of the variables there is T_{eff}, the uncertainty contributions $\Delta D(T_{eff})$ and $\Delta D(R_S)$ due to T_{eff} and R_s are in fact linked. However the error introduced into the derived distance by treating the $\Delta D(R_S)^2$ term as a fourth independent contribution to Eqn. 3.5 is small. It can be estimated for the two stars where inverse density versus T_{eff} diagrams are available i.e. WASP 12

(Hebb et al. 2009, Fig. 6) and WASP-14 (Joshi et al. 2008, Fig. 8). By noting that the mean stellar density can be determined effectively exactly, it is easily shown that the uncertainty in T_{eff} leads to an added uncertainty of 1 – 1½ % in the distance, which is much less than the total estimated uncertainty of ~ 5%. Thus the uncertainty ΔD in distance is therefore taken here as that given at first sight by Eqn. 3.5 i.e.

$$\Delta D^2 = \Delta D(K_S)^2 + \Delta D\left(T_{eff}\right)^2 + \Delta D(\Delta s)^2 + \Delta D(R_S)^2 \qquad 3.6$$

Values for these uncertainties may be obtained from the corresponding uncertainties $\Delta(K_S)$ and so on by recalculating the distance for each end of the error bar. The parent uncertainties can be obtained from the literature as follows.

$\Delta(K_S)$	From either the SIMBAD data base SIMBAD.u-strasbg.fr/SIMBAD) or the 2MASS catalogue (Cutri et al., 2003; also VizieR catalog II/246).
$\Delta(T_{eff})$ and $\Delta(R_S)$	From published papers.
$\Delta(\Delta s)$	Kervella et al. state that this uncertainty is less than 1% and is "undetectable from (their) data" (their Sect. 4.3), hence a value of 1% is adopted.

The average percentage uncertainties in the derived distances is about ±5%, which is much lower than the average percentage uncertainty in distances quoted in the literature, namely ± 11%.

Justification of method

For two BTS stars the distances determined as above can be compared with *Hipparcos* measurements from the new reduction by van Leeuwen (2007). The comparison between distances determined by the two methods is shown in Table 3.3 below.

Table 3.3. Comparison of distances from present method and from Hipparcos.

Star	Diatance (pc)	
	Present method	Hipparcos
HAT-P-2	132 ± 12	135 ± 16
WASP-18	123 ± 5	99 ± 11

The agreement is regarded as satisfactory.

3.6 Positions and velocities in the LSR

The Local Standard of Rest (LSR) is a frame where the averaged motion of stars in the immediate neighbourhood is zero, and is a coordinate system which makes a circular orbit around the Galactic centre in step with the Sun.

The steps to calculate the positions and velocities in the LSR are as follows.

- Calculate these parameters in the equatorial frame.
- Transform to heliocentric Galactic coordinates
- Transform velocities relative to the Sun to velocity components along the axes of the LSR
- Correct these for the motion of the Sun within the LSR.

Positions and velocities in the equatorial frame

Positions in the equatorial frame i.e. where the $z = 0$ plane contains the Earth's equator can be obtained from the equatorial coordinates of Right Ascension and declination by simple geometry. The coordinates were obtained from the NOMAD catalogue (Zacharias et al. (2004), also VizieR catalogue I/297). Velocities in the equatorial frame were obtained similarly from the proper motions in the Hipparcos

catalogue where available or the NOMAD catalogue otherwise, and from the radial velocities. The latter are inherent in the analysis techniques and were obtained from the original discovery papers or later papers reporting updated values.

Transformation to heliocentric galactic coordinates

The transformations to the heliocentric galactic frame of reference were carried out by the standard equations of Johnson and Soderblom (1987) adjusted for Epoch 2000.0. These authors give matrix expressions i) for the transformation from equatorial coordinates to galactic coordinates, ii) for the components of velocity in the heliocentric frame and iii) the uncertainties in these components. This thesis follows the convention of these authors and denotes velocities in this frame by:

U in the Galactic plane towards the Galactic Centre

V in the Galactic plane in the direction of rotation around the centre

W perpendicular to the Galactic plane, towards the North Galactic Pole.

These velocities were corrected to those in the LSR by the transformation of Dehnen and Binney (1998) i.e.

$$[U_{LSR}, V_{LSR}, W_{LSR}]\text{Sun} = [10.00, 5.23, 7.17] \text{ km/sec.} \quad 3.7$$

3.7. Positions and velocities in the absolute galactic frame

The next step is to transform distances and velocities to the absolute galactic frame. This is defined so that Galactic centre is at the origin, the *XY* plane is in the plane of the thin disk and *Z* is positive towards the North Galactic Pole. In this frame the Sun is assumed to be at a position (*X*,*Y*,*Z*) = (8, 0, +0.017) kpc. The Sun's distance from the Galactic centre is based on Table 7.1 of Binney and Merrifield (1998) who quote values

obtained by five different methods and which range from 7.2 to 8.4 kpc. Measurements of this distance have been reviewed by Reid (1993). The Sun's position above the galactic disk was adopted from Joshi (2007), who gives an uncertainty of 0.003 kpc. The parameter *Z* is positive in the direction of the North Galactic Pole. A result used later is that the median values of the perpendicular distances *Z* from the galactic plane are 124 pc for the BTS and 21 pc for the RVS.

Velocities in the absolute Galactic frame were calculated by assuming i) that the velocity of the Local Standard of Reference (LSR) in the absolute frame is given by $[U,V,W]_{LSR} = [0, 220,0]_{ABS}$ km s^{-1}. This assumes that the LSR has no components of motion towards the Galactic centre or perpendicular to the Galactic Plane. The issue of the orbital velocity of the LSR about the Galactic centre has been discussed in detail by Majewski (2008), who quotes several determinations, mostly between 200 and 240 km s^{-1}. Galactic warp is less than 2° within 2 kpc for any galactic longitude (Momany et al., 2006) and so is ignored.

3.8 Calculation of Z_{max}

Method

These Z_{max} values were calculated from positions and velocities in the absolute Galactic frame by a program of Aarseth (private communication), which traces stellar orbits by numerical integration. This program starts from the input values of the current position and velocity in the absolute Galactic frame. It assumes simple analytical expressions for the mass distribution and gravitational potential of the Galaxy, developed by Miyamoto and Nagai (1975), where the Galaxy is regarded as axisymmetric with a central bulge and thin disk of finite thickness. Thus this ignores structure such as spiral

arms and any galactic bar which may exist. The model contains two free parameters, which can be associated with the radius of the Galaxy and the thickness of the thin disc.

The values finally adopted for distances and Z_{max} are available on request.

Distribution of Z_{max} values

The normalised distributions of the values of Z_{max} so calculated for the BTS and RVS are shown on Fig. 3.2a, and the corresponding distributions for the actual distances in Fig. 3.2b. It will be seen that although the difference between the two samples is obvious for the distance itself, as explained in the Introduction, it is less marked for Z_{max}. For the actual distance the median values are 264 pc and 44 pc for the BTS and RVS respectively but for Z_{max} they are 219 pc and 112 pc.

The median Z_{max} value lies within the range of observed distances from the galactic plane for the BTS, but well outside most of the range for the RVS. (In the RVS the distances of only two outliers out of the 129 stars exceed the median Z_{max} value) This shows an observational bias; the RVS stars are studied only during a relatively small part of their oscillation period about the Galactic plane i.e. when they are near this plane, whereas the BTS stars are studied over a much wider part of this period. This is the reason why the difference between the normalised distributions is much more striking for the actual distances than for Z_{max}.

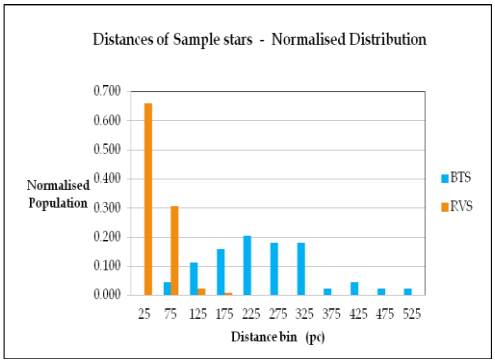

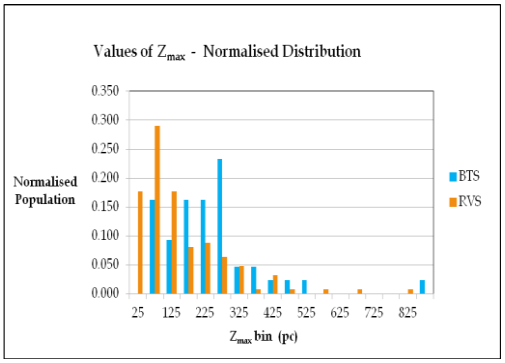

Fig. 3.2a (left) Normalised population distribution of actual distances for the BTS and RVS.

Fig. 3.2b (right) Normalised population distribution of Z_{max} values for the BTS and RVS.

Comparison with Z_{max} values of Holmberg et al.

The values of Z_{max} for the calibration stars as calculated by the program of Aarseth may be compared with the values actually given in GCS. The median values are respedtively Aarseth: 119 pc and GCS 150 pc (to the nearest 10pc, since GCS quotes only to two decimal places of kpc). The average of the absolute percentage differences is 35%. Although this difference is relatively large, this has little effect in the conclusions of this study. First, the important requirement for this work is that values of Z_{max} are compared on a consistent scale, rather than that the absolute values are correct. Secondly our conclusions are tested by the much greater and fundamental change to the Z_{max} values of shuffling them randomly and finding that even then they remain unaffected.

3.9 Homogenisation of Values of Stellar Parameters

3.9.1 Need for homogenisation

Many values of T_{eff} in the exoplanet literature are based on spectroscopically based temperature scales. Frequently used spectroscopic scales are UCLSYN for WASP host

stars (Smith, 1992; Smalley et al. 2001), the SME (Spectroscopy Made Easy) package (Valenti and Piskunov, 1996) as revised by Valenti and Fischer (2005) hereafter VF05, and those of Santos et al. (2004), hereafter Sant04. Further the determination of metallicity and age depends on that of T_{eff}.

The issue of temperature scales is discussed in detail in Holmberg et al. (2007), hereafter H07. These authors refer to problems with spectroscopic determinations based on the excitation balance in 1D static LTE models and point out that a correction used by VF05 appears to eliminate part of the resulting biases.

This study requires consistent scales for all three parameters T_{eff}, metallicity and age throughout and follows GCS in basing them on the photometric scale in H07. No adjustments are needed for most of the RVS stars which are near enough and hence bright enough to appear in GCS. Here "most" means that of the 129 RVS stars, there are only 14 for which GCS does not give all the data and for two of these GCS gives T_{eff} and metallicity but not age. In contrast none of the BTS stars appear in the GCS so adjustments are needed for the BTS stars and the few remaining RVS stars. The adjustments made for temperature, metallicity and age are as follows.

3.9.2 Homogenisation procedures

The starting point for the homogenisation procedures is the basic definition given by H07 of T_{eff} in terms of the bolometric flux F_{Bol} over all wavelengths i.e. $F_{Bol} = (\theta^2/4).\sigma.T^4_{eff}$, where θ is the angular diameter and σ the Stefan-Boltzmann constant. However these basic T_{eff} values are difficult to obtain mainly because only a few data for θ are available and also the bolometric flux has to be integrated over all wavelengths. The H07 authors point out that temperature scales in the literature are either essentially

photometric or spectroscopic. After a detailed survey of these scales they show that out of the scales they consider, the photometric scales are closer to the fundamental bolometric scale than the spectroscopic ones. They therefore state that a photometric scale is to be preferred and so construct a new photometric T_{eff} scale based on the (b-y) index described in Appendix G, calibrated by a V-K scale. The choice of scale for T_{eff} affects the value derived for *[Fe/H]* through the interpretation of spectral intensities, and this in turn affects the derived age through theoretical isochrones.

The relations for T_{eff}, metallicity and age are now considered in turn. A preliminary issue is that these relations were given in H07, and the GCS values used here are from the later paper H09. The later paper after further detailed discussion finds no reason to modify either the T_{eff} or metallicity scale. Thus we use the values in GCS, and adopt the relations given in H07 for T_{eff} and *[Fe/H]*.

Temperature. The values of T_{eff} and hence of metallicity and age derived from UCLSYN are likely to be closer to photometric scales than spectroscopic ones (Smalley, private communication) and so are not adjusted. Thus the packages for which adjustments are needed are those of VF05 and Santos et al (2004). Temperatures derived from VF05 were adjusted by the relation given by H07 and shown on the first line of Table 3.4. In contrast H07 do not give a relation between their own scale and that of Santos et al. To do this we first denote T_{eff} values derived on the bolometric scale as *T(Bol*), and those on the GCS, VF05 and Santos scales as *T(GCS),T(VF*) and *T(Sant)*. The desired relation *T(Sant04) – T(GCS)* is derived indirectly in the remainder of Table 3.4 by combining the relations which H07 do give between *T(Sant04) – T(Bol),* and *T(VF) – T(Bol*). In order to clarify the procedure the relations given in the literature are assigned reference numbers 1 to 3 in Table 3.4, and the derived relations reference numbers 4 and 5. The last column of the table shows how these last two relations were derived.

Table 3.4 - Differences between temperature scales for stellar parameters.

	Mean Difference (K)	Dispersion (K)	Ref. No	How derived
T(VF) – T(GCS)	43	91	1	
T(Sant) – T(Bol)	92	91	2	
T(VF) – T(Bol)	64	124	3	
Hence:				
T(Sant) – T(VF)	28	154	4	(2) – (3)
T(Sant) – T(GCS)	71	179	5	(4) + (1)

The differences between the scales are quoted as "mean" since they derive from a large number of stars. The values given for the dispersion and mean error for *T(VF) – T(Holm)* are the RMS values from the intermediate relations.

The required values of T_{eff} were obtained from the discovery or refined data papers As discussed in the next section they do not have to be adjusted on to a photometric temperature scale.

Metallicities. For metallicities H07 give the relations directly. For VF05, the relation is *[Fe/H]VF) – [Fe/H](GCS) = 0.08 dex* with a standard deviation of 0.10 dex, for Santos et al. it is *[Fe/H](Sant) – [Fe/H](GCS) = 0.162, 0.082 and 0.022* for F,G and K stars respectively.

Ages. In H07 the authors give an approximate relation between the VF05 ages and their own, stating that the VF05 ages are on average 10% lower than their own. However they give no relation for Santos et al. The H09 paper rederives individual ages and shows graphically (their Fig. 3) how the new ages relate to the previous values. Inspection of this

figure shows that on average the difference does not exceed the percent level, although some individual ages change to a much larger extent. Thus for VF05 ages we adopt the 10% correction of H07. We assume the same for Santos et al. Some support for this is that for T_{eff} and *[Fe/H]*, the VF05 and Santos values differ from GCS in the same direction.

Table 3.5 Comparison of distances of exoplanet host stars detected by major ground and space surveys.

Survey	Ground or space	Distance (pc)		
		Min.	Max.	Median
HAT	Ground	38	642	300
WASP	Ground	80	470	210
COROT	Space	150	1670	680
Kepler	Space	39	2700	829

4 COMPARISON OF SAMPLES

4.1 Comparison of Actual Samples

The samples are compared by the metallicity *[Fe/H]* and age, since these parameters strongly influence the frequency of exoplanets as discussed later (Sect. 4.2). The comparison is shown by histogram in Fig.4.1, and by sample parameters in Table 4.1.

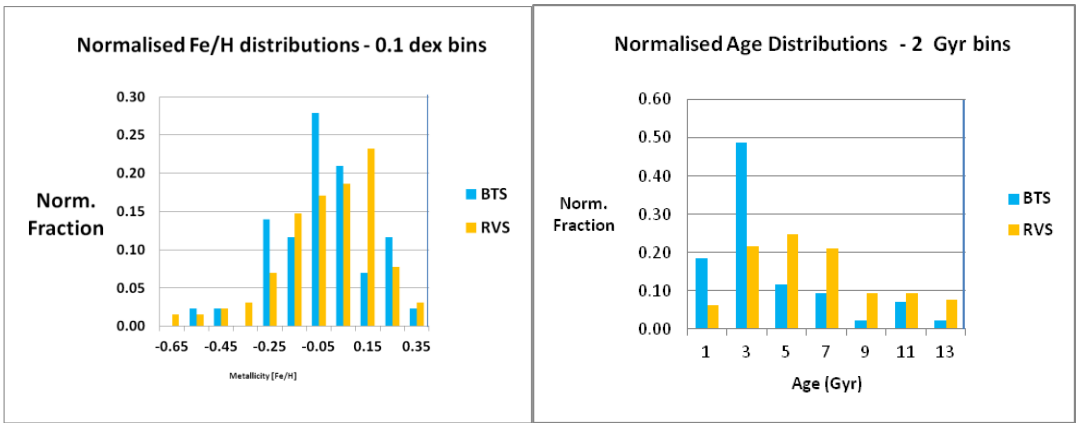

Figure 4.1. Normalised distributions of *[Fe/H]* and age in BT and RV samples.

Table 4.1 - Metallicity and ages of the actual BT and RV samples.

	Metallicity *[Fe/H]*		Age (Gyr)	
Sample	BTS	RVS	BTS	RVS
Number of stars	43	129	43	129
Sample median	-0.02	0.03	3.3	5.6
Sample average and spread of values (see text)	-0.03 ± 0.19	-0.01 ± 0.20	4.2 ± 3.1	6.2 ± 3.3
Difference in averages RVS – BTS	0.01		2.0	
KS probability BTS/RVS	0.525		< 0.001	
Measurement uncertainties	~0.05		~2 (see text)	
Uncertainties due to T_{eff} scales (see text).	~0.08		~ ±10% (~0.5 Gyr)	

In Table 4.1 the uncertainties quoted for the averages for each sample and parameter are only indicative of the spread of values because they assume that the samples are normally distributed, whereas the standard skewness and kurtosis tests show that they are not. The values quoted for measurement uncertainties are representative of values quoted in the literature, but are only a very broad indication for age since the uncertainties quoted for this parameter differ widely. The uncertainties arising from the use of different temperature scales are those discussed earlier. Because of rounding errors, the difference (RVS – BTS) in the average metallicities is quoted as 0.01, instead of the 0.02 expected from the values themselves.

Since the samples are not normally distributed, parametric tests e.g. the t- and chi squared tests to determine the probability that they come from the same distribution cannot be used. Thus the appropriate method is the non-parametric Kolmogorov-Smirnov (KS) test (e.g. www.physics.csbsju.edu/stats/KS-test.html). Consider the general case of two data sets $[a_1, a_2 .... a_n]$ and $[b_1, b_2...b_n]$ where the values are in ascending order. In the KS test each value a_1, a_2 ... is assigned a number f_1, f_2 ... *to* f_n which is the fraction of the data set members which are less or equal to $a_1, a_2 .... a_n$. The set f_1, f_2 ... to f_n is known as the cumulative distribution function. A similar function may be defined for the data set $[b_1, b_2 ...b_n]$. The two functions may be plotted together. The next step is to calculate "*D*", the maximum difference between the two functions as shown. Standard tables have been prepared which give values of "*D*" as a function of a) the number of members of each data set and b) the probability that the two data sets come from the same distribution. Given a value of "*D*" for a particular case, the probability that the two data come from the same distribution can be read off from tables or, as was done here, from the internet website above. The probabilities that the BTS and RVS come from the same distribution are given for *[Fe/H]* and age in Table 4.1.

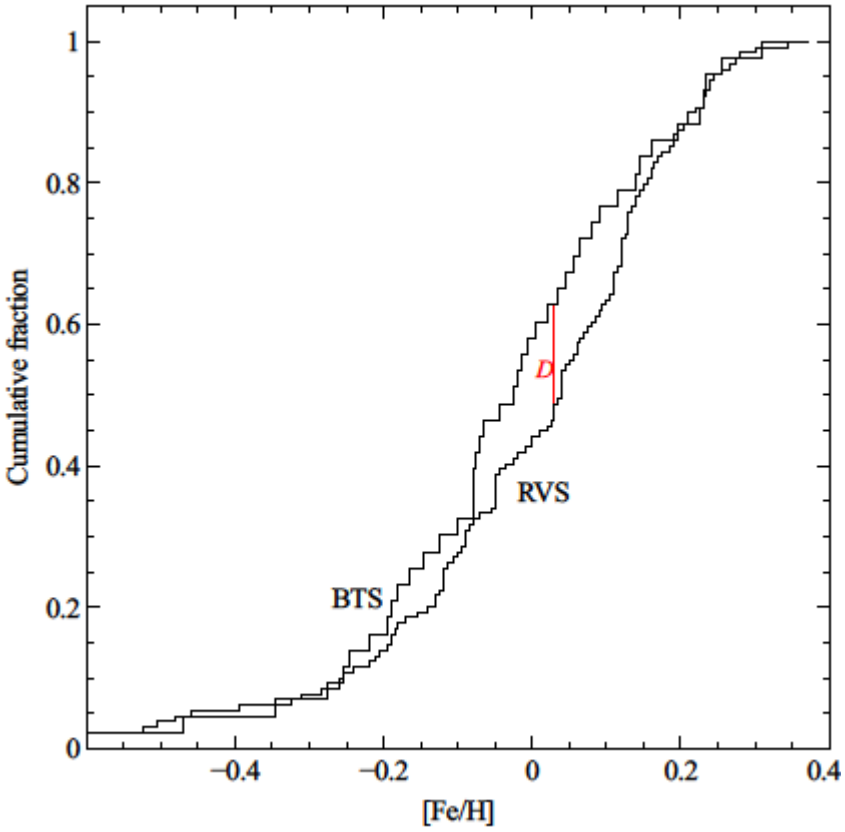

Fig. 4.2. Cumulative distribution fractions for the *[Fe/H]* values for the BTS and RVS.

The KS cumulative distribution diagrams for the metallicities and ages of the two samples are shown in Figures 4.2 and 4.3. For metallicity, inspection by eye shows no clear difference between the BTS and RVS and the KS probability $p = 0.525$ is consistent with this. For age, inspection by eye shows a clear difference between the samples and the KS probability $p < 0.001$ supports this. Thus the ages of the BTS and RVS samples do not come from the same distribution and the difference in average ages is therefore real.

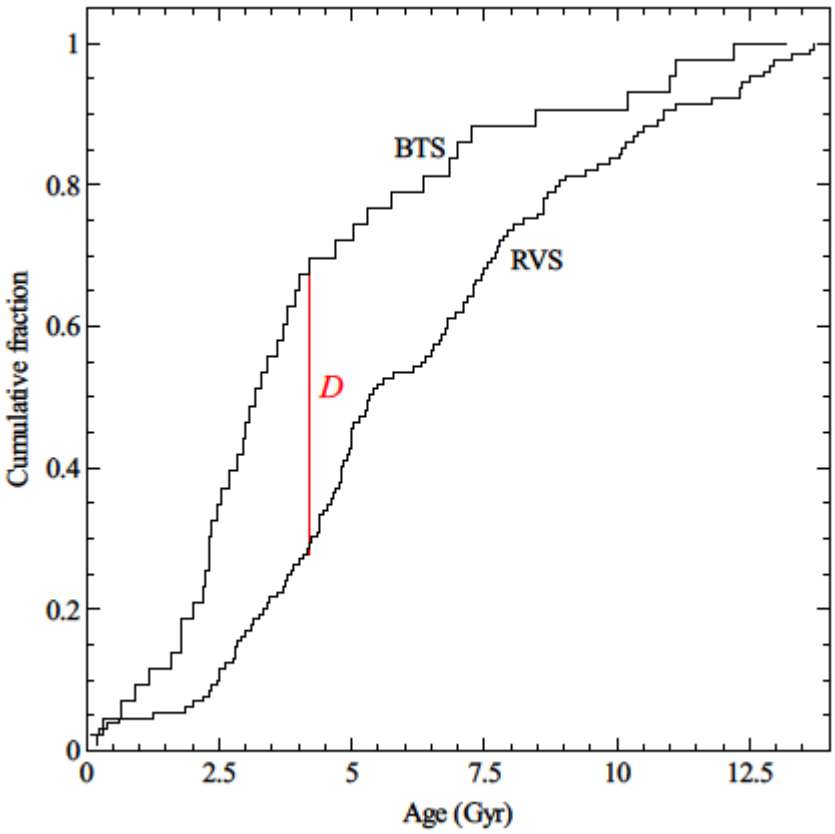

Fig. 4.3 Cumulative distribution fractions for the ages of the BTS and RVS.

The BTS has effectively the same metallicity as the RVS although it is younger. This is not a cause for concern because the scatter on the age/metallicity relation is very large, as may be seen by plotting the values for the host stars listed in the Extrasolar Planets Encyclopaedia.

4.2 Possible Explanations of Differences.

Given that the difference between the ages of the BTS and RVS is real, possible causes may be considered under the headings of biases in observational procedure and those due to the nature of exoplanet systems. The differences in the discovery techniques do provide strong grounds that a selection effect does exist. The detailed arguments are as follows.

4.2.1 Biases due to observational procedure

Magnitude range of BTS sample. The BTS is biased towards more distant stars due to the magnitude range of the detectors used. The target star must be bright enough to measure the order of 1% intensity dip due to the transit, but not so bright that it saturates the CCD detector. These limits set a magnitude range of about 9 to 13 (Mazeh, 2009). For main sequence stars each spectral type corresponds to a certain range of absolute luminosities. Thus a given range of apparent magnitudes corresponds to a range of distances. Hence a given spectral type can be regarded as defining a spherical shell, centered on the Sun, where the inner and outer radii correspond to this range. Progressively earlier spectral types correspond to higher absolute luminosities and more distant shell boundaries, hence larger shell volumes and more stars, but the relative population of that spectral type of stars decreases (Baldwin, 1944). The balance of these opposing dependencies is that ground based transit surveys are biased in spectral type, towards late F- and early G-type stars, at distances between broadly 100 to 500 pc. These limits were obtained by simply listing the stars in the BTS and adopting limits which contained most of the stars. The distances are calculated as described in Sect.3.5. Since the BTS stars lie on the Main Sequence, the bias in spectral type translates into a bias in age. This is because standard models of stellar structure show that for progressively earlier spectral type the mass and luminosity of a star increase and the lifetime on the Main Sequence shortens;

Binney and Merrifield (1998, Sect. 5.1.7) derive simple approximate numerical relationships between these parameters and give references to some then recent models.

Distances of BTS from Galactic Plane. Transit surveys avoid low galactic latitudes where the observation field is more crowded with stars, to prevent images of two or more stars being formed on the same CCD pixel. This would produce a misleading light curve. Further to this, if two stars were closer than 2″ (corresponding to about an eighth of a pixel for a typical 8 degree square field and 2048×2048 pixel detector), it would be hard to carry out follow-up radial measurements because of the difficulties in obtaining an uncontaminated spectrum of a star with a nearby companion (Vogt et al., 2000). Hence BTS stars will tend to have larger distances from the galactic plane, not only because they are further away from the Sun, but also because they are at higher galactic latitudes. In fact the median value for Z_{max} for the BTS calculated above (Sect. 3.8) is 112 pc. This

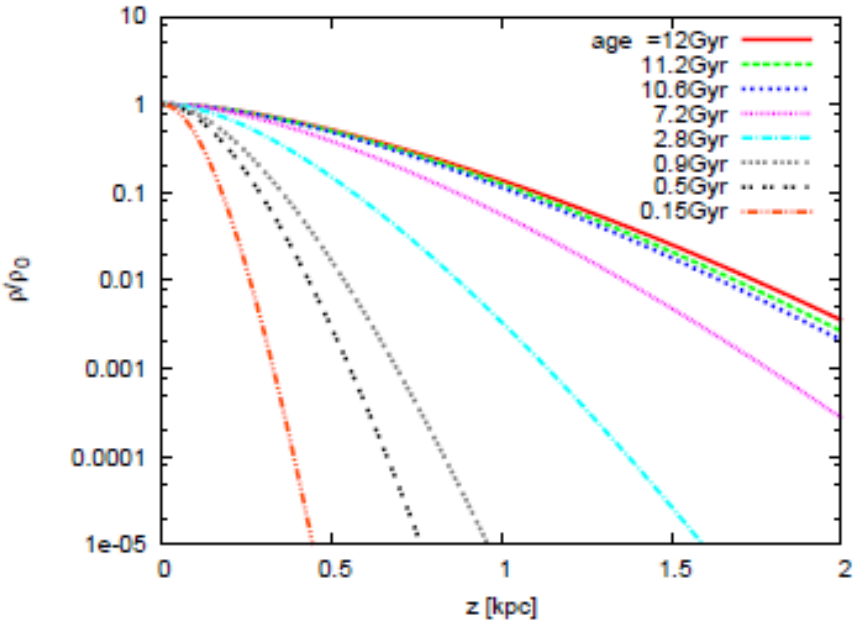

Fig. 4.4. Normalised density profiles of stellar sub-populations as a function of age, taken from Fig. 11 of Just and Jahreiß (2010).

introduces another bias due to distance. Stars further away from the Galactic plane tend to be older as has been shown quantitatively by Just and Jahreiß (2010), who present population densities for a series of age groups as a function of distance from this plane (their Fig. 11, reproduced above as Fig. 4.4). It is thought that this is because although stars form near the Galactic Plane, the older stars will have undergone more collisions which tend to eject them away from this plane. (Here "collision" means that the star suffers a significant change in direction of motion through gravitational interaction, not that the stars actually collide). In principle then the BTS sample is towards older ages. Reference to Fig. 4.3 shows that for a median distance of 124 pc from the galactic plane this bias is small but could be measurable. This bias is in the opposite direction to that introduced by spectral type i.e. that the earlier spectral types of the BTS stars correspond to younger ages. It will be seen from Fig. 4.1 and Table 4.1 that the spectral type bias appears to be dominant i.e. the BTS is in fact on average younger.

Spectral type of RVS sample. Since the radial velocity surveys rely on extremely small wavelength shifts in spectral profile features, they are targeted towards stars with high signal to noise ratios. Thus the stars have brighter apparent magnitudes (4 to 10), but they are also chosen for their lower surface temperatures i.e. later spectral type, because the lines in the stellar spectrum are narrower and the detailed profile measurements less difficult. Further reasons for targeting cooler stars are first, they tend to be older and rotate more slowly due to magnetic braking from the stellar wind, so reducing Doppler broadening, and secondly their chromospheres are less active and this reduces the contribution to jitter due to flows and inhomogeneities in the stellar atmosphere (Wright 2005). The magnitude and surface temperature requirements together constrain distances to be usually within 100 pc. Thus the distances of the exoplanet stars as discovered by each method lie in distinct and almost non-overlapping groups.

Thus there are reasons to believe that biases in age and metallicity exist, that some biases pull in opposite directions, and the BTS is observed to be biased towards younger stars. The consequence of these biases for studies for exoplanets is that it may be unsafe without further consideration to regard exoplanets as a single group regardless of how the planet was discovered. The purpose of this study is to understand these biases by comparing matching calibration samples, and to assess their significance.

These two parameters of metallicity and age are in turn thought to be associated with the probability that a star hosts a planet. Exoplanets are more common orbiting stars of higher metallicity (Fischer and Valenti, 2005); these authors argue that this correlation arises because host stars are born from high metallicity molecular clouds instead of an alternative mechanism whereby planets spiral into the star and so increase the stellar metallicity. There is in principle some association with age because a closely orbiting planet will raise tides on the host star, and the resulting torque on the planet will cause it to spiral into the star and break up when it crosses the Roche limit (Jackson et al. 2009). The lifetime of an exoplanet against tidal interactions has also been discussed in detail by Levrard et al. (2009), (Appendix K, Sect. K3).

4.2.2 Biases due to the nature of exoplanet systems.

The nature of exoplanet systems can in principle lead to further biases.

Infalling of planets. The infalling of exoplanets can in principle introduce opposing biases: i) the lifetime of a planet is limited so if one is observed the host star is young, or ii) the planet needed time to migrate to the short period orbits associated with transiting planets, so the star will tend to be older. Detailed considerations of these mechanisms were judged to be outside the terms of reference of this project.

Correlations between the masses of the planet and the star. It has been suggested that more massive planets may be associated with more massive stars (Sozzetti et al. 2007). However both main detection methods favour more massive planets and it is not obvious what bias this would introduce between the samples, as discussed in Chapter 5.

Correlations between the metallicity of low mass stars and the frequency of low mass, small radius exoplanets. The analysis of the *Kepler* data by Schlaufman and Laughlin (2011) hints that such a correlation may exist. However exoplanets discovered by *Kepler* tend to be in a lower mass range than those discovered by ground based surveys, often in the range 0.01 to 0.1 M_J whereas the ground based survey planets have masses of order $1M_J$. Thus correlations discovered for *Kepler* planets have limited relevance to this study.

4.3 Splitting of samples

Nearly all of the BTS planets have orbital periods shorter than 10 days for observational reasons.

In contrast, many RVS planets have much longer periods and the distribution of periods shows a "desert" between 6 and 15 days i.e. the periods of the exoplanets tend to fall into distinct ranges. A KS test was therefore carried out where the the RVS is split into short period (SP) and long period (LP) subsamples, defined by the periods of exoplanets being less or more than 10 days respectively. The KS probabilities "*p"* that the two RVS subsamples come from the same distribution are:

Metallicity *[Fe/H]*: $p = 0.067$
Age: $p = 0.339$

The *p* value for *[Fe/H]* suggests that the two subsamples do not come from the same distribution, but this is not definite. No conclusion can be drawn for age. The splitting of the RVS is not considered further.

4.4 Relation between period and distance.

Mazeh (2009) has suggested that because of selection effects the period of a planet discovered by the transit method decreases with the distance. This is because the more distant systems are fainter and as explained by Mazeh, following Gaudi et al. (2005), this favours shorter period planets. The present study requires a set of homogeneously calculated distances for the BTS. This set allows this hypothesis to be tested and a weak correlation does in fact exist. A linear regression analysis of the BTS systems gives P/days = $(4.5 \pm 0.5) - (0.004 \pm 0.002)$ (d/pc).

4.5 Construction and comparison of calibration samples.

Calibration samples were constructed for the reasons explained in Chapter 1. They were synthesised from a catalogue of a large number of stars which as far as is known do not possess exoplanets. They are constructed to match the BTS and RVS as closely as possible, and are called here the BTS/RVS-matched samples.

4.5.1 Parameters for constructing calibration samples

A basic question for the calibration samples is to choose appropriate parameters by which they should be formed. These are as follows.

1. A parameter to describe the nature and evolution of the star. The effective temperature T_{eff}, defined below, is chosen because it is an observable parameter which is obtained relatively readily and it is a function of the mass, the basic parameter which

determines the evolution of the star. Since the samples will be formed from main sequence stars, T_{eff} will constrain the values of other stellar parameters to within close limits.

2. Since planet formation is thought to depend on metallicity and age, and there is a distribution of these parameters perpendicular to the Galactic plane, the other kinematical parameter should be a measure of the motion of a star along this axis. The parameter chosen is Z_{max}, the amplitude of the oscillation of a star's position perpendicular to the galactic plane. This is one of the constants of motion in a star's orbit around the Galaxy. The parameter Z_{max} is a more appropriate kinematic parameter than the actual perpendicular distance Z from the galactic plane, because that merely provides a snapshot of the star's position at one moment during one of its many oscillations about that plane. The calculation of Z_{max} was described earlier. It is also a more appropriate kinematic parameter than the amplitude of the oscillations parallel to the galactic plane because there is no reason to believe that stellar metallicities or ages vary within this plane on the distance scales considered here.

4.5.2 Method for constructing calibration samples.

The source catalogue for the calibration samples is the Geneva-Copenhagen Survey (GCS) catalogue of Holmberg et al. (2009), hereafter H09. This is the most recent and extensive catalogue of solar-type stars published by the GCS. It contains about 14000 F- and G-type stars in the solar neighbourhood, lists many stellar parameters and uses the parallaxes obtained from the new reduction of the *Hipparcos* data undertaken by van Leeuwen (2007). Importantly for the purpose of this study, it also contains most of the RVS stars, since their apparent magnitudes are bright enough to satisfy the GCS inclusion criteria.

The first step is to sift H09 to remove stars according to the same exclusions as were used for the actual samples. This means removing all stars which cannot be legitimately compared with those in the BTS and RVS i.e. stars flagged as giants or binaries, stars where the age, metallicity or Z_{max} is unknown, or stars known to possess an exoplanet.

First all the stars in a) the actual samples and b) the eligible calibration stars from H09 were plotted on a Z_{max} versus T_{eff} diagram. The diagram for the BTS is shown on Fig. 4.5 (generated by Maxted, private communication), where the heavy black dots show some of the actual stars and the small dots some of the calibration stars. Some stars in both groups were omitted for the sake of clarity. The calibration sample contains just those stars in this diagram which lie closest to the sample stars. To form the total calibration sample there is defined for each BTS or RVS star a calibration group which contains just those calibration stars lying within a small elliptical area on this diagram around that star. For each actual sample, BTS and RVS, the corresponding calibration sample contains just those calibration stars in all the calibration groups. A typical calibration group is shown on Fig.4.4 in the approximate position T_{eff} = 5670 K, $log\ (Z_{max})$ = 2.0. The groups are elliptical and their area is characterised by a normalised radius parameter $\rho = R_g/Dist_d$. Here R_g indicates the radii of the groups along each axis; $R_{g\text{-}temp}$ and $R_{g\text{-}Zmax}$ are the radii along the temperature and Z_{max} axes respectively. The parameter $Dist_d$ is the length of the two axes; for the T_{eff} axis this length is between the minimum and maximum temperatures

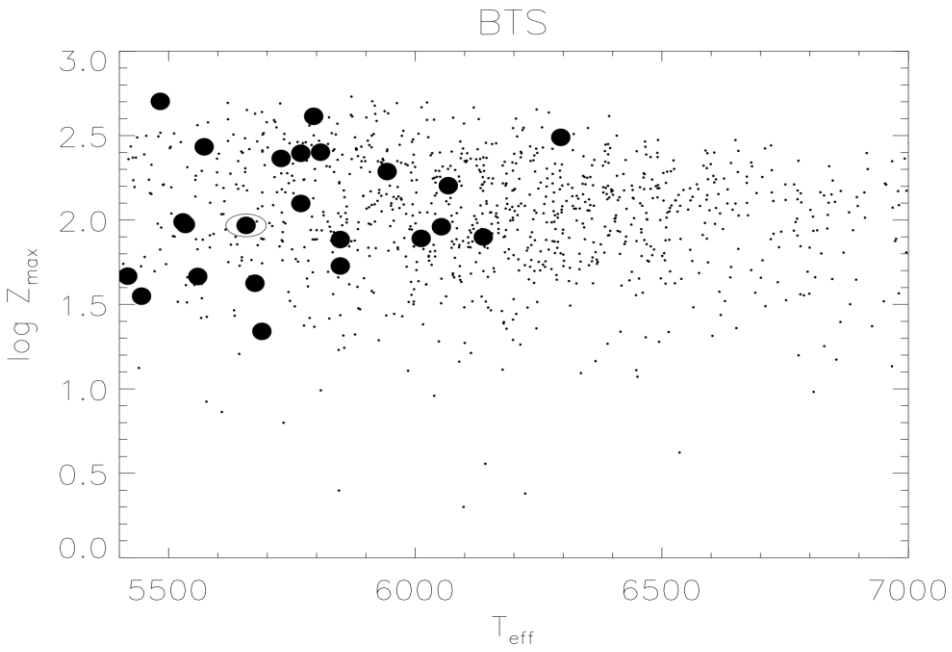

Figure 4.5. Z_{max} versus T_{eff} plot for BTS actual and calibration samples, (Maxted, private communication).

considered, 5400 and 7000 K for $T_{eff.}$, similarly for the Z_{max} axis it is between 0 and 800 pc. These cutoffs were chosen to exclude regions where only a few sample or GCS stars reside. A constant value of $\rho = 0.025$ was used for all calibration groups; this was adopted as the best compromise between a) using as many calibration stars as possible and b) minimising the number of calibration stars lying in two or more calibration groups. This choice was based on the results of runs with a series of values of ρ. As ρ is progressively increased from 0.01, the results for the main BTS/RVS comparison settle for ρ greater than about 0.025. However for this value of ρ about 40% of the calibration stars for the RVS are already being used twice. The total number of calibration stars used for each actual sample is shown in Table 4.2. By combining this Table with Table 3.2 it may be seen that the average number of calibration stars per sample star is 1447 calibration/43 sample ~ 34 stars for the BTS and similarly ~ 32 stars for the RVS.

The T_{eff} value of each calibration star is randomly adjusted by up to ±7 K on the calibration diagram. This is done because the values actually given in GCS are $\log(T_{eff})$ to three decimal places, and for T_{eff} = 6000K a step of 0.001 in $\log(T_{eff})$ corresponds to twice this amount, about 14K. Otherwise the positions of the calibration stars on the diagram would lie in a series of lines of constant T_{eff} separated by ~14K, which was regarded as too large a fraction of the 0.025×(7000-5400) = 40K radius of a calibration group along the temperature axis. This line grouping would introduce a significant extra randomness into the analysis. The ±7 K blurring removes microscopic discontinuities in the distribution over T_{eff}.

For each real sample an average metallicity and age is obtained for all the stars in the calibration groups, and these averages are the quantities used to compare the calibration samples.

4.6 Method for comparing calibration samples

The BTS and RVS calibration samples as obtained above were again compared by the KS test. Cumulative distribution functions were obtained for both the metallicity and age and the maximum vertical deviation D (e.g. Figs. 4.2 and 4.3) calculated. Because the composition of the calibration samples is not entirely free from subjective choice (through the size of the calibration groups) a further test was carried out to determine how probable this value of D is. This is achieved by repeating the KS test 10000 times, but with the age of the calibration stars randomly shuffled each time. If a proportion p of these tests yields a value of D less than that for the true calibration samples, then the probability that the two calibration samples come from the same distribution is taken to be p.

4.7 Results of comparisons

The results from comparing the calibration samples are shown in Table 4.2. The standard deviations quoted for the average metallicities and ages are only indicative, as for the actual samples.

Metallicity. The KS probability that the metallicity of the BTS/RVS calibration samples come from the same distribution is $p = 0.002$. Thus there does appear to be a small but statistically significant selection bias of about 0.02 dex in favour of lower metallicities for the BTS stars. Here the KS test has the power to reveal even small differences in metallicity in this case due to the large sample size. However this difference is negligible in practice because it is smaller than both the ~0.05 dex typical uncertainty in determining metallicity and the ~0.08 dex difference between the GCS and VF05 metallicity scales. The difference is broadly similar to the value BTS – RVS = -0.01 dex for the actual samples.

Since GCS do not give uncertainties for metallicities the same average uncertainty is adopted as for the real samples. For ages the 1-σ confidence limits in GCS is adopted. As for the actual samples, the uncertainties in the ages for each star vary widely and the value of ± 1 Gyr in Table 4.2 is only broadly representative. Values for uncertainties due to the use of different temperature scales are subject to the same qualifications as for the real samples.

Age. The KS test for the ages also shows a clear difference ($p < 0.001$). This is by ~1.3 Gyr in favour of younger BTS stars and is somewhat larger than the measurement and scale uncertainties. This is broadly consistent with the result for the actual samples; for

those the average age of the BTS is 2.0 Gyr younger than for the RVS; and the difference is statistically significant, again with $p < 0.001$.

Table 4.2 - Metallicity and ages of calibration BTS and RVS samples.

	Metallicity *[Fe/H]*		Age (Gyr)	
Sample	BTS	RVS	BTS	RVS
Number of stars	1447	4186	1487	4182
Sample average	-0.18 ± 0.19	-0.16 ± 0.19	4.2 ± 3.0	5.6 ± 3.3
Difference in averages RVS – BTS	0.02		1.3	
Maximum vertical deviation *D* (see text).	0.074		0.282	
KS probability BTS/RVS	0.002		< 0.001	
Measurement uncertainties	~0.05		~1 (see text)	
Uncertainties due to T_{eff} scales (see text).	~0.08		~ ±10% (~0.5 Gyr)	

Ideally the cumulative distribution fractions for the calibration samples should be shown in plots analogous to those for the actual samples (Figs. 4.2 and 4.3). However the program written by Maxted (private communication) which was used to generate Fig. 4.5 does not list the calibration sample stars explicitly. Thus the cumulative distribution fractions are not readily available.

As for the actual samples parametric statistical tests cannot be used to determine whether the calibration samples come from the same distribution.

It may be noticed that the BTS has effectively the same metallicity as the RVS although it is younger. This is not a cause for concern because there is a very wide scatter in the relationship between age and metallicity.

4.8 Sensitivity of conclusions to stellar data

The conclusions are not significantly affected by changes in adopted stellar data. To demonstrate this, the comparison of the BTS and RVS calibration samples was repeated with a change much more drastic than any due to revision of data i.e. where the T_{eff} values of the actual RVS stars were randomly shuffled around with the Z_{max} values unchanged. The KS probabilities showed no significant difference.

CHAPTER 5 DISCUSSION AND CONCLUSION

5.1 Discussion

The comparisons made in earlier chapters are real BTS sample/real RVS sample and calibration BTS sample/calibration RVS sample. Decisions on what can, or cannot, be deduced from this comparison follow from the principle that the calibration samples were constructed to match the real samples by mass (via T_{eff}), and by Z_{max} and hence (loosely) by age.

In Chapter 3 it was shown that the average or median age of the bright transit sample (BTS) is about 2 Gyr younger than for the radial velocity sample (RVS) and that this difference is statistically significant. The same comparison for the calibration sample i.e. those with no known exoplanets (Chapter 4) yielded a similar result i.e. that the calibration stars corresponding to the BTS are on average 1.3 Gyr younger than for the RVS. This is ascribed to the different survey techniques since the ground based transit surveys are biased towards an earlier spectral type. Since the actual and calibration samples yield similar results this explanation is regarded as sufficient without any need to invoke mechanisms involving exoplanets e.g. those listed in Sect. 4.2.2.

Comparison of Tables 3.2 and 4.1 shows that the average metallicities of the actual samples are about 0.15 to 0.17 dex higher than for the calibration samples. This must be related to some other parameter than the mass and T_{eff} used for the matching. The natural alternative explanation is the presence of the exoplanet. This supports earlier findings Fischer and Valenti (2005) that planet host stars have higher metallicities than comparable solar type stars. These authors discuss two rival theories why this should be so: 1) the exoplanets and their host star form from a primordial gas cloud with high metallicity and 2) the higher metallicity arises from accretion after the star has formed. In their

"Discussion" section they give a series of observational reasons why they judge 1) to be correct. For example if the metallicity were due to accretion the upper boundary in stellar metallicity would rise as the mass of the convective envelope in main sequence stars decreased. This is not observed.

It is not valid to draw any conclusions about the limited lifetime of exoplanets from this study since if this limit is real the existence of the exoplanets has already defined the composition of the calibration samples. Neither does this study lead readily to any conclusions about biases in correlations between the mass of an exoplanet and the mass or metallicity of the host star. With regard to mass, the intensity dip due to a transit scales as R_p^2 where R_p is the planetary mass and if, contrary to reality, exoplanets had uniform density this is equivalent to $M_p^{2/3}$ where M_p is the mass of the planet. The radial velocity method relies on the amplitude of the reflex stellar velocity due to the exoplanet and this amplitude scales as M_p. The two scalings differ by only $M_p^{1/3}$ and so even then any bias would be weak. Since as is well known the density of exoplanets varies widely it is at least difficult to take this discussion further.

The uncertainties noted earlier due to the use of different temperature scales shows the need for consistent measurements on all exoplanet stars, e.g. by the V-K index or by the (b-y) index scale based on (V-K) as used by GCS. A further uncertainty in this investigation is the frequently wide error bars in the estimated stellar ages.

5.2 Conclusions

This study has investigated samples of exoplanet host stars defined by the two main methods of discovery i.e. ground based transit or radial velocity surveys, to determine whether any inherent observational biases in metallicity and age can be expected between them. Comparison of the actual samples shows that the average metallicity of the BTS is lower than that of the RVS by a very small amount (0.01 dex) which has no practical significance and is also negligible compared with observational uncertainties or uncertainties arising from the use of different temperature scales for T_{eff}. The corresponding difference for the calibration samples is: BTS calibration is lower than RVS calibration by 0.02 dex.

Thus statistical surveys of exoplanets need not consider the method of discovery if metallicities or associated properties are considered. However if the surveys discuss ages or properties related to them, an observational bias of about 2 Gyr in favour of younger ages for exoplanets discovered by ground based transit surveys should be taken into account.

.

PART II DETAILED ANALYSIS OF THE ECLIPSING BINARY V1094Tau

CHAPTER 6 INTRODUCTION AND JUSTIFICATION FOR PROJECT

Part II of this thesis describes a detailed study of the eclipsing binary V1094 Tau. This short chapter outlines the justification for this study; the points made are explained in later chapters as required. The standard abbreviations "EB" and "dEB" are used throughout for "eclipsing binary" and "detached eclipsing binary"; the distinction between them is explained later. The suffixes 1, 2 and S are used throughout to denote the primary, the secondary, and a star in general.

This study has also been described in a forthcoming paper (Maxted et al., 2015).

Section 6.1 Reasons for studying dEB's with periods in region of 8 days

6.1.1 Importance of mass-radius relation

The Vogt-Russell theorem as originally formulated (Vogt, 1926; and Russell 1927) states that the course of a star's evolution and the value of stellar parameters are determined completely by its mass and distribution of chemical composition. This formulation has been stated precisely as follows:

(www.mpagarching.mpg.de/~weiss/Cox_Vol_II_CD/ch18.pdf).

"The complete structure of a star in hydrostatic and thermal equilibrium is uniquely determined by the total mass M and the run of chemical composition throughout the star, provided that the total pressure P, internal energy per unit mass E, opacity κ, and energy generation rate ε are functions only of the local values of density ρ, temperature T, and chemical composition."

A more recent description has been given by e.g. Carroll and Ostlie (2007).

Modern stellar models allow for rotation and whether the star is a member of a binary system. The need to include rotation in a complete model was recognised by Russell (1931).

The mass is the main determinant of the stellar evolution because each layer of a star is in hydrostatic equilibrium between gravitational and kinetic pressure. The kinetic pressure depends on the temperature which in turn determines the rate at which nuclear fusion generates the energy in the star. The chemical composition is another determinant because it determines the optical opacity and hence how efficiently energy is transported outwards from the stellar core by radiation. The relations between the stellar mass and other basic properties such as the radius, surface temperature and luminosity are therefore fundamental to understanding stellar evolution.

The mass/radius relation is particularly important since these are the two parameters which can be measured to the percent level in dEB's. The analysis of exoplanet systems discovered by the transit method requires a mass/radius relation (Seager and Mallén-Ornelas, 2003), or some other assumption derived from stellar properties (Collier Cameron et al. (2007), Torres et al. (2008)). This assumption can be in the form of a stellar model which relates the radius to the mass; an approach adopted by Southworth (2009 and 2010). An alternative approach which obtains the stellar mass and radius in terms of semi-empirical fits to T_{eff}, average density and *[Fe/H]* has been described by Enoch at al. (2010).

As has been known since the study by Hoxie (1973) stellar models underpredict the radius by up to 15% in a mass range 0.3 to 1.1$M_{\odot}$; relevant references have been listed by Southworth (2009) and by Feiden and Chaboyer (2013). In other words, the stars are inflated with respect to theoretical models. Torres et al. (2010) state that it is widely

accepted a discrepancy exists between theoretical and observed stellar radii. Thus the fundamental properties of stars in this mass range are still not fully understood. Chabrier et al. (2007) have proposed a phenomenological explanation by which the rotation of the star inhibits the convection within it through magnetic effects and so influences its evolution. Very recently this problem has been discussed in detail by Feiden and Chaboyer. This investigation is described in some detail later; very briefly these authors conclude that the convection within the star supplies energy to the magnetic field which in turn makes the transport of heat towards the stellar surface by convection less efficient.

The stellar mass range in which this discrepancy exists includes many exoplanet systems and a large proportion of all stars; this is because stellar formation favours low mass stars as explained later (Sect. 6.1.4).

6.1.2 Importance of dEB observations

Detached eclipsing binaries are the main source of accurate masses and radii of stars. In these systems both the mass and radius can be determined to 3% or better as stated in the major review of available data by Torres et al. (2010). Further reasons for studying binary and multiple stars have been comprehensively listed with references by Southworth (2006, Thesis, Sect. 1.5; www.astro.keele.ac.uk/jkt/pubs.html); for example the distribution of orbital elements can in principle be used to constrain star formation theory. However, if tidal interactions between the two stars are significant, it may be unsafe to use binary star data to test stellar models for single stars. Further reasons why the evolution of a binary component can differ from a single star of the same mass and composition are gravitational interactions, mutual irradiation and mass transfer by stellar wind.

Tidal interactions are predicted theoretically to fall off very sharply for orbital periods longer than about 8 days (Zahn and Bouchet, 1989). As explained in Appendix K the strength of these interactions depends as $(R/a)^6$ where R is the stellar radius and "a" the separation. There is therefore a need to produce a detailed map of the strength of tidal interactions versus period and masses in dEB's, with particular reference to eclipsing binaries with periods straddling the 8 day cut off to test the theoretical predictions. This in turn will determine which dEB observations could serve as points in a map of the mass/radius/metallicity relation for single low mass stars. Such a program is timely since large-scale photometric surveys such as ASAS (Pojmanski, 1997), *Kepler* (Basri et al., 2005; Borucki et al., 2010a,b) and SuperWASP for transiting exoplanets enable hundreds of bright, solar-type eclipsing binary stars to be identified. A good understanding of tidal interactions can in principle lead to theoretical estimates of the life time of exoplanets against spiralling into their host stars (Appendix K, Sect. K3).

6.1.3 Reasons for studying V1094 Tau

The star HD 284195, now widely known as V1094 Tau, was discovered to be a detached eclipsing binary by Kaiser (1994). It is a particularly suitable candidate to provide one point on this map. Both stars in this system are solar-type main sequence stars, which is important since tidal interaction theory has so far been developed only for such stars, and the orbital period is about 8.99 days, close to the 8 day cutoff. It is relatively bright (V = 8.96) and the light curve shows deep well defined primary and secondary eclipses (Fig. 9.5). A complete analysis of an eclipsing binary requires good radial velocity data and good photometric light curve data. Both have recently been obtained for V1094 Tau. A luminosity ratio is needed to constrain the light curve analysis. This thesis reports the first such detailed combined analysis of V1094 Tau.

6.1.4 Mass distribution of newly formed stars

The statement earlier that the mass range 0.3 to 1.1 $M_\odot$ contains a substantial proportion of all stars can be justified from considering the Initial Mass Function (IMF). This is the distribution of masses after a hypothetical burst of star formation. It favours low mass stars. Salpeter (1955) proposed an observationally based power law distribution $\xi(M) \propto M^{-2.35}$ for the range $-0.4 < \log(M_S/M_\odot) < 1$ i.e. $0.4 < M_S/M_\odot < 10$, where M_S is the mass of the star. This is known as the Initial Mass Function (IMF). More recently multi-stage distributions have been proposed, segmented by different power laws in a series of mass ranges. Scalo (1998) has proposed $\xi(M) \propto M^{\alpha}$ where

$\alpha =$ -1.2 ± 0.3 for $0.1 \leq M_S/M_\odot < 1$
-2.7 ± 0.5 for $1 \leq M_S/M_\odot < 10$
-2.3 ± 0.5 for $10 \leq M_S/M_\odot < 100$

Kroupa (2001, his Eqn. 6) has proposed

$\alpha =$ -0.3 ± 0.7 for $0.01 \leq M_S/M_\odot < 0.08$
-1.8 ± 0.5 for $0.08 \leq M_S/M_\odot < 0.50$
-2.7 ± 0.3 for $0.50 \leq M_S/M_\odot < 1.00$
-2.3 ± 0.7 for $1.00 \leq M_S/M_\odot$

The IMF is often written in the logarithmic form

$$dN = \xi(\log M_S)\, d(\log M_S) \propto M_S^{-\Gamma} \qquad 6.1$$

as is done by Salpeter (1955), so that $\alpha = \Gamma + 1$.

These distributions are shown in Fig.6.1. Since they have been presented for different mass ranges they are displayed by a relative normalisation so that they equal unity for $1M_\odot$. It will be seen that all three IMF proposals have very similar dependencies for $M_S > M_\odot$.

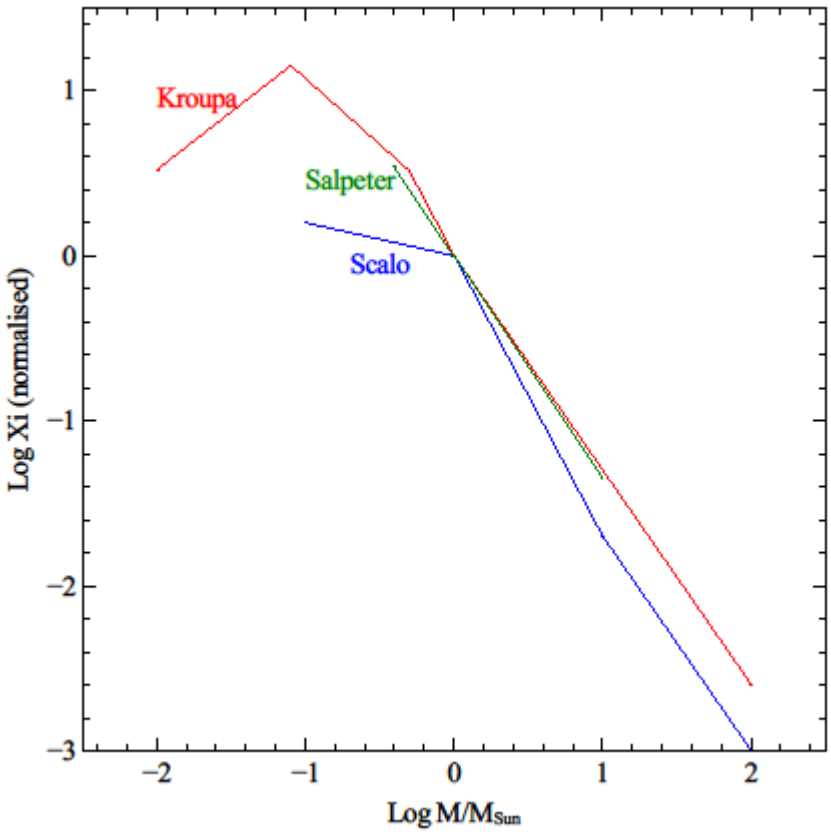

Fig.6.1 **Variation of the normalised initial mass function ξ(M) with stellar mass according to Salpeter (green), Scalo (dark blue) and Kroupa (red).**

Section 6.2 Studies of dEB's with similar periods.

The importance of a study of V1094 Tau for eclipsing binary studies can be assessed in part by considering the number of systems for which accurate data exist. The most up to date and comprehensive survey available is the DEBCAT website of Southworth (www.astro.keele.ac.uk/jkt/debcat), which listed 172 systems as at 1 January 2015. The studies of dEB's of broadly similar periods are listed in Tables 6.1a and 6.1b below, The term "broadly similar" here means 5 to 12 days i.e. about 50% on either side of the 8 day cutoff and includes 28 dEB's. The value of 50% is chosen to provide a large

variation in the strength of the tidal interaction without an impracticably wide range of period. For given stellar mass and radius the $(R/a)^6$ dependence of the interaction strength translates into a (R^6/P^4) dependence where P is the period; hence a 50% change in the period for a given radius will change the interaction strength by a factor $1.5^4 \sim 5$. Table 6.1a lists the dEB's with periods 5 to 8 days and Table 6.1b those with periods 8 to 12 days. Most of the dEB's in these Tables have been studied to a similar level of detail as in the present work, however in general they report more extensive spectroscopic measurements and discussion of how the measurements relate to evolutionary tracks.

Table 6.1a List of dEB's described in the literature with periods between 5 and 8 days.

Star	Period	Sp. Type	Mass/$M_\odot$	Radius/$R_\odot$	Reference abbreviation
HD 71636	5.013	F2 V	1.513 ± 0.009	1.571 ± 0.009	Hen06
		F5 V	1.285 ± 0.007	1.361 ± 0.008	
RT CrB	5.117	G5 IV	1.343 ± 0.010	2.615 ± 0.044	Sab03
		K0 IV	1.359 ± 0.009	2.946 ± 0.051	
BK Peg	5.49	F8 V	1.414 ± 0.007	1.988 ± 0.008	Cla10
		F7 V	1.257 ± 0.005	1.474 ± 0.017	
V396 Cas	5.505	A1 V	2.398 ± 0.022	2.592 ± 0.013	Lacy04
		A3 V	1.901 ± 0.016	1.474 ± 0.017	
V530 Ori	6.111	G	1.0038±0.0066	0.980 ± 0.013	Tor14
		M	0.5955±0.0022	0.5873± 0.0067	
V785 Cep	6.504	G type	1.103 ± 0.007	1.424 ± 0.019	Mei09
		G type	1.081 ± 0.007	1.373 ± 0.019	
GG Ori	6.631	A2 V	2.342 ± 0.016	1.852 ± 0.025	Tor00
		A2 V	2.338 ± 0.017	1.830 ± 0.025	
BW Aqr	6.72	F7 V	1.488 ± 0.022	2.064 ± 0.044	Cla91
		F8 V	1.386 ± 0.021	1.788 ± 0.043	Cla10
CV Vel	6.889	B2.5V	6.066 ± 0.074	4.126 ± 0.024	Yak07
		B2.5V	5.972 ± 0.070	3.908 ± 0.027	
EW Ori	6.937	G0 V	1.173 ± 0.011	1.168 ± 0.005	Pop86
		G2 V	1.123 ± 0.009	1.097 ± 0.005	Cla10
V364 Lac	7.352	A7 m	2.333 ± 0.015	3.307 ± 0.038	Tor99
		A7 m	2.296 ± 0.025	2.985 ± 0.035	
V1143 Cyg	7.641	F5 V	1.355 ± 0.004	1.346 ± 0.023	And87
		F5 V	1.327 ± 0.003	1.323 ± 0.023	Alb07
KW Hya	7.75	A5 Vm	1.978 ± 0.036	2.125 ± 0.016	And84
		F0 V	1.488 ± 0.017	1.480 ± 0.014	And87
EY Cep	7.971	F0 V	1.523 ± 0.008	1.463 ± 0.008	Lacy06
		F0 V	1.498 ± 0.014	1.468 ± 0.010	

Table 6.1b List of dEB's described in the literature with periods between 8 and 12 days.

Star	Period	Sp. Type	Mass/$M_\odot$	Radius/$R_\odot$	Reference abbreviation
M4 V66	8.111	G	0.7842±0.0045	0.9347±0.0048	Kal13
		G	0.7443±0.0042	0.8298±0.0053	
EI Cep	8.439	F3 IV	1.772 ± 0.007	2.896 ± 0.048	Tor00
		F1 V	1.680 ± 0.006	2.329 ± 0.044	
V459 Cas	8.458	A1 m	2.02 ± 0.03	2.009 ± 0.013	Lacy04
		A1 m	1.96 ± 0.03	1.965 ± 0.013	
TZ Men	8.57	A0 V	2.487 ± 0.025	2.016 ± 0.020	And87
		A8 V	1.504 ± 0.010	1.432 ± 0.015	
M55 V54	9.269	F	0.726 ± 0.015	1.006 ± 0.009	Kal14
		K	0.555 ± 0.008	0.528 ± 0.005	
MU Cas	9.653	B5 V	4.57 ± 0.09	3.67 ± 0.04	Lacy04
		B5 V	4.66 ± 0.10	4.19 ± 0.04	
HS Aur	9.815	G8 V	0.900 ± 0.019	1.004 ± 0.024	Pop86
		K0 V	0.879 ± 0.017	0.873 ± 0.024	
RR Lyn	9.945	A6 IVm	1.927 ± 0.008	2.57 ± 0.02	Tom06
		F0 Vm	1.507 ± 0.004	1.59 ± 0.03	
RW Lac	10.369	G5 V	0.928 ± 0.006	1.186 ± 0.004	Lacy05
		G7 V	0.870 ± 0.004	0.964 ± 0.004	
DI Her	10.55	B5 V	5.185 ± 0.108	2.680 ± 0.046	Pop82
		B5 V	4.534 ± 0.066	2.477 ± 0.045	Alb09
HP Dra	10.762	F9 V	1.133 ± 0.005	1.371 ± 0.012	Mil10
		F9 V	1.094 ± 0.007	1.052 ± 0.010	
IC 1128562	10.79	Early F	1.543 ± 0.013	2.123 ± 0.010	Deb13
		Early F	1.200 ± 0.016	1.472 ± 0.014	
EP Cru	11.077	B5 V	5.02 ± 0.13	3.590 ± 0.035	Alb13
		B5 V	4.83 ± 0.13	3.495 ± 0.034	
BF Dra	11.211	F6 V	1.414 ± 0.003	2.086 ± 0.012	Lacy12
		F6 V	1.375 ± 0.003	1.922 ± 0.012	

Key to Reference abbreviations.

Alb07 – Albrecht et al. (2007)
Alb09 - Albrecht et al. (2009)
Alb13 – Albrecht et al. (2013)
And84 – Andersen and Vaz (1984)
And87 – Andersen et al. (1987)
Cla91 – Clausen (1991)
Cla10 – Clausen et al. (2010)
Deb13 – Debosscher et al. (2013)
Hen06 – Henry et al. (2006)
Kal13 – Kaluzny et al. (2013)
Kal14 - Kaluzny et al. (2014)
Lacy04 – Lacy et al. (2004)
Lacy05 – Lacy et al. (2005)
Lacy06 – Lacy et al. (2006)
Lacy12 – Lacy et al. (2012)
Mei09 – Meibom et al. (2009)
Mil10 – Milone at al. (2010)
Pop82 - Popper et al. (1986)
Pop86 – Popper et al. (1986)
Sab03 – Sabby and Lacy (2003)
Tom06 – Tomkin and Fekel (2006)
Tor99 – Torres et al., (1999)
Tor00 – Torres et al. (2000)
Tor14 – Torres et al. (2014)
Yak07 – Yakut at al. (2007)

The distribution by period and spectral type is summarised in Table 6.2 below. If each member of a dEB belongs to a different spectral type e.g. KW Hya where one member is an A-type and the other an F-type, the binary is listed under the more luminous type.

Table 6.2 Distribution of dEB's in Table 6.1 by period and spectral type.

Period (days)	Spectral type O,B,A	F	G	All
5.0 to 7.0	3	3	4	10
7.0 to 8.0	2	2	0	4
8.0 to 9.0	2	1	1	4
9.0 to 12.0	4	4	2	10

For periods between 7 and 9 days, which will provide a particularly precise test of tidal interaction theories, Table 6.2 shows that DEBCAT lists just 8 binaries. In all but two of these, V1143 Cyg and M4 V66, one or both stars have masses heavier than $1.4M_{\odot}$. In M4 V66 both stars are significantly less massive ($< 0.8M_{\odot}$) than the Sun. Thus a study of

V1094 Tau will help fill a major gap of a map of tidal interactions against a grid of mass/radius and metallicity.

The periods and masses of all the dEB's listed in Tables 6.1a and b are plotted in Fig. 6.2, and the corresponding mass/radius diagrams in Figs. 6.3a and b. Figure 6.2 plots each member of a dEB separately so each system appears as a pair of points. In order to identify them more easily they are colour coded by cycling the entries in the Tables 6.1 in order of period through the set of colours in the palette provided by the graphical output software used (Veusz). This coding is shown in Table 6.3.

Table 6.3 Colour coding for period-mass plot (Figs 6.2a and b) and mass radius plot (Fig. 6.3)

Green	HD 71636	BW Aqr	M4 V66	RR Lyn
Dark blue	RT CrB	CV Vel	EI Cep	RW Lac
Light blue (cyan)	BK Peg	EW Ori	V459 Cas	DI Her
Magenta	V396 Cas	V364 Lac	TZ Men	HP Dra
Yellow	V530 Ori	V1143 Cyg	M55 V54	IC 1128562
Grey.	V785 Cep	KW Hya	MU Cas	EP Cru
Dark red	GG Ori	EY Cep	HS Aur	BF Dra

The V1094 Tau system appears on these plots as bright red squares, to distinguish it more easily from the other systems which are shown as circles.

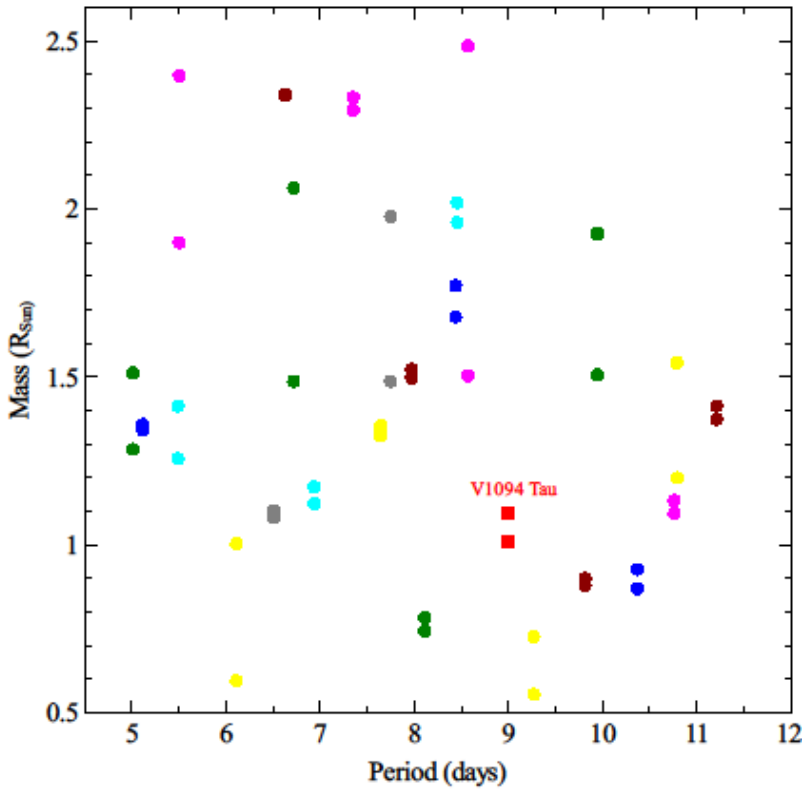

Figure 6.2 Periods and masses of the dEB's listed in Tables 6.1a and b. Each system is shown as a pair of dots, one for each star. The systems are colour coded as in Table 6.3. The V1094 Tau system is shown as a pair of red squares.

It will be seen that the V1094 Tau system lies in what would otherwise be a relatively empty region of the period-mass plot and that the masses of each star is closer to that of the Sun than any of the other dEB's listed.

All the dEB's listed in Tables 6.1a and b are shown on the mass-radius plots Figs 6.3a and b. Because Fig. 6.3a is congested for lower masses and radii, in particular because the point for the V1094 primary is there obscured, the region for solar-type parameters is shown in the expanded plot Fig. 6.3b.

Figs. 6.3a and b also plot the relation $R_S/R_\odot = (M_S/M_\odot)^{0.8}$ used by Seager and Mallen-Ornelas (2003) and referred to elsewhere in this thesis, from which it may be seen:

i) that V1094 Tau is one of the less massive dEB systems in this period range and
ii) the stars in many of these systems are evolved in that the radii are much larger than predicted by the $R \propto M^{0.8}$ relation.

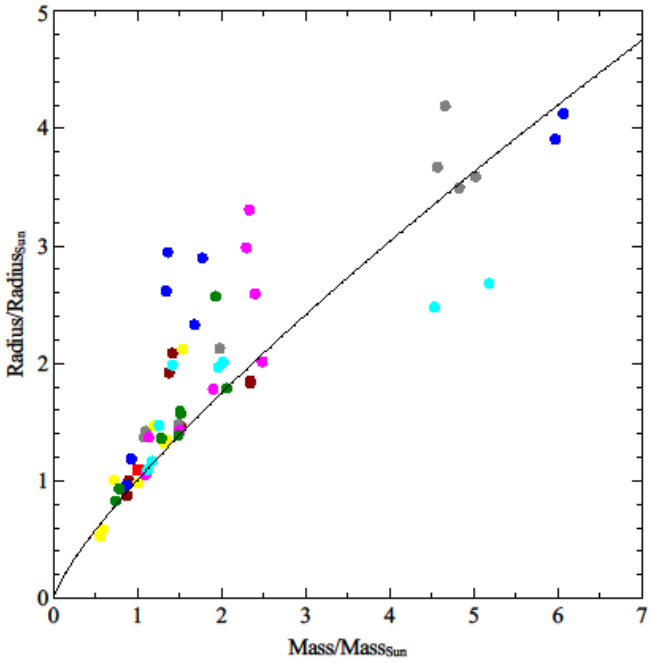

Fig. 6.3a Mass-radius plot for dEB's with periods between 5 and 12 days (Figs. 6.1a and b). The dEB's are colour coded as in Table 6.2. The curved line shows the relation $R_S/R_\odot = (M_S/M_\odot)^{0.8}$

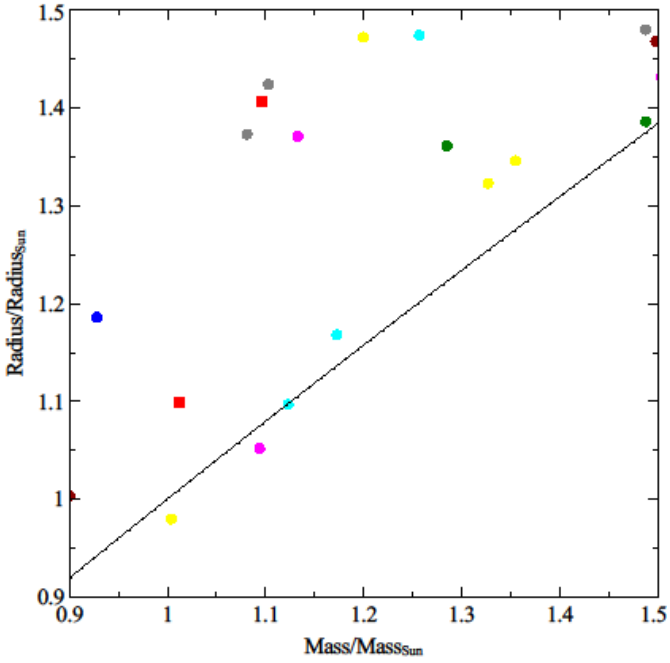

Fig. 6.3b Expanded section of Fig. 6.3a.

CHAPTER 7 BACKGROUND REVIEW

This chapter briefly reviews the relevant background. It is in six sections.

Section 7.1 Stellar formation, evolution and models

Section 7.2 The mass/radius relation and the discrepancies between stellar models and observation.

Section 7.3 Description of eclipsing binaries.

Section 7.4 Importance of eclipsing binaries.

Section 7.5 Limitations of dEB's for providing accurate stellar data.

Section 7.6 Literature and Data Reviews for dEB's.

7.1 Stellar formation, evolution and models

A star is an approximate sphere of hot plasma held together by gravity in which fusion energy generated in the core is transported to the surface by either radiation or convection.

7.1.1 Formation of stars

Stars are formed from molecular clouds in the interstellar medium, which lies between existing stars in a galaxy.

The interstellar medium is a tenuous gas composed of 70% hydrogen, 28% helium and 1.5% other elements by mass, i.e. 91% hydrogen 9% helium and 0.1% other elements by atoms. The hydrogen and helium were formed shortly after the Big Bang, and other elements formed by nucleosynthesis in previous generations of stars. Most of the hydrogen exists in the molecular form.

If the cloud is sufficiently massive that the kinetic pressure of the gas is too weak to withstand gravitational attraction, it will undergo runaway contraction. The critical mass is

typically three or four orders of magnitude greater than the mass of the Sun. The collapse may be triggered by the collision of molecular clouds or shock waves from the explosion of a nearby supernova. As the cloud collapses it breaks up. The fragments then condense until the kinetic pressure is sufficient to slow the collapse, and become approximately spherical. When the density is sufficiently high, the fragments become opaque to their own radiation, and since this cannot now escape the interior of the fragments heats up. As the fragments condense initial turbulence develops and they begin to rotate. The collapse continues along the axis of rotation, but less so in the plane of rotation because the rotation inhibits collapse there. These fragments become flattened discs and are now protostars. The clouds in which this process tales place are sometimes known as "stellar nurseries".

The protostar continues to collapse more slowly and because of conservation of angular momentum rotates more quickly. The surface temperature remains stable but since the star is contracting the surface area and hence the luminosity decrease. It follows a evolutionary track which depends on the mass. For stars with masses below $0.5M_{\odot}$ the track is a Hayashi track (Hayashi, 1961) which is vertically downwards on the Hertzsprung–Russell (HR) diagram. These low mass stars are cool and highly opaque and so are fully convective. For stars with masses between $0.5M_{\odot}$ and $1.0M_{\odot}$ the star initially follows a Hayashi track and then veers off towards higher surface temperatures to join the Main Sequence by a Henyey track (Henyey et al., 1955). For these stars a radiative zone forms around the core. More massive protostars move straight on to a Henyey track. Examples of Hayashi and Henyey tracks are shown in the references above. The Hertzsprung-Russell diagram is shown in Fig. 7.1 in a form which illustrates the stellar types and parameters and in Fig. 7.2 to show the population of stars in each parameter cell. Fig. 7.1 shows the absolute magnitude M_V in the V spectral band (Appendix G and

Fig. G1). The relation between this magnitude and the Hipparcos magnitude M_{HP} shown in Fig. 7.2 can be obtained from Table 2 of Bessell (2000)

The core heats up and deuterium fusion begins. Eventually the core reaches a point where it becomes hot enough for hydrogen fusion by the proton-proton chain reaction to begin. This point is known as the ZAMS (Zero Age Main Sequence). The protostar has now become a star is in a long-lived steady state in which the hydrogen in the core is

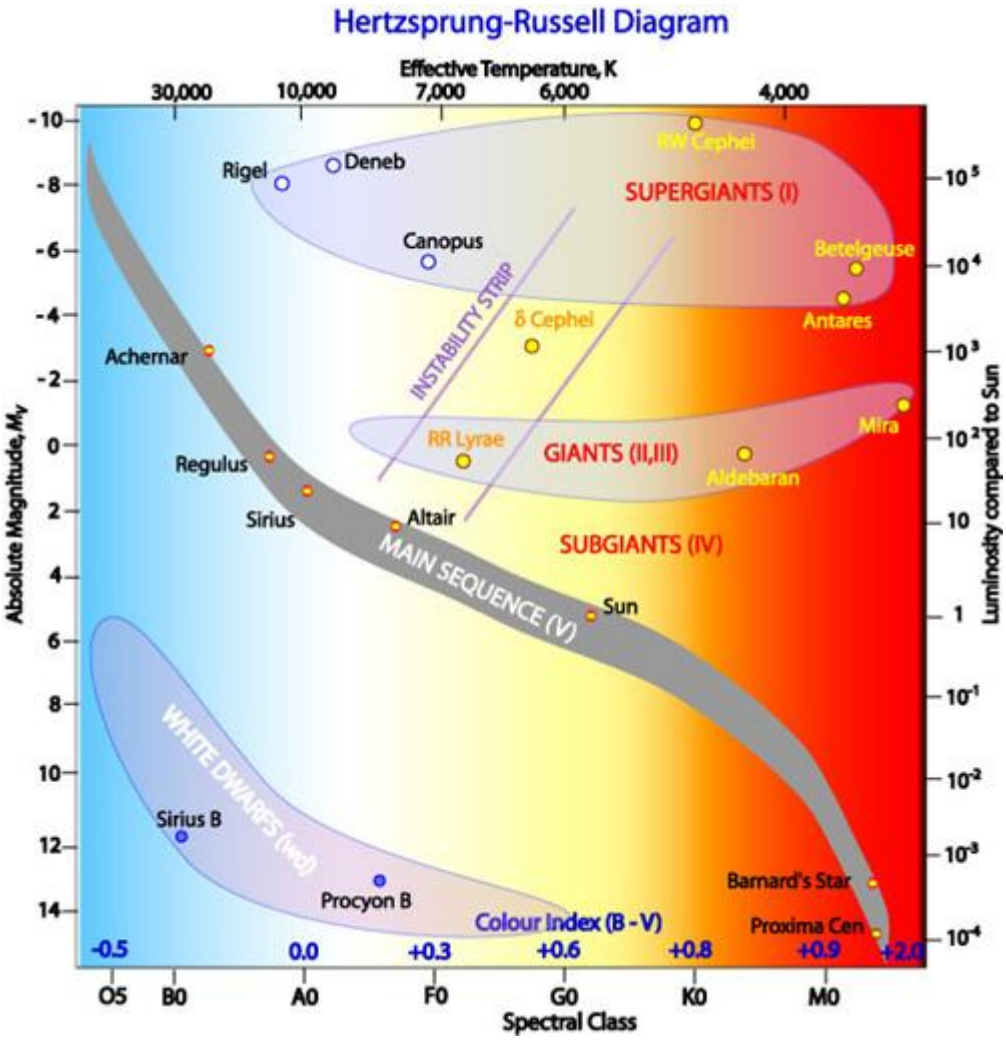

Fig. 7.1 Hertzsprung-Russell diagram with stellar parameters, spectral types and representative stars.
Taken from www.atnf.csiro.au/outreach/education/senior/astrophysics/stellarevolution_hrintro.html

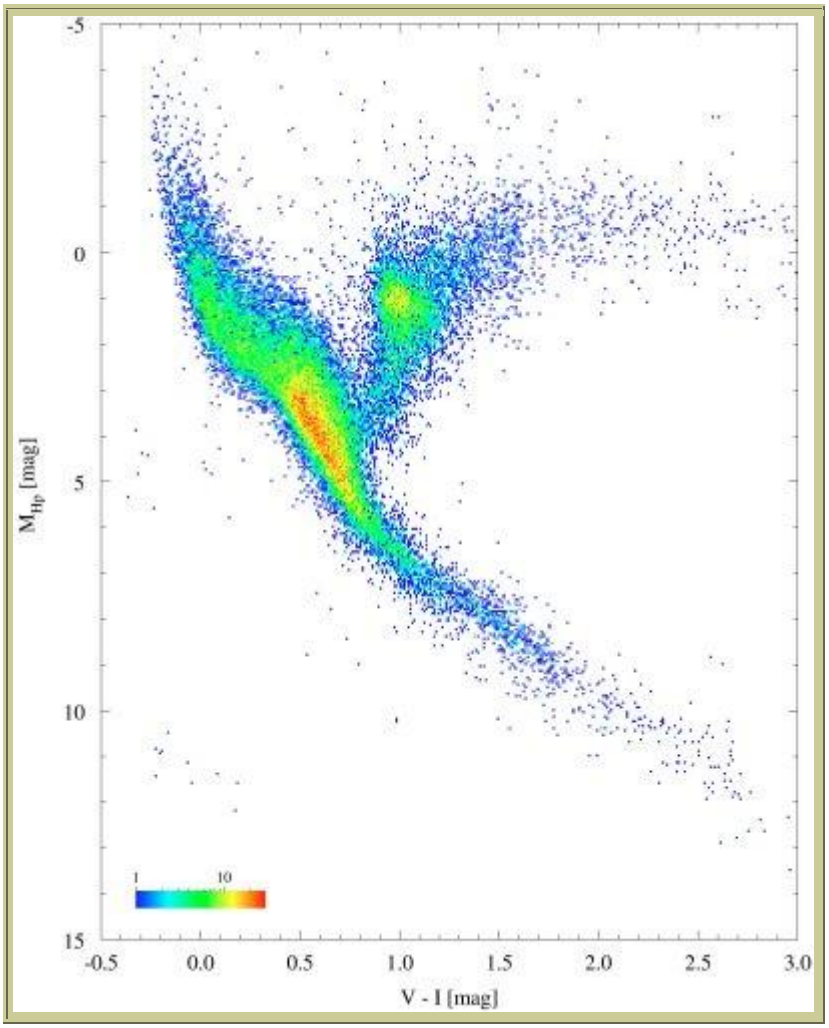

Figure 7.2: HR diagram generated from data on 41 453 stars in the Hipparcos catalogue. The colour scale indicates the number of stars in a cell of 0.01 mag in V-I and 0.05 mag in the Hipparcos magnitude M_{HP}.
Taken from www.sci.esa.int/education/35774-stellar-radiation -stellar-types/?fbodylongid=1703.

converted into helium. The lower mass limit for a star to form is about $0.08M_{\odot}$, or else the hydrogen fusion does not ignite. The upper limit on the mass is less well defined but is of the order of $100M_{\odot}$ and the main limitation is that the intense radiation pressure prevents the star from condensing.

The nuclear reaction cycle by which the hydrogen is converted into helium in the stellar core depends on the mass. For stars with masses up to $1.3M_{\odot}$, the main cycle is the proton-proton chain reaction (Bethe, 1939). For more massive stars the main process is the CNO reaction, first proposed by von Weizsäcker (1938) and Bethe (1939). The processes by which the fusion energy is transported to the stellar surface also depend on the mass. These are radiation and convection, and the zones where each is dominant are known as the convection and radiation zones. Main sequence stars with masses below $0.3M_{\odot}$ are wholly convective, thus they have no radiative zone. Between 0.3 and $1.2M_{\odot}$ the region around the core is radiative and the upper regions convective. In the Sun nuclear fusion takes place in a core which extends out towards about $0.2R_{\odot}$, the region lying between 0.2 and $0.71M_{\odot}$ is radiative and the upper layers convective. Above 1.2 $M_{\odot}$ the core region is once again convective and the upper layers radiative. The composition influences the opacity and hence the radiative energy transport to the surface. In the stellar interior hot plasma rises and loses heat to its surroundings. If the temperature gradient is steep, the hot plasma will rise faster than it can cool and will continue to rise until the temperature gradient decreases, and then descends to form a circular current. This is the mechanism of the convective zone and is dominant when radiation cannot by itself transport energy away from the core quickly enough. The kinetic energy associated with the current can propel stellar matter into the radiative zone; this phenomenon is known as “convective core overshooting”

7.1.2 Main features of stellar models

A star on the Main Sequence is in a long-lived hydrostatic equilibrium between kinetic pressure and gravity, determined by the mass. This is what mainly defines the stellar evolution. The star remains on the Main Sequence while the nuclear fusion in the

core converts the hydrogen into helium. The precise details of the evolution after the hydrogen is exhausted depend on the mass. Stars with masses between about $0.5M_{\odot}$ and $10M_{\odot}$ become red giants. The helium in the core undergoes fusion, and hydrogen fusion continues in a shell and the upper layers expand. The evolution of the star may be predicted by theoretical models. Progress on such models has been reviewed recently by Serenelli (2014). Their aim is to start from given mass, composition, rotation period and age and to predict observable parameters such as radius, surface temperature and total luminosity. The models can predict the period of stellar oscillations in terms of the internal stellar structure and this can be measured by asteroseismology (Sect. 7.1.3). Knowledge of the internal structure leads to estimates of the age; this parameter determines the rate at which fusion energy is generated in the stellar core and hence transported to the surface. The dependence on age arises because as the star ages the hydrogen abundance in the core decreases, the core heats up, and the rate of energy production increases. The composition determines the optical opacity and hence affects the energy transport by radiation. The rotation will affect the convection. Sophisticated stellar models take into account that the rotation rate varies both with depth and stellar latitude. Since the stellar material is a plasma i.e. where most of the atoms or molecules are ionised and hence charged this helps to generate a magnetic field which again affects the convection.

One-dimensional stellar models treat the star as a series of one-dimensional layers where each layer is treated by numerical integration. A typical resolution is that adopted by Bressan et al. (1993) whose model used 500 layers in the hydrogen burning phase and 1500 in later phases, and 2000 time steps over the whole evolutionary sequence. As pointed out by Serenelli, one-dimensional models are inadequate but the computer time required by a full multi-dimensional model is prohibitive. He suggests that multi-dimensional models could be used to study particular physical processes and the results

incorporated into one-dimensional models. The description above shows that a stellar model requires data for the nuclear reactions in the core, an equation of state, and opacity data for the radiative transport. Serenelli has reviewed the recent progress in all three areas. The main points of his description are as follows. The most commonly used opacities are from the OPAL model (Iglesias and Rogers, 1996). The equation of state corresponds to an ideal gas in the first order but relativistic corrections are needed to model the electrons, and a very accurate equation of state is needed to model the abundance of helium in the radiative and convective zones. Serenelli also reviews the theoretical and experimental progress in determining key nuclear reaction rates.

The convection within a star is frequently described by a single parameter *"α_{MLT}"* the mixing length parameter. Mixing length theory was developed in the German language article by Böhm-Vitense (1958). If a mass element rises or falls by convection, the height difference over which the material thermalises with the environment is the mixing length "*l*". The hypothesis is then made that *l* scales with the pressure scale height $\lambda_P = P/(dP/dr)$ where *P* denotes the pressure and *r* the radius. The mixing length parameter α_{MLT} is then defined as the proportionality constant between *l* and λ_P i.e. $l = \alpha_{MLT}\lambda_P$. The convection efficiency is proportional to $(\alpha_{MLT})^2$ (Lastennet et al. 2003). The dependence of λ_P on other stellar parameters may be derived the equations for hydrostatic equilibrium and the ideal gas equation. The balance of gravity and internal pressure on a mass element leads to the hydrostatic equilibrium equation

$$\frac{dP(r)}{dr} = -\frac{GM(r)\rho(r)}{r^2} \qquad 7.1$$

(this may be readily derived by considering the upward and downward forces on an infinitesimal rectangular element). In this equation the negative sign indicates that the pressure decreases with increasing radius. The symbols have their usual meaning. Rewriting Eqn. 7.1 in terms of the local acceleration of gravity g and dropping the (r) indices leads to

$$\frac{dP}{dr} = -g\rho \qquad 7.2$$

The ideal gas equation is

$$\rho = -\frac{\mu P}{kT} \qquad 7.3$$

where μ is the mean atomic/molecular weight and other symbols are as usual.

Hence

$$\frac{dP}{P} = -\frac{dr}{(kT/\mu g)} \qquad 7.4$$

Eqn. 7.4 shows that the pressure scale height is given by $\lambda_P = kT/\mu g$ since substituting this into Eqn. 7.4 and integrating leads to $P \propto exp(-\lambda_P)$.

A current deficiency in solar and stellar modelling are that it is not possible at present to calculate α_{MLT}, so that it is estimated by finding the value which matches observed solar properties most closely. It has not been established whether α_{MLT} is the same for all stars.

Detailed models need to treat linkages between the stellar parameters. For example the heavier elements tend to sink towards the core and so the chemical composition and hence opacity varies with depth. As the star ages, the conversion of hydrogen to helium in the core affects the opacity. The coupling between the stellar magnetic field and the stellar

wind (the flow of neutral or charged gas ejected from the upper atmosphere of the star) will brake the stellar rotation and so affect the convection.

Recent theoretical models were also reviewed in detail by Southworth (Thesis, 2006), and some of them are used later in this thesis in an attempt to determine the age of the V1094 Tau system.

Model stellar atmospheres are needed to set the boundary conditions for stellar models and to predict the emergent spectrum. The atmosphere is again treated as a one dimensional series of layers where each layer is distinguished by a different set of plasma parameters e.g. electron temperature and density. It is assumed that the photosphere is in hydrostatic equilibrium and local thermodynamic equilibrium (LTE). The term "LTE" means that:

- the inflow of radiation is determined by a blackbody spectrum for the local temperature.
- the population distribution of ionisation stages is described by the Saha-Boltzmann equation.
- the distribution over the energy levels of the molecules or ions is described by the Maxwell- Boltzmann equation.

The distributions must therefore be determined by collisional processes and their inverse, with radiative processes as a small perturbation. The term "inverse" indicates an atomic process in the reverse direction. For example if an atom with an electron in its ground energy state collides with another electron which excites the original electron to an upper atomic level, the inverse process is collisional de-excitation back to the ground state. The models rely on the standard equations for radiative transfer and on opacities, and take account of convection. A widely used solar atmosphere model is that of Kurucz (1993). More advanced models including convective 3-D effects (Freytag et al., 2002) and non-

LTE effects (Fontenla et al., 2009) have been developed but are computationally expensive and so less widely applied than 1-D LTE models.

Given a model atmosphere and spectral line data, a theoretical spectrum can be calculated. A widely used code is the UCLSYN code (Smith, 1992). Modern codes take into account microturbulence i.e. small scale turbulence in the photosphere. These broaden the spectral lines.

7.1.3 Asteroseismology

Stars undergo very low amplitude sound waves, driven by convection, which are reflected at the stellar surface and so form standing wave patterns. These are manifested in periodic oscillations of brightness and radial velocities. The amplitude of the brightness variation is of order a few parts per million and that of the radial velocity of order metres per second. The period is of order of minutes. Asteroseismology is a field which interprets these vibrations in order to probe the interior of stars in terms of fundamental parameters e.g. density profiles. The power spectrum of the oscillations is determined uniquely by the properties of the overall stellar structure and so may be used to test stellar evolution models. Asteroseismology has emerged in the last two or three decades as a major diagnostic technique and is the only quasi-direct method to determine the internal structure of a star with high precision. The field has been described in detail by for example in the lecture notes of Aerts (2007, www.ster.kuleven.be/ ~zima/helasna5/Downloads/ astero2007.pdf) and by Aerts et al (2010).

The stellar velocity oscillations can be either radial or transverse; in the latter case they may be described by spherical harmonics. The purely radial oscillations are characterised by a radial wavenumber *n* and the transverse oscillations by additional non-

radial wavenumbers *l* and *m*. Vibrations on the stellar surface are a superposition of these modes. There are two main types of oscillations: the high frequency pressure p-modes where pressure is the restoring force and the lower frequency g-modes where gravity is the restoring force. The g-modes and non-radial modes can penetrate most deeply into the interior of the star, although none penetrate all the way into the core. The oscillations are excited when some layers of the star trap the energy radiated outwards from the stellar core during a small contraction and release the energy during the subsequent expansion.

The oscillations may be detected either through periodic changes in brightness or Doppler shifts in photospheric absorption lines. For brightness where the oscillation amplitude is of order parts per million, measurements require sensitive instruments, freedom from atmospheric distortions and long observing runs. Thus space missions using the exoplanet transit method with their large instrument apertures are suitable for this work and in fact the COROT and Kepler missions, and the forthcoming PLATO mission (Sect. 10.4.2) were designed with asteroseismology as a significant part of their scientific objectives. Applications of asteroseismology to the analysis of Kepler data have been described by e.g. Huber et al. (2012, 2013) and by Metcalfe at al. (2014). The papers by Huber et al. explain how values of the well known stellar parameter *log g* can be obtained from asteroseismological observations and be used as a constraint to lift the degeneracy on the values of stellar parameters obtained from spectroscopic observations. The radial velocity variations can be studied by the instrumentation used to detect exoplanets by the radial velocity method; one such study using a CORALIE fiber-fed echelle spectrograph has been described by Bouchy and Carrier (2001).

There are in general many standing wave modes and a periodogram of the power or frequency spectrum (depending on whether oscillations of the brightness or line profile are observed) can be obtained by sophisticated Fourier analysis techniques. An example of a periodogram obtained by observing brightness variations of the Sun is presented in Fig. 1.2 of Aerts (2007), which shows some modes with n = 19 to 22 and l = 0 to 3. The methods for mode identification have been described by e.g. Aerts (2007, Sect.5); for line profile analysis theoretical profiles need to be constructed by summing over segments of the stellar surface to allow for e.g. the varying projection angle. As discussed by e.g. Huber et al. (2013) the mean stellar density is related to the frequency difference between modes with consecutive radial wavenumbers n and the same spherical wavenumber l.

7.2 The Mass/Radius/Metallicity Relation

7.2.1 Basic theoretical principles underlying the mass/radius relation

A simple power law relation between the mass and radius can only be empirical and approximate. The processes within a star are too complex to be exactly expressed in this way. Stars cover about four orders of magnitude in mass, and as explained above the mass determines which of the two nuclear burning cycles dominates, and also the regions in which convection or radiation dominates in transporting energy away from the stellar core. Thus an exponent in an empirical power law will change along the Main Sequence.

A rough relation can be obtained by a crude physical model which splits a star into an inner and outer region, balances the gravitational force from the outer shell with the kinetic pressure from the inner core, and makes some severe simplifying approximations. This gives $R \propto M$ (www.astronomy.ohio-state.edu/~dhw/Intro/lec6.html). In practice the relation $R \propto M^{0.8}$ is a good approximation over a wide range of the Main Sequence, and

this is assumed by Seager and Mallen-Ornelas in their discussion described earlier of analytical solutions for transit light curves.

7.2.2 Discrepancies between observations and stellar models – overview.

Existing stellar evolution models underpredict the radius by typically 15% in the mass range 0.3 to 1.1$M_{\odot}$ (Southworth, 2009, who lists references to earlier measurements), which includes many exoplanet host stars. This discrepancy exists both for single and binary stars. The main findings are listed in Table 7.1 and the papers listed there are then described in somewhat more detail individually.

The picture which emerges from these studies is that stellar models underpredict the radii of low mass (0.3 to 1.0$M_{\odot}$) stars by 10% or more if the stars are fast rotators (period << 10 days), but not if they are slow rotators. The accurate measured radii are inflated with respect to theoretical models. It is now widely accepted that such a discrepancy exists (Torres et al., 2010). However Winn et al. (2011) describe the counter-example of Kepler 16A where the radius is not inflated. They note this but do not provide an explanation.

Table 7.1 Summary of findings in papers about underprediction of stellar radii

Author		Stars	Period (days)	Underprediction
Single				
1973	Hoxie	Some nearby	-	Up to 40%
2006	Berger	Six GJ stars	-	Up to 15-20%
2007	Lopez-Morales	14 GJ stars	-	Up to 35%
2008	Morales	695 K- and M-type	-	See text
Binary				
1977	Lacy	See text	Mostly < 8d	Up to 25%
1997	Popper	3 stars, see text	All < 1 day.	See text
1998	Clausen	Not listed	5 out of 8 have periods < 1d.	See text
2002	Torres + Ribas	YY Gem	0.814	10/20 %
2003	Ribas	CU Cnc	2.77	10 to 15%
2006	Torres et al	V1061 Cyg	2.35	0/10%
		FL Lyr, RW Lac,	2.18, 10.37	
		HS Aur ,	9.82	
2007	Lopez-Morales	See above (single)	See text	Up to 35%
2009a	Morales et al.	CM Dra	1.268	~ 5%
2009b	Morales et al.	IM Vir	1.309	3.7 and 7.5%
2011	Kraus et al.	12 low mass stars	≤ 1 day	4.8% + std.dev 1.0%
			1.5 – 2.0 days	1.7% + std.dev 0.7%
2011	Irwin et al.,	LSPM J1112+7626	41.03	See text

7.2.3 Further details of papers discussing underprediction of stellar radii

Single stars

Data for single stars are limited because masses and radii can be determined only for nearby stars where the direct methods briefly dscribed later are possible. Nevertheless Hoxie as long ago as his 1973 study cited earlier found that the theoretical mass/radius relation underpredicts radii by up to 40% for low mass stars in the solar neighbourhood. Hoxie does not list these stars explicitly.

Berger et al. (2006) used the CHARA interferometer array to measure the radii of six early and slowly rotating M-type stars (GJ 15A, GJ 514, GJ 526, GJ 687, GJ 752A, GJ 880) and they review other measurements from optical interferometry and eclipsing

binaries. They find (their Fig.4) that the stellar model of Chabrier and Baraffe (1997) underpredicts the radius by up to 20% in the range $0.4M_{\odot}$ to $0.7M_{\odot}$, and that the discrepancy with the model of Siess et al. (1997) is up to 10% greater. They find also (their Fig. 5) that the degree of underprediction increases roughly linearly with metallicity. They suggest that higher metallicity leads to larger radii through an opacity effect.

Lopez-Morales (2007) has reviewed mass and radius measurements for 14 single stars, 9 dEB's and 16 secondaries in binaries. The masses were between 0.12 and $0.79M_{\odot}$ for single stars and between 0.11 and $0.98M_{\odot}$ for binaries. She finds that for stellar masses below $0.35M_{\odot}$, there is no discrepancy between measured radii and those predicted by stellar evolution models, but for fast rotating stars in the mass range 0.35 to $1M_{\odot}$ the models do underpredict the radius. As shown in her Fig.1 the stellar model of Baraffe et al. (1998) underpredicts radii by up to 35% in this range for both single and dEB stars. She also finds that a correlation between radius and metallicity appears to apply for single stars, but not binaries, but cautions that for binaries her conclusion is provisional since metallicities are available for only a few binaries.

Morales et al. (2008) have surveyed a large sample of 695 late K- and M-type single stars. They compare magnetically active and inactive stars by binning by bolometric magnitude. They find that in the active stars the radii are inflated by 5 to 12% compared to the inactive stars, depending on criterion and bin (their Tables 4 and 5) and that the T_{eff} values are 60 to 130 K lower. They conclude that this mass-radius discrepancy exists for any magnetically active star in this range, whether it is single or a binary member.

Binary stars

Lacy (1977) surveyed 55 eclipsing binaries where all but 7 have periods shorter than 8 days, and 160 single stars mainly of spectral type G to M. The stars had reliably determined distances. Lacy derived the radii and concludes (in his Section IIIa and IIIb) that it had been conclusively demonstrated that the theoretical models for stars less massive than the Sun predict radii which are systematically up to 25% smaller than the real stars.

Popper (1997) reports accurate measurements of the three dEB's UV Leonis (spectral type G0+G2), UV Piscium (G5+K3) and BH Virginis (F8+G5) and suggests that our understanding of low mass main sequence stars is not satisfactory. All three orbital periods are shorter than 1 day i.e. tidal interaction theory predicts that these systems are tidally locked and therefore the orbital and rotational periods are synchronised.

Clausen (1998), in his review of EB's, points out that these systems are the main source of accurate data on stellar masses and radii, but also that data for stars less massive than $1M_{\odot}$ were then scarce. At that time data were available for about 100 stars, but in the range $0.7M_{\odot}$ to $1.1M_{\odot}$ only for 12 stars in 8 systems. Five have periods shorter than one day and for these systems Clausen finds (his Sect. 3) that if the condition is imposed that the two binary members have the same age, the stellar models underpredict the radii.

Torres and Ribas (2002) present accurate (1% level) measurements of the masses and radii of the EB YY Geminorum (a member of the six star Castor system), which again has a period of < 1 day, precisely 0.814 days. They find that (their Fig. 11a) that the stellar models of Baraffe et al. (1998) and Siess et al. (1997) underpredict the radius by 10% and 20% respectively and that these discrepancies are over 10 and 20 times the measurement uncertainty.

Ribas (2003), in his study of the EB CU Cancri (masses 0.433$M_\odot$ and 0.398$M_\odot$, period ~ 2.77 days), finds (his Fig. 4) that the stellar models underpredict the radius by about 10-15%.

Torres et al. (2006) describe a detailed study of the dEB V1061 Cygni and also discuss the dEB's FL Lyrae, RW Lacertae and HS Aurigae. They find (their Sect. 5.2) that for V1061 Cygni and FL Lyrae (periods 2.35 and 2.18 days respectively) the stellar models follow the pattern of underpredicting radii by about 10%, whereas for RW Lacertae and HS Aurigae (periods 10.37 and 9.82 days respectively) there is no significant discrepancy.

Ribas (2006) surveyed 14 well characterised M-type stars from 8 dEB's, where 10 have radii determined to within 4%, and finds (his Abstract, Sect. 4 and Fig.1) that the radius is inflated by 5-15 % with respect to theoretical models.

The survey by Lopez-Morales (2007) described above includes binaries. Four of them (CM Draconis, YY Geminorum, CU Cancri and GU Bootis) are listed in the review of (Torres et al., 2010) and have periods between 0.49 and 2.77 days.

Morales et al. (2009a) describe a detailed study of the low mass eclipsing binary CM Draconis similar to that described here for V1094 Tau. The system has a period of 1.268 days, the masses are M_1 = 0.2310 ± 0.0009 $M_\odot$ and M_2 = 0.2141 ± 0.0010 $M_\odot$. They find (their Sect. 6) that compared with theory the radii are inflated by ~4.7% and 5.0% and the values of T_{eff} lower by 6.8% and 6.3%.

Morales et al. (2009b) describe detailed measurements, to the 1 to 2 percent level, of the EB star IM Virginis again similar to the present study. The system has a period of 1.309 days, the masses are M_1 = 0.981 ± 0.012 $M_\odot$ and M_2 = 0.6644 ± 0.0048 $M_\odot$. In their

Sect.6 they state that compared with theory the radii are inflated by ~3.7% and 7.5 % and the values of T_{eff} lower by 1.8% and 3.1%.

Kraus at al. (2011) have studied 6 dEB's with M-type stars, with masses between 0.38 and 0.59 $M_{\odot}$ and orbital periods between 0.6 and 1.7 days. They combine their results with six previously studied dEBs and find (their Sect. 6 and Figs. 9 and 10) that, in the mass range 0.35 to 0.80$M_{\odot}$, radii are inflated by up to 10% for short period ($\lesssim$1 day systems) but by much smaller amounts of 1.7 ± 0.7% for systems with longer periods of > 1.5 days. They propose that the short period systems are tidally synchronised, so the stars are forced to rotate rapidly and this enhances magnetic activity and so inhibits convection. This is consistent with those studies listed above where the radii were inflated for short period (order 1 day) binaries.

Irwin et al. (2011) have described a study of the M-type dEB LSPM J1112+7626, which has a period of about 41.032 days, and find (their Sect. 5 before subsection 5.1 and Table 12) the the sum of the component radii is inflated by 3.8 +0.9 -0.5%. Thus the radius of a low mass star may also be inflated for a system where magnetic activity is not enhanced by rapid rotation due to tidal locking.

Some of the studies mentioned above have considered the metallicity. This is determined from an analysis of the stellar spectrum. Currently this is done by standard packages for the analysis of spectral intensities; for example Southworth et al. (2004b) used UCLSYN (Smith, 1992; Smalley et al. 2001) in their study of V453 Cygni. Metallicities are expressed in the form [Me/H], which is the ratio of the logarithm of the star's metal abundance relative to hydrogen compared to that of the Sun.

Thus it is expressed as

$$[Me/H] = \log(Me/H)_S - \log(Me/H)_{\odot} \quad 7.5$$

It is commonly given only for the iron content *[Fe/H]* because the abundance of iron is relatively easy to measure due to the large number of iron spectral lines in the visible region.

7.2.4 Reasons for discrepancies between observed radii and stellar models.

Chabrier et al. (2007) have presented a phenomenological explanation for the radius discrepancy in low mass stars, by invoking enhanced magnetic activity in rapidly rotating stars. They argue that the magnetic fields within these stars inhibit rotation dominated convection, hence the convective heat flux away from the stellar core is reduced, and the star must grow larger to radiate away the same amount of energy. Provided that the inflation does not significantly change the total energy radiated from the star, the larger surface area leads to a lower effective temperature T_{eff}. A related mechanism is starspots. The heat flux from the star spot areas is reduced, therefore the star must grow larger to radiate the same amount of flux from the interior via the remaining areas. The word "phenomenological" used above here meant that reasonable values of relevant physical parameters could resolve the discrepancies, but that a full detailed physical model had not been produced. These physical parameters are a) the mixing length parameter and b) the fraction of the stellar surface covered by star spots. This explanation for the radius discrepancy is widely accepted (Torres et al. 2006; Clausen et al. 2009). It is supported by the result of Kraus et al. (2011) that the greatest inflation of the radii occurs for the short period binaries where the magnetic activity is expected to be the strongest. If this is correct there is no need to invoke inaccurate equation of state or opacity problems. A corollary is that this mechanism would not operate for very low mass stars, because they rotate slowly,

nor for stars with masses somewhat higher than the Sun, where the radiative zone extends to the surface, nor for the slowly rotating stars studied by Berger et al. (2006). The effect of metallicity invoked by Berger et al., also by López-Morales (2007) for these stars is still under debate.

Very recently the hypothesis that magnetic fields inhibit the convection has been examined in a long and very detailed paper by Feiden and Chaboyer (2013). These authors study three low mass dEB's UV Psc, YY Gem and CU Cnc. All three have been studied previously (Table 7.1 and subsequent expanded list); accurate masses and radii are available, and the radii are inflated with respect to theory. They are listed in order of decreasing mass, where the values span the range 0.4 to 1.0$M_{\odot}$, the mass range where the stars are expected to have an inner radiative zone and outer convective zone. Feiden and Chaboyer use a version of the Dartmouth stellar evolution code modified to include a magnetic field in thermodynamic equilibrium with the surrounding plasma (Feiden and Chaboyer, 2012; Feiden, 2013). Thus these authors included magnetic effects as an integral part of their stellar model, in contrast to the earlier work by Chabrier at al., who assumed reasonable values of magnetic parameters and then calculated their effects. After a lengthy analysis of UV Psc, with the constraint that both stars should have the same age and metallicity, they conclude that the observed radii and surface temperatures agree with theoretical predictions if magnetic models are used for both components and a value for the surface magnetic flux is assumed. These authors find agreement for YY Gem with the caveat that the metallicity needs to be near the edge of the range predicted by observations for the corresponding theoretical lithium abundance. For CU Cnc the use of a magnetic stellar evolution model reduces the discrepancies with observation but does not eliminate them.

This apparent agreement or improved agreement is not the complete explanation. The surface magnetic fluxes invoked to explain the discrepancies, hereafter called the model fluxes, are inconsistent with those predicted from X-ray observations. Feiden and Chaboyer first derive an empirical relation between X-ray luminosity and surface magnetic flux. The data set for X-ray luminosities were obtained from various X-ray satellites and from data for the surface magnetic flux from terrestrial Zeeman effect measurements. X-ray data are available for the three dEB's studied from observations with the ROSAT X-ray satellite (Voges et al., 1999). The corresponding surface magnetic fluxes are barely consistent with the model flux for UV Psc and grossly inconsistent for YY Gem and CU Cnc. This discrepancy can be partially resolved in two ways. First, it had been assumed that the magnetic field dynamo was driven by differential rotation between the radiative and convective zone; this is why the three binaries were chosen so that both stars are partially radiative and partially convective. The magnetic stellar evolution model was modified so that the magnetic field dynamo was driven by turbulent convection. Secondly Feiden and Chaboyer introduce a free parameter "*f*" (their Sect. 4.4.2) which describes the relation between the magnetic energy gradient of a convecting element and that of the surrounding plasma. These changes lead to a surface magnetic flux for YY Gem and CU Cnc which agree much more closely with the X-ray fluxes. However it was then not possible to obtain a self-consistent model for UV Psc in agreement with the observations.

This work is a significant development in allowing for magnetic fields in stellar modelling. However it studied only three dEB's and discrepancies still remain for one of them. It also requires the free parameter "*f*".

7.3 Description of Eclipsing Binaries.

7.3.1 Classification of binaries

Many stars belong to binary systems where each star follows an elliptical or circular orbit around a common centre of mass and so orbit with the same period. If the orbital plane is sufficiently well aligned to the line of sight each star passes in front of the other and the combined luminosity dips periodically. The system is then an EB. The star with the hotter surface temperature and hence higher surface brightness is called the primary and the cooler star the secondary. The deepest luminosity dip is called the primary eclipse, and generally occurs when the secondary eclipses the primary, although this is not always true for elliptical orbits. The dip when the primary eclipses the secondary is called the secondary eclipse. Photometric light curves i.e. profile of combined intensity against time for V1094 Tau are shown in Figs. 9.5 and 9.6 and a radial velocity curve in Fig.9.3. Light curves for the potential target systems considered for the SAAO run described in Part III are shown in Fig. 11.1.

It is convenient to define a rotating coordinate frame in which the two stars are stationary. In this frame each star in a binary is surrounded by a continuous series of gravitational potential surfaces as shown in Fig. 7.3 which is drawn for the case where the mass of the star shown on the lower left is twice that on the upper right. The upper part of this Figure shows a three dimensional plot of the potentials themselves. It may be seen how the potential varies along the axis passing through the two stars. There are three contributions to the gravitational potential in this frame i.e. a) and b) from the two stars themselves and c) *as if* there were a centrifugal force; this represents the transformation from the rotating stationary frame.

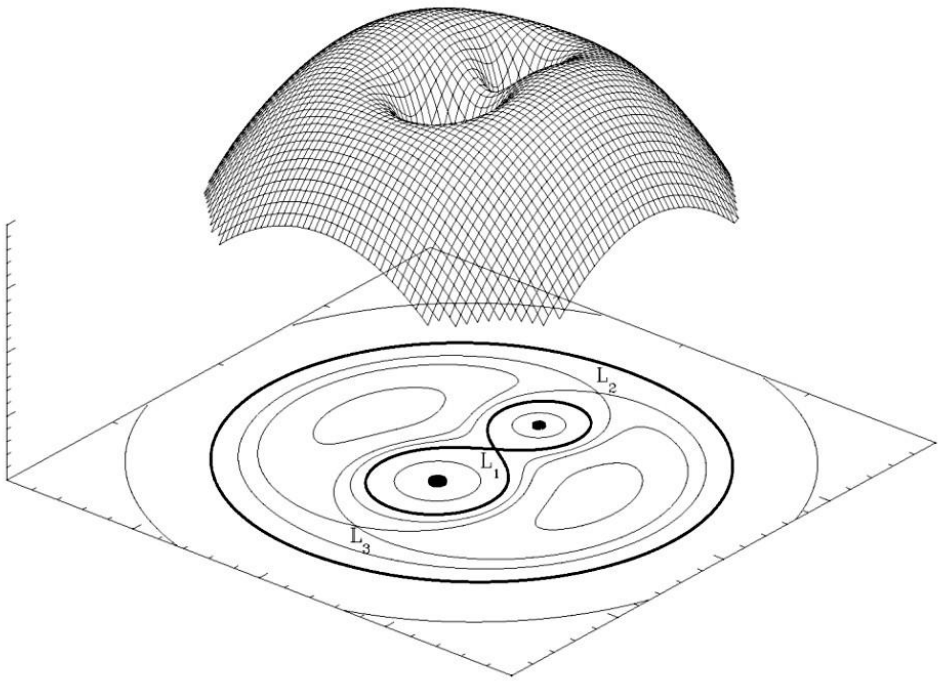

Fig. 7.3 Equipotentials and Roche lobes for a binary system.

From www.hemel.waarnemen.com/Informatie/Sterren/hoofdstuk6.html#mtr

One particular equipotential surface intersects at the Lagrangian point L1, the point between the two stars where the gravitational forces from each star cancel. This surface defines a volume called the Roche Lobe. If a binary component lies wholly within the Roche lobe the material of that star is gravitionally bound to that star only. The only mass transfer from one star to the other is then by stellar wind. Eclipsing binaries for which both stars are within their Roche lobes are detached eclipsing binaries.

If a star evolves and expands to overfill its Roche lobe, some of its material can escape its gravitational pull and be transferred to the other star. Binaries in which this has occurred are known as semi-detached or contact binaries, depending on whether one or both stars overfill the Roche lobe. A full discussion of the various classes of binary stars is outside the scope of this thesis but has been given by e.g. Hilditch (2001).

An approximate formula for the radius of the Roche lobe, insofar as it can be considered to be spherical, has been derived by Eggleton (1983) and is:

$$\frac{r_1, L}{a} = \frac{0.49q^{2/3}}{0.6q^{2/3} + \ln(1 + q^{1/3})} \qquad 7.6$$

This formula gives the radius $r_{1,L}$ of the lobe surrounding the star M_1, where a is the distance between the stars and $q = M_2/M_1$. For V1094 Tau $q = 0.9232$ and the relative radius of the primary is $r_1/a = 0.06028$. The radius of the Roche lobe is therefore $r_{1,L}/a = 0.372$, thus $r_1/a << r_{1,L}/a$ and the V1094 Tau system is a detached eclipsing binary.

The Lagrangian points L2 and L3 are those where due to the combined gravitational attraction of the two stars an object is stationary in unstable equilibrium in the corotating frame.

7.3.2 Formation and frequency of binaries

It is thought that binary stars are formed through the fragmentation of the molecular cloud during the formation of protostars (Boss, 1992). They may form together from the same fragment. In principle an alternative formation mechanism is that one star captures another but because of conservation of energy this is possible only in the presence of a third star, in which case one of the three stars is eventually ejected from the system to form a stable binary system. This mechanism may however still be significant in the molecular clouds where protostars form because the population density of the young stars there is high. Binaries where the stars are formed together confer the advantage that the stars will have the same age and metallicity although the masses and radii will be different and the stars will be at a different stage of their evolution. Hence the mass/radius dependence can be isolated.

The fraction of star systems which are multiple is substantial and depends on spectral type (Lada, 2006). Raghavan et al. (2010) surveyed a sample of 454 F6 to K3 stars, selected from the Hipparcos catalogue, lying within 25 pc and with a V-band flux between 0.1 and 10 times that of the Sun. They found that the percentage ratio of single:double:triple:quadruple systems was 56±2:33±2:8±1:3±1. A previous survey by Duquennoy and Mayor (1991) found similar results. Raghavan et al. also discuss how the frequency of multiple systems depends on spectral type and find that this frequency steadily decreases for progressively cooler types. This is shown strikingly in their Fig. 12. These authors quote (their Sect. 5.3.2) previous studies that most O-type stars seem to form in binary or multiple systems, but that estimates for the frequency for M-type stars range from 10% to 40%. For the cooler M stars Delfosse et al. (2004) find (their Sect. 5) a lower fraction of multiple systems i.e. 26 ± 3% and quote previous studies which find multiplicities ranging from 25% to 42%.

7.4 Importance of eclipsing binaries

The importance of eclipsing binaries is that they provide the main direct method of determining the mass and radius of a star. This statement is justified as follows.

Mass. The only approach to determine the mass of a star, in contrast to estimating it indirectly, is to observe the gravitational effects from a nearby star. In principle this can be done with visible, spectroscopic and eclipsing binaries. For visible binaries the motion of each component can be observed directly by astrometry, but only a relatively few binaries are near enough for this to be feasible. Further, visible binaries tend to have wide absolute separations, otherwise they would not be visible, and hence long orbital periods which are more difficult to measure accurately. Spectroscopic binaries are those which are

not eclipsing but where radial velocities are available for one or both of the stars. If they are available for both stars they provide only the projected radial velocities along the line of sight and hence a minimum mass. If radial velocities are available for just one of the stars it is possible only to determine a function of both the masses known as the mass function (Sect. 9.4.2).

Eclipsing binaries provide the true orbital velocities and stellar masses because the inclination can be determined from photometric light curves. It is intuitively clear that the time profile of the combined intensity depends on whether the eclipse is grazing or on the other hand total or annular. Combining the analysis of the light curves and of the Doppler shifts of each component yields a complete solution of the binary system i.e. masses and radii of each star and the orbital radii and period. The analysis of the light curves is analogous to that described earlier for transiting exoplanets, but with one basic difference. This is that for dEB's the light curves and Doppler measurements from each component are sufficient for a complete analysis of the system. For exoplanet systems the planet does not emit line radiation of its own, therefore its orbital velocity (in contrast to the host star) cannot be determined from Doppler measurements, and in consequence a complete analysis needs further data or a further assumption as explained earlier (Sect. 2.2.2).

Radius. As for the mass, the radii of most stars have been determined from eclipsing binaries. In principle radii can also be determined directly from the angular diameter and parallax measurements but again this is possible only for relatively near stars. Techniques used to measure the angular diameter are intensity interferometry (e.g. Baines et al. 2009) and lunar occultation (e.g. White, 1987).

The radii of dEB's are determined by analysing the photometric light curves and orbital velocities in combination as for the masses. The light curves by themselves can determine the relative dimensions of the system (i.e. ratio of stellar radii to semi-major axis of the relative orbit) and the inclination; if the orbital velocities are also known, Kepler's Third Law can be used to determine the semi-major axis of the orbit and hence the relative radii from the lightcurve analysis can be converted to absolute radii.

Thus the mass and radius can be determined to high precision without relying on stellar models, apart from a weak dependence on limb and gravity darkening coefficients explained later. Insofar as they can be considered to be effectively free of tidal interactions they can provide a stringent test of stellar evolution theory. If interaction between binary star members is significant, the relation between fundamental stellar parameters of dEB's and those of single stars is a basic astrophysical issue in itself.

Use as distance indicators. If accurate masses and radii are available, and the intensity in a spectral band is also available, stellar models may be used to calculate the absolute luminosity of the star and hence its distance. This is done here for V1094 Tau. Another application to date is to determine the distance of a stellar cluster by observing a dEB in stellar clusters and so define further the calibration of the distance scale for the δ Cepheid variable stars e.g. Southworth et al. (2004a). However this will become much less important or even redundant when accurate parallaxes from the *Gaia* mission are available (Sect. 10.4).

7.5 Limitations of dEB's for providing accurate stellar data.

Although dEB's provide accurate data for the stars themselves, they undergo tidal interaction. Each member of the binary raises tides upon the other. The unequal gravitational attractions on the two tidal bulges on each star will tend to synchronise the rotational period with the orbital period. The characteristic parameter for the strength of the tidal interaction is $(R/a)^6$, where R is the stellar radius and a is the semi-major axis of the relative orbit of the two stars. A detailed theory of tidal interactions has been developed by Zahn in a series of papers, referenced later where appropriate (Appendix K). This Appendix also gives a partial explanation of the $1/a^6$ term. The key result is that tidal synchronisation is significant for orbital periods shorter than about 8 days, that it falls off sharply for longer periods, and this critical cutoff is very insensitive to the masses of the stars because of the overwhelmingly dominant $(R/a)^6$ dependence of the interaction strength. The region of orbital periods shorter than 8 days includes the majority of known eclipsing binaries. The theoretical framework of Zahn also predicts that for a range of rotational periods longer than 8 days the rotational period is determined by an equilibrium between angular momentum exchange due to tidal interaction and loss of angular momentum due to stellar wind braking through magnetic interactions.

Thus for orbital periods shorter than about 8 days the rotational period, being locked to the orbital period, differs from what it would be for a single star. This in principle affects the convection and hence the evolution and structure of the star. Mass exchange may occur between the stars for very short period binaries, where the stars are extremely close. Thus it may be unsafe to use a mass/radius relation derived from eclipsing binaries to test models for single stars. Although exoplanet systems can in principle be analysed by empirical mass/radius relations such as those derived by Torres et al., (2010, Sect. 8) this still leaves our understanding incomplete. This is particularly serious problem

because as will become clear later, the majority of known EB's have periods shorter than 8 days.

7.6 Literature and Data Reviews for dEB's

Accurate data for eclipsing binaries, in particular masses and radii have become available from the mid-1970's onwards. There are strong observational biases. Low mass binaries are fainter and so are harder to discover. They are also smaller and so are less likely to be sufficiently well aligned to be eclipsing. Binaries with long periods have wider separations and so the range of inclination angles for eclipses to occur is narrower; moreover the eclipse lasts for a shorter fraction of the full cycle. These biases show a basic difficulty in studying the mass-radius relation in these EB's; if the orbital period is less than about 8 days the mass-radius relation may be affected by tidal interactions as discussed in Appendix K; if it is longer the systems are hard to find and the data relatively meagre. The recent major reviews and catalogues are described below. Note that a complete analysis of EB's requires both photometric light curves and radial velocity measurements (Sect. 7.3.3).

DEBCat. Southworth (www.astro.keele.ac.uk/jkt/debcat) is maintaining an up-to-date catalogue of well studied dEB's. Here "well studied" means guided by the criterion that masses and radii are accurate to better than ±2%. As of 16 March 2015, this catalogue contains 173 dEB's; a measure of the discovery frequency is that 23 new dEB's have been added since 6 August 2013. For each dEB the catalogue lists period, V-band magnitude and B-V colour index, spectral type, mass, radius, *log g*, log T_{eff}, log (luminosity), metallicity, literature reference, and website links.

Torres et al. (2010). The review by Torres et al. includes a critical compilation of accurate measurements of the masses and radii of 95 detached binary systems, of which all but one (α Centauri) are eclipsing binaries. The masses and radii were obtained by combining photometric and spectroscopic radial velocity measurements. The data extend as far back as the 1970's and cover two orders of magnitude in mass. It extends the previously definitive review of Andersen et al. (1991) and is the result of an exhaustive search of literature for binaries satisfying two conditions. The first is that masses and radii have been determined to 3%; a criterion which was set because this level of accuracy is required to test the validity of candidate stellar evolution models. The second is that the separation of the two stars is wide enough for the stars to be regarded as non-interacting i.e. having evolved separately. Most of the EB's in this review are short period systems with massive stars. In only 15 of these EB's is the mass of either component less than 1 $M_{\odot}$; all but seven of these systems have periods shorter than 10 days. Torres et al. emphasise that the criterion for including a binary system in their sample is solely quality of data only, and that they do not attempt to keep the sample free of selection biases. Thus they caution that their sample is unsuitable for any kind of statistical analysis. They explicitly point out that the observed rotational velocities of most of the binaries in their sample agree very closely to what would be expected if they were tidally synchronized with the orbital period, as would be expected from the ideas of Appendix K. Since most of these data refer to EB's with periods shorter than 8 days where tidal interactions are believed to be strong, it is unsafe to use them to test models for single stars.

Coughlin et al. (2011). Coughlin et al. (2011) have published a catalogue of 231 EB's from the newly released Cycle 0 dataset from the *Kepler* mission (Sect. 2.2.3). This mission is confined to a relatively small area of the sky and observes objects with magnitudes in the range 11 to 16, thus there is little overlap with the SuperWASP archives

which in common with other ground-based surveys covers a magnitude range of about 9 to 13 (Sect. 4.2.1). Here the photometric light curves were modelled by JKTEBOP eclipsing binary code (Appendix G), but in contrast to Torres et al. the masses and radii were obtained, not by radial velocity measurements, but from the photometric curves and initial assumptions by an iterative technique. Coughlin et al. do not quote uncertainties for their mass and radius values. Of these 231 EB's, 142 have one component with $M < 1M_{\odot}$, and 79 have both components lighter than this. This catalogue is particularly important since it is the first to provide significant amounts of data for systems in the previously unexplored regions where periods are longer than 8 days and tidal interactions are thought to be not significant. However the method for obtaining the masses and radii is only indirect. Twenty-five of the listed EB's systems have periods longer than 10 days. Consistently with the theories of tidal interaction, for EB's with periods longer than 10 days region, the radii agree with theoretical models to within 5% for 40% of the systems; but for periods shorter than 1 day only 9% do so.

All Sky Automated Survey (ASAS). The Polish All Sky Automated Survey (ASAS) (Paczyński et al. 2006) has discovered over 50000 variable stars, including about 11000 EB's, at positions south of declination +28°. The survey is approximately complete in the magnitude range 8<V<12, but detection efficiency falls off in the range 12<V<14. It uses the 7 cm telescope at the Las Campanas Observatory in Chile, and in a five year period ending in 2005 it had observed about 17 million stars for at least 5 years. Paczynski et al. plot a histogram of periods of EB's with galactic latitude $|30°|$ which shows that many of the systems shown there have periods shorter than 1 day and most have periods shorter than 10 days. Thus most of these EB's are likely to be subject to tidal interactions. However this catalogue lists photometric light curves only, with no orbital velocities and so cannot by itself provide accurate masses and radii.

In a later paper from this group Helminiak et al (2009) published spectroscopic follow-up measurements where they reported radial velocity measurements on 18 selected detached EB's, 16 on the 3.9 metre Anglo-Australian Telescope (AAT) and 2 on the 1.9 metre Radcliffe telescope at the South African Astronomical Observatory (SAAO) with the GIRAFFE spectrograph (Sect. 11.5)**.** These authors were able to determine the masses to an accuracy of 0.2% to 4%, and the radii to between 1% and 30%. Further papers describing the analysis of specific EB's have been published by Helminiak and Konacki (2011) and by Helminiak et al. (2011). Of the 18 systems studied by Helminiak et al (2009), five have periods longer than 8 days, and three of those have periods 8-9 days. However these authors do not give rotational periods and so their results cannot be used to test tidal interaction theories, although the orbital periods do lie in the ideal range.

SuperWASP Archives. A potential rich source of EB data is the SuperWASP archives (www.superwasp.org). These contain light curves for many EB's with periods longer than 10 days. These archives can be sifted for suitable systems for follow-up observations of the rotational and orbital velocities and so in principle yield masses and radii to ± 1% or better. This would be another important source of long period EB data. The first stage in the radial velocity measurements of selected SuperWASP EB's is the subject of Part III.

CHAPTER 8. PREVIOUS KNOWLEDGE AND MORE RECENT DATA FOR V1094 TAU.

8.1 Main features of V1094 Tau

The V1094Tau binary lies in Taurus roughly halfway between Aldebaran and the Pleiades. Charts of the region of the sky around V1094Tau appear in Appendix L. Table 8.1 shows entries for this system in all the catalogues listed in SIMBAD.

Table 8.1 Catalogue Entries for V1094Tau

Catalogues since discovery in 1994 as an EB, and other catalogues using commonly cited designations.

Catalogue	Designation	Reference
Bonner Durchmusterung	BD +21° 605	1
Henry Draper Extension Catalogue	HD 284195	2
Tycho Catalogue	TYC 1263-00642-1	3
2MASS catalogue	2MASS J04120358+2156508	4
NOMAD	1119-0053098	5
IBVS 4119 (Discovery as EB)	DHK 41	6
General Catalogue of Variable Stars	V1094 Tau	7
Washington Catalogue of Double Stars	WDS 04121+21571	8
9th Catalogue of Spectroscopic Binary Orbits	SBC9 2334	9

Catalogues before discovery as an EB.

Yale Zone Integrated	YZ 21 1349	10
Index catalogue of Double Stars	IDS 04062+2141 A	11
Smithsonian Astronomical Observatory	SAO 76494	12
AGK3 Catalogue	AG +21 394	13
Positions and Proper Motions	PPM 93323	14
CCDM	CCDM J04121 +2157A	15

References

Author	VizieR Ref. No.
1. Argelander (1903)	I/122
2. Cannon and Mayall (1949)	III/182
3. Høg et al. (2000)	I/259/tyc2
4. Cutri et al. (2003)	II/246
5. Zacharias et al. (2004)	I/297
6. Kaiser (1994).	-
7. Samus et al. (2012)	B/gcvs
8. Mason et al. (2001)	B/wds
9. Pourbaix et al. (2004)	B/sb9
10. Barney (1954).	I/141/yale00
11. Jeffers et al.(1963)	-
12. SAAO staff (1966)	I/131A
13. Heckmann (1975)	I/61B
14. Roeser and Bastian (1988)	I/146
15. Dommanget and Nys (1994)	I/274

The identifications, locations and magnitudes of the system are listed in Table 8.2.

Table 8.2 Location, spectral type and combined photometric indices for V1094 Tau

Parameter	Value	Ref. + VizieR catalogue	
R.A (2000,NOMAD) Dec. (2000, NOMAD)	4h 12′ 3.5926″ +21° 56′ 50.551″	1	I/297
Spectral Type	G0 + G3 (see text)	2	-
B_N (NOMAD) V_N (NOMAD)	9.645 ± 0.032 8.981 ± 0.024	1 + 5, 1 + 5	I/297 + I/259, See note.
J_{2MASS} H_{2MASS} K_{2MASS}	7.784 ± 0.021 7.528 ± 0.039 7.424 ± 0.021	3 3 3	II/246
(b – y) m_1 c_1 β	0.415 ± 0.004 0.199 ± 0.021 0.330 ± 0.011 2.596 ± 0.005	4 4 4 4	

References:
1) NOMAD, Zacharias et al. (2004)
2) Griffin and Boffin (2003)
3) 2MASS, Cutri et al. (2003)
4) Clausen (private communication – see "Acknowledgements")
5) TYCHO-2, Høg et al., (2000).

Note: For the NOMAD magnitudes Item 1 refers to the value and Item 5 to the uncertainty. The NOMAD catalogue redirects to the TYCHO-2 catalogue for the latter, and the TYCHO-2 uncertainty is adopted.

SIMBAD does not give any value for the radial velocity; a value for this is one of the results of this study.

Griffin and Boffin estimate the spectral types by two different methods;

	Primary	Secondary
From mass	F9 V	G2 V
From integrated colour index derived from Tycho photometry	G0 or G1	G3 or G4

The program *jktabsdim* used later (Sect. 9.9) has provision to input the magnitudes and light ratios (L_2/L_1) in the U,B,V,R,I,J,H,Kand L bands and calculates the absolute magnitudes and dimensions calculated for each spectral band for which data were entered. For the J, H and K bands it requires magnitudes in the Johnson-Cousins photometric system instead of in the *2MASS* system as quoted above. The spectral band used here to calculate the distance was the K band for the same reasons as for the exoplanet host stars (Sect. 3.5). Thus it is necessary to convert the *2MASS* K band magnitude. For the sake of completeness the J and H band magnitudes were converted as well. The required conversion was carried out by the equations given by Bessell (2005, Sect. 5.5). Bessell gives four equations for three colour indices and in consequence two values for the transformed colour indices can be calculated for each of the J and H bands. These were averaged. Thus the Johnson-Cousins magnitudes finally adopted as input are:

J	7.868 ± 0.021
H	7.561 ± 0.039
K	7.468 ± 0.021

The transformation introduces a change of order 0.05 into the magnitudes. The extra uncertainty of this already small magnitude change is unknown but is assumed to be much smaller and was ignored.

The V1094 Tau system is marginally too faint to appear in the original Henry Draper catalogue and is included only in the second extension to it. It does not appear in the Harvard Bright Star catalogue (which corresponds roughly to naked eye stars). Neither does it appear in the *Hipparcos* catalogue; this has a faint magnitude limit of V = 7.3 to 9.0 depending on galactic latitude and spectral type (Perryman et al., 1997, Table 1). Thus no parallax is available. This investigation provides a distance of 120.8 ± 2.2 pc (Sect. 9.9.2)

Throughout this chapter and the next the parenthetical notation 0.1234(56) means 0.1234 ± 0.0056 i.e. the digits in the brackets indicate the uncertainty in the immediately previous ones.

8.2 Previous studies

8.2.1 Discovery and period

The discovery of V1094 Tau was announced by Kaiser (1994) who quoted a period which was later found to be the time between secondary and primary minimum. The correct period was first given by Kaiser and Frey (1998), who described how this was finally obtained after another incorrect period had been given. Kaiser and Frey gave a period of

$$T_{min1} = \text{HJD } 2\,449\,701.7059(3) + 8^{d}.988487(7) \times E \qquad 8.1$$

based on observations between Oct. 1994 and Jan. 1997. The work of Kaiser and Frey also established that the orbit is eccentric, with the secondary minimum falling at a phase $\phi \sim 0.65$. Part of the present work has been to determine an improved ephemeris as described in Sect.9.2.

8.2.2 Spectroscopic study by Griffin and Boffin (2003)

A detailed spectroscopic study has been described by Griffin and Boffin (2003), cited hereafter as GB. These authors give radial velocities measured over 22 cycles from 2002 September 28 to 2003 April 2, and quote 36 observations where the radial velocity of each component could be determined separately, and a further eight where the two radial velocities could not be resolved. Their report does not quote a signal to noise ratio. Their study used the CORAVEL radial velocity spectrophotometer with echelle grating (Baranne et al., 1979, summarised by Imbert and Prevot, 1981) mounted at the Coudé focus of the 36 inch reflector at Cambridge. Griffin and Boffin point out that because the orbital period is an almost integral period of about 9.0132 sidereal days, the measurements of radial velocities tend to bunch along the velocity curve. This may be seen on the radial velocity curves shown in Fig. 9.4; this figure also shows bunching for the INT spectra described later (Sect. 8.3.1 and 8.3.3).

Griffin and Boffin state explicitly (in their Abstract) that their work is only a radial velocity study and not a comprehensive analysis. Thus with regard to the stellar radii they simply refer to "estimated" radii of $R_1 \sim 1.1R_\odot$ and $R_2 = 1.0R_\odot$. They do not state explicitly how this estimate was derived, but these values would follow from the spectral type and by assuming that the stars have not evolved significantly. This thesis describes an analysis of light curves, which was not available to Griffin and Boffin, and shows that the primary is in fact slightly evolved with a radius of $1.406 \pm 0.010\ R_\odot$. Hence the radius for the primary given by Griffin and Boffin is too small.

8.3 Spectroscopic observations

8.3.1 List of observations

Four sets of spectroscopic observations now exist.

- The published measurements of Griffin and Boffin desecribed above.
- Radial velocities made available to the author by Professor Torres and his colleagues at the Centre for Astrophysics at Harvard (hereafter CfA) (private communication)

Two further new sets of high quality spectra, both so far unpublished. Their basic features are listed in Table 8.3.

Table 8.3 New spectra of V1094Tau

Telescope	Date	No. of exposures	Spectral Range (Å)
INT 2.54 m	14-23 Oct. 2002	65	4227-4499
Calar Alto 2.2m /FOCES	11-16 Aug. 2008	8	3964-7100

The abbreviation INT stands for the Isaac Newton Telescope at La Palma in the Canary Islands; these spectra were supplied by Southworth and Maxted (private communication). FOCES stands for the **F**ibre **O**ptics **C**assegrain **E**chelle **S**pectrograph (Pfeiffer et al.,1998), formerly mounted on 2.2 metre telescope at the Calar Alto Observatory, near Almeria in Spain. The FOCES spectra are not discussed further, except in the context of possible future work, since analysing them would require a disproportionate amount of work to obtain relatively little extra data.

8.3.2 CfA observations

The CfA observations comprise 59 pairs of radial velocity measurements obtained from 1995 December 29 to 1997 April 3. They are listed, together with the other radial velocity measurements used here, in Appendix E. The measurements were made with the 1.5 metre Wyeth reflector at the Oak Ridge Observatory, described by Latham (1985). This telescope was used with an echelle spectrograph covering a spectral region centered on the Mg I triplet ($3s4s\ ^3S_1 \rightarrow 3s3p\ ^3P_{0,1,2}$) at 5187Å and 45Å wide, with a resolving power of 35000. The exposure time varied between 210 and 1980 seconds with a median time of 900 seconds, and the signal to noise ratio was between 12 and 24 (Torres, private communication) The spectra were analysed by Torres to obtain radial velocities with the TODCOR cross-correlation software (Sect. 9.4 and Appendix D) and synthetic spectral templates constructed with stellar parameters obtained with trial cross-correlation spectra.

The CfA observations also include a luminosity ratio in the Mg I triplet window. They give $L_2/L_1 = 0.504 \pm 0.020$. This ratio is used as an important constraint in the analysis.

The CfA and GB observations were both made with instruments specifically designed to measure precise stellar radial velocities.

8.3.3 INT spectra

The 65 INT spectra span just over one orbital period, from 2002 October 14 to 2002 October 23. Thus these observations overlap the early part of those by Griffin and Boffin. They were obtained during the same telescope run as observations of other dEB's previously reported in the literature by Southworth et al. (2004a,b,c; 2005). Thus the details of the instrumentation are the same, except that different exposure times were used

for each object. Specifically the Intermediate Grating Spectrograph was used with a holographic 2400 grooves/mm grating and a 500 mm camera equipped with an EEV 4000 × 2000 pixel CCD. The exposure time was 300 s. The resolution was estimated from the FWHM of arc spectrum lines used for wavelength calibration and was approximately 0.2 Å, corresponding to two pixels. An observing log appears in Appendix A.

A typical INT spectrum is shown in Fig. 8.1. This is for exposure 43, the same as is used later to illustrate the output from TODCOR, and chosen for the large difference between the radial velocities of the two stars. The intensity dip at about 4310Å is due to the Fraunhofer G band, which is composed of absorption lines from neutral and singly ionised iron and calcium, and fron the hydrocarbon CH band. Other major features are the Hγ Balmer (absorption) line at 4340Å and a Fe I line at 4383Å.

The whole of the INT spectra, from 4227Å to 4498Å was used for the cross-correlation.

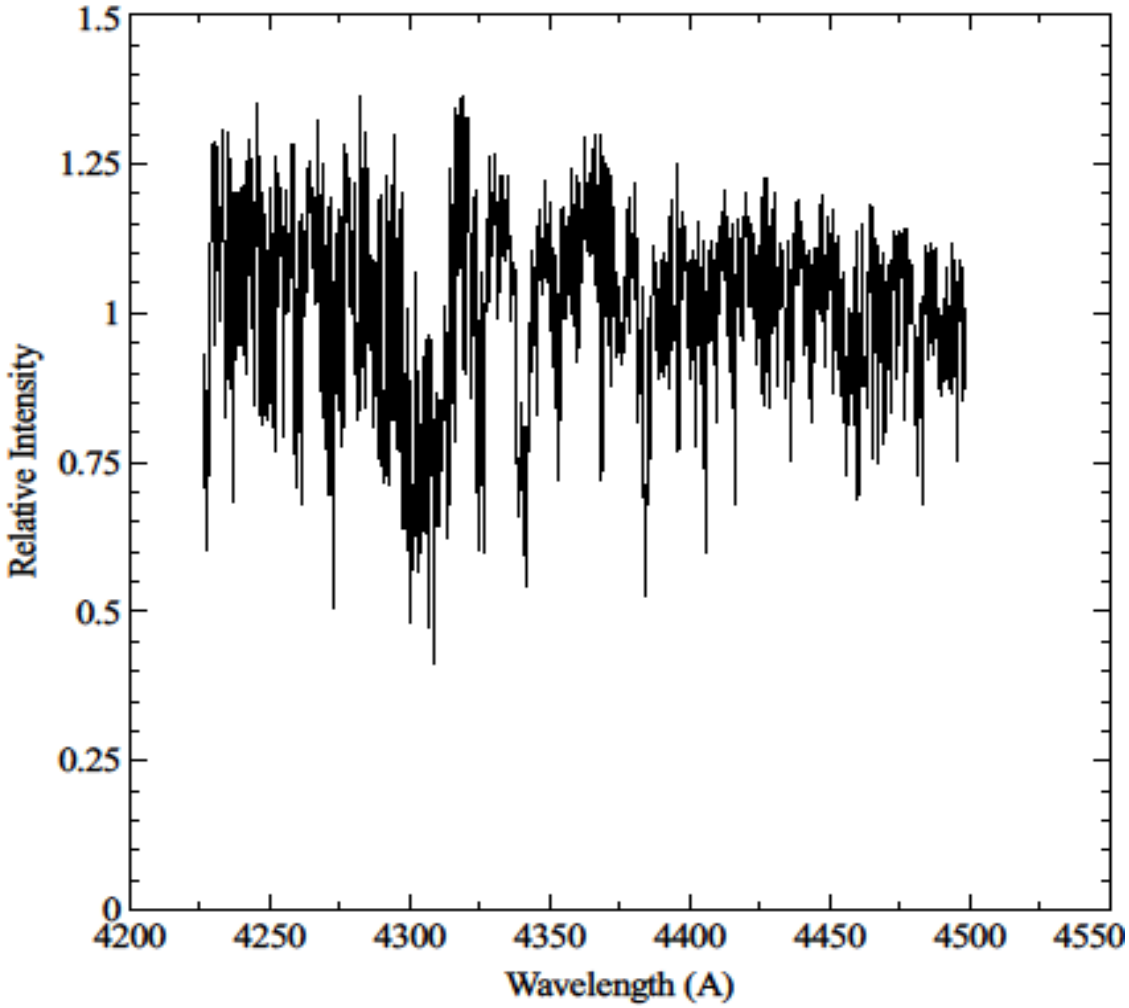

Fig. 8.1 Spectrum from exposure 43 of the INT spectrum.

8.4 Photometric observations

8.4.1 Principles

Photometric light curves are obtained by measuring the differential magnitude between the target system and a nearby comparison star in a series of exposures. Each exposure typically lasts for the order of a minute. The target system is observed in several pass bands to provide independent data sets and to estimate third light. This requires a compromise between the number of spectral bands and the signal to noise ratio.

8.4.2 List of Light curves

Two sets of photometric light curve data of sufficient quality to measure precise radii are now available, which allow a photometric and hence complete analysis of the V1094Tau system to be carried out for the first time. They are:

- i) Light curves from the URSA and NFO Web Scopes and supplied to the author by Lacy (private commmunication).
- ii) Light curves (Clausen – private communication) from the SAT (Strömgren Automatic Telescope) (Florentin-Nielsen, 1993)

Some additional photometric data for V1094 Tau are available from the STEREO mission (Wraight – private communication), but these add very little compared to the NFO, URSA and SAT data and so they are not considered further for two reasons. First the interval between each data point on the light curve is 2400 s which as will be seen below is much longer than for either the NFO/URSA or SAT data. Thus the uncertainty in the times of minima is much larger. Secondly the light curves are of lower quality and the JKTEBOP software used later to analyse the NFO/URSA and SAT light curves broke down for the STEREO light curves in that it outputted badly inconsistent results at each stage of the analysis.

The SuperWASP archives records the V1094 Tau system as 1SWASPJ041203.59+215650.5 on three observation fields, with 14720, 4004 and 2357 data points. No secondary minimum can be discerned in the folded curves for any of these fields so these data are also not considered further.

8.4.3 NFO and URSA light curves

The NFO (www.webscope.nfo.edu) and URSA (described first by Lacy et al., 2001, and in more detail by Lacy and Fekel, 2010) telescopes are both automatic telescopes operated by the University of Arkansas. The NFO telescope is an automatic 24 inch Cassegrain reflector located near Silver City, New Mexico. It is equipped with a field widening correcting lens near the focus and a 2102 × 2092 pixel Kodak KAF 4300E CCD with a field view of about 27×27 arcmin. The URSA telescope is an automated 10 inch Meade LX-20 Schmidt-Cassegrain telescope mounted on the roof of the Kimpel Hall on the University of Arkansas campus at Fayetteville. It is equipped with a SBIG ST8EN 1020 × 1530 pixel CCD. Lacy and co-workers have reported the times of minima obtained with these telescopes for many dEB's in a series of issues from 2001 onwards of the IBVS (International Bulletin of Variable Stars – www.konkoly.hu/IBVS/IBVS.html) published by the Konkoly Observatory, Budapest).

This instrument observed V1094 Tau on 116 nights between 2006 January 2 and 2012 March 24, with 5714 exposures in the Johnson V-band. The exposure cycle and integration times do not appear to be explicitly stated in the literature but examination of the light curves shows that the cycle time is similar to that quoted below for the URSA telescope. Results were supplied in the form of differential magnitudes with the combined brightnesses of the nearby comparison stars HD 284196 (Vmag = 9.28, SIMBAD) and HD 284197 (Vmag = 9.96, SIMBAD). These stars lie 14.3 and 11.1 arc minutes away from V1094 Tau respectively and are shown in Appendix L, star chart L3. The standard errors on the photometry were 5.3 mmag. The 10 minima obtained from the NFO light curves are indicated in the last column of Table 9.1 as Lacy NFO, where the number in brackets following each entry is the number of data points in the light curve used to define that particular minimum. The time of each minimum is given in the first column of this Table.

It will be seen that the total number of data points in all ten minima i.e. 1216 is less than the 5714 points in all the light curves supplied to the author. This is because some of the light curves showed no minimum at all, and the minima in some others were incomplete.

URSA. This instrument observed V1094Tau on 92 nights between 2001 March 6 and 2012 March 25, with 8085 exposures, again in the V-band with exposure integration time was 60 seconds followed by typically downloading time of 30-40s to give an exposure cycle of 90-100s. Results were again supplied in the form of differential magnitudes, but this time with just one of the two comparison stars above, namely HD 284196. The standard errors on the photometry were 8.9 mmag. The URSA light curves provided another 10 minima, listed in Table 9.1 in a similar manner as for the NFO minima. As for the NFO light curves, not all the data points could be used. The 10 URSA minima contained 2948 data points in all, compared with 8085 data points in all the light curves supplied.

8.4.4 Strömgren Automatic Telescope (SAT) light curves

The Danish Strömgren Automatic Telescope (SAT) is a 52 cm. Cassegrain telescope at ESO (European Southern Observatory) La Silla, Chile (Florentin-Nielsen, 1993). It is an automated telescope equipped with a four colour uvby + Hβ photometer. It is used solely for photoelectric photometry, mainly for EB's.

The light curves supplied contain 670 exposures for 72 nights over the period 2000 October 11 to 2008 January 15. The r.m.s. uncertainty in the photometry was about 0.005 mmag, somewhat closer than for the NFO/URSA exposures. Four curves, one each for the four Strömgren u-, v-, b- and y- pass bands (Strömgren, 1956 and Crawford, 1958) were obtained simultaneously. They contain just one analysable minimum, that at HJD 2 454 447.6562 (2007 December 13, UT 0345). The light curve for this minimum contained just

38 data points. The interval between each data point is typically 450 to 500 s. Observations for two other nights were cut off close to a minimum and were judged too incomplete to analyse. These minima lie at about HJD 2 451 837.86 and HJD 2 451 846.85.

The NFO, URSA and SAT light curves are shown in Sect. 9.6.

CHAPTER 9 ANALYSIS OF DATA FROM V1094 TAU

9.1 Structure of analysis

The analysis described here falls under three main headings

- Derivation of new ephemeris
- Analysis of spectroscopic data
- Analysis of light curve data

This section uses standard terms and symbols throughout, which are listed in Appendix B.

9.1.1 Analysis sequence.

The sequence of analysis steps is determined by

- The input and software required to analyse each kind of observational data.
- The correlation between some of the steps i.e. a pair of steps where each requires the output from the other. For example determining the ephemeris (partly by JKTEBOP) needs the orbital elements, and determining the orbital elements (again partly by JKTEBOP) requires the ephemeris.

The sequence of analysis adopted is as follows.

1. Perform an initial light curve analysis with JKTEBOP (Sect.9.2.1)
2. Determine times of minima and hence an updated ephemeris with a specially written program *ephem* (Maxted, private communication) with input data derived from JKTEBOP. (Sect. 9.2.3)
3. Determine radial velocities (R.V's). This is independent of 1) and 2). This was necessary only for the INT run, since the R.V's for the CFA and GB runs were already available to the author. (Sect. 9.4).
4. Obtain values of e, ω, K_1 and K_2, M_1 *and* M_2, and the mass ratio, by inputting the R.V. data to SBOP (Sect. 9.4.2).

5. Obtain improved values of the orbital elements, and values for the period of apsidal motion (Sect. 9.3) and any offsets between the R.V. data sets with the specially written program *Omdot* (Maxted, private communication), (Sect. 9.5).

6. Use the values of $e\cos\omega$ and $e\sin\omega$ as constraints on a definitive light curve analysis with JKTEBOP. This also uses the mass ratio as determined from 4) as a fixed parameter (Sect. 9.6).

7. This solution is degenerate between the luminosity ratio of the stars and $k = R_2/R_1$. Use the luminosity ratio derived from the CfA observations as a further constraint on the JKTEBOP runs to lift this degeneracy. (Sect. 9.6.3)

8. Use the specially written program *jktabsdim* (www.astro.keele.ac.uk/jkt/codes/jktabsdim.html) to determine definitive values of the stellar parameters and a_1 and a_2, and also the distance of the system (Sect. 9.9).

9. Repeat for another iteration, but with the difference of using input values from *jktabsdim* if available, otherwise from *Omdot* and if not there, from JKTEBOP. As explained later, two main iterations were carried out with JKTEBOP, one with a constraint on $e\cos\omega$ and $e\sin\omega$ and the second with both this constraint and one on the luminosity ratio.

9.1.2 Justification and further explanation of analysis sequence.

The first two steps need further justification.

Initial JKTEBOP run (step 1). This was carried out to provide input data for the JKTEBOP runs used to derive the ephemeris (Item 2). These data are: Sum and ratio of the radii, orbital inclination and the surface brightness ratio. The other data needed for this initial run were obtained from the following sources:

- Initial values of the period and time of minimum from the literature
- Eccentricity and angle of periastron from an initial SBOP run
- Limb and gravity darkening coefficients calculated from the masses calculated by the initial SBOP run, and from radii and temperatures based on a preliminary analysis of the data by Dr Jens Viggo Clausen.

Revised ephemeris with ephem with input data from JKTEBOP (step 2). The iteration proper starts at this point because the times of minima as calculated by JKTEBOP depend

only very weakly indeed on the JKTEBOP input data. This was tested for pilot cases by randomly perturbing the input orbital element parameters to the JKTEBOP files by amounts comparable to their uncertainties and repeating the analysis. The difference introduced into the calculated time of minimum was typically an order of magnitude smaller than its uncertainty. This is supported by visual examination of the NFO or URSA light curves. The data points are closely spaced with a separation of about 0.004 days, and a minimum could be determined to within one or two data points even only by eye.

The problem of circular dependence is also eased because some of the analysis programs include fitting routines where the input values need only be approximately correct.

9.2 Derivation of new ephemeris

9.2.1 Sources of data

The ephemeris quoted in the literature is that published by Kaiser and Frey (1998), (Sect. 8.2.1). The more recent light curves (Sect. 8.4) allow an updated ephemeris to be determined.

The input data used for the new ephemeris are as follows

- All the minima listed in Table A11 of Wolf et al. (2010), except the discovery minimum of Kaiser (1994), since for that minimum the discrepancy between the calculated and observed times is large (Kaiser and Frey, 1998).
- Minima derived by applying JKTEBOP to the NFO and URSA light curves (Sect. 8.4.3) and SAT light curves (Sect. 8.4.4). A critical survey of these light curves did not reveal any further minima. The average difference between the rederived times of minima and those reported by Lacy is 0.00056 days. The input data also included three minima listed by Wolf et al.

Input data which were not used were:

- The STEREO data, for reasons given earlier (Sect. 8.4.2).
- A primary minimum recently reported by Hübscher and Lehmann (2013) since the time carries a very large (0.0104 days) uncertainty.

The data were processed in two steps: 1) to determine the times of minima where this was necessary and 2) to use a fitting program to determine an ephemeris from these times.

9.2.2 Times of minima

The times of minima finally adopted for fitting are listed in Table 9.1. In short the minima listed there as from Lacy and Clausen/SAT were derived by the author but the remainder were taken from the literature, mainly from Table A.11 of Wolf et al (2010). The details of the input times used for the fitting program and the uncertainties assigned to them are as follows.

Although minima for the NFO and URSA curves are already quoted by Lacy in his IBVS bulletins, the minima for the SAT curves are unpublished and it was judged necessary to derive all the minima consistently with JKTEBOP. This software contains a routine which returns the minimum of a light curve as standard output.

Input times. For the initial input times, those listed by Wolf et al., were adopted as they stand, except for the discovery minimum and those in the NFO and URSA light curves. For the NFO and URSA minima these initial times were taken from the IBVS bulletins. For the SAT values it was considered adequate to obtain the initial time simply by inspecting the light curve minimum by eye because the exposure cycle is short, about 0.004 days, and the light curve points are closely spaced.

Uncertainty in input times. For the minima listed by Wolf et al., uncertainties were assigned which were guided by the weighting factor listed by these authors and also judged

to be realistic. These adopted uncertainties are in general wider than the differences the authors themselves give for the difference between the observed and calculated minima. The bulletins of Lacy do quote uncertainties and these were adopted. The uncertainties were then widened further as explained below.

9.2.3 Fitting program

It is shown later that there is measurable apsidal motion (precession of the orbits), hence the ephemerides for the primary and secondary minima will be slightly different. Each of these two sets of minima with their uncertainties was fitted separately by the program *ephem*, which fits an ephemeris to the times of minima by linear regression. Before fitting, a further constant uncertainty was then added quadratically to the initial uncertainties so that *ephem* returned a χ^2 value of *Nfit(number of minima) – Nparam*, where *Nparam (the number of free parameters) = 2*. The complete list of the minima finally adopted is shown in Table 9.1, where the last column was explained earlier (Sect.8.4.3). It will be seen that the SAT observations covered only one minimum, albeit in four separate wavelength bands. The column (O-C) stands for Observed minus Calculated time, where the calculated time is a best fit. Fitting the primary minima only leads to an ephemeris

$$T(prim) = HJD\ 2\ 454\ 555.51832(22) + 8^d.98854463(131) \times E \qquad 9.1a$$

Fitting the secondary minima only and projecting forward the base time outputted by *ephem* by 8.5 cycles to match that of the primary ephemeris leads to

$$T(sec) = HJD\ 2\ 454\ 561.38137(24) + 8^d.98855458(126) \times E \qquad 9.1b$$

These are the ephemerides which are important in preparing observations.

A variant program *ephem2* of *ephem* fits primary and secondary minima together to provide a single averaged ephemeris. Projecting forward the base time returned by *ephem2* by 11 cycles to match the primary ephemeris leads to:

$$T(\text{min,prim}) = \text{HJD } 2\,454\,555.51836(25) + 8^{d}.98854775(102) \times E \qquad 9.2$$

The newly derived single period is therefore about 0.000061 days i.e. 5.2 seconds longer than that of (Kaiser and Frey, 1998) (Eqn. 8.1). It is about one third of the way between the primary and secondary periods, which may be intuitively expected given that roughly two-thirds of the minima (25 out of 41) are primary.

Combining the separate ephemerides Eqn. 9.1 with the period of Eqn. 9.2 leads to a secondary minimum phase of 0.652279(37), but this will vary over time due to the apsidal motion.

Table 9.1 Light curve minima used to rederive ephemeris.

Time of min. (HJD) Adopted	Epoch	Prim /Sec	Quoted Uncert (days)	O - C (days)	Source (Literature)	Author/ Observer (see text)
49653.632	-545.35	2	0.003	-0.00218	IBVS 4168	Kaiser/Baldwin
49656.762	-545.00	1	0.003	0.00217	IBVS 4544	Kaiser/Baldwin
49680.597	-542.35	2	0.003	-0.00283	IBVS 4168	Kaiser/Baldwin
49683.727	-542.00	1	0.003	0.00152	IBVS 4544	Kaiser/Baldwin
49701.7061	-540.00	1	0.0013	0.00353	IBVS 4168	Kaiser/Terrell
49707.5649	-539.35	2	0.0018	-0.00057	IBVS 4168	Kaiser
49710.695	-539.00	1	0.002	0.00388	IBVS 4544	Kaiser
49755.6355	-534.00	1	0.002	0.00164	IBVS 4168	Kaiser
50456.7393	-456.00	1	0.002	-0.00128	IBVS 4544	Kaiser/Frey
50474.7156	-454.00	1	0.002	-0.00208	IBVS 4544	Kaiser
52278.2875	-253.35	2	0.001	-0.00263	Wolf	Wolf/Ondrejov
52362.3148	-244.00	1	0.001	0.00209	Wolf	Wolf/Ondrejov
52601.8778	-217.35	2	0.00014	-0.00005	IBVS 5357	Lacy URSA (397)
52628.84325	-214.35	2	0.00030	-0.00024	IBVS 5487	Lacy URSA (329)
52637.83158	-213.35	2	0.00021	-0.00046	IBVS 5487	Lacy URSA (163)
52898.49893	-184.35	2	0.001	-0.00099	Wolf	Wolf/Ondrejov
52997.3708	-173.35	2	0.0027	-0.00315	IBVS 5643	Hubscher/Jungbluth
53045.4406	-168.00	1	0.0035	-0.00174	IBVS 5657	Hubscher/Achterberg
54438.66519	-13.00	1	0.0002	-0.00205	IBVS 5910	Lacy URSA (399)
54447.65487	-12.00	1	0.0003	-0.00092	IBVS 5910	Lacy NFO (69)
54447.65602	-12.00	1		0.00023		Clausen/SAT (38)
54447.65604	-12.00	1		0.00025		Clausen/SAT (38)
54447.65613	-12.00	1		0.00034		Clausen/SAT (38)
54447.65617	-12.00	1		0.00038		Clausen/SAT (38)
55157.75013	67.00	1	0.0003	-0.00093	IBVS 5972	Lacy NFO (227)
55175.72858	69.00	1	0.0003	0.00043	IBVS 5972	Lacy NFO (184)
55181.59081	69.65	2	0.0003	-0.00024	IBVS 5974	Lacy URSA (246)
55202.69394	72.00	1	0.0006	0.00014	IBVS 5972	Lacy NFO (207)
55208.55713	72.65	2	0.0002	0.00043	IBVS 5972	Lacy URSA (241)
55247.6364	77.00	1	0.0003	-0.00014	IBVS 5972	Lacy NFO (125)
55274.60204	80.00	1	0.0003	-0.00014	IBVS 5972	Lacy URSA (91)

55813.91459	140.00	1	0.0004	-0.00046	IBVS 6014	Lacy	URSA (229)
55831.89207	142.00	1	0.0002	0.00061	IBVS 6014	Lacy	URSA (290)
55831.89275	142.00	1	0.0002	-0.00007	IBVS 6014	Lacy	NFO (104)
55849.87	144.00	1	0.0014	0.00076	IBVS 6011	Diethelm	
55855.73235	144.65	2	0.0002	0.00022	IBVS 6014	Lacy	URSA (295)
55882.6986	147.65	2	0.0003	0.00082	IBVS 6014	Lacy	NFO (45)
55894.8108	149.00	1	0.0002	-0.00117	IBVS 6014	Lacy	NFO (268)
55936.62917	153.65	2	0.0002	0.00011	IBVS 6014	Lacy	NFO (182)
55945.61739	154.65	2	0.0003	-0.00022	IBVS 6014	Lacy	NFO (73)
55945.6205	154.65	2	0.0006	0.00289	IBVS 6029	Diethelm	

References:

IBVS + number: Information Bulletin on Variable Stars, number as given, published by the Konkoly Observatory, Budapest, Hungary. Website www.konkoly.hu/IBVS

Wolf: Wolf et al. (2010).

Clausen Private communication
Lacy Private communication

Revising the ephemeris changes the calculated phase for the light curves. The phase difference so introduced is compared with the exposure times in Table 9.2

Table 9.2 Phase difference introduced by revising ephemeris.

Observations	Phase difference (New – Old ephemeris)	Exposure time (units of period)
CFA	-0.000056 to -0.000572	0.000270 to 0.00250 (210 to 1980 s)
GB	-0.001768 to -0.001909	Not known
INT	-0.001780 to -0.001784	0.0039 (300 s)

Thus the phase difference introduced by revising the ephemeris is much smaller than the phase change during an exposure period for the CfA observations, and somewhat smaller than that for the INT observations.

The angle of periastron derived later i.e. ω = 333.58 ± 0.18 degrees, leads to a periastron phase of 0.24052 with respect to the primary minimum. The primary periastron precedes the primary minimum by 2.16193 days. These values were derived from the equations of elliptical motion as described by e.g. Hilditch (2001, Sect. 2.5).

9.3 Apsidal motion

9.3.1 General description.

If the two stars of a binary system had a spherically symmetric mass distribution, their gravitational fields would vary as $1/r^2$ and the orbits would be stationary in an inertial reference frame. In reality the stars are oblate due to their centrifugal rotation and by the mutually exerted tidal bulges. These deformations generate an additional gravitational field which varies as $1/r^3$. The orbits of the stars are elliptical and hence apsides may be defined as the points on the orbit where each star is closest or furthest from the other. These are respectively known as periastron and apastron. Classical mechanics predicts that the $1/r^3$ gravitational field causes the line joining the apsides to precess in the plane of the orbital motion. This is known as apsidal motion. General relativity predicts a further contribution to the apsidal motion.

An analytical expression for the apsidal motion period was first derived by Russell (1928) and improved by Cowling (1938). An expression separating the rotational and tidal contributions was formulated by Sterne (1939). As formulated by Claret and Gimenez

(1993), the ratio of the orbital period *P* and the non-relativistic apsidal period *U* can be written

$$\frac{P}{U} = c_{21}k_{21} + c_{22}k_{22} \qquad 9.3$$

In this expression the constants c_{21} and c_{22} are (Claret and Gimenez, 1993, Eqn. 2).

$$c_{2i} = \left[\left(\frac{\omega_i}{\omega_K}\right)^2 . \left(1 + \frac{m_{3-i}}{m_i}\right) f(e) + \frac{15 m_{3-i}}{m_i} g(e)\right] \left(\frac{R_i}{a}\right)^5 \qquad 9.4$$

where

the suffixes 1 and 2 denote the two stars.

ω_i is the angular rotational velocity of each star.

ω_K is what would be the angular rotational velocity if it were synchronised to the average orbital velocity.

and the functions *f(e)* and *g(e)* are:

$$f(e) = \frac{1}{(1 - e^2)^2} \qquad 9.5a$$

and

$$g(e) = \frac{(8 + 12e^2 + e^4) f(e)^{2.5}}{8} \qquad 9.5b$$

Equation 9.4 follows Sterne in that it has separate terms for the rotational and tidal contributions.

It may be seen that all the parameters entering into the expressions for c_{21} and c_{22} can be determined observationally. The last term of Eqn.9.4 show that these constants vary as $(R/a)^5$.

The constants k_{21} and k_{22} depend on the mass distribution within the stars, and are known as the apsidal constants or alternatively the internal structure constants. They can be calculated theoretically e.g. by Claret and Gimenez (1992).

The form of Eqn. 9.3 shows that the apsidal period provides a constraint on the internal structure, but cannot provide information on each star separately without some added assumption. A weighted observational apsidal constant may however be defined (Claret and Gimenez, 1993, Eqn. 5) as:

$$\bar{k}_{2obs} = \frac{1}{c_{21} + c_{22}} . \frac{P}{U} \qquad 9.6$$

A weighted theoretical constant may be defined (Claret and Gimenez, 1993, Eqn. 8) as

$$\bar{k}_{2theo} = \frac{c_{21} . k_{21} + c_{22} k_{22}}{c_{21} + c_{22}} \qquad 9.7$$

Einstein showed that the General Relativistic contribution ω_{rel} to the angular apsidal precession velocity is:

$$\omega_{rel} = \frac{6\pi G\,(M_1 + M_2)}{P\,c^2\,a\,(1 - e^2)} \qquad 9.8$$

where ω_{rel} is in radians per period.

The non-relativistic and relativistic contributions are separable down to the level of observational accuracy (Gimenez, 1985) and so to this approximation the total apsidal angular velocity ω_{aps_tot} is simply

$$\omega_{aps\_tot} = \omega_{non\_rel} + \omega_{rel} \qquad 9.9$$

where the term ω_{non_rel} is that given by Eqn. 9.3.

The theoretical value $k_{2\text{theo}}$ does not take account of the relativistic contributions to the apsidal motion. Thus the appropriate comparison is between $k_{2\text{theo}}$ and the non-relativistic contribution only to the observed apsidal motion.

Due to the apsidal precession, two orbital periods can be defined.

- The sidereal period P_{sid}, which is the average time derived above between successive primary or secondary minima (the actual time varies through the apsidal cycle).
- The anomalistic period P_{anom}, which is the time between successive times of periastron.

Standard theoretical treatments consider only the linear term to quadrupole expression for the gravitational field due to the elliptical distortions and also assume that the orbital and rotational axes are aligned. The constants c and k are then all positive and so the apsidal precession is in the same sense as the orbital motion, hence $P_{anom} > P_{sid}$. The relation between them is

$$P_{sid} = P_{anom}\left(1 - \frac{P_{anom}}{U}\right) \qquad 9.10$$

If the misalignment angle between the two axes is large then the apsidal motion can be retrograde i.e. in the opposite sense to the orbital motion (Shakura, 1985). This may occur in young binaries where tidal interactions have not had time to align the rotational axes with the orbital axis.

The apsidal motion causes the observed time of minimum to deviate from the calculated time based on a single period. This has been discussed theoretically by Hilditch (2001, Sect.4.2.1) after a detailed treatment by Smart (1953). The deviations are conventionally shown on a plot of the (observed - calculated) time, hereafter cited as (O-C), against time. An example of such a plot, for a system where the apsidal period is short enough for observations to be made over a whole period, is shown on Fig. 9.1. This

is an O-C diagram for the eccentric eclipsing binary MACHO 79.5377.76 in the Large Magellanic Cloud and is taken from Fig. 10 of Zasche and Wolf (2013). In this figure the rows at the top show the heliocentric Julian Date and the year; and the continuous and dashed curves show the predicted values for the primary and secondary minima repectively.

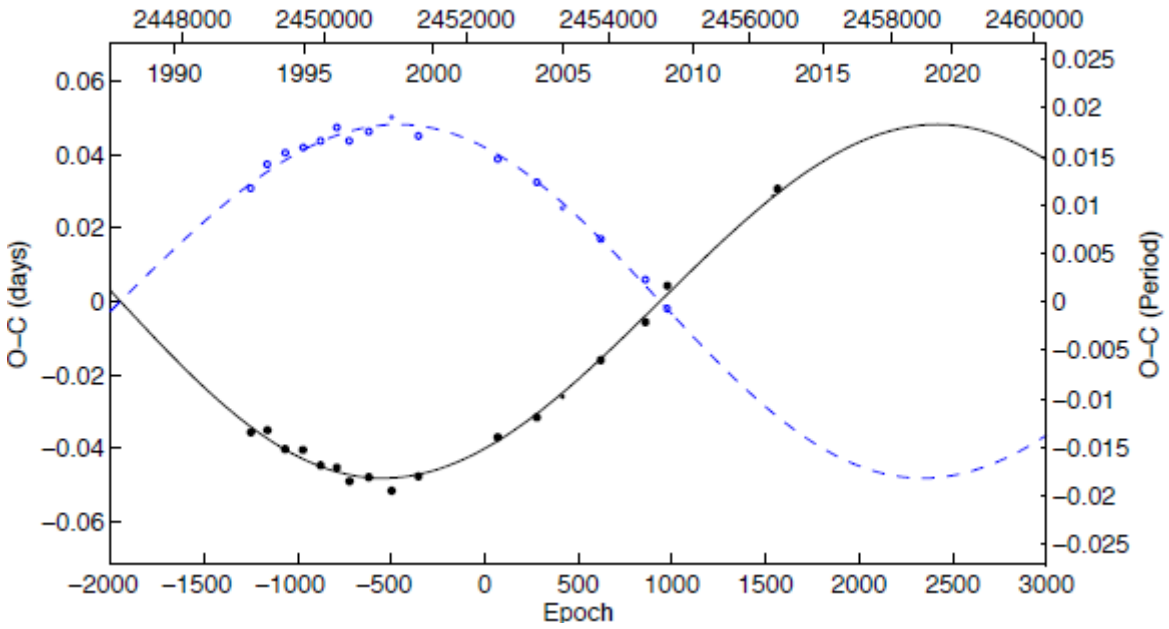

Fig. 9.1 O-C diagram for the minima of the eccentric eclipsing binary MACHO79.5377.76 in the Large Magellanic Cloud (taken from Fig.10 of Zasche and Wolf, 2013).

It may be seen that the (O-C) values for the primary and secondary minima lie on waveforms in opposite directions. A more detailed discussion shows that this is a particular signature of apsidal motion. The waveforms depart from sinusoidal to the extent that the eccentricity is significant.

9.3.2 Apsidal motion in V1094 Tau

Period of apsidal motion. Comparison of the two equations (9.1) shows that the periods of the primary and secondary ephemerides differ by 0.00000687(182) days, where the uncertainties of each period are added quadratically. The difference corresponds to 3.78σ i.e. a confidence level of 99.984%. Thus the V1094 Tau system does show apsidal motion. Applying the *Omdot* analysis as described later (Sect. 9.5) to find the best fit to the minima of Table 9.1 and other data predicts an apsidal period *U* of

$$U = (14.5 \pm 3.9) \times 10^3 \text{ years.} \qquad 9.11$$

Combining this with the sidereal period (Eqn. 9.2) and with Eqn (9.10) gives an anomalistic period of:

$$P_{anom} = 8.9885630(40) \text{ days} \qquad 9.12$$

The quoted uncertainty is the quadratic sum of:

a) the uncertainty in the sidereal period i.e. 102×10^{-8} days (Eqn. 9.2)

b) the difference between the anomalistic and sidereal periods, multiplied by the relative uncertainty in the apsidal period.

Evaluating Eqns. 9.3 to 9.9 shows that for the apsidal period given by *Omdot* the relativistic contribution is a fraction 0.366 of the total angular velocity; alternatively in the absence of relativistic effects the apsidal period would be $(22.9 \pm 6.2) \times 10^3$ years.

O-C diagram. The O-C diagram for V1094 Tau is shown in Fig.9.2. Because the apsidal period is much longer than the time over which observations have been made, only a very small section of the O-C waveforms appear. It will be seen that this section corresponds to the far right of the curves in Fig 9.1. The O-C values are calculated with respect to the linear single ephemeris Eqn. 9.2. The solid lines are the best fits calculated by *Omdot.* As

pointed out by Hilditch (2001, caption to his Fig. 4.3), an incorrect choice of average sidereal period would lead to a linear drift of O-C values with time. Confidence that the fit provides the correct values is based on i) *Omdot* uses a well-established and powerful fitting algorithm from all available data sets (Sect. 9.5.1) and ii) if the fitted values were significantly different from the true values the best fits in Fig. 9.2 would not slope in opposite directions.

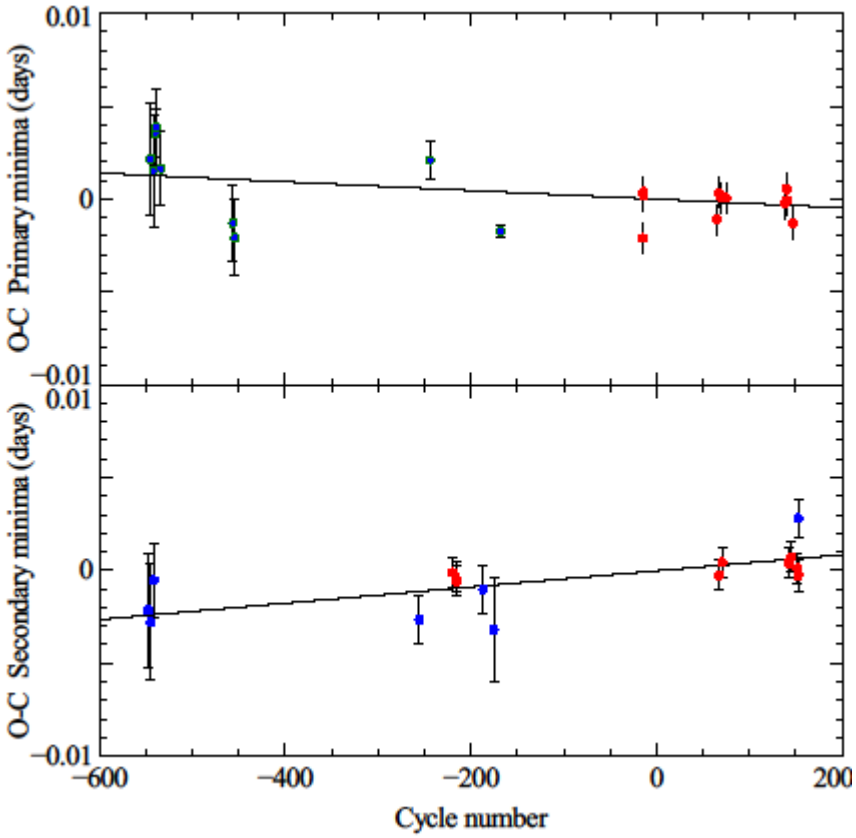

Fig. 9.2 O-C diagram for eclipse minima of V1094 Tau. The points are colour coded by origin i.e. Blue - from Wolf et al. (2010): and
Red – from the NFO and URSA observations.

9.3.3 Comparison of observed and theoretical apsidal constants.

The available data can be used to derive an averaged observed value which may be compared with the theoretical value.

Theoretical value.

The *modelplot* program used later to estimate the age of the V1094 Tau system from theoretical stellar models (Sect. 9.10) has provision to output the theoretical apsidal constants k_{21} and k_{22} for the one model which calculates them. Specifically, Claret and Gimenez (1992) calculate these constants for a grid of values of mass, metallicity and age. The *modelplot* program then interpolates within this grid for input values of these parameters, but only if the input stellar model is the Granada 2007 model of Claret (2007). In Sect. 9.10 six stellar models are compared to assess which gives the best fit to the values determined for the mass, radius and T_{eff}, and ranked by goodness of fit. Unfortunately the model of Claret (2007) could only be ranked as fourth out of the six. The *modelplot* program there returns *log* k_{21} = -1.56 and *log* k_{22} = -1.37; hence the weighted theoretical value (Eqn. 9.6) is *log* $\bar{k}_{2theo}$ = -1.50.

Observed value.

The observed value for the weighted apsidal constant $\bar{k}_{2obs}$ can be obtained from Eqn. 9.6, where all the terms on the right hand side can be determined observationally. The main uncertainty is the ~27% uncertainty in the (non-relativistic) apsidal period *U*. Other uncertainties are about an order of magnitude less or more and so are ignored. The non-relativistic contribution to the apsidal period gives $\mathrm{Log}(\bar{k}_{2obs})_{\text{non-rel}}$ ~ -1.42 ± 0.10, consistent with the theoretical value.

9.3.4 Comparison with study of Wolf et al. (2010)

The apsidal motion of V1094Tau has also been considered by Wolf et al. (2010). These authors find an apsidal motion period of $U = (13.6 \pm 1.5) \times 10^3$ years, in agreement with this work. Their O-C values are shown as the blue circles in Fig. 9.2; thus their work covered fewer minima than those analysed here. Wolf et al. (their Eqn. 11) then subtract the calculated apsidal motion from their (O-C) minima and plot these residuals against epoch. This diagram is reproduced as Fig. 9.3 below. By fitting a sinusoidal curve to these residuals they infer the existence of a third body. This claim is rejected here on two grounds.

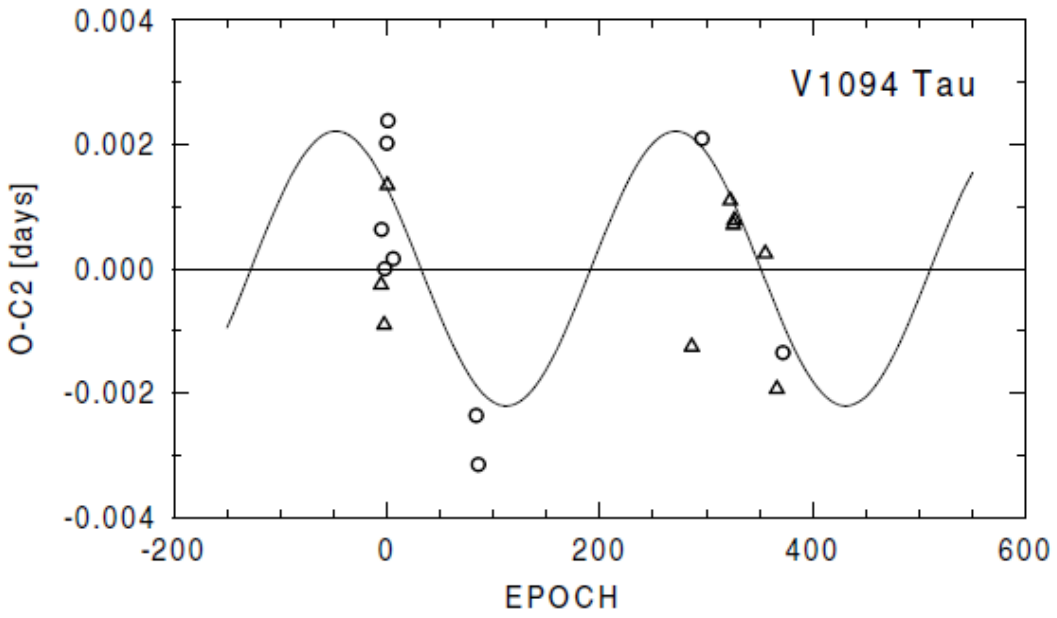

Fig. 9.3 (O-C) residuals for the eclipse minima of V1094 Tau, reproduced from 9. 11 of Wolf et al. (2010). The sinusoidal curve is what these authors claim to be a fit to these residuals, which indicates the presence of a third body. This claim is rejected here (see text).

1. The fitting of the residuals shown in Fig. 9.3 is equivalent to fitting a sinusoidal curve to the residuals shown as blue points in Fig. 9.2. It is understandable how these points *by themselves* may suggest such a fit. The present work has considered further minima, shown as the red points in Fig. 9.2. It is clear even by eye that no sinusoidal curve can be fitted to all the minima taken together.

2. Even if the (O-C) minima shown in Fig. 9.3 were all that were available, the sinusoidal fit shown in this figure would still have been regarded as unconvincing.

9.4 Determination of radial velocities and radial velocity amplitudes.

This subsection describes first how the radial velocities were extracted from the spectra where this was necessary, and then how the radial velocity amplitudes were obtained from the velocities.

9.4.1 Radial velocities

The spectroscopic observations by the CfA and by Griffin and Boffin are already available in the form of radial velocities and it was therefore necessary to derive them only for the INT observations.

The INT spectra were supplied to the author as files in the MOLLY software format (Appendix C). These files were wavelength calibrated and intensity normalised. Although the author did not carry out this part of the data reduction, he did take part in similar data reduction for the SAAO data described in Part III. The MOLLY files were converted to .dat files by the MOLLY command `wasc` and analysed by the powerful TODCOR software described in Appendix D. TODCOR is a two (parameter) dimensional subroutine in that it fits for two cross-correlation spectra simultaneously. It therefore needs two stellar template spectra from stars which have spectral types closely matched to the

target stars. These were chosen by the author and are HD 115617 and HD 216435; their spectral type and radial velocities are shown in Table 9.3.

Table 9.3 Template stars for TODCOR analysis of the INT spectra.

Star	Spectral Type		Radial Velocity (km s^{-1})
	ESO	SIMBAD	SIMBAD
HD 216435 (Tau Gruis)	G0 V	G0 V	-1.1 ± 0.3
HD 115617 (61 Virginis)	G5 V	G7 V	-8.5 ± 0.9

Thus the template stars are reasonably closely matched to the spectral types G0 + G3 of the target V1094Tau system.

The radial velocities were checked by an independent preliminary analysis carried out with the `xcor` spectral cross-correlation routine in MOLLY; this was also done to gain experience with cross-correlation analysis. This used the star HD 20807 (ζ^2 Reticuli, SIMBAD spectral type G0) used as a template. MOLLY yielded radial velocities consistent with those from TODCOR, but these were not used since the TODCOR software is superior.

Radial velocities were also obtained by one routine of the STARFIT spectral disentangling software used later in an unsuccessful attempt to determine T_{eff} and *log g* by that method (Sect. 9.8.3). The results for radial velocities were consistent with those obtained from TODCOR. It may be that the routine which calculated the radial velocities could give reliable results whereas the related routine which calculated T_{eff} and *log g* could not; a proper consideration of this point would have required a detailed study of the routines and would have been outside the scope of this thesis project. The author judged that since the STARFIT routines could not give reliable results for T_{eff} and *log g* it was unsafe to use them for radial velocities even though they were consistent with TODCOR.

The results from TODCOR were corrected for the usual systematic errors arising from blending of spectral lines and of the correlation peaks. (Sect. D.2).

The radial velocities from all three sets of observations are tabulated in Appendix E and shown in Fig. 9.4.

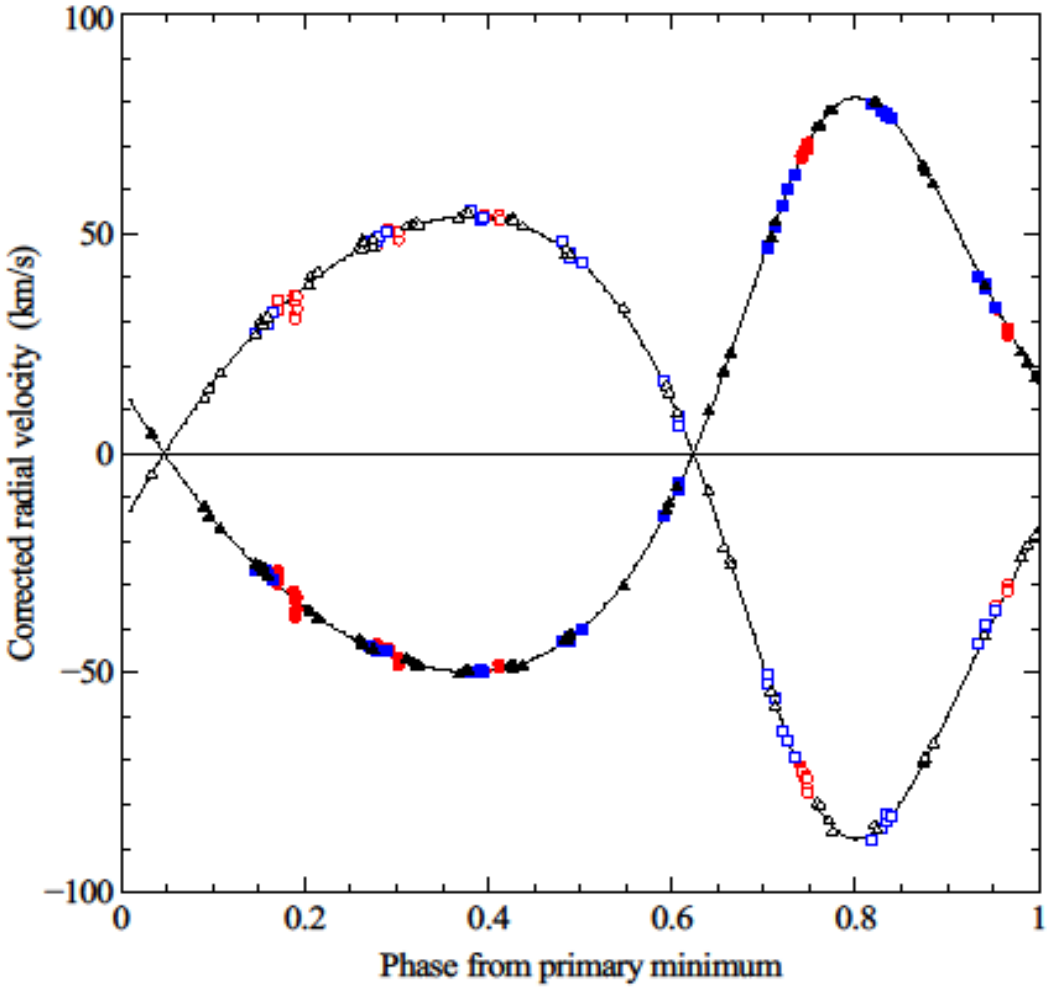

Fig. 9.4 Radial velocities from the CfA, GB and INT observations plotted against phase Full and hollow symbols refer to the primary and secondary; the observations are coded as black triangles - CfA, Blue squares – GB and Red circles INT.

The radial velocities have been corrected for the systemic velocities derived in the following subsections. Each set of observations were corrected for its own derived systemic velocity.

Radial velocities were obtained by the author for 48 of these spectra with TODCOR; for the other 17 the difference between the two velocities is small and TODCOR could not resolve the cross-correlation peaks and so could not determine radial velocities. In fact TODCOR could not resolve any peaks which could not be resolved by the preliminary MOLLY analysis, and outputted unphysical results. This was surprising since TODCOR has been shown to provide finer resolution than one dimensional cross-correlation techniques, and the reason for this is not understood. The author did not pursue this point because the 48 spectra which TODCOR could analyse did define the radial velocity curve to adequate accuracy. (The spectral disentangling approach discarded earlier could resolve the remaining 17 spectra, but the author reluctantly did not use these results for the reasons given earlier).

9.4.2 Analysis by SBOP

If a series of radial velocities is known, the orbital elements (radial velocity amplitudes, systemic velocity, eccentricity, angle of periastron) and stellar masses can be determined. The standard software for analysing these velocities is SBOP (Spectroscopic Binary Orbit Program, developed by Etzel (1978, revised 1985, private communication), www.mintaka.sdsu.edu/faculty/etzel) which is a descendant of a code by Wolfe et al. (1967). This is the software used for example by Southworth et al. (2004a,b,c and 2005). It requires initial values of the ephemeris and the orbital elements; the latter were obtained from trial runs of JKTEBOP.

There does not appear to be a detailed description of the code itself in the standard astronomical journals, although the Lehmann-Filhes method used in the code has been explained by Hilditch (2001, Section 3.2.10). An approximate radial velocity curve is obtained by the Russell-Wilsing method (Wilsing (1893) and Russell (1902), rediscussed

by Binnendijk (1960)). The final curve is then obtained from this preliminary solution by the method of Lehmann-Filhes (1894), rediscussed by Underhill (1966, p.127). This method uses an iterative least squares fitting procedure to the residuals from a trial solution. The maximum harmonic order of Fourier series used for the Russell-Wilsing first stage is specified by the input to SBOP. As the order is progressively increased the values of the orbital elements returned reach an asymptotic value. The highest order which may be used is one less than the number of points in the radial velocity curve; otherwise the solution is undefined and the program breaks down.

The SBOP suite gives an option of increasing the harmonic order for the first stage up to 7. For the three sets of V1094Tau radial velocities analysed here, test runs showed that increasing the order beyond 2 made made negligible difference and in fact an order of 4 was used.

The suite can be applied either to each member of a binary system separately, or to both stars together. The output data are eccentricity, angle of periastron, systemic velocity, amplitude of radial velocities, and $a \sin i$ and $m \sin^3 i$ for both stars.

The analysis here obtains initial values of the orbital elements and stellar masses by SBOP. The definitive values were obtained by the *Omdot* software described in the next section (9.5).

The SBOP software requires the radial velocities with weightings, timings from the ephemeris and orbital elements. The assignment of weighting factors was determined by what data was available and was as follows.

CfA velocities: Inverse of the sigma values listed for each velocity by Torres.

GB velocities: Griffin and Boffin do not list individual uncertainties for each velocity. They do however give the r.m.s residuals for the primary and secondary fitting i.e. 0.46 km/s (primary) and 0.83 (secondary). The primary velocities were therefore assigned a uniform weighting of unity and the secondary velocities the inverse ratio of these residuals i.e. 0.46/0.83 = 0.55.

INT velocities: The approach was similar except that the r.m.s residuals were derived by the author to give 1.40 km s^{-1} (primary) and 1.70 km s^{-1} (secondary). Thus the weighting factors assigned were unity (primary) and 1.40/1.70 = 0.82 (secondary)

For convenience of later discussion the r.m.s residuals are summarised below (the r.m.s values for the CfA observations were derived by the author from the individual residuals listed in Appendix E).

Table 9.4 R.M.S residuals for radial velocity observations.

Observations	R.M.S residuals (km s^{-1})	
	Primary	Secondary
CfA	0.48	0.76
GB	0.46	0.83
INT	1.40	1.70

The input ephemeris timings and orbital elements were obtained from trial values or previous iterations as available.

The results obtained for the orbital elements and stellar masses are shown in Table 9.5. This table shows the independent SBOP solutions for the CFA, INT and GB observations. All the SBOP runs were carried out by the author. For each set of observations the first row shows the values and the second the uncertainties. The table shows the elements and masses obtained from the observations of Griffin and Boffin a) exactly as presented in their paper and b) with their published radial velocity values but

with the ephemeris, eccentricity and angle of periastron derived here. It will be seen that these agree to within experimental uncertainty. They also agree with the CfA runs except for the systemic velocities. The values obtained from the INT observations with the TODCOR software stand apart from the other observation sets. Some of the INT values differ from those from the other sets by more than the combined observational uncertainty and the uncertainties themselves are much higher. This is probably (Maxted, private communication) due to a combination of image motion within the spectrograph slit and instrument flexure during the exposure. A further possible reason is that Griffin and Boffin obtained their radial velocity set with the sophisticated CORAVEL instrument (Sect. 8.2.2). The CORAVEL spectra cover a much wider (1500Å) spectral region than the 272Å wide region covered by the INT spectra. There are therefore many more lines available for cross-correlation analysis and hence the accuracy and resolution of the derived radial velocities are improved.

The agreement between the CfA and GB results is very good and is generally between the one sigma error bars. This might be expected because the observations were made with instruments which were specifically designed to measure precise stellar radial velocities and are well characterised. The INT results show some systematic errors compared to the GB and CfA results at a level similar or somewhat greater than the combined error bars. The INT error bars are themselves much wider. The grating and analysis details of the three sets of measurements are compared in Table 9.6 below

Table 9.5 Orbital elements and stellar masses as calculated by SBOP from available sets of radial velocity determinations for the complete system.

Data	Omega	Eccent	System velocity km s^{-1}	K_1 km s^{-1}	K_2 km s^{-1}
i) ω, e and velocities					
Griffin and Boffin	333.2	0.2697	4.59	65.30	70.98
as their paper	0.3	0.0018	0.07	0.12	0.20
Griffin and Boffin	333.27	0.2695	4.60	65.28	70.96
with new ephemeris	0.34	0.0018	0.08	0.13	0.18
CfA	333.56	0.2668	3.46	65.49	70.95
	0.27	0.0012	0.06	0.11	0.13
INT	331.85	0.2651	-0.07	65.03	69.67
	1.62	0.0081	0.15	0.63	0.68

ii) Masses and semi-major axes

Data	$M_1/M_\odot$	$M_2/M_\odot$	M_2/M_1	$a_1 \sin i$	$a_2 \sin i$	$a \sin i$
Griffin and Boffin	1.099	1.011	0.920	11.175	12.147	23.321
as their paper		0.007	0.005			
Griffin and Boffin	1.095	1.008	0.920	11.170	12.142	23.312
with new ephemeris	0.007	0.004	0.003	0.029	0.029	0.041
CfA	1.101	1.016	0.923	11.216	12.152	23.368
	0.004	0.003	0.002	0.019	0.023	0.030
INT	1.056	0.985	0.933	11.142	11.935	23.077
	0.018	0.017	0.013	0.111	0.117	0.162

.

Table 9.6 Comparison of experimental details for radial velocity observations

Measurements	Grating	Analysis technique
GB	Echelle (?, see text)	CORAVEL (template mask on instrument)
CfA	Echelle	TODCOR
INT	Holographic	TODCOR

There is no literature reference to the grating used for the GB CORAVEL measurements, but the author has assumed that the grating is the same as for measurements reported in the literature on other CORAVEL instruments.

The *sin i* factors in Table 9.5 are very close to unity. This can be seen even from simple considerations. For main sequence binary stars of $1M_{\odot}$ and a period of 9 days, Kepler's Third Law predicts a separation of $a \sim 22.95$ solar radii. Simple geometry shows that the condition for the orbit to be sufficiently well aligned to the line of sight for eclipses to occur at all may be derived from elementary ideas and is (Hilditch, 2001, Eqn. 5.36):

$$Sin(90° - i) \leq \frac{(R_1 + R_2)}{a} \qquad 9.13a$$

For $R_1 = R_2 = R_{\odot}$ and a as above, this gives $i > 85.00°$ and hence $\sin i > 0.9962$.

In the particular case of V1094 Tau, the definitive values given later (Table 9.17) lead to $\sin i \sim 0.999543$.

A similar argument shows that both eclipses are partial. The condition for the primary eclipse to be annular, and hence the secondary to be total is

$$Sin(90° - i) \leq \frac{(R_1 - R_2)}{a} \qquad 9.13b$$

The definitive values given in Table 9.19 lead to $Sin(90° - i) = \cos i = 0.03056$, and $(R_1 - R_2)/a = 0.0132$, hence this condition is not fulfilled. If it were, the ratio of the surface brightnesses would simply equal the ratio of the eclipse depths.

An SBOP analysis was also carried out for the primary and secondary separately with the results shown in Table 9.7. In this table the parameters which differ for each star

are shown unbracketed e.g. K_1 and K_2, and parameters which have a single value for the system but are derived from each star separately are shown bracketed e.g. $\omega(1)$ and $\omega(2)$. The two values obtained for the single valued parameters agree with each other to within observational uncertainty and with the values obtained when the radial velocity data sets for each star are treated together (note that ω(secondary) = ω(primary) – 180° by definition). Note also that a data set for one star only does not provide enough parameters to determine the stellar mass but only the mass function, which is a function of the masses of both stars and is:

$$f(m_{1,2}) = \frac{{m_{2,1}}^3 \, sin^3 i}{(m_1 + m_2)^2} \qquad 9.14$$

Table 9.7 Orbital elements and stellar masses as calculated by SBOP from available sets of radial velocity determinations for each star separately

	CfA		GB		INT	
	Value	Uncert	Value	Uncert	Value	Uncert
$\gamma_{(1)}$ (km s^{-1})	3.393	0.062	4.585	0.082	-0.095	0.651
$\gamma_{(2)}$ (km s^{-1})	3.582	0.101	4.725	0.150	0.277	0.796
K_1 (km s^{-1})	65.480	0.097	65.268	0.115	65.662	1.901
K_2 (km s^{-1})	70.929	0.158	71.001	0.209	69.846	1.867
$e_{(1)}$	0.2670	0.0013	0.2682	0.0019	0.2756	0.0294
$e_{(2)}$	0.2673	0.0020	0.2723	0.0032	0.2679	0.0287
$\omega_{(1)}$ (deg)	333.715	0.307	333.321	0.369	334.448	2.490
$\omega_{(2)}$ (deg)	153.295	0.461	153.279	0.608	149.842	2.809
Mass fn.1	0,23401	0.00107	0.23151	0.00128	0.23420	0.02125
Mass fn.2	0,29737	0.00205	0.29698	0.00275	0.28380	0.02382
$a_1 \sin i$ ($R_\odot$)	11.214	0.017	11.174	0.021	11.217	0.339
$a_2 \sin i$ ($R_\odot$)	12.147	0.028	12.141	0.038	11.959	0.335

Comparison of Tables 9.5 and 9.7 shows that the SBOP results obtained from treating the stars i) together and ii) separately agree to within observational uncertainty.

9.4.3 Corrections to radial velocity

Lindegren and Dravins (2003) have discussed the concept of radial velocity in detail and the ambiguities within it. They describe rigorous definitions, adopted by the IAU, of the "astrometric radial velocity" obtained from astrometric observations and the "barycentric radial-velocity measure" obtained from spectroscopic observations. They explain also how the astrometric radial velocity differs from the "true" kinematic radial velocity due to relativistic and other effects.

Two of the main reasons why the astrometric and spectroscopic radial velocities differ are a) gravitational red shifts and b) convective blue shifts due to convective motions on the surfaces of F- and later type stars. Both of these are ignored for the following reasons.

Gravitational red shift. The standard expression for the change in the measured radial velocity due to the gravitational red shift from the surface of a spherical emitter is:

$$\nabla V(grav) = \frac{+GM}{rc} \qquad 9.15$$

where:

G is the gravitational constant = 6.67384(15) × 10^{-11} N. $(m/kg)^2$ (i.e. m^3 kg^{-1} s^{-2})

m and r the mass and radius of the emitter, and c the velocity of light.

For the Sun ΔV(grav) = 0.636 km s^{-1}. Thus for the components of V1094 Tau the masses and radii derived later give:

ΔV(grav,prim) = 0.498 km s^{-1}
ΔV(grav,sec) = 0.595 km s^{-1}

These are ignored because

a) they are either smaller or comparable with the uncertainties in the derived radial velocities.

b) they are constant throughout the orbit, and the difference between them is very small.

The red shift introduced into the measured radial velocity of one star by the gravitational field of the other one, and the blue shift introduced by the Earth's gravitational field are both very small and also ignored.

Convective blue shifts. Convective motions on the surfaces of stars cause granulation effects which lead to a blue shift. This is of order 1.0 km s^{-1} for F-type stars, decreasing to 0.2 km s^{-1} for K type stars (references in Sect. 2 of Shporer and Brown (2011), who discuss this effect in detail). Thus it is below 1.0 km s^{-1} for the early G-type stars which comprise the V1094 Tau system and is ignored on similar grounds.

9.5 Definitive analysis of orbital elements (*Omdot*)

9.5.1 Description

The *Omdot* software written by Maxted (private communication) obtains a simultaneous least squares best-fit solution for all the parameters of an eccentric binary star orbit with apsidal motion, where the input data are all the times of minima and all the R.V. data sets. It calculates not only definitive values of the orbital elements e, ω and the orbital velocity amplitudes K_1 and K_2, but also the offset between different sets of radial velocity observations and the apsidal period U. The fitting is carried out by the powerful program MRQMIN which uses the Levenberg-Marquardt minimisation by gradient descent algorithm (Press et al., 2007).

Omdot requires the following input.

- Data set for the times of minima
- Data sets for the radial velocities. There are two radial velocity data sets, one for each star. Each data set contains the radial velocities from all three observational runs (CfA, GB and INT).
- Initial estimate for the base time for the ephemeris
- Initial estimate for the anomalistic period
- Initial estimate for the systemic velocity
- Initial estimate for the radial velocity semi-amplitudes
- Angle of inclination.

These were obtained as described above from *ephem*, SBOP and JKTEBOP as appropriate. *Omdot* requires the angle of inclination to be fixed (Maxted, private communication). It will be seen that the input to *Omdot* consists entirely of observational data.

Table 9.8 Uncertainties in radial velocity files. Units km s^{-1} throughout.

	CfA		Griffin and Boffin		INT	
	Prim.	Sec.	Prim.	Sec.	Prim.	Sec
Input [a]	0.467	0.763	0.46	0.83	1.40	1.55
Added uncertainty (separate R.V. files)	0.0575	0.100	0.048	0.457	0.32	0.25
Combined uncertainty	0.471	0.770	0.46	0.948	1.44	1.57
Added uncertainty [b] (single R.V.file)	0.166	0.207	0.166	0.207	0.166	0.207
Combined uncertainty	0.499	0.797	0.491	0.970	1.446	1.584

Notes:

a) The input uncertainties were based on those for individual radial velocities where available and r.m.s uncertainties where not. In detail:

CfA: The average of the sigma values for each radial velocity of the primary was 0.478 km s^{-1}. To ensure proper weighting the value of χ^2 should be equal to *Nfit* – *Nparam* where *Nfit* (the number of data points) - *Nparam* (the number of free parameters, here 2). An initial χ^2 test led to a value less than this. A constant uncertainty of 0.1 km s^{-1} was quadratically subtracted to bring the χ^2 value back up to the required value. For the secondary the average of the sigma values was used.

GB: The input uncertainties are those quoted by the authors and are the r.m.s residuals to the fitted radial velocity curve.

INT: The input uncertainties are the r.m.s residuals of the O-C values derived by the present author. An uncertainty of 0.7 km s^{-1} was quadratically subtracted from the original value of 1.7 km s^{-1} to bring χ^2 down to *Nfit* – *Nparam*.

b) This added uncertainty is applied to a single combined radial file and so is the same for all three columns.

In order to achieve a proper overall fit, the relative weights of the different data sets must accurately match the real uncertainties on the data. This again requires that the χ^2 value

must equal *Ndf*, the number of degrees of freedom i.e *Nfit – Nparam* (where *Nparam* is the number of free parameters in the *Omdot* fits). This was achieved in two stages.

- Run *Omdot* with the complete set of light curve minima and with each set of radial velocities (CfA, Griffin and Boffin, INT) separately. These separate data sets include initial uncertainties, details of which are listed under Table 9.8. The initial χ^2 value is usually higher than *Nfit – Nparam*; thus it was again necessary to add or subtract an additional systematic uncertainty quadratically to bring χ^2 to this value. Since two sets of uncertainties are added quadratically *Nparam* is again taken as 2.
- Form a complete radial velocity set from the three component sets and repeat.

This process together with preceding work provides four measures of the uncertainties in the radial velocities, set out in Table 9.8.

9.5.2 Results

The *Omdot* software was run before each of the two main JKTEBOP iterations (Sect. 9.1.1, item 9). Results from the final iteration are shown in Table 9.9. It will be seen by comparing Tables 9.5 and 9.9 that the results from the initial analysis by SBOP agree with the definitive *Omdot* results. The apsidal period of $U = (14.5 \pm 3.9) \times 10^3$ years agrees with the $(13.6 \pm 1.5) \times 10^3$ years derived by Wolf et al. (2010, their Table 1).

Table 9.9 Parameters calculated by Omdot

Parameter	Value	Uncertainty
$P_{sidereal}$ (days)	8.98854738	
$P_{anomalistic}$ (days)	8.98856259	0.00000365
e	0.26766	0.00039
ω (deg)	333.58	0.18
$d\omega/dt$ (radians/period)	0.0000106	0.0000027
K_1 (km s^{-1})	65.40	0.07
K_2 (km s^{-1})	70.84	0.11
U (years)	14500	3900 (Note a))
γ (CfA) (km s^{-1})	3.46	0.05
γ (GB) – γ (CfA) (km s^{-1})	1.136	0.092
γ (INT) – γ (CfA) (km s^{-1})	-3.540	0.164
Derived γ (GB) (km s^{-1})	4.60	0.11 (Note b))
Derived γ (INT) (km s^{-1})	-0.08	0.17 (Note b))

Note a) This uncertainty was derived from the uncertainty in dω/dt

Note b) Derived from γ (CfA) and the differences γ (GB) – γ (CfA) and γ (INT) – γ (CfA). The uncertainties were added quadratically.

The reduced radial velocity is introduced to allow radial velocity data obtained during different parts of the apsidal motion cycle to be displayed on a single plot with a single model fit. The lower two panels show the differences (Observed R.V. – Calculated R.V), abbreviated as O-C for the primary and secondary repectively. The individual radial velocities are colour coded by the same system as in Fig. 9.2. The averages of the absolute differences (O-C), i.e. those with the sign disregarded, are shown below in Table 9.10.

Table 9.10 Average absolute (O-C) residuals for each set of observations.

Observation	Average absolute residual (km s^{-1})	
	Primary	Secondary
CfA	0.38	0.62
GB	0.37	0.68
INT	0.94	1.18

It will be seen that the average absolute residual is much larger for the INT observations than for the other two sets.

The residuals from the *Omdot* fitting are shown in Fig. 9.5; the software was again written by Maxted (private communication). This Figure includes an overlap of 0.2 periods at each end of a cycle to show the time context of the results more clearly. The top panel shows the reduced radial velocity:

$$V\,(\text{reduced}) = V\,(\text{observed}) - e\,.K.\cos\omega - \text{systemic velocity for data set} \qquad 9.16$$

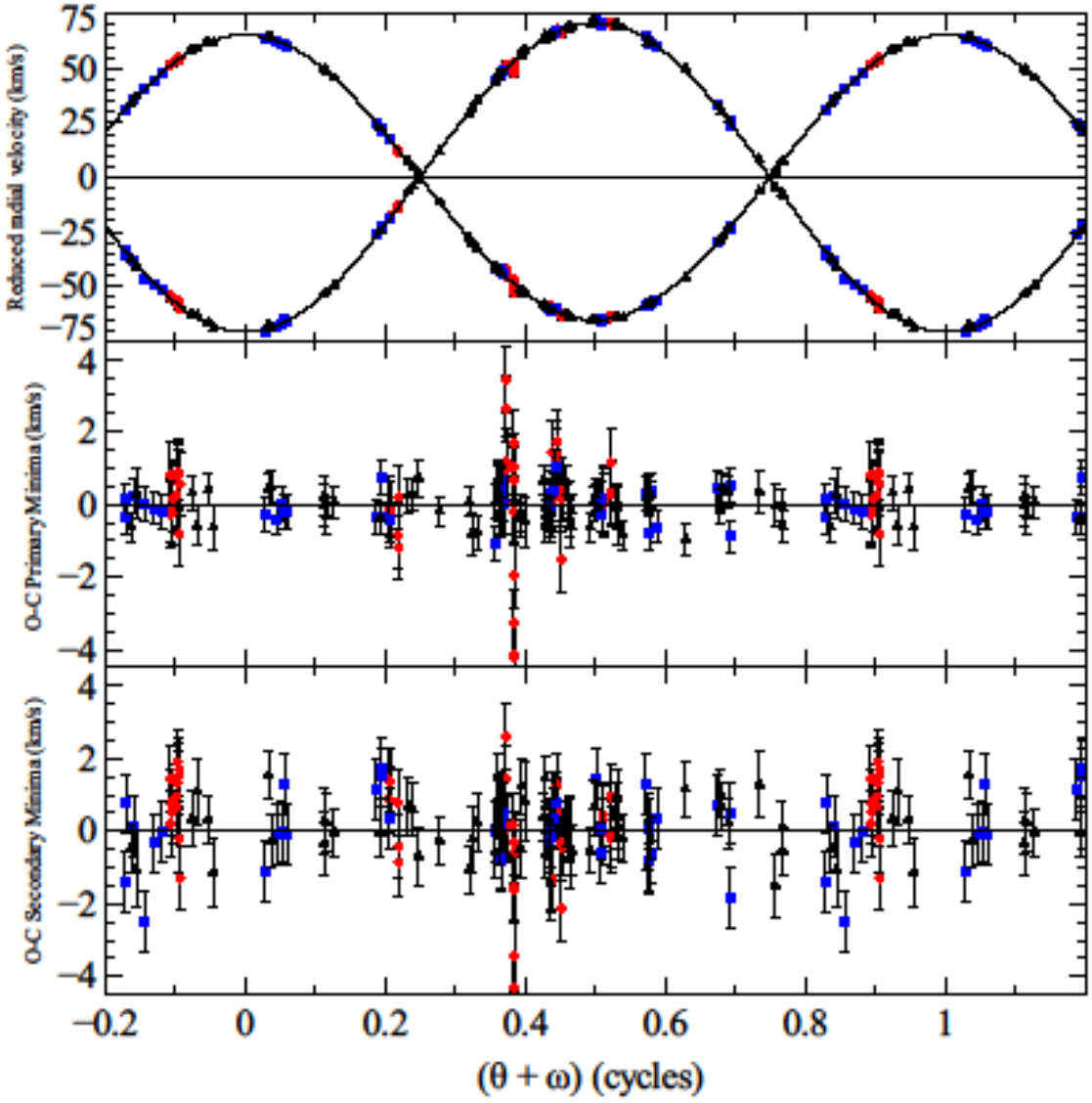

Figure 9.5 O-C residuals for each set of observations. The three panels show: top - the reduced radial velocity against true anomaly in units of period; middle and bottom - the O-C residuals for the primary and secondary minima against true anomaly. The observations are colour coded as black triangles - CfA, Blue squares – GB and Red circles INT.

9.6 Definitive Analysis of photometric light curves (JKTEBOP)

The photometric light curves were analysed with the eclipsing binary suite JKTEBOP (Appendix F) to obtain $(R_1 + R_2)/a$, R_2/R_1, i, $e \sin\omega$ and $e \cos\omega$, and the surface brightness ratio S_2/S_1. The suite was run for six cases: the V-band curves from NFO and URSA, and the four SAT curves (*u*-, *v*-, *b*- and *y*-bands). The output values finally adopted are the weighted averages over the six cases, except for S_2/S_1 which depends on the wavelength band. The initial solution was repeated with further constraints (Sect. 9.6.3).

9.6.1 Light curve plots

The complete light curves for the NFO, URSA and SAT observations are shown in Figure 9.6.

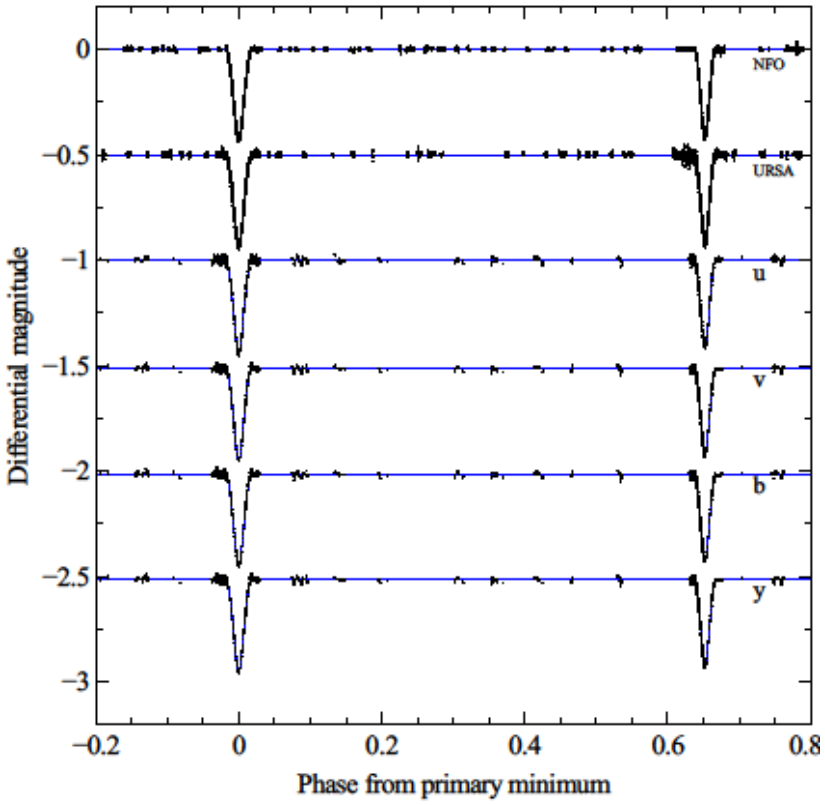

Fig. 9.6 Complete light curves for the NFO, URSA and SAT observations. The blue lines indicate theoretical light curves calculated by JKTEBOP. The curves are separated by 0.5 magnitudes for clarity.

This Figure shows all the points from all the observed cycles under a single period. The phase is shown from -0.2 to +0.8 to show the primary minimum more clearly. The SAT *u-,v-,b- and y-* bands are indicated simply as *u, v, b* and *y* for clarity.

Figures 9.7a and b show the minima on an expanded scale. The top panels show the primary and secondary minima for the URSA observations. The lower panels show the (O-C) values relative to the best fit calculated by JKTEBOP for all six sets of observations (NFO,URSA, SAT *u-,v-,b-* and *y*-bands) for the two minima, and are displayed in a manner similar to Fig. 9.6. Close examination of the upper panels shows that the eclipses are of unequal duration; this is a consequence of the orbits being elliptical.

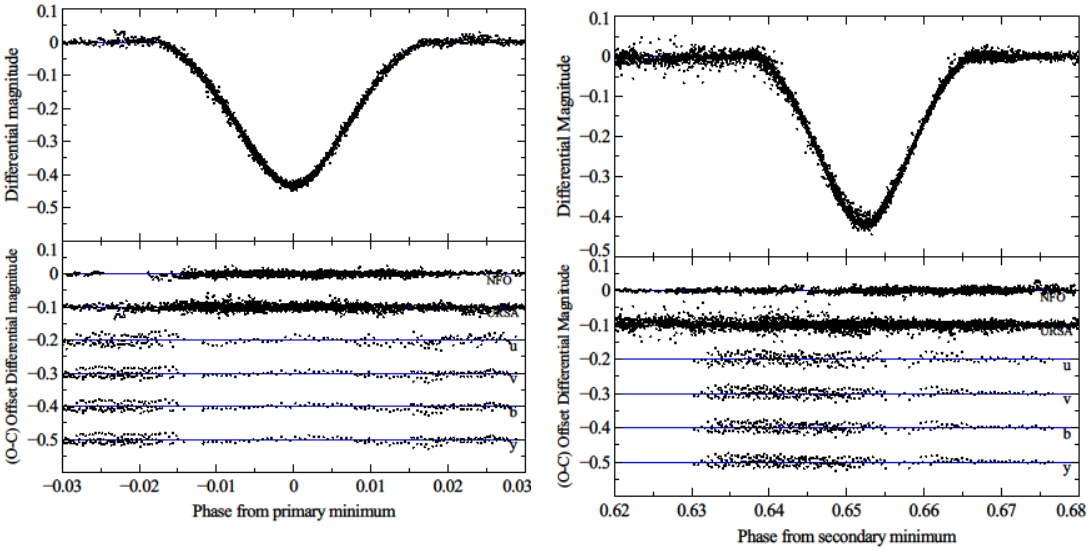

Figs. 9.7a and b. Expanded light curves and O-C plots for the primary and secondary minima. The O-C curves are separated by 0.1 magnitudes for clarity.

It will be seen that the luminosity dip is about 0.44 and 0.41 magnitudes for the primary and secondary minima respectively, corresponding to a reduction of observed combined luminosity of about 33% and 31%.

9.6.2 Input parameters

A JKTEBOP solution requires input parameters, which were obtained from the following sources.

$(R_1 + R_2)/a$, R_2/R_1, i, $e \sin\omega$ and $e \cos\omega$, and S_2/S_1.
From a previous iteration or a trial run. Values of $e \sin\omega$ and $e \cos\omega$ were corrected for apsidal motion in the final iterations (Sect. 9.6.3).

M_2/M_1 From *jktabsdim* (Sect. 9.1.1 and 9.9) or from SBOP for the first iteration.

T_0 and P From *ephem2* (Sect. 9.2.3).

Gravity and limb darkening parameters: As described below.

The input values for the orbital elements and S_2/S_1 are not critical because JKTEBOP searches for a best fit solution. The mass ratio was taken from the previous iteration of jktabsdim (Sect.9.1.1 Item 8, and Sect. 9.9) and held constant during a run since it has a negligible effect on the light curve (This ratio is used to correct the gravitational deformation of the stars if they are close, but for V1094 Tau the stars are sufficiently far apart that this effect can be ignored). The value used for the period is the sidereal period, not the anomalistic one, since it is the light curves which are being analysed by JKTEBOP.

Fitting light curves from eclipsing binaries will clearly need to account for how the surface flux varies over the stellar surface due to darkening. The JKTEBOP suite requires coefficients for both gravity and limb darkening. These effects are briefly explained in Appendix F.

Gravity darkening coefficients:

Since the V1094Tau system has a relatively large separation for a dEB, gravitational distortion of the stars and hence gravitational darkening is expected to be only a very minor effect. The gravity darkening coefficients β were nevertheless calculated since JKTEBOP requires them as data input, and they are easily obtained. The coefficients used by JKTEBOP are those defined by flux (in contrast to the value defined by temperature (Hilditch, 2001, Sect. 5.5.6)). These coefficients depend on the wavelength band, T_{eff}, *log g*, the metallicity parameter *Z* and the surface microturbulence parameter (a parametrisation of small scale convective motion in the atmosphere). Values were taken from the tables of Claret and Bloemen (2011) for the appropriate spectral bands and derived by linear interpolation of the tables grid first by *log* (T_{eff}) as this dependence is stronger, then by *log g*, and finally by *[Fe/H]*. The input values used were as follows.

T_{eff}: Values obtained the program *tbest* (Sect. 9.7) namely $T_{eff,1}$ = 5840K, $T_{eff,2}$ = 5680K. The tables require further input parameters and the values assumed were as follows.

Log g: Derived from values of mass and radius obtained from previous iterations.

Metallicity: *[Fe/H]* = -0.088 (Sect.9.8)

Surface microturbulence parameter: 2 km s^{-1}. No specific value is available; the value used is typical for solar-type stars.

The values of β finally obtained are shown in Table 9.11.

Table 9.11 Values of the gravity darkening coefficients defined by flux.

Band	Primary	Secondary
V (NFO,URSA)	0.399	0.430
u (SAT)	0.724	0.805
v (SAT)	0.608	0.658
b (SAT)	0.475	0.510
y (SAT)	0.405	0.435

These coefficients are assumed to have an uncertainty of ± 0.030. This value is guided by Fig. 3 of Claret and Bloemen (2011), which shows a plot of coefficients calculated by two different model atmospheres.

Limb darkening coefficients (u): A linear limb darkening law was assumed, whereby the the variation of surface brightness *I* over the projected surface disc can be approximated by a cosine law i.e.

$$\frac{I}{I_0} = 1 - u + u\cos\gamma \qquad 9.17$$

where I_0 is the surface brightness at the centre of the stellar disc, u is the limb darkening coefficient and γ the angle between the surface normal at a given point and the line of sight. Future work should assess the effect of including higher order terms (e.g. Southworth, 2008) and how this compares with the the effect of uncertainties in the coefficients themselves. The coefficients were obtained from the suite *jktld* which is an auxiliary to JKTEBOP. These coefficients depend on wavelength band and T_{eff}. The *jktld* suite therefore requires a value of T_{eff}, the filter type and a choice of published table as input data and returns a value of the coefficient. The values used for T_{eff} were as for the gravity darkening coefficient, and the values adopted for the coefficient u were the

averages over all the tables listed. The coefficients obtained are shown in Table 9.12**.** The quoted uncertainties are the standard deviations of the values given by the five models available on *jktld* (Van Hamme et al. 1993, Diaz-Cordaves et al. 1995, Claret et al 2000, Phoenix and Atlas model atmospheres; and Claret and Hauschildt. 2003).

Table 9.12 Values of the limb darkening coefficients

Band	Primary	Secondary
V (NFO,URSA)	0.662 ± 0.043	0.678 ± 0.039
u (SAT)	0.821 ± 0.031	0.841 ± 0.048
v (SAT)	0.810 ± 0.016	0.822 ± 0.015
b (SAT)	0.753 ± 0.041	0.769 ± 0.035
y (SAT)	0.662 ± 0.045	0.677 ± 0.039

9.6.3 Additional constraints

The JKTEBOP solution was obtained in two final iterations. The first was with constraints on e and ω and the second was with both this constraint and that on the luminosity ratio.

Constraint on e and ω.

The JKTEBOP values for e and ω are shown in Figs. 9.8a,b,c, which are in the form of a data point cloud. Each point in this cloud corresponds to a best fit solution as obtained when uncertainties are calculated by the residual shift method in JKTEBOP (Appendix F). As explained there the data point cloud contains as many points as in the light curve being analysed. The data point clouds for ω versus e are shown for the NFO

and URSA data in Figs. 9.8a and for the SAT data in Fig. 9.8b. The corresponding data point clouds for $e\ sin\omega$ versus $e\ cos\omega$ for all the data are shown in Fig. 9.8c. The colours which denote the SAT bands were chosen to correspond as far as possible to the actual colours transmitted by the bands, given the palette of colours available in the Veusz plotting package used. The value finally adopted for $e\ sin\omega$ and $e\ cos\omega$ are the centroid of the weighted data points and the uncertainties are taken as the 1-sigma error bars.

A feature of JKTEBOP is that the values returned for e and ω are quite strongly correlated, but the combination terms $e\ sin\omega$ and $e\ cos\omega$ are much less so (Fig. 9.8c). The degeneracy shown in Figs 9.8a and b for the solution for e and ω arises essentially because JKTEBOP calculates values for more parameters than those needed to define a light curve.

The terms $e\ sin\omega$ and $e\ cos\omega$ are related respectively to the time of secondary minimum relative to the primary, and to the relative duration of the eclipses (Southworth, 2012), who quotes the following expressions, derived by Kopal (1959), for the approximation of small e and $i \sim 90°$

$$e\ \cos\omega = \frac{\pi}{2}\left(\frac{t_{sec} - t_{prim}}{P} - 0.5\right) \qquad 9.18a$$

$$e\ \sin\omega = \frac{d_{sec} - d_{pri}}{d_{sec} + d_{pri}} \qquad 9.18b$$

In these expressions t and d denote the times and durations of the eclipses. The form of the expression for $e\ sin\omega$ shows that it is correlated with the ratio of the radii.

Although these expressions are approximations, the first one gives a value $e\ cos\omega = 0.2392$ which agrees well with the JKTEBOP value.

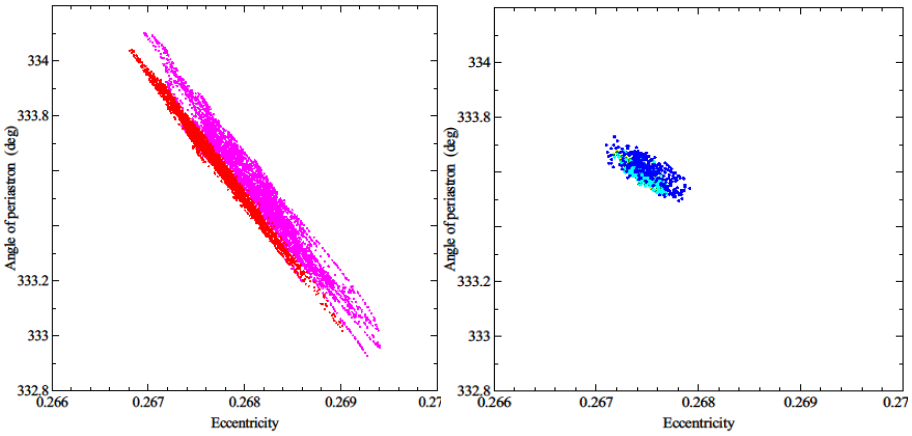

Fig. 9.8a,b Plots of data points for ω versus e for the NFO and URSA data (9.8a) and the SAT data (9.8b).
The data points are colour coded as NFO – Red; URSA – Pink:
SAT u-band – Deep blue; SAT v-band – light blue.
The b- and y-band data points are obscured by the u- and v-band points.

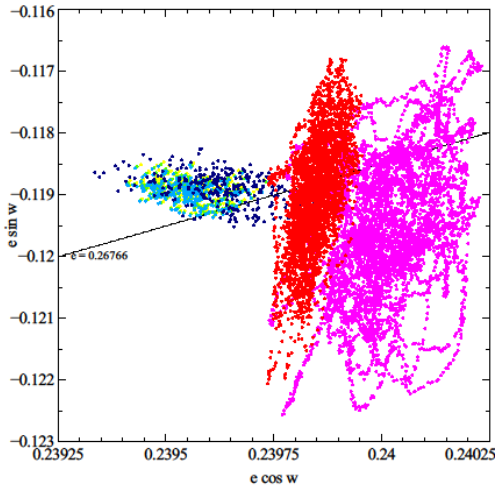

Fig. 9.8c Plots of data points for $e\,sin\omega$ versus $e\,cos\omega$ for all the data sets (NFO,URSA and SAT). The locus of constant e = 0.26766 is also shown.
The data points are colour coded as NFO – Red; URSA – Pink:
SAT bands: u– Deep blue; v – Light blue, b – Green; y – Yellow.

The first definitive solution was constrained by the values of these terms with their uncertainties. Because of the apsidal motion, the orbits precess and hence the angle of

periastron and the primary and secondary periods vary with time. Thus the values of $e \sin\omega$ and $e \cos\omega$ also change. A rigorous solution with JKTEBOP will treat the primary and secondary minima in separate runs with the appropriate values of the combination terms. This was not practical within the time scale of this thesis. The course adopted here was to treat the primary and secondary minima together in a single JKTEBOP run and a single value of the period, but to tailor the values of $e \sin\omega$ and $e \cos\omega$ for each run. This means that for the NFO, URSA and SAT runs, the JKTEBOP code was run for the angle of periastron for the time halfway through the time covered by the run. The values used are shown in Table 9.13.

Table 9.13 Values of $e \cos\omega$ and $e \sin\omega$ for individual runs

	NFO	URSA	SAT
Base time for ephemeris (JD)	54456.64438	54456.64438	54456.64438
Time at start of run (JD)	53737.71229	51974.64548	51828.82569
Time at end of run (JD)	56010.64561	56011.62120	54480.59803
Time at midpoint of run (JD)	54874.17895	53993.13334	53154.71186
Period (single)	8.98854775	8.98854775	8.98854775
No. of periods – see note	46.452	-51.567	-144.843
dω/dt (rad/sidereal period)	0.0000106	0.0000106	0.0000106
Value of ω from Omdot (deg)	333.580	333.580	333.580
$\Delta\omega$ base time to midpoint (deg)	0.028	-0.031	-0.088
Mean ω for run (deg)	333.608	333.549	333.492
e	0.26766	0.26766	0.26766
Mean $e \cos\omega$ for run	0.23976	0.23964	0.23952
Mean $e \sin\omega$ for run	-0.11898	-0.11923	-0.11946

Note: This is the number of periods from the ephemeris base time to the midpoint of the run, and so can be negative if the midpoint precedes the base time.
The abbreviation JD means Heliocentric Julian Day – 2 400 000.

Constraint on stellar light ratio.

A JKTEBOP solution is degenerate between $k = R_2/R_1$ and the stellar light ratio L_2/L_1, hereafter cited as LRAT, which is the ratio of the two fluxes observed in the relevant band multiplied by $(R_2/R_1)^2$. The fluxes observed in each band are convolutions of the stellar luminosities and the transmission profiles for the band filter. An example of the degeneracy is shown in Fig. 9.8a, which is a plot of k against LRAT for the NFO and URSA data in the manner of the Figs. 9.7. The constraint LRAT = 0.526 ± 0.025 derived below is also shown as the two lines corresponding to the error bars (the lower one lies at the very foot of the plot).

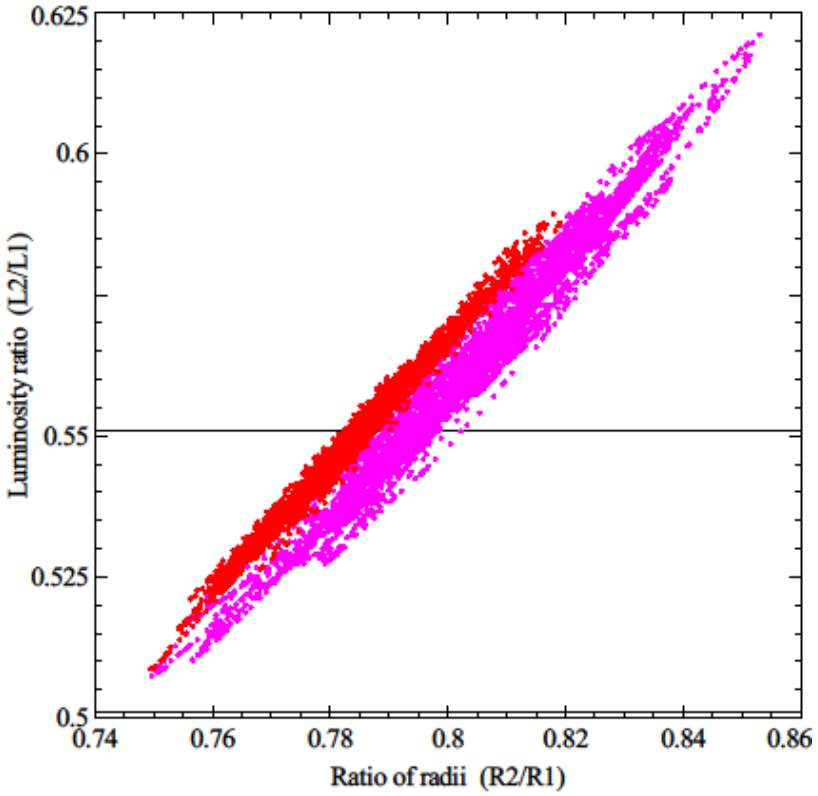

Fig. 9.9a Plot of data points for luminosity ratio (L_2/L_1) against ratio of radii (R_2/R_1) for the NFO and URSA data.
The data points are colour coded as NFO – Red; URSA – Pink:
The constraint L_2/L_1 = 0.526 ± 0.025 on the luminosity ratio LRAT is shown as a pair of horizontal lines.

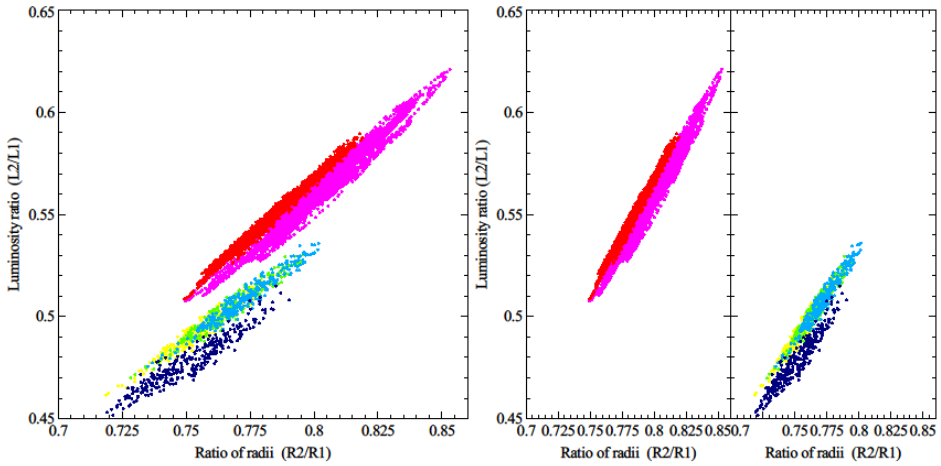

Figs. 9.9b and c. Plots of luminosity ratio against radius ratio for all six data sets combined (9.9b) and grouped (9.9c)
Fig. 9.9c shows the NFO and URSA data on the left hand panel and the SAT data on the right hand panel.
The data points are colour coded as NFO – Red; URSA – Pink:
SAT bands: u– Deep blue; v – Light blue, b – Green; y – Yellow.

The degeneracy was lifted by imposing a constraint on LRAT. The method used to calculate this constraint depends on the wavelength band.

NFO, URSA and SAT y-band runs.

The starting point is the observation by Torres that the luminosity ratio L_2/L_1 = 0.504 ± 0.020 in a 45Å window centred around 5190Å (Sect. 8.3.2). This band is sufficiently close to the V-band used for the NFO and URSA runs, and to the *y*-band used for one of the SAT runs, that the stellar light ratio of Torres can be corrected for these three runs by stellar flux models. The stellar light ratio may be written as

$$LRAT = \frac{(R_2)^2.S_2 \otimes T(\lambda)}{(R_1)^2.S_1 \otimes T(\lambda)} \qquad 9.19$$

where $S_{1,2}$ denote the stellar fluxes and
$T(\lambda)$ the band transmission profile and
the ⊗ symbol denotes the convolution.

The argument below depends on the dependencies of the stellar fluxes i.e.

$S_1 = S_1(T_{eff,1}; log\ g_{,1}; [Fe/H]_1$ and other parameters)
$S_2 = S_2(T_{eff,2}; log\ g_{,2}; [Fe/H]_2$ and other parameters)

Writing the stellar light ratio in this way explains the procedure for calculating the light ratio constraint, the main steps of which are as follows.

1. Start with the best value of T_{eff} and radii for both stars. Calculate the stellar light ratio for the spectral band used by Torres.

2. This will differ from the value actually obtserved by Torres, so force it to be equal his value. Torres. Eqn. 9.19 shows that in principle this can be done either by adjusting one of the temperatures or one of the radii to a nominal value. The course followed here was to adjust the nominal radius of the secondary, for the reason that this shows more clearly the effect of uncertainty in the T_{eff} values.

3. With this nominal radius ratio, calculate the stellar light ratio in the V-band with the V-band filter profile.

This procedure requires flux models and filter profiles. The flux model used was that of Kurucz (1993), and values were interpolated by T_{eff} and *log g* by the standard IDL interpolation routine. The filter profiles were obtained from Maxted (private communication) for the CfA band and Bessell (1990, Table 2) for the V-band. The choice of initial T_{eff} is explained later (Sect. 9.7.2). Values of *log g* were taken from the values of mass and radius returned by the previous iteration. The calculation was repeated with the BaSeL stellar flux models (Westera et al., 2002) to check the effect of using different flux models. The results are shown in Table 9.14 below.

Table 9.14 Calculation of corrected L_2/L_1 ratio for the V-band

Initial values of T_{eff}	5880 K (prim), 5640 K (sec)
L_2/L_1 for CfA band	0.504 ± 0.020
Corrected L_2/L_1 for the V-band	0.526 ± 0.021
Uncertainty in L_2/L_1 corresponding to 100K uncertainty in $T_{eff,1}$	0.006
Uncertainty in L_2/L_1 corresponding to 100K uncertainty in $T_{eff,2}$	0.009
Uncertainty in L_2/L_1 corresponding to uncertainty of 0.5 in *[Fe/H]*	0.007
Effect of using another (BaSeL) stellar flux model	0.001
Combined total uncertainty (quadratic sum of all the contributions)	0.025
Final value for LRAT constraint	0.526 ± 0.025
L_2/L_1 ratio obtained from JKTEBOP	
NFO	0.553 ± 0.010
URSA	0.561 ± 0.011

The final LRAT constraint is shown as the horizontal lines on Fig. 9.9a. It will be seen that the constraint passes through the lower tip of the data point cloud i.e. the agreement between the corrected CfA ratio and the ratio generated by JKTEBOP/NFO or URSA is poor. This is not understood. In view of this poor agreement, it was decided not to use the NFO/URSA ratio as a base for deriving an LRAT constraint for the SAT light curves, apart from the *y*-band as explained above.

9.6.4 Adjustment of error bars

In order for the LRAT constraint to be enforced within its error bar, the assumed error on the photometric differential magnitudes must be closely equal to the root mean square error of the best fit. The reason for this is a consequence of the least squares fitting process used in JKTEBOP for this constraint, which calculates the χ^2 value from the sum of the residuals from a) the differential magnitude photometric fitting and b) the luminosity ratio fitting. If the magnitude error is not equal to the root mean square error, is must be adjusted to be so by adding or subtracting a constant error term to the magnitudes. If this were not done, those trial solutions which predict an LRAT value far from the observed value would be weighted wrongly.

9.6.5 Results

The values and uncertainties in the values of L_2/L_1 and R_2/R_1 for each light curve were calculated by the JKTEBOP residual shift method (Appendix F) whereas the uncertainties in the adopted mean are 1σ standard deviations over all the light curves. This explains for example the apparent discrepancy in the uncertainties in the inclination angle.

Table 9.15 Light curve parameters for V1094Tau, as derived by JKTEBOP

		Lacy		SAT	band			Adopted
		NFO	URSA	u	v	b	y	
Number of datapoints		5714	8085	670	670	670	670	
Observational scatter (mmag)		5.3	8.9	12.1	10.3	9.2	8.5	
Fractional total radii of the stars		0.10731	0.10775	0.10767	0.10805	0.10755	0.10653	0.10748
$(R_1 + R_2)/a$	±	0.00028	0.00018	0.00061	0.00042	0.00041	0.00041	0.00053
Fractional radius of primary star		0.06010	0.05984	0.06010	0.06087	0.06073	0.06078	0.06028
R_1/a	±	0.00089	0.00131	0.00123	0.00108	0.00041	0.00052	0.00018
Fractional radius of secondary star		0.04721	0.04792	0.04721	0.04719	0.04682	0.04575	0.04712
R_2/a	±	0.00070	0.00105	0.00096	0.00083	0.00084	0.00081	0.00072
Eccentricity		0.26771	0.26875	0.26774	0.26772	0.26770	0.26770	0.26776
(e)	±	0.00060	0.00096	0.00021	0.00018	0.00018	0.00018	0.00042
Angle of periastron		333.627	333.241	333.499	333.469	333.478	333.484	333.482
(ω)	±	0.115	0.180	0.021	0.023	0.023	0.024	0.125
Orbital inclination		88.229	88.204	88.311	88.221	88.276	88.262	88.249
(*i*)	±	0.027	0.038	0.039	0.027	0.032	0.030	0.060
Surface brightness ratio		0.8539	0.8538	0.8598	0.8689	0.8968	0.8738	N/A
(J)	±	0.0071	0.0072	0.0072	0.0072	0.0024	0.0029	
Light ratio		0.4737	0.5108	0.5029	0.4902	0.5511	0.5567	N/A
(L_2/L_1)	±	0.0116	0.0152	0.0146	0.0135	0.0076	0.0098	
Limb dark. coefft. - Primary		0.662	0.662	0.821	0.810	0.753	0.662	
- Secondary		0.678	0.678	0.841	0.822	0.769	0.677	
Gravity dark. coefft - Primary		0.399	0.399	0.724	0.608	0.475	0.405	
- Secondary		0.430	0.430	0.805	0.658	0.510	0.435	

It will be seen that there is broad agreement between each set of light curves but there are some disagreements larger than the combined error bars. A possible explanation is sources of systematic error not taken into account by JKTEBOP e.g. starspot activity and instrumental effects.

This analysis combined with that by *Omdot* provides a complete solution for the system.

9.7 Values of T_{eff}

The effective surface temperatures for each star were determined from three sources.

1. Adjusting the temperatures derived by Torres (see below, private communication) for *log g* and metallicity.

2. Temperature difference estimated from the luminosity ratio determined by JKTEBOP.

3. Estimates obtained by treating the complete system as a single star.

The value of T_{eff} finally adopted is a best fit within these three constraints. This fit was obtained by a specially written program *tbest* (Maxted, private communication).

9.7.1 Adjustment of temperatures of Torres.

Torres has derived T_{eff} values of 6080 ± 100K (primary) and 5760 ± 100K (secondary) by a spectroscopic method based on TODCOR and on correlations with a grid of template spectra for a series of temperatures and rotational velocities. The values adopted for these parameters are those which maximise the peak of the correlation function. They assume *[Fe/H]* = 0.0 and *log g* = 4.5. Torres also states that:

- Reducing the adopted *[Fe/H]* by 0.5 lowers the derived T_{eff} estimate for both stars by 350K.

- Reducing the *log g* value by 0.5 at solar metallicity lowers the derived T_{eff} estimate by 220 K at solar metallicity.

Corrections for these dependencies were applied as follows.

1. Assume the provisional value *[Fe/H]* = -0.088 (Sect. 9.8).

2. Then apply the second correction with the values of *log g* obtained by the program jktabsdim (Sect. 9.9).

These two corrections are assumed to be linear and independent.

The corrected spectroscopic values are

$T_{eff,1}$= 5880 ± 100K $T_{eff,2}$ = 5640 ± 100K 9.20

A further observation by Torres gives some slight support to the adopted value of *[Fe/H]*. He has analysed the 2-D cross-correlation coefficient from TODCOR for three trial values *[Fe/H]* = 0.0, -0.5 and -1.0, and finds that *[Fe/H]* = 0.0 gives the best match.

9.7.2 Temperature difference estimated from luminosity ratio

The temperature difference ΔT_{eff} can be estimated essentially by assuming a reasonable temperature for one star and adjusting the temperature of the other star to reproduce the observed stellar light ratio L_2/L_1 The defining equation is derived from Eqn. 9.19 but since the procedure treats each spectral band by itself, the convolution with the spectral profile can be dropped and this equation may be written simply as

$$\frac{L_2}{L_1} = \frac{(R_2)^2.S_2}{(R_1)^2.S_1} \qquad 9.21$$

where the dependencies of S_1 and S_2 are repeated for convenience i.e.

$S_1 = S_1(T_{eff,1}; log\ g_{,1}; [Fe/H]_1$ and other parameters)
$S_2 = S_2(T_{eff,2}; log\ g_{,2}; [Fe/H]_2$ and other parameters)

It is essential to recognise the strong correlation between L_2/L_1 and R_2/R_1 as shown on e.g Fig.9.9a. Thus the appropriate value of $(R_2/R_1)^2$ is that corresponding to the observed value of L_2/L_1 and may be read off from a best fit of L_2/L_1 against R_2/R_1 as obtained by linear regression, using a statistical analysis routine in the TOPCAT astrophysical analysis software (www.star.bristol.ac.uk/~mbt/topcat). The error bars on the temperature difference correspond to those in the input L_2/L_1 ratio.

The values for the surface flux *S* were obtained from the Kurucz stellar flux models as before. They depend mainly on on T_{eff} and only weakly on *log g*, *[Fe/H]* and other parameters. Here the proper *log g* value was used for each star, *[Fe/H]* was taken as 0.0 and the other parameters were ignored. As before this procedure was applied to the NFO, URSA and SAT *b*- and *y*-bands only because stellar flux models were judged not to be sufficiently accurate for the *u*- and *v*- bands. The calculation is based on the value $T_{eff,1}$ = 5880 K obtained by Torres and corrected for *[Fe/H]* and *log g*.

This calculation was made with the results from the last JKTEBOP iteration carried out before the LRAT constraint on the stellar light ratio. It is invalid in principle to use the iteration after this constraint because this constraint depends on the estimated temperature difference through the stellar light ratio constraint on the V-band CfA spectra and the procedure would be circular.

The estimated temperature differences for each spectral band are shown in Table 9.16 below.

Table 9.16 Estimated Temperature differences for spectral bands

Run	Spectral band	Temperature difference (K)
NFO	V	138 ± 7
URSA	V	171 ± 11
SAT	b	164 ± 12
SAT	y	174 ± 13
Weighted average		159 ± 16 (standard deviation)

In order to calculate total uncertainty other sources of uncertainty must be included i.e.

Source	Uncertainty (deg K)
Standard deviation calculated above	16.4
Uncertainty in L_2/L_1	10.8
Uncertainty in $T_{eff,1}$	5.8
Uncertainty of 0.1 in *[Fe/H]*	6.7
Uncertainty due to stellar flux model	2.9
Quadratic sum	21.7

Thus the value finally adopted for the temperature difference as calculated from the stellar light ratio is:

$$\Delta T_{eff} = 159 \pm 22 \text{ deg K.} \qquad 9.22$$

9.7.3 "Single star" temperature from Strömgren colour indices

An attempt was made to determine metallicities from the Strömgren colour indices (Sect. 9.8). This also leads to an estimate of

$$T_{eff} = 5801 \pm 100 \text{ K} \qquad 9.23$$

when the system is treated as a single star.

9.7.4 Values finally adopted for T_{eff}

The three data inputs Eqns. 9.20, 9.22 and 9.23 to the program *tbest* are illustrated in Fig. 9.10.

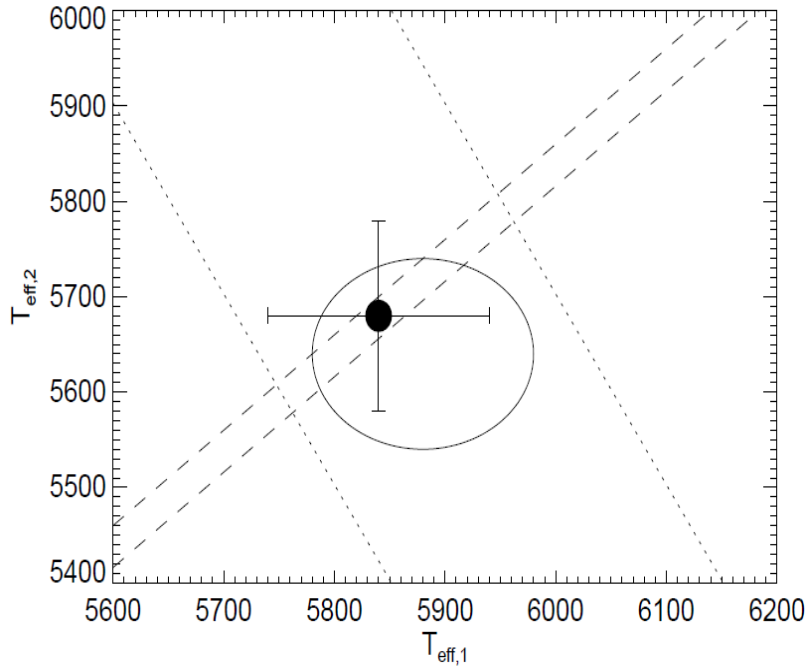

Fig. 9.10 Data inputs and output for the program *tbest*.
The constraints on T_{eff} are indicated as follows.
Dotted lines: 1-sigma constraint from Strömgren colour indices (Eqn. 9.23)
Dashed lines: 1-sigma constraint from stellar light ratios (Eqn. 9.22)
Solid (oval) line: 1-sigma constraint from the adjusted CfA values (Eqn. 9.20)
Solid point and error bars: Temperatures and uncertainties finally adopted.

Thus the values of T_{eff} satisfying all three constraints lie in the roughly trapezoidal area of Fig. 9.10 bounded by the dashed lines and the oval. The value finally adopted was fitted by eye to the centre of this relatively small region. The ± 100K error bars were adopted as representative of determinations of T_{eff}. The values are:

Primary: 5840 ± 100 K 9.24

Secondary: 5680 ± 100 K

In principle the best value could be calculated by an analytical method. This was not done for two reasons. First, the assumed error bars are considerably wider than the dimensions of the "trapezoidal" area satisfying the constraints. Secondly it was judged that fitting by eye introduces an uncertainty of say 10 or 20 °K and removing this by an analytical method did not justify the computational effort required. Any analytical solution would be much more complicated than simply finding the centroid of the "trapezoidal" area, because the probability of satisfying any one of the three constraints varies within that area. Each of the two pairs of lines on Fig. 9.9, and the oval are the locus of a 1-sigma constraint and so define a normal distribution.

The values of T_{eff} used to determine the stellar light ratio constraint for the V-band and y-band runs (Sect. 9.6.3) was taken from the corrected temperatures of Torres only, not from the output of *tbest*. This is because the latter is based in part on the stellar light ratio and so using it would be a circular argument.

9.8 Metallicity

9.8.1 Treatment of binary as single system

A partially successful attempt was made to determine the effective temperature T_{eff} and metallicity *[Fe/H]* from values of magnitudes, Strömgren colour indices and index differences supplied to the author by Clausen (private communication). This analysis does not require other input. The term "partially successful" means that values of T_{eff} and *[Fe/H]* were obtained for V1094 Tau treated as a single star. The Strömgren colour index system is described in detail in Appendix G. Briefly the *u, v, b* and *y* indices are colour indices for spectral bands; and two derived indices provide diagnostics as follows:

(b-y)	Sensitive to T_{eff} in the OB to G range of spectral type.
$c_1 = (u-v) - (v-b)$	Sensitive to luminosity for A- and F-type stars.
$m_1 = (v-b) - (b-y)$	Sensitive to metallicity.
β	Related to the intensity ratio of narrow and relatively wide spectral bands centred on the Hβ line and hence sensitive to

The values of these magnitudes, colour indices and index differentials as supplied by Clausen are shown in Table 9.17.

Table 9.17 Magnitudes, Strömgren colour indices and index differences supplied by Clausen.

Band or Index	Value
V	9.020 ± 0.009
(b-y)	0.415 ± 0.004
m_1	0.199 ± 0.009
c_1	0.330 ± 0.011
β	2.596 ± 0.005

Since the index differential *(b-y)* is sensitive to T_{eff} and m_1 *= (v-b) – (b-y)* is sensitive to blanketing by metallic lines, it may be expected that a semi-empirical relation exists that expresses T_{eff} and *[Fe/H]* in terms of the index differentials. Such a relation has been derived by Holmberg et al. (2007, Sect. 4.2) and is:

$$\begin{aligned}[Fe/H] = \; & -2.19 - 1.02(b-y) + 7.34m_1 - 0.27c_1 \\ & +5.86(b-y)^2 - 43.74{m_1}^2 - 0.14{c_1}^2 + 25.03(b-y)m_1 \\ & +5.29(b-y)c_1 + 25.95m_1c_1 - 31.10(b-y)^3 + 46.19{m_1}^3 \\ & -3.86{c_1}^3 + 4.54(b-y)^2m_1 + 19.31(b-y)^2c_1 - 17.46{m_1}^2(b-y) \\ & +18.36{m_1}^2c_1 - 9.99{c_1}^2(b-y) + 6.60{c_1}^2m_1 - 59.65(b-y)m_1c_1 \end{aligned} \qquad 9.25$$

Holmberg et al. give semi-empirical relations for T_{eff} in terms of *(b-y)* for a series of ranges of the latter, and for the range $0.33 < (b-y) < 0.50$ give:

$$\theta_{eff} = 0.754 - 0.365(b-y) - 0.001[Fe/H]^2 + 1.635(b-y)^2 - 0.091(b-y) \qquad 9.26$$

These relations cannot be used to estimate *[Fe/H]* and T_{eff} as they stand because the colour index parameters (apart from β) are affected by reddening. This is the absorption due to interstellar dust and is due to Mie scattering. The strength of this is proportional to $1/\lambda$ (Hilditch, 2001, Sect. 5.3.1) and so preferentially removes shorter wavelengths. Interstellar dust may be clumped and so reddening can depend strongly on direction. There is therefore no simple general analytic expression for it. A typical value for A_V, the interstellar extinction near the Sun in the V-band, is (Binney and Merrifield, 1998, Sect.3.7.1) A_V~1.6 magnitudes per kiloparsec. It is customary to assume that the interstellar reddening *E(B-V)* i.e. the differential extinction between the B- and V- bands is proportional to the extinction; Binney and Merrifield give $E(B\text{-}V) = A_V/3.1$ i.e. a typical *E(B-V)* is ~ 0.53 per kiloparsec.

The reddening thus has to be estimated from observational data. This was done by an iterative method described by Crawford (1975a) and Olsen (1988). Essentially this relies on base relations between the Stromgren indices β, *b-y*, m_1 and c_1, representative of stars without reddening, and then calculates the corrections δm_1 amd δc_1 by which reddening causes the observed m_1 and c_1 values to depart from the base relation. The observed value of the index β can be used as input data because it is a function of the flux ratio of the wide and narrow Hβ bands and, because these bands have the same effective wavelength, the flux ratio is to a good approximation free of reddening and blanketing effects.

A standard empirical relationship between β, *(b-y)*, m_1 and c_1 has been derived by Crawford (1975a, his table I) from a detailed survey of stars where reddening is not significant. Crawford plots *(b-y)*, m_1 and c_1 against β and defines an envelope of points on the graphs. The plot of c_1 against β for bright F-type stars is reproduced in Fig 9.11.

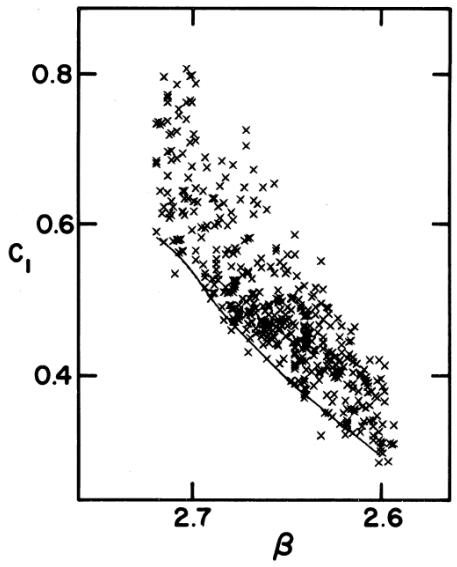

Fig. 9.11 Plot of the c_1 versus β relation for bright F-type stars, after Crawford (1975a, Fig.6)

Because of the definition of c_1 the full line in Fig. 9.11 essentially represents the c_1 versus β relation for zero age main sequence stars. This relation and the corresponding ones for *(b-y)* and m_1, are known as the standard relations. These have been revised and extended by Olsen (1988, Sect. 2) and the relevant part of his table is shown in Table 9.18.

Table 9.18 Standard empirical relation between selected colour indices

β	*(b-y)*	m_1	c_1
2.60	0.394	0.214	0.290
2.59	0.412	0.230	0.270
2.58	0.431	0.255	0.253

For the value β = 2.596 obtained by Clausen, linear interpolation gives

(b-y) = 0.401, m_1 = 0.220, c_1 = 0.282.

It will be seen from Fig. 9.11 that most stars do not follow the standard relation exactly. It is customary to define quantities $\Delta\beta = 2^m.720 - \beta$ and δm_1 and δc_1 as the degree to which the actual value of m_1 and c_1 for a given star depart from the standard relation. By fitting to the residuals δm_1 and δc_1, Olsen derives (his Eqn. 7) the final calibration

$$(b-y)_0 = 0^m.217 + 1.34\Delta\beta + 1.6(\Delta\beta)^2 + C\,\delta c_0$$
$$- (0.16 + 4.5\,\delta m_0 + 3.5\Delta\beta) \quad \text{for } \delta m < 0^m.060$$
$$\text{or} \quad - (0.24 + 0^m.035) \quad \text{for } \delta m \geq 0^m.060 \qquad 9.27$$

where $C = -0.05$ for the values of δm relevant here (Olsen gives a full expression with boundary conditions, which is not quoted here). Olsen states that Eqn. 9.26 is valid for the spectral type range F0 to G2 and so is also valid with slight approximation at most for the G0 + G3 spectral type of V1094 Tau.

The reddening and hence the corrected parameters for Eqns. 9.25 to 9.27 can be calculated by iteration. The procedure is as follows. It assumes that the reddening is the same for both stars since they lie in effectively the same direction and have similar spectral type.

1. Calculate corrections $\delta c =$ c_1 (observed, Clausen, Table 9.17)
   $- c_1$ (standard, Table 9.18)
   and similarly $\delta m =$ m_1(standard) – m_1(observed)

2. Calculate a corrected value of *(b-y)* from Eqn. 9.27.

3. Calculate a *(b-y)* colour excess as
   E(b-y) = *(b-y)* observed – *(b-y)* corrected (as equation above)

4. Calculate new values of m_1 and c_1 from the expressions (Crawford, 1975b)
   c_1 *(new)* = c_1 *(observed)* – *0.2E(b-y)*
   m_1 *(new)* = m_1 *(observed)* + *0.32E(b-y)*

5. Repeat as necessary, starting the next iteration by
   $\delta c_1 = c_1(new) - c_1(std)$
   $\delta m_1 = m_1(new) - m_1(std)$

The corrected colour index *(b-y)* may then be used to obtain a value of *[Fe/H]* by the empirical calibration equation (9.25).

The uncertainties were estimated by perturbing the values of *(b-y)*, m_1 and c_1 by randomised uncertainties and repeating the iteration 20 times with these perturbed values. The randomisation was carried out as follows.

- Generate 60 random numbers $x_1, x_2 \ldots x_{60}$ between -1 and 1 and multiply them by 3 for reasons explained below to obtain $3x_1, 3x_2 \ldots 3x_{60}$. . Sixty numbers are needed because each of the 20 iterations requires 3 input values. Calculate a Gaussian probability factor $exp(-(3x_n)^2/2)$ for each value of x_n.

- For the first iteration perturb the input values of *(b-y)* by the uncertainty multiplied by $3x_1$, and similarly m_1 and c_1 by $3x_2$ and $3x_3$. Weight the output values of *[Fe/H]* and T_{eff} by the average of the three Gaussian factors $exp(-(3x_{1,2,3})^2/2)$

- Repeat for the second iteration but using x_4, x_5 and x_6, and so on for the remaining 18 iterations.

The uncertainty in the values of the output parameters is taken as the weighted standard deviation of the weighted mean, where the weights are those assigned to the output values.

If the multiplication by 3 were omitted from the procedure above, all the perturbations of the input values would be less than one standard deviation and the uncertainty in the output values would be underestimated. Some multiplication factor is therefore required. If it is too large some weighting factors would be extremely small and the corresponding iteration of little value. If the multiplication factor is too small the output uncertainties are underestimated. The factor 3 was chosen as a compromise value and then the smallest Gaussian weighting factor is about 1% since $(exp(-3^2/2) \sim 0.011)$.

The uncertainties in T_{eff} and *[Fe/H]* so calculated were taken as the random uncertainties and are shown as (rand) below. The uncertainties marked as (syst) for T_{eff} and *[Fe/H]* are typical uncertainties for the determination of these parameters. The value for

the *[Fe/H]* uncertainty is taken from the average uncertainties for the stars surveyed in Part I, i.e. ~ ±0.04 for the BTS and ~ ±0.06 for the RVS.

This finally gives:

$(b-y)_0$ = 0.396 ± 0.005 (rand)

E(B-V) = 0.025 ± 0.008 (rand)

T_{eff}/K (combined) = 5801 ± 22 (rand) ± 100 (syst)

[Fe/H] = -0.088 ± 0.050 (rand) ± 0.06 (syst) 9.28

m_1 = 0.205 ± 0.007 (rand)

c_1 = 0.326 ± 0.009 (rand)

As explained in Sect. 9.10 the *modelplot* software was run in an attempt to determine the age of the V1094 Tau system by an indirect method. This revealed an unresolved discrepancy between estimates of the metallicity which are *[Fe/H]* = -0.088 ± 0.050 (spectroscopic as above) and +0.18 ± 0.04 from *modelplot.*

9.8.2 Temperature determination for each individual star

An attempt was made to extend this procedure to determine the temperature and metallicity for the two individual stars by using the program *uvbysplit* (Southworth, private communication and webpage at www.astro.keele.ac.uk). This program takes the V-band magnitude, the *u*-, *v*-, *b*- and *y*-band light ratios, and the *(b-y)*, c_1 and m_1 indices from the combined system and calculates these indices for the individual stars. The latter were then used as the input indices as before. However, the temperature derived for the secondary was higher than that for the primary by over 100K. This result was regarded as unphysical since it is grossly inconsistent with all other studies of this system. The author understands that Torres has encountered the same problem (Maxted and Torres, private communications) and the solution to it is not known. Thus he has not proceeded further with this attempt.

9.8.3 Attempt to determine T_{eff} by spectral disentangling

The spectral disentangling method first described by Simon and Sturm (1994) and more recently by Pavlovski and Hensberge (2010), is a fundamentally different approach which takes a series of composite binary spectra and calculates the disentangled single star spectra which provide the best fits to them. It does not need a template spectrum. Pavlovski (private communication) made his *STARFIT* disentangling software available to the author who, after discussions with Maxted (private communication) attempted to run them with the INT spectra. However the results for surface temperature and gravity were too scattered to be usable and this approach was discontinued. In more detail the INT spectra was split into five sections and the STARFIT software run ten times for each section. However the results for T_{eff} were inconsistent with standard deviations and differences between regions were frequently above 200K. A possible reason for this failure is that the INT spectra covered too narrow a spectral range. Although the FOCES spectra cover a much wider range and so in principle could overcome this problem, the amount of work required to apply the disentangling methods to them would have been prohibitive for a thesis project.

9.9 Final values of system parameters (*jktabsdim*)

The definitive values for the parameters of the V1094 Tau system were obtained with the *jktabsdim* software where possible. Otherwise they were obtained from *Omdot*, except for the inclination which was obtained from JKTEBOP. The *jktabsdim* code written by Southworth (www.astro.keele.ac.uk/jkt/codes/jktabsdim) calculates the absolute masses, dimensions and associated parameters of a detached eclipsing binary system from the results of radial velocity and light curves analyses. The software uses standard expressions; for example the major axis and stellar masses are calculated from Eqns. 2.51 and 2.52 of Hilditch (2001), expressed differently and with very small adjustments of

numerical constants. A major advantage of using *jktabsdim* instead of using the standard expressions themselves is that it also takes proper account of propagating uncertainties and provides final uncertainties in the output. Doing this manually would require considerable computational effort.

9.9.1 Input data for *jktabsdim*

The input data used for *jktabsdim* were as follows.

Anomalistic period	*ephem2* (Sect. 9.2.3) and *Omdot* (Sect. 9.5.2)
K_1, K_2, ω, i	*Omdot* (Sect. 9.5.2)
i, R_1, R_2	JKTEBOP analysis (Sect. 9.6.5)
T_{eff} (1 and 2)	*tbest* (Sect. 9.7.4)
Reddening *E(B-V)*	Stromgren/Crawford differential colour indices (Sect. 9.8.1).
Metallicity *[M/H]*	Rounded value of 0.0 adopted (Sect. 9.8.1)
Magnitudes B,V,J,H,K Johnson-Cousins system	NOMAD catalogue, with Bessell transformations for the J, H and K bands (Sect. 8.1).
Luminosity ratio	Available only for the V band from JKTEBOP (Sect. 9.6.5)

The *jktabsdim* software requires the anomalistic periods as it is based on the mechanics of the system. This contrasts with JKTEBOP, which requires the sidereal period as it analyses observed light curves. It also requires a value of *[Fe/H]* to the nearest step of 0.5. A value of 0.0 was adopted. This is indicated by the spectroscopic value derived earlier and an indirect value derived by the modelplot software (Sect. 9.10).

The analysis by *jktabsdim* refines the masses and radii, and hence *log g*. Hence the values of the limb and gravity darkening coefficients are also refined and thus at first sight another iteration of JKTEBOP is required with the new values of these coefficients. In fact

this is not necessary since pilot calculations showed that the change introduced into the relative radii of the stars is at least two orders of magnitude smaller than the uncertainty.

9.9.2 Definitive values of V1094 Tau parameters

The definitive results obtained in the previous subsections are encapsulated in Table 9.19 below.

The input values of R_1/a and R_2/a lead to the derived values

$$\begin{array}{ll} (R_1+R_2)/a & 0.10740 \pm 0.00085 \\ R_2/R_1 & 0.7817 \pm 0.0133 \end{array} \qquad 9.29$$

where the uncertainties are the relative input uncertainties quadratically added.

These uncertainties are shown diagrammatically on Figs. 9.12a,b and Fig. 9.13 which show the data point clouds from the definitive JKTEBOP solutions. These figures code the light curve data by the same colours as for the solutions for e and ω. (Sect. 9.6 and the Figs. 9.8). The adopted values and the uncertainties are obtained from JKTEBOP in the same way as for those parameters. An attempt to use the Veusz software to superimpose the error bars from Eqn. 9.29 on to Fig. 9.13 was unsuccessful in that the x error bar could not be seen and the y error bar was faint. (Some of the locus of constant eccentricity in Fig. 9.8c was obscured for a similar reason).

Since the absolute radii are known, the *jktabsdim* software provides a distance by means of the empirical relations between angular diameter, temperature and band magnitude derived by Kervella et al. (2004) as described in Sect. 3.4. The relation for the K-band yields a distance of 120.8 ± 2.2 pc.

This distance together with the typical reddening constant $E(B\text{-}V)$ = 0.53 per kiloparsec predicts a reddening of 0.064. The spectroscopically derived value is 0.026 ± 0.005. Since the former value is only typical and depends on direction, this apparent disagreement is not regarded as a cause for concern.

Table 9.19. Definitive values for parameters of the V1094 Tau binary

Parameter	Value	Source
P_{sid}/*days*	8.98854775 (102)	Ephem2
P_{anom}/*days*	8.98856259 (365)	Ephem2/Omdot
$M_1/M_\odot$	1.0969 (37)	jktabsdim
$M_2/M_\odot$	1.0127 (27)	jktabsdim
$R_1/R_\odot$	1.406 (10)	jktabsdim
$R_2/R_\odot$	1.099 (17)	jktabsdim
$a/R_\odot$	23.324 (22)	jktabsdim
$log\ g_1$	4.182(6)	jktabsdim
$log\ g_2$	4.361(13)	jktabsdim
e	0.26766 ± 0.00039	Omdot
ω (deg)	333.58 ± 0.18	Omdot
i (deg)	88.249 ± 0.060	JKTEBOP
U (10^3 years)	14.5 ± 3.7	Omdot
K_1 (km/s)	65.40 ± 0.07	Omdot
K_2 (km/s)	70.84 ± 0.11	Omdot
γ (CfA)	3.46 ± 0.05	Omdot
γ (GB) – γ (CfA)	1.14 ± 0.09	Omdot
γ (INT) –γ(CfA)	-3.54 ± 0.16	Omdot
$T_{eff,1}$ /K	5840 ± 100	tbest
$T_{eff,2}$ /K	5680 ± 100	tbest
$L_1/L_\odot$	2.07 ± 0.14	jktabsdim
$L_2/L_\odot$	1.13 ± 0.09	jktabsdim
L_2/L_1		
u band	0.473 ± 0.024	JKTEBOP
v band	0.517 ± 0.028	JKTEBOP
b band	0.507 ± 0.026	JKTEBOP
y band	0.489 ± 0.022	JKTEBOP
V band	0.560 ± 0.017	JKTEBOP
Distance (pc)	120.8 ± 2.2	jktabsdim

The derived absolute bolometric magnitudes are

$M_{bol,1}$ = 3.957 + 0.076

$M_{bol,2}$ = 4.613 + 0.083

For comparison the absolute bolometric magnitude of the Sun is (Mamajek, 2013), (Website: sites.google.com/site/mamajeksstarnotes/bc-scale)

$M_{bol,\odot}$ = 4.7554 ± 0.0004

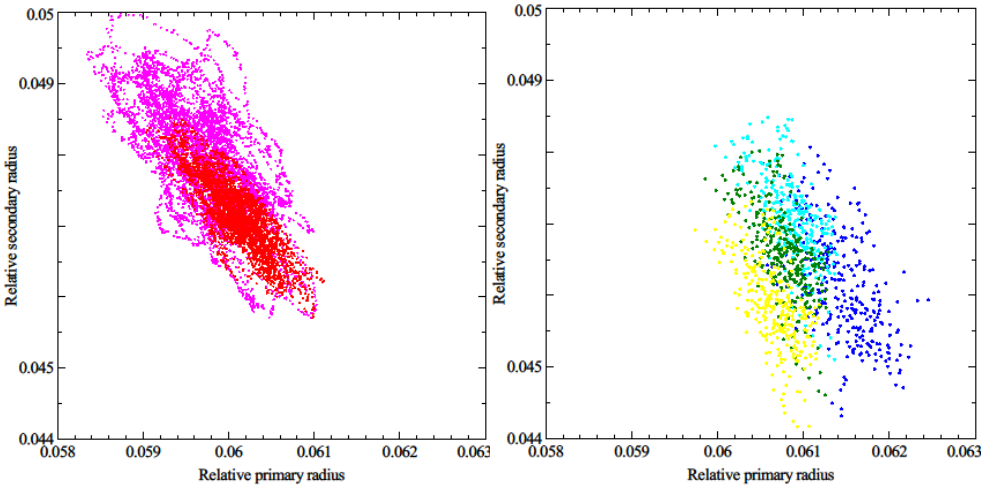

Figs. 9.12a and b. Data point clouds for R_2/a versus R_1/a as generated by JKTEBOP for the NFO and URSA data (fig. 9.12a) and for the SAT data (Fig. 9.12b)

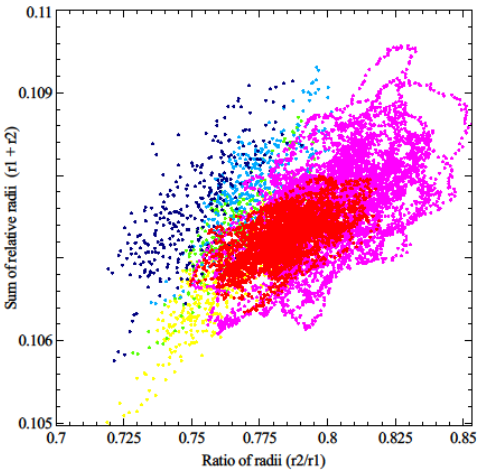

Fig. 9.13. Combined data point clouds for $(R_1 + R_2)/a$ versus R_2/R_1 as generated by JKTEBOP for the NFO ,URSA and SAT light curves.

The precision achieved here is ±0.34% and ±0.27% for the masses and ±0.71% and ±1.54% for the radii. Except for the radius of the secondary the precision achieved here appears to compare well with other published work. The website DEBCat maintained by Southworth (www.astro.keele.ac.uk/jkt/debcat) is a catalogue of the stellar properties of well-studied eclipsing binaries. In the subset where both stars have spectral classification F V or G V, the average uncertainty is 0.75% for the masses and 0.98% for the radii.

9.10 Pseudosynchronisation

If the tidal interaction between the members of a binary is sufficiently strong, and the orbits are circular, the stellar rotation becomes synchronised with the orbital motion (Appendix K). If the orbits are elliptical, it is impossible for the rotation to keep in true synchronisation with the orbital motion. Since the orbital radius vector must sweep out equal areas in equal times (Kepler's Second Law) the rate of change $d\theta/dt$ of the true anomaly (Sect. 12.4) with time cannot be constant. The detailed study by Hut (1981) has shown that a binary system with elliptical orbits can still evolve into an equilibrium state where there is no net torque on a star's rotation, so that the rotational period does not change over time. This equilibrium rotational period is known as the pseudosynchronous period P_{ps} and is related (Hut, Eqn. 42) to the orbital period P_{orb} by

$$P_{ps} = P_{orb} \frac{\left(1 + 3e^2 + \frac{3}{8}e^4\right)(1 - e^2)^{\frac{3}{2}}}{1 + \frac{15}{8}e^2 + \frac{45}{8}e^4 + \frac{5}{16}e^6} \qquad 9.30$$

and e is the eccentricity. For the physically admissible range $0 \leq e \leq 1$, the fraction A/B (where Eqn. 9.30 is written as P*ps* = P*orb*.(A/B)) is always below 1 (except for A/B = 1 for $e = 0$) and hence the pseudosynchronous period is always shorter than the orbital period.

The pseudosynchronous angular velocity ω_{ps} also differs from the angular velocity ω_p at periastron. This may be seen from the relation between ω_p and the orbital angular velocity ω, which is (Hut, Eqn. 44)

$$\omega_p = \omega \frac{(1+e)^2}{(1-e^2)^{\frac{3}{2}}} \qquad 9.31$$

Torres (private communication) has measured the rotational velocities (Sect. 9.7.1) and obtained

$$v_1 \sin i = 9.0 \pm 2 \text{ km/s} \qquad 9.32$$
$$v_2 \sin i = 4.4 \pm 2 \text{ km/s}$$

where v is the equatorial velocity and sin i has its usual meaning.

Simple geometry shows that the relation between v sin i and the rotational period is:

$$v \sin i = 50.58 \text{ km/sec} \times (R/ R_{\odot})/(\text{Period in days}) \qquad 9.33$$

Combining these equations with the values of R and i leads to:

$$P_{rot\_1} = 7.9 \pm 1.8 \text{ days} \qquad 9.34$$
$$P_{rot\_2} = 12.7 \pm 5.8 \text{ days}$$

The eccentricity of 0.26766 ± 0.00039 entails that the pseudosynchronous period P_{ps} is shorter than the orbital period by a factor 1.4390 ± 0.0013 i.e. P_{ps} = 6.246 ± 0.006 days i.e. $P_{ps} \sin i$ = 6.243 ± 0.006 days.

The error bars are too wide to draw firm conclusions but the pseudosynchronous period for the primary is only just consistent with the observed rotational period; that for the secondary just fails to be. It may be that the primary is pseudosynchronised and the secondary is not. This underlines the need for detailed spectroscopic measurements.

9.11 Are the tidal interactions significant?

. The observations described above show that V1094 Tau system is obviously not circularised since the eccentricity is approximately $e \sim 0.268$, and it is on the borderline of being pseudosynchronised. Thus the tidal interactions may be strong enough to pseudosynchronise the stars but not to circularise the orbits. This is consistent with an 8 day cutoff for significant tidal interactions.

The approximate theoretical expressions for the synchronisation and circularisation times given by Zahn (1977, reproduced in App.K, Eqns. K1 and K2) predict a synchronisation time of 71 Myr and a circularisation time of longer than 100 Gyr. Thus the the theory is consistent with observation for circularisation but it is unclear whether it is consistent for synchronisation.

9.12 Age and rough metallicity estimate (Analysis by *modelplot*)

9.12.1 Description of software

An attempt was made to determine the age of the V1094 Tau system by means of the *modelplot* program of Southworth, (private communication). This program contains a library of several recent stellar evolution models, with grids of the parameters *X,Y,Z* (abundances respectively of hydrogen, helium and all other elements) and age. The software requires as input a) a specified model with one of the available set of abundances, b) a trial value of the age and c) the values of the masses, radii, $log\ T_{eff}$ and *log g* value of each member of a binary, and then interpolates for the input values between the grid values. There is an option to use models which include convection overshooting. The software generates two isochrone plots; one is a plot of radius against mass and the other a plot of $log\ T_{eff}$ against mass. An example of a modelplot output is shown on Fig. 9.14. On

each plot the input values of mass and radius/(log T_{eff}) with their uncertainties are shown as crossed error bars, one pair for each member of the binary.

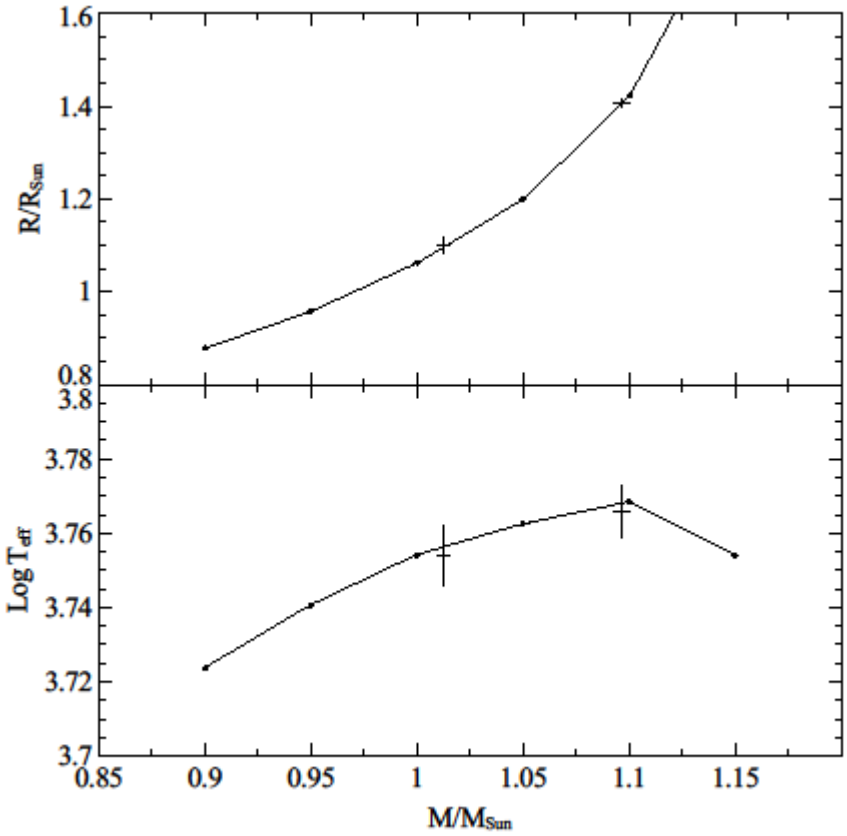

Fig.9.14 Example of (graphical) output from *modelplot* software.

9.12.2 Estimate of age

The software was run for the definitive values stellar masses and radii, and for a series of likely ages for all suitable stellar models with $0.01 \leq Z \leq 0.03$. An analytical criterion was implemented to assess how closely an isochrone fits the input data points. This is to measure the vertical distance between the isochrones and the four data points in units of the half-height of the error bar, sum the squares of the distances and take the

square root. The cases for which this yielded a sum of below 2 are listed in Table 9.20, where the sum is labelled "Goodness of fit". The best fits correspond to a *Z* value in the region 0.02 – 0.025. The age obtained by weighting the listed values by the goodness of fit parameter is about 6.87 Gyr with a standard deviation of 0.15 Gyr. This result agrees with the approximation (Binney and Merrifield, 1998, Eqn. 5.6) that the lifetime τ_{ms} which a star spends on the Main Sequence is

$$\tau_{ms} = 10 \times \frac{M}{M_{\odot}} . \frac{L_{\odot}}{L} \; Gyr \qquad 9.35$$

With the definitive values in Table 9.17, this expression gives τ_{ms} = 5.3 Gyr for the primary and 9.0 Gyr for the secondary. Thus for a system age of ~ 6.9 Gyr it can be expected that the primary is somewhat evolved, but the secondary is not. This agrees well with the stellar radii determined here.

Table 9.20 Best isochrone fits to calculated masses, radii and *Log* T_{eff} values.

Model	X	Y	Z	Age Myr	Goodness of fit (see text)
Yonsei-Yale 2004	0.7	0.28	0.02	6670	0.5
Dartmouth 2008	0.688	0.2864	0.0256	7030	0.7
Cambridge 2000	0.7	0.28	0.02	6670	1.2
Granada 2007	0.7	0.28	0.02	7300	1.4
Cambridge 2000	0.69	0.28	0.03	7350	1.5
Padova 2000	0.708	0.273	0.019	6200	1.9

References:

Cambridge 2000 Pols, O.R. et al., Mon.Not. Roy. Astr. Soc., 298, 525-536 (1998).

Dartmouth 2008 Dotter, A. et al., Astrophys. J. Supp. Ser., 178, Issue 1, 89-101 (2008).

Granada 2007 Claret, A., Astron. and Astrophys., 467, 1389-1396, (2007).

Padova 2000 Girardi, L. et al., Astron. and Astrophys. Supp., 141, 371-383, (2000).

Yonsei-Yale 2004 Demarque, P. et al., Astrophys. J. Supp. Ser., 155, Issue 2, 667-674, (2004).

9.12.3 Rough estimate of metallicity

The *modelplot* software was also used in an attempt to obtain a second estimate of the metallicity. The principle is to plot the best fits from all the available models in the form of age versus metallicity and look for the metallicity which yields the most consistent age. The phrase “all available models” means those listed in Table 9.20 and those of VandenBerg et al. (2006).

The results are shown in Fig.9.15. The procedure is as follows. The available models between them cover a series of values of *Z*, although not all the models are available for any one value. For each value of *Z*, Fig. 9.15 shows the best fit ages from all the available models, where each model provides four fits, derived from the radius and T_{eff} value of the primary and secondary. The results for the best fits to radius and T_{eff} are shown in black and blue respectively, and results for the primary and secondary stars as full and hollow circles. In some cases the models are not listed in Table 9.20 because the goodness of fit parameter in the last column exceeds 2. The value of *Z* is taken as that where the fitted ages are most consistent.

It will be seen that this approach suggests a value for *Z* in the region 0.025 to 0.030. By assuming the frequently adopted value of $Z = 0.018$ for the Sun, this is equivalent to $[Fe/H] \cong 0.18 \pm 0.04$. There is a clear discrepancy between this and the value $[Fe/H] = -0.088 \pm 0.024$ (rand) $\pm$ 0.06 (syst) derived from the differential Strömgren indices. The reason for this is unknown. The author has judged that the Strömgren value is linked more directly to observation and has adopted it throughout this thesis.

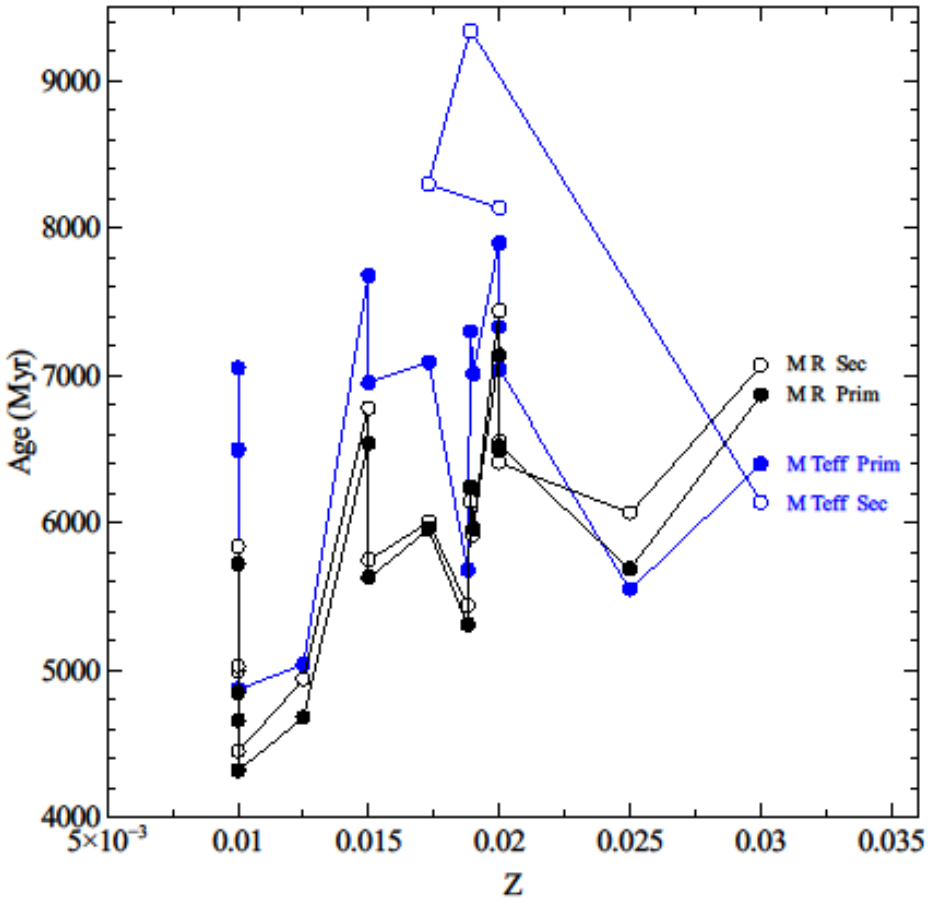

Fig. 9.15 Best fits for ages for all available stellar models, plotted against metallicity.

9.13 Kinematics

Since the distance, systemic velocity and proper motion are all known, it is of interest to calculate the galactic kinematic parameters as was done in Part I.

9.13.1 Galactic coordinates and kinematics

The celestial coordinates correspond to the galactic coordinates e.g. Zacharias et al. (2004)

Longitude (deg)	172.64716
Latitude (deg)	-21.00619
Position (X,Y,Z) (pc)	(-113, 15, -27) ± (3,1,1)

The galactic velocity components are:

Velocity $(U,V,W)_{LSR}$ (km s^{-1})	CFA:(-3.6, -64.7, 9.4) ± (0.2, 1.3, 0.3)
	GB: (-4.7, -64.6, 9.0) ± (0.2, 1.3, 0.3)
	INT (-0.4, -65.1,10.7) ± (0.3, 1.3, 0.3)

Velocities are given for the three sets of spectroscopic data separately since a different systemic velocity was derived for each run.

The notation (a,b,c) ± (d,e,f) is shorthand for a ± d, b ± e and c ± f.

The values of the derived kinematic parameter Z_{max} (Sect. 4.1) derived for each set of spectroscopic observations are:

Observations	Z_{max} (pc)
CFA:	105.3 ± 3.1
GB:	101.0 ± 3.2
INT:	118.9 ± 3.2

Thus V1094 Tau lies near the Galactic anti-centre, which is in the neighbouring constellation of Auriga. The difference noted earlier between the derived orbital elements for the INT observations and the other two sets feeds through into the value of Z_{max}.

9.13.2 Implications for stellar parameters

The position of V1094 Tau with respect to the Galactic Plane does not lead to any conclusion about age and metallicity.

Age: Part I of this thesis showed the density profiles of a series of age groups with respect to the Galactic coordinate *Z* (Fig. 4.4). It will be seen that the value *mod(Z)* = 10 pc derived above is consistent with any age.

*Metallicity***:** According to Table 4 of Bilir et al. (2012), the average vertical metallicity gradient for stars in the thin disk is -0.109±0.008 dex/kpc. Thus any variation over 0.010 kpc will be completely masked by variations between stars and experimental uncertainties.

9.13.3 Plot of Galactic orbit

The software of Aarseth used in Part I allows the orbit of V1094 Tau around the Galaxy to be plotted. This is shown in Fig.9.16 for the XY plane in absolute galactic coordinates and the kinematic parameters derived from the GB observations. The author generated this figure from the output of the Aarseth software by means of the *Veusz* graphical output program. It shows the next five orbits around the Galactic centre, with each orbital period assumed to be 230 Myr. The time interval between each point is about 9 Myr, except for about 1.5 Myr between the first two points. Since the Sun is assumed to be at a position (*X*,*Y*,*Z*) = (8, 0, +0.017) kpc in the absolute galactic frame the heliocentric galactic coordinates given above become *X* = 8.113 kpc, *Y* = 0.015 kpc, *Z* = -0.010 kpc in this frame (the Z coordinate cannot be shown).

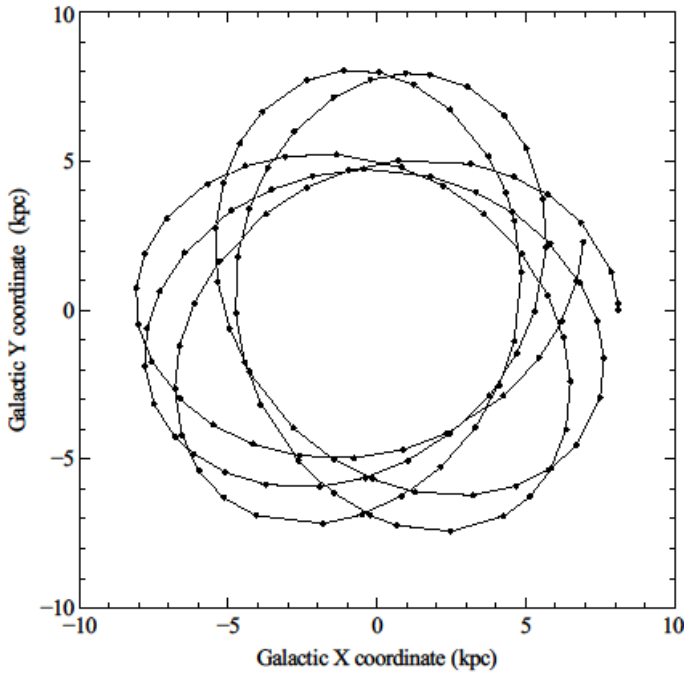

Fig. 9.16 Plot of the galactic orbit of V1094 Tau in the XY galactic plane.

CHAPTER 10 DISCUSSION AND CONCLUSIONS

10.1 Summary and discussion of stellar properties

The V1094 Tau binary consists of solar type stars. The primary has a mass of about $1.10M_{\odot}$ and a radius of $1.41R_{\odot}$ and so according to the mass/radius relation discussed earlier is somewhat evolved. The secondary has a mass and radius very similar to our own Sun, with values $1.01M_{\odot}$ and $1.10R_{\odot}$. If we assume an age of 7 Gyr, the stars are about 2 to 3 Gyr older than the Sun. The metallicity is uncertain but is broadly similar, probably within 0.2 dex, to that of the Sun.

This work has determined the masses and radii of the V1094 Tau components to an accuracy better than for most of the dEB's listed in Tables 6.1a and 6.1b. This has been done for a binary which lies in an important gap in a map of tidal interactions against a mass/radius/metallicity grid.

Table 10.1 below shows the measured radii of the two stars and also what the radii would be if they followed the relation $R \propto M^{0.8}$.

Table 10.1 Observed radii and predicted values from the $R \propto M^{0.8}$ relation.

Star	Mass	Observed radius	Radius predicted from $R \propto M^{0.8}$
Primary	1.0969(37)	1.406(10)	1.0768(30)
Secondary	1.0127(27)	1.099(10)	1.0101(22)

Thus the primary does appear to be somewhat evolved. The secondary is slightly larger than predicted by the $R \propto M^{0.8}$ relation but this may be of little significance since this relation is only an approximation.

10.2 Recommendations for future work on V1094 Tau

Our understanding of the V1094 Tau system is still not complete. A major uncertainty is the metallicity. The method based on the Strömgren colour indices could be applied only to the system treated as a single star (Sect. 9.8) and an estimate based on stellar modelling showed a substantial discrepancy with this. In order to realise the full potential of the V1094 Tau binary further spectroscopic analysis is needed. These should be with high resolution, good wavelength coverage, high signal to noise ratio and good phase coverage. A detailed analysis of the spectrum by spectral intensities or disentangling will provide robust values for T_{eff}, a direct measurement of *[Fe/H]* and a rotational velocity sufficiently accurate to assess to what extent rotation is synchronised with the orbital period. It is unclear whether the FOCES spectra (Sect. 8.3.1) will be suitable for this. Further consideration of this point was judged to be outside the scope of this thesis; the author's brief experience with these spectra during his project suggests that a proper assessment and analysis of these spectra would be a major task. A drawback of the FOCES spectra is that they cover just five days and hence only a fraction 0.56 of a cycle, and this is too short a period to apply the spectral disentangling method (Maxted and Pavlovski, private communication). Thus the application of this particular method requires further high quality spectra.

It was not possible to answer conclusively the question of how significant is the tidal synchronisation. Theoretical analysis predicts that rotational periods should be synchronised; observations indicates that they are on the border of being so. It also predicts that the orbits should not be circularised, as of course is the case. A complete investigation of the degree to which tidal interactions are significant requires two advances. First, the uncertainty on the rotational velocities should be narrowed if possible. The value available

here for the rotational velocity of the V1094 Tau secondary is $v \sin i = 4.4 \pm 2.0$ km s^{-1} (Sect. 9.10) i.e. an uncertainty of about ±45%. Secondly, theoretical results similar to Fig. K1 in Appendix K should be available for i) the evolution of the eccentricity, and ii) for the orbital and rotational periods, for a grid of the two stellar masses and periods on the main sequence. At present they are available for only two representative values. This would require a long and extensive theoretical programme.

10.3 Impact of future missions on studies of dEBs in general

The study of dEB's will be transformed in the near future by four major new projects: *Gaia*, LSST, TESS and PLATO. These are briefly described below and their impact on the study of dEB's discussed.

10.3.1 Description of missions

Gaia

The *Gaia* mission (www.sci.esa.int/gaia/) is an ESA satellite launched on 19 December 2013 and is positioned at the L2 Lagrangian point 1.5 million kilometres from the Earth away from the Sun. The main aim is precision astrometry and the mission is also capable of photometry and spectroscopy. The satellite is built on a 3 metre base on which is mounted an astrometric instrument, a photometer and radial velocity spectrometer. It has a projected 5 year lifetime and is expected to survey all the stars between magnitude 6 and 20 in our Galaxy, 1 billion in number.

The effect which the *Gaia* mission will have on the study of dEB's has been discussed by Eyer et al. (2011). The photometer is expected to observe an object 280 times (Eyer et al.) in the band 320 – 1000 nm (www.sci.esa.int/gaia/40129-payload-module). The spectrometer obtains high resolution spectra in the range 847-874 nm and is able to measure R.V's for stars down to magnitude V=17 to an accuracy to 1 to 10 km s^{-1}

depending on the spectral type of the star. The spectral resolution $\lambda/\Delta\lambda$ is 11,500. It will observe each star 40 times. Munari (2001) has estimated that *Gaia* will observe about 100 000 double-lined eclipsing binaries (binaries where spectra are observed from both stars).

LSST

The LSST (Large Synoptic Survey Telescope, www.lsst.org/lsst/news and faq) project is a ground based 8.36 metre (6.5 metre effective) survey reflecting telescope which is planned to be built in northern Chile. It has an exceptionally wide field of view of diameter 3.5 degrees. It will survey the sky in the declination range $\delta < +34.5°$ and it is intended that 90% of the observing time will be allocated to a survey mode in which each field of view within a total area of 20 000 deg^2 will be observed 1000 times. The LSST will observe in the six Sloan bands which between them provide an almost complete spectral coverage between 320 and 1040 nm; their profiles are shown in Fig.3 of Ivezic et al. (2008). There do not appear to be any plans to mount a high resolution spectrometer on the LSST, and so no radial velocity measurements are foreseen. Prša et al. (2011) estimate that the LSST will be able to observe about 2 billion stars down to a Sloan *r* magnitude of 22.5, and have estimated the number of eclipsing binary stars which the LSST will observe. By synthesizing a wide representative range of synthetic light curves and combining this with the expected performance, they estimate that the LSST will provide about 1.7 million eclipsing binary curves with a signal-to-noise ratio ≥ 10 ready for detailed modelling. According to the LSST public website construction was planned to start on 1 July 2014 and that the scientific first light will be observed in 2021.

TESS

TESS (The Transiting Exoplanet Survey Satellite, www.tess.gsfd.nasa.gov) is a space-borne mission selected by NASA in 2013 with a projected launch date in August

2017 and will be positioned in a high Earth orbit. It is intended as a successor to *Kepler*, but in contrast to that mission it is intended to survey the whole sky and is planned to survey 500 000 host stars with the aim of discovering small planets around bright stars. Bright stars are chosen as they will be easier targets for follow-up observations. Two future large telescopes which could be used for these are i). the space borne 6.5 metre James Webb Space Telescope (JWST) (www.stsci.edu/jwst/) to be launched later in this decade and ii) the ground based 40 metre European Extremely Large Telescope (E-ELT) in Chile (www.eso.org/sci/facilities/eelt) for which on site work began in March 2014 and which will start operating in 2024. TESS is expected to catalogue 3000 transiting exoplanet candidates in a radius range between 0.8 to 20 Earth radii (Website ref.list). The instrument payload will consist of 4 wide view CCD cameras, each with a 24° × 24° field of view and a 100 mm pupil diameter in a 600 to 1000 nm band pass.

PLATO

PLATO is a space-borne mission selected by ESA for launch in the period 2022-24, and has been described in detail by Rauer et al. (2013). It will, like *Gaia*, be positioned at the L2 Lagrangian point and will consist of 34 small telescopes each with aperture of 12 cm and a combined wide field of view of 2232 deg^2. It is planned to survey 1 000 000 bright stars in the magnitude range 4 to 11. Suitable targets will then be subjects for follow-up observations. Stellar masses and ages will be obtained by astroseiemology (by studying short period periodic oscillations in the stellar brightness), and stellar radii will be available from the *Gaia* and LSST missions as explained later. PLATO will generate 1000 000 high quality light curves and is expected to increase significantly the number of known binaries (Rauer et al., Sect. 4.7) but no more precise estimate is available.

10.3.2 Comparison of mission specifications

The capabilities of these four missions are compared in Table 10.2.

Table 10.2 Comparison of specifications for future major missions relevant to eclipsing binaries.

	Gaia	LSST	TESS	PLATO
Location	L2 point	Ground	High Earth orbit	L2 point
No. of stars observed	10^9	2×10^9	500 000	1 000 000
No. of dEB's observed	100 000	1 700 000	No estimate	Significantly above 100.
Photometer?	Yes	Yes	Yes	Yes
No. of photometric observations of each object	280	1000	N/K	N/K
Spectrometer?	Yes	No	No	No
No. of R.V observations of each object	40	-	-	-
Accuracy of R.V determinations (km/s)	1 to 10.	-	-	-

N/K means Not Known.

10.3.3 Impact on future missions on the field of dEB studies

It will be seen that these future missions will provide a huge increase in the number of known dEBs. The impact which this will have on the field of EB research can be assessed by recalling the requirements for a complete accurate analysis of an EB. These are a radial velocity curve with preferably 30 or more data points reasonably evenly spaced through an orbit and a photometric light curve with several thousand points. A criterion for selecting a target dEB for the observing run described in Part III is that a light curve with at least 5000 points be available.

Table 10.2 shows that the *Gaia* mission is the only one of these four missions which carries a spectrometer. Inspection of the number of observations of a binary by the *Gaia* spectrometer and the LSST photometer shows that the two missions between them could provide solutions for up to 100 000 dEB's. Two qualifications need to be considered. First, the R.V's determined by *Gaia* are accurate to only 1 to 10 km/s, whereas in recent literature studies (e.g. Griffin and Boffin, 2003; Clausen et al., 2009; Southworth et al. 2011) radial velocities are routinely determined to an uncertainty of typically 0.5 to 1.0 km/s. Secondly although the LSST will provide 1000 photometric data points per binary (more than the 280 from *Gaia*), this is still less than for some ground based surveys. (In a survey of 140 SuperWASP light curves described in Sect. 11.2.2, the average number of points per curve is about 13 700 plus or minus several thousand, (although some curves with less than 1000 data points had already been removed from this sample). The first point was assessed by taking the R.V. data set of Griffin and Boffin used earlier and perturbing each velocity in a manner analogous to that used for the calculation of T_{eff} and *[Fe/H]* from colour indices as described in Sect. 9.8.1. Each radial velocity was assumed to have a nominal uncertainty of 3 km s^{-1} (an approximate geometrical mean of the 1 to 10 km s^{-1} error bars quoted above), the perturbations were allowed to extend to three times this value, and each radial velocity was weighted by $exp(-((perturbation)^2/2))$. These perturbed velocities were used as input to SBOP. The results for the "projected" stellar masses $M \sin^3 i$ obtained for each case are shown in Table 10.3.

Table 10.3 Effect on derived masses of randomly perturbing radial velocity data.

	R.V. data set	
	Unperturbed	Perturbed
$M_1 \sin^3 i \ /M_\odot$	1.095 ± 0.005	1.071 ± 0.020
$M_2 \sin^3 i \ /M_\odot$	1.008 ± 0.004	0.978 ± 0.019

This pilot calculation indicates that the larger uncertainties in the R.V's measured by the *Gaia* spectrometer do translate into wider error bars on the derived projected masses. Nevertheless, the masses are still sufficiently accurate to determine whether the stars are Main Sequence, slightly or strongly evolved. This is essential for proposals to study some given system in detail. It is uncertain what will be the effect of the fewer number of photometric data points.

The detailed study of V1094 Tau described here accounted for a substantial fraction of a Ph. D project. Some reasons for this are that the author had to fit every radial velocity measurement from the INT measurements individually and set up each stage of the JKTEBOP analysis manually, and the time required to analyse some tens of thousands of binaries in the same way is prohibitive. There is therefore an urgent need to develop an integrated and automated software suite which accepts as input data a set of radial velocities and a light curve, and returns a complete set of stellar parameters similar to the *jktabsdim* output reported here.

There will still be a need for precision follow-up measurements with terrestrial telescopes. This is because the *Gaia*/LSST data will not be sufficiently accurate to test the theory of the tidal interactions which could introduce uncertainties in applying dEB data to test stellar evolution theories for single stars. The $\lambda/\Delta\lambda$ = 11 500 spectral resolution available with the *Gaia* spectrometer is only slightly finer than the 8 500 available from the SpCCD spectrograph system used for the observations reported in Part III. As described there, this was only just sufficient to measure rotational velocities with a wide error margin for only one of the binaries observed.

10.4. Relevance of future missions to V1094 Tau

The relevance of these projects to V1094 Tau will be discussed by mission.

Gaia

The *Gaia* mission should provide a much more accurate distance but may not provide significant amounts of good radial velocity data.

Distance. The distance of V1094Tau as derived in Sect. 9.9 is 120.8 ± 2.2 pc i.e a parallax of 8.28 ± 0.15 mas. Eyer et al. (2011, Fig.1) show that for a Sloan magnitude r = 12 the uncertainty in the parallax of a target star is 10 μas and that this uncertainty narrows for brighter target stars. If this accuracy can be obtained for V1094 Tau with magnitude V(NOMAD) ~ 8.98, the uncertainty in the distance will be narrowed by over an order of magnitude.

Radial velocities. The r.m.s radial velocity residuals from the CfA, GB and INT observations (Table 9.4) are all much smaller than the 1 to 10 km s^{-1} accuracy expected from *Gaia*. Thus if *Gaia* observes V1094 Tau and obtains the 40 expected spectra, it is at least uncertain whether this will provide more accurate values of the orbital elements.

LSST

The LSST is expected to observe down to a Sloan magnitude r = 22. Since the V-band magnitude of V1094 Tau is 8.98 it may be expected at first sight that the LSST could observe this system with a much higher signal to noise ratio and hence improvement in the accuracy of stellar parameters. However the author understands (Maxted, private communication) that the photoelectric detectors on the LSST would saturate for magnitudes brighter than 15; hence the LSST cannot be used to study V1094 Tau.

PART III. OBSERVATIONS OF SELECTED ECLIPSING BINARIES AT SAAO SUTHERLAND

CHAPTER 11 INTRODUCTION, PREPARATION, INSTRUMENTATION AND DATA REDUCTION

11.1 Introduction

In Part II, Chapter 6 it was explained why it is particularly important to study detached eclipsing binaries (dEB's) with orbital periods of about 8 days, and later chapters described a detailed study of one such dEB. It also explained the need for a detailed map of tidal interactions within dEB's in this period range, which is necessary to produce a map of the mass/radius/metallicity relation for low mass stars. This Part describes the initial steps of a programme intended to survey more dEB's in this period range with the ultimate aim of choosing binaries for detailed follow-up observations. One week was awarded for this on the 1.94 metre Radcliffe telescope at the South African Astronomical Observatory (SAAO) at Sutherland for the seven nights 20 to 27 July 2011. Unfortunately the run was curtailed by bad weather and instrumental limitations, and observing was possible only for the first three nights. Nevertheless it was possible to identify two eclipsing binaries which merit further observations. Preliminary values of the masses, radii and luminosity ratios were obtained from very limited observations.

The programme outlined above requires definitive data for stellar masses and radii to the 1% level, for orbital and rotational velocities, and for metallicities. The measurements must be made on a 3 to 4 metre class telescope because of the high signal to noise ratio required. They are costly and time consuming, so preliminary observations with smaller, typically 2 metre class, telescopes are needed to identify "good" dEB candidates for definitive measurements. "Good" here means that both stars are on the main sequence

and that other conditions explained later are met. This stage needs masses and radii accurate to 10% or better.

The SAAO run described here is intended as a contribution to such preliminary observations. The time on the Radcliffe telescope was awarded in response to a proposal under the names of the author, Dr. Maxted of Keele University; Dr. Chew of the Queen's University, Belfast; Prof. Pavlovski of the University of Zagreb, Croatia and Dr. Hebb of the Vanderbilt University.

The role of the author was to act as coordinator, receive input from the external collaborators, help write the proposal after an original draft by Maxted, submit it, and choose the targets. The observing run and the analysis of the data up to the generation of input files for the MOLLY software were carried out by Maxted and the author together. The preliminary analysis of potential targets before the run, and the analysis of MOLLY files after it were carried out mainly by the author.

11.2 Selection of targets for SAAO observations.

The selection of targets proceeded in two steps

- Searching data archives for eclipsing binaries where light curves are available.
- Sifting these light curves for those of sufficient quality.

11.2.1. Searching EB archives and catalogue

Suitable candidates for observations were drawn from the SuperWASP photometric database. This is a valuable resource for studying variable stars because it contains over 400 billion photometric measurements for 30 million stars obtained over several years. This archive was searched in two ways.

1. Maxted (private communication) inspected WASP lightcurves for objects flagged as ED (for Eclipsing Detached) in the ACVS (ASAS Catalogue of Variable Stars) section of the ASAS catalogue (Pojmanski, 1997 and www.astrouw.edu.pl/asas/) and with periods longer than 6 days. The criteria for a match were that:

- The object should be flagged in the ACVS as ED rather than ED/ESD (Eclipsing Semi_Detached)or ED/Misc.
- The position listed in the ACVS should be within 15 arc seconds of the SuperWASP position.
- The SuperWASP light curves should contain 1000 or more data points after filtering of obviously unsuitable data.

This led to 125 matches. The average number of points per light curve is 13700, but with wide variation in this number between curves. The author subsequently tightened the minimum number of data points to 5000.

2. Maxted (private communication) identified further potential dEBs by inspecting the WASP lightcurves of objects that had been rejected as exoplanet host stars. Objects with periodic lightcurve dips are identified by the WASP transit detection software. The lightcurves are inspected "by-eye" and categorised and flagged according to the appearance of the lightcurve and other criteria. One flag is "EB" for eclipsing binaries. Maxted examined some thousands of these flagged EB lightcurves and picked out 58 binaries with long periods (P>~ 8 days) and narrow eclipses.

These two searches identified 183 EB’s between them.

11.2.2 Sifting of photometric lightcurves

It is clear from the analysis of V1094 Tau that the SAAO observations should be made on binaries for which a good quality photometric light curve is available. The binaries should consist of solar type stars on the main sequence since it is for these stars that tidal interaction theory has been developed. The 183 EB light curves identified above were sifted for those which met the following criteria.

The stars should be sufficiently bright, specifically with a V-band magnitude below 11.5.

The light curves should have a sufficient number of data points, specifically 5000.

The light curves should show well marked dips and be reasonably free from noise.

The light curves should be flat between the dips. Curvature there shows that the stars are close together. This is because gravity from one star then distorts the other away from a spherical shape, hence the surface gravity and emergent flux vary over the surface. Further the surface heating which one star receives from the other also varies significantly over the surface. If the stars are close, the orbital period will be much shorter than the ~8 day cut-off of interest here and the system may even be a semi-detached or contact binary.

The light curves should be free from ripples. These are a sign of starspots which would introduce systematic errors in the derived radii (Morales et al. 2010).

The dips should sufficiently deep, so that the lightcurve solution by JKTEBOP is not strongly degenerate. The criterion for this was set at $\Delta M > 0.2$ for both dips

The dips and hence the luminosities of the two stars should be of comparable magnitude. Otherwise the two binary components are of widely differing spectral types whereas the purpose of this project is to investigate the simpler case of stars of comparable types. Further, the cross-correlation techniques used to measure the orbital and rotational velocities would be more difficult because one of the genuine peaks in the correlation profile could be confused with false peaks. A corollary of this is that neither dip should exceed a magnitude difference of $\Delta M > 1$.

The periods should broadly straddle the 8 day cut off for significant tidal interactions. A corollary of this is that the dips should be narrow.

In short, the light curves should have a similar appearance to those for V1094 Tau shown earlier (Fig. 9.5).

The binaries themselves should have a V-K colour index within the range 1.0 to 2.0 i.e. spectral type within the range F4 to K0. Since one justification for detailed study of EB's is the analysis of exoplanet systems the target stars should be in the same spectral type range as host stars for transiting exoplanets i.e. about F5 and later.

The targets should lie higher than 30° above the horizon. Since the SAAO is situated at latitude 32° 23′ South, this means that the targets should not lie further north than declination +28°.

This sifting left 25 dEB's, which are listed in Table 11.1 below. The first column in this Table assigns a reference number to each dEB. The binaries not listed by ASAS/ACVS are marked as "No" in the last column but one.

Light curves for these 25 dEB's are shown in Figs 11.1 for a phase range -0.2 to 1.2 where the label at the bottom right of each curve corresponds to the reference number in Table 11.1.

This thesis part uses the full SuperWASP designations 1SWASPJaaaaaa.bb±cccccc.d, where aaaaaa.bb and ±cccccc.d refer to the R.A. and declination respectively, and also the shortened designations where 1SWASPJaaaaaa.bb±cccccc.d is written as Jaaaa±cc.

Table 11.1 Sifted dEB's with periods longer than 6 days.

Ref. No.	Designation 1SWASPJ +	Period (days)	Mag. V	Mag. Prim.	Dips Sec.	V-K	No. points	ASAS?	Score
1	100832.74-351028.2	6.10387	10.18	0.65	0.64	1.14	19459		6.7
2	070513.83-512349.2	6.446809	10.77	0.41	0.38	1.15	17454		2.1
3	114358.40+095716.3	6.469231	10.93	0.47	0.47	1.35	12506		1.6
4	004032.41-062851.0	6.563875	10.59	0.31	0.26	1.29	9786		0[b]
5	222816.34+173602.4	6.564307	11.32	0.54	0.29	1.07	13418		0[b]
6	032858.40-421536.6	6.585975	10.4	0.49	0.34	1.61	8456		1.5
7	150448.31-432202.0	6.851387	10.62	0.5	0.35	1.33	7933		1.2
8	215442.98+041031.9	6.957664	10.85	0.38	0.36	1.67	26056		2.8
9	053113.65-270904.2	7.056852	10.67	0.5	0.42	1.38	15617		2.4
10	022947.74-131452.7	7.103556	8.62	0.23	0.22	1.41	9462		4.8
11	182718.45+190833.1	7.14594	11.49	0.49	0.47	1.49	6212		0[b]
12	050351.14-154153.9	7.279176	9.74	0.45	0.41	1.07	8810		3.0
13	162702.56+120010.8	7.395	10.99	0.33	0.28	1.23	15869		1.2
14	060349.10-313242.5	7.62	11	0.3	0.36	G9	25423	No	2.1
15	140807.34-393548.8	7.832634	10.73	0.72	0.63	1.62	33309		7.2
16	154951.82-232318.3	8.018836	11.01	0.53	0.38	1.83	14214		1.6
17	035346.64-360523.5	8.715623	11.03	0.38	0.33	1.22	9407		0.8
18	083149.82-152859.9	8.740733	11.19	0.62	0.47	1.31	10572		1.2
19	042724.11-275607.7	8.946519	9.89	0.26	0.21	1.17	16689		0.0[a]
20	143021.54-401704.5	9.376	9.9	0.35	0.28	F7	8376	No	1.8
21	070132.08-490747.8	9.886049	10.7	0.21	0.2	1.27	17464		1.2
22	223351.42-235152.8	10.35148	10.7	0.36	0.21	1.55	15507		1.5
23	124012.98-403639.9	12.1814	11.4	0.2	0.35	G8	14591	No	0.7
24	132716.78-324400.7	19.75765	8.83	0.49	0.33	1.10	11766		0[b]
25	062926.36-251329.5	26.38218	11.43	0.58	0.51	1.35	17032		0.4

Note a) - Already studied (Sect. 11.2.3).

Note b) - Light curve minima too noisy (Sect. 11.2.4).

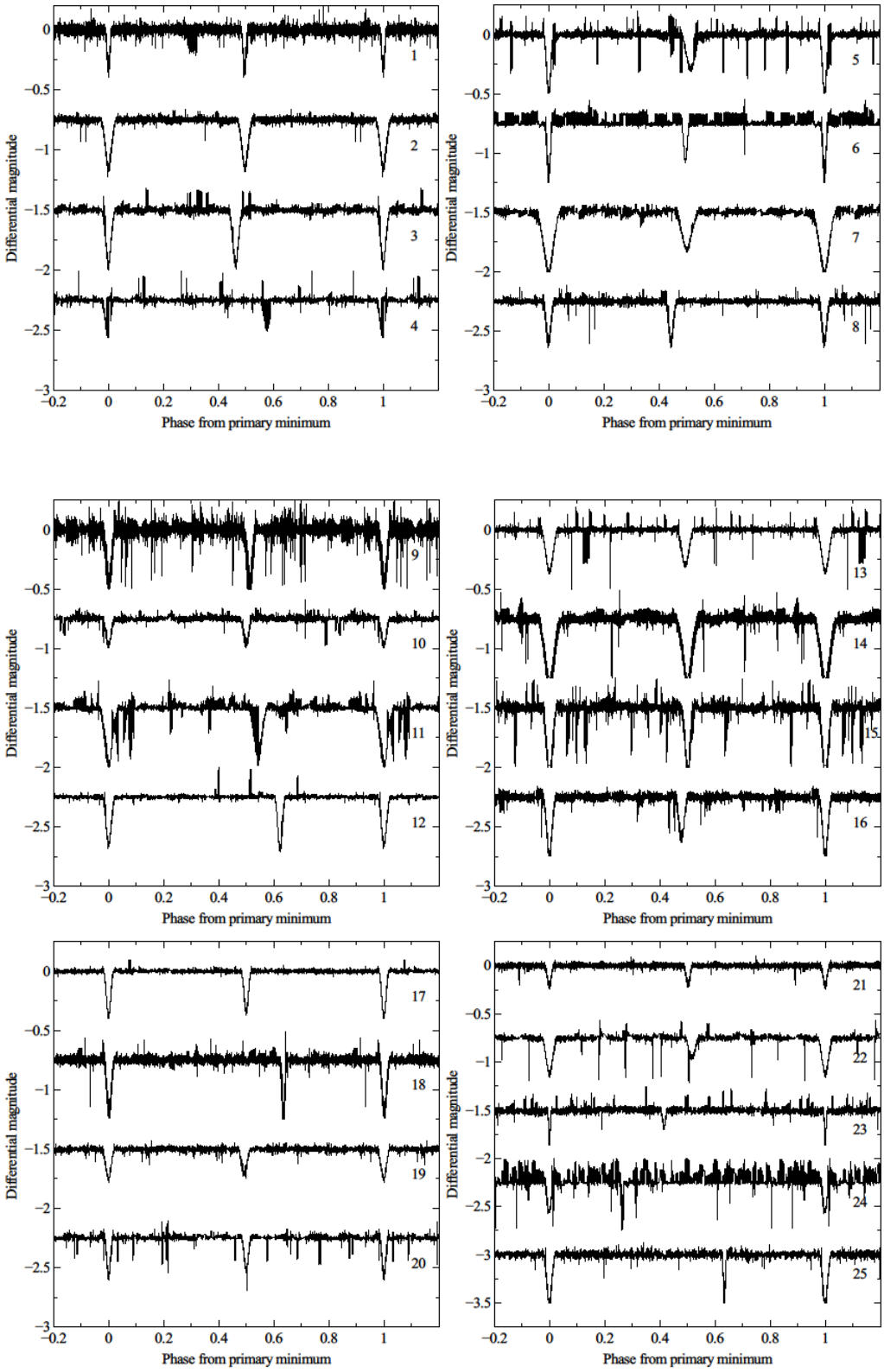

Fig. 11.1 Light curves for sifted dEB's with periods longer than 6 days. The curves are separated by 0.75 magnitudes for clarity. Each curve is labelled by the reference number in Table 11.1.

11.2.3 Previous observations of targets.

All these potential targets were queried by SIMBAD to check whether any previous observations have been made. This revealed that one of them, 1SWASPJ042724.11 -275607.7 – Ref. No. 19, has already been studied by Helminiak et al. (2009) by an approach similar to that which was intended here; in fact their Table 1 shows that these authors studied two objects by the Radcliffe/GIRAFFE instrumentation originally proposed for the present work (Sect. 11.5). Most of the other potential targets are listed in major catalogues; the details appear in Table 11.2 below. The references to the catalogues shown there are as follows.

Key to catalogue references

Catalogue		Reference	VizieR Catalogue reference
HD	Henry Draper Catalogue	Cannon and Pickering (1918 – 1924)	III/135A
BD	Bonner Durchmusterung	Argelander (1903)	I/122
NOMAD		Zacharias et al. (2004)	I/297
2 MASS		Cutri et al. (2003)	II/246
RAVE		Kordopatis et al. (2013)	III/272

Table 11.2 Previous catalogue entries and study of potential dEB targets

Ref No.	Designation	HD	BD	NOMAD	2MASS	RAVE	Other
	1SWASPJ+						
1	100832.74 -351028.2	88078		✓	✓		IBVS 5542, Note a)
2	070513.83 -512349.2			✓	✓		
3	114358.40 +095716.3			✓	✓		
4	004032.41 -062851.0		-07 99	✓	✓	✓	
5	222816.34 +173602.4			✓	✓		
6	032858.40 -421536.6			✓	✓		
7	150448.31 -432202.0			✓	✓		
8	215442.98 +041031.9			✓	✓		
9	053113.65 -270904.1			✓	✓		
10	022947.74 -131452.7	15554	-13 462	✓	✓		HIP 11614
11	182718.45 +190833.1	348698		✓	✓		IBVS 5570, Note a)
12	050351.14 -154153.9	32615	-15 933	✓	✓	✓	
13	162702.56 +120010.8			✓			
14	060349.10 -313242.5						Not listed in SIMBAD.
15	140807.34 -393548.8			✓	✓		
16	154951.82 -232318.3			✓	✓.		
17	035346.64 -360523.5			✓	✓	✓	
18	083149.82 -152859.9			✓	✓		
19	042724.11 -275607.7						Studied by Helminiak et al. (2009).
20	143021.54 -401704.5	127081		✓	✓	✓	
21	070132.08 -490747.8			✓			
22	223351.42 -235152.8			✓	✓		
23	124012.98 -403639.9			✓			
24	132716.78 -324400.7	116921		✓	✓	✓	
25	062926.36 -251329.5			✓	✓		

Note a) The IBVS bulletins for dEB's reference numbers 1 and 11 give just a period or updated period and magnitude range.

11.2.4 Drawing up of target list

The observing run was carried out in late July when the Sun was at R.A. 8 hours to 8 hours 30, and hence objects with R.A. between about 5 and 12 hours were in daylight. Thus the binaries 1,2,3,9,12,14,18,21 and 25 in Table 11.1 could not be observed. The Table shows that this restriction unfortunately excluded many of the dEB's with the strongest dips in the light curves. Binaries within an hour of R.A on either side of this range were checked that they remained more than 30° above the horizon for at least two hours of astronomical darkness. This was done by means of the INT STARALT website (www.catserver.ing.iac.es/staralt/index.php). The Moon entered its Last Quarter on 2011 July 23 and so was above the horizon towards dawn during the run, but moonlight was not a serious problem.

After these exclusions, there are 16 binaries suitable for observation. This was sufficient for a one week observing run. This follows because each dEB needed a bare minimum of two exposures (to determine radial velocities), each exposure needed 30 minutes, and telescope operating procedures needed significantly more time. A longer run would need more targets; one problem for observing suitable targets at Sutherland is that SuperWASP and other transit surveys do not observe close to the galactic plane (Sect. 3.3.1), but this plane is overhead at Sutherland for much of the year; thus potential targets tend to lie at lower altitudes above the horizon.

The JKTEBOP light curves shown in Fig. 11.1 were examined to check whether the minima themselves (as distinct from the periods between the minima) were reasonably free from noise. It was judged by eye that the minima for the dEB's with reference numbers 4,5,11 and 24 were too noisy to be analysed. They were therefore not considered further. (With his present experience of handling light curves the author would have eliminated these systems at the stage listed at the start of Sect. 11.2.2)

An attempt was made to prioritise these remaining 16 binaries. Each binary was assigned a score where possible given by the product of brightness, depth of dip and number of data points. The score was defined according to the expression

$$\text{Score} = 100 \times 10^{(12-V)} \times (\text{Average magnitude of dip}) \times (\text{Number of data points}/10000) \times \text{Function of period (see text below)} \quad 11.1$$

Here the "V" in the (12-V) term is the V-band magnitude.

For the binaries which do not appear in the ASAS/ACVS catalogue, the number of data points was taken from the SuperWASP archives. The last term was included because binaries with periods further away from the 8 day cutoff are assumed to be of less interest for the present project. The semi-arbitrary values assumed for this function were Period 6 to 10 days – 1; 10 to 16 days – 0.5 and over 16 days - 0.25. The powers of ten in Eqn. 11.1 were included to keep the result in a convenient numerical range. The scores so derived appear in the last column of Table 11.1.

The remaining binaries in order of priority score can therefore be listed as in Table 11.3

Table 11.3 List of dEB targets in order of priority score

Priority No.	1	2	3	4	5	6	7	8	9	10	11
Reference No.	15	10	8	20	16	6	22	13	7	17	23

The next step was to draw up an observing schedule. The requirement is that a binary should be observed broadly around the time when the radial velocities of each star differ the most i.e. for circular orbits at phase 0.25 and 0.75. If the binary is observed close to an eclipse the radial velocities are similar and the cross-correlation peaks cannot be resolved; this was the reason why radial velocities could not be obtained for some of the INT spectra (Sect. 8.3). The appropriate observing times were calculated from the period and times of minima.

11.2.5 Preparatory analysis

The aim of this observing run requires that the binary components should be solar-type stars on the Main Sequence. An attempt was made to make preliminary estimates of the mass and radius by a method which combines analysis by JKTEBOP with theoretical isochrones. The light curves from the SuperWASP archives can be analysed by JKTEBOP to obtain the ratios of the radii and of the luminosities. Theoretical isochrones lead to theoretical radii and luminosities for a trial input mass and age. Thus the isochrones for a pair of trial masses lead to corresponding trial ratios of radii and luminosities. Matching these to the JKTEBOP results leads to estimates of the masses and radii, and in principle also for ages.

Isochrones can be obtained from e.g. the Dartmouth Stellar Evolution Database (www.adsabs.harvard.edu/abs/2008ApJS..178...89D). For a given age and series of masses, these give values of T_{eff}, surface gravity ($log\ g$), absolute magnitudes and luminosities in the standard spectral bands. Radii can be obtained from the isochrones from the definition of $log\ g$ i.e.,

$$log\ g = log\ g_{\odot} + log(M/M_{\odot}) - 2 \times log(R/R_{\odot}) \qquad 11.2a$$

Since $log\ g_{\odot} = 4.438307$

$$log\ (R/R_{\odot}) = (log(M/M_{\odot}) - log\ g)/2 - 2.119154 \qquad 11.2b$$

The luminosities can be obtained directly from the isochrones.

Thus in principle it is possible to take a pair of masses for which isochrones are available and calculate a series of ratios of radii and luminosities. These theoretical series can be matched with the mass and luminosity ratio calculated by JKTEBOP. Unfortunately the error bars on the luminosities were so wide that this method was impractical.

11.3 Aims of telescope run

The aims of the telescope run can now be stated as follows.

1. Obtain enough radial velocity measurements of a binary to define a radial velocity curve and hence use SBOP (cf. Sect. 9.4.2) to determine the true or projected orbital elements, depending on the parameter.

2. Measure the luminosity ratio of the binary. This is necessary to a) confirm that both stars in the binary are on the Main Sequence and have not evolved and b) to break the degeneracy between the radius ratio and luminosity ratio returned by JKTEBOP (Sect. 9.6.4).

3. Attempt to measure the rotational period for longer periods and so assess the degree of synchronism between the rotational and orbital periods.

It will be seen from the next section that these aims could only be partially realised.

11.4. Summary of observations

Table 11.4 lists all the exposures of the target stars which had adequate intensity and were free of obvious contamination. They comprise 18 exposures for 9 EB systems.

In this table the listed times are SAST (South African Standard Time), two hours ahead of UT, and refer to the middle of the exposures, all of which were for 30 minutes except for 1SWASPJ042235.22-412900.1 at 6.40 SAST on July 21, which was for 15 minutes. The exposure time of 30 minutes was a compromise between a) being as long as

Table 11.4 List of satisfactory exposures.

Object 1SWASPJ +	Short designation	Ref. No.	Priority number	Date and time (SAST)	Phase
143021.54-401704.5	J1430-40	20	4	Jul. 20 23.59	0.476
213846.63-685150.0	J2138-68	None	None	Jul. 21 1.13	0.772
				Jul. 21 3.21	0.773
022947.74-131452.7	J0229-13	10	2	Jul. 21 4.28	0.915
				Jul. 21 5.02	0.915
035346.64-360523.5	J0353-36	17	10	Jul. 21 5.57	0.427
042235.22-412900.1	J0422-41	None	None	Jul. 21 6.40	0.101
154951.82-232318.3	J1549-23	16	5	Jul. 21 23.55	0.102
				Jul. 22 0.28	0.102
213846.63-685150.0	J2138-68	None	None	Jul. 22 1.41	0.786
				Jul. 22 2.20	0.786
				Jul. 22 3.01	0.786
223351.42-235152.8	J2233-23	22	7	Jul. 22 4.31	0.177
022947.74-131452.7	J0229-13	10	2	Jul. 22 6.17	0.066
132716.78-324400.7	J1327-32	24	None	Jul. 22 20.07	0.168
143021.54-401704.5	J1430-40	20	4	Jul. 22 21.06	0.676
222658.71-172528.1	J2226-17	None	None	Jul. 23 1.13	0.160
223351.42-235152.8	J2233-23	22	7	Jul. 23 4.15	0.273

possible to obtain a good signal to noise ratio and b) needing to observe as many targets as possible in the allotted telescope run of 7 days. Order of magnitude estimates show that for a 30 minute exposure the smearing of the radial velocity due to the change of phase during the exposure will still be less than the typically 2 km/sec uncertainty in radial velocity determinations (Maxted et al., 2001, Sect. 3.2).

The binaries observed are numbers 2, 4, 5, 7 and 10 in the priority list and other binaries requested by collaborators. Departures from the priority list were caused by observational constraints. The extreme long period 73 day EB 1SWASPJ213846.63-

685150.0 was included in the observing programme because it is intended to combine these observations with future ones as part of an overall program. For this object, one week is too short a fraction of an orbital period to provide a proper analysis. The combined observations will provide a limiting long period case. The binary J1327-32 was observed before it was realised that the minima of the light curve are noisy. A further consequence of the curtailed run is that no EB could be observed more than thrice, whereas ideally at least 6 to 8 observations should be made spread through an orbital period to define accurately the orbital elements i.e. semi-amplitudes of the radial velocities, and eccentricities of the elliptical orbits. This number of spectra per target is also required in order to examine the targets carefully for contamination of the spectra by light from a third star (which may only be visible at a small range of phases). In particular only one spectrum could be obtained for the dEB assigned priority 1, J1408-39, and so this dEB could not be analysed.

Exposures were made mainly in the short wavelength range 3930 to 4260Å; the correlation spectrum analysis was discarded the range 3930 to 3990Å to exclude the CaII H and K lines, which may show emission features due to magnetic activity. These lines are strong absorption lines, and experience has shown that such lines lead to broad wings in the correlation spectrum. (The broad absorption profile may show a narrower chromospheric emission feature at the centre due to magnetic activity). The first two exposures listed, at the start of the first night, were made at a longer range of about 4935Å to 5185Å. This was changed to the shorter wavelength range because that provided more counts on the CCD. An advantage of this shorter range is that it contains the prominent spectral lines of Ca I (4226.74Å), Ca II H and K lines (3968.49Å and 3933.66Å), Fe I (4045.82Å and 4250.79Å) and hydrogen Hδ (4101.75Å). It was intended to use these lines to determine the spectral type from intensity ratios, but this proved unsuccessful

(Sect.12.6). This was probably due to contamination from the second order spectrum of telluric lines (i.e. from the Earth's atmosphere). This contamination does not fatally compromise the main results obtained here since those were derived from a cross-correlation of two spectra over a complete spectral range (Sect. 12.3), not just a line pair. This contamination and the steps taken to correct for this are described below. There is no contradiction between a) masking the CaII lines for the correlation analysis and b) including them in an attempt to interpret spectral line ratios.

It was noticed by Maxted (private communication) that during the SAAO run that there was clear contamination of the spectra by light in the second diffraction order. This was indicated by a strong telluric absorption band at 8400Å (i.e. from molecules in the Earth's atmosphere). Maxted corrected the spectra by using the TELSYN routine in the stellar spectral synthesis code UCLSYN to generate a grid of synthetic absorption spectra for a range of airmasses. TELSYN uses the 6-layer model atmosphere of Nichols (1988). Maxted varied the selected airmass and a scaling factor over a grid of values to find the combination that minimized the peak in the cross correlation function between the synthetic absorption spectrum and the observed target spectrum. The observed spectrum was then divided by the shifted and scaled telluric spectrum. This succesfully removed much of the contamination.

11.5 Telescope and instrumentation

Description of instrument

The Radcliffe telescope was used with a long slit spectrograph system equipped with a CCD, known as the SpCCD. The spectrograph is mounted at the Cassegrain focus of the telescope. This introduced flexure in the instrument and so each spectrum was calibrated in wavelength by bracketing with an arc spectrum before and after. The

telescope has an aperture ratio f/18. A photograph, taken by the author, of the telescope appears in Fig. 11.2.

Fig. 11.2 Photograph of the 1.94 metre Radcliffe telescope at SAAO Sutherland.

The spectrograph was used with a 1200 lines/mm grating blazed to 6800Å in first order, and used in the second order i.e. blazed to 3400Å in that order, providing a resolution of 0.5Å i.e. an resolving power $\lambda/\delta\lambda \sim 8000$ for the wavelength range used. The diffracted light was focused on to a SITe CCD chip of dimensions 266 × 1798 pixels where the pixel size is 15 μm. Thus the limit on spectral resolution set by the pixel size is (350Å

(the spectral range used)/1798 pixels)×2 for Nyquist sampling i.e. ~ 0.4Å, less than the 0.5Å set by the combination of instrumental resolution and the adopted slit width. The spectrograph slit width was set at 175μm, a value determined by the ~ 1 arc second seeing and which is an order of magnitude larger than the radius $1.22\lambda f/D$ given by the diffraction limit. The slit to detector reduction factor was 8.2, thus a perfectly imaged slit in the absence of pixel crosstalk would have a width of about 20μm i.e. less than 2 pixels.

Observing procedure

At the start of each night's observing the spectrograph was focused by the Hartmann knife edge test (Hartmann, 1908), and then a calibration spectrum was taken of a well characterized radial velocity standard star, usually HD 131977. In the event these standard spectra were not used for the main analysis (Sect 12.3). A wavelength calibration of the CCD was carried out with a copper/argon arc lamp, where the argon lines provided the calibration. Because the telescope suffers flexure when it is moved to different positions, a wavelength calibration of the CCD was carried out both before and after every main exposure. The true calibration was interpolated between these two calibration exposures.

It was originally intended to use the GIRAFFE (**G**rating **I**nstrument for **R**adiation **A**nalysis with a **F**ibre **F**ed **É**chelle) spectrograph with its much superior resolving power of 40000. This would have allowed good measurements of rotational velocities. Unfortunately, previous users of this instrument had reported that it was difficult to use and suffers from poor throughput and so it was decided to use the SpCCD system instead with its much lower resolution.

CHAPTER 12 ANALYSIS

In contrast to the analysis of V1094 Tau, the analysis of the spectra started from raw data, from the incidence of the photons on to the CCD, instead of from processed spectra or previously determined radial velocities. Thus the first step was to reduce the two-dimensional CCD traces to one-dimensional wavelength calibrated spectra, as described in Appendices H and J.

12.1 Evaluation of spectra

The one-dimensional spectra were first examined by eye. It was judged that 16 were of sufficient quality i.e. an adequate number of counts and sufficiently free of noise for further analysis. These spectra are listed in Table 12.1 with their abbreviated names in order of number of usable spectra, and within that in order of R.A.

Table 12.1 List of spectra suitable for further analysis

Full name	Abbreviation	No. of usable spectra.
1SWASPJ022947.74-131452.7	J0229-13	3
1SWASPJ143021.54-401704.5	J1430-40	2
1SWASPJ154951.82-232318.3	J1549-23	2
1SWASPJ213846.63-685150.0	J2138-68	2
1SWASPJ223351.42-235152.8	J2233-23	2
1SWASPJ035346.64-360523.5	J0353-36	1
1SWASPJ042235.22-412900.1	J0422-41	1
1SWASPJ132716.78-324400.7	J1327-32	1
1SWASPJ140807.34-393548.8	J1408-39	1
1SWASPJ224636.37-243111.7	J2246-24	1

12.2 Preferred method of analysis

Ideally these extracted one dimensional spectra should have been analysed by the TODCOR/SBOP or Omdot/JKTEBOP*/jktabsdim* procedure used for V1094 Tau.

This procedure had to be modified to analyse the SAAO data because there were not enough observations to define a radial velocity curve. Nevertheless for four of the target systems two spectra could be obtained and for one target, J0229-13, three could be. (Table 12.2). If the phase, period, inclination and eccentricity are already known from analysis of the light curve, two observations during a cycle are the absolute minimum number sufficient to define a radial velocity curve although clearly more are desirable. The method for doing this is described in Sect. 12.4. If only a single radial velocity is available this is not sufficient to define a radial velocity curve over a complete orbit. Even if the phase is known, there are still two unknowns i.e. the systemic velocity and the amplitude of the radial velocity. Thus out of the 10 EB's listed in Table 12.1, orbital elements can be in principle obtained for only the first five listed there.

A further basic limitation of these measurements was imposed by the short time over which they could be made.

12.3 Analysis by MOLLY/`xcor`

Spectra from these five EB's were processed by MOLLY/`xcor` program to generate correlation spectra. This also provided a luminosity ratio used later. Some of these correlation spectra could not be analysed further because there was no obvious second peak at all, or the two peaks could not be resolved. Thus correlation spectra could be analysed for just eight exposures, from four out of the five EB's. They are listed in Table

12.2 together with the spectral type as given by the *paramfit* software in the SuperWASP/HUNTER archives. This software fits model flux profiles with wavelength to available measurements in spectral bands (e.g. B, V and R bands from NOMAD and J, H, K from 2MASS). Thus it estimates the main spectral parameters including T_{eff}, mass and radius.

Table 12.2 Number of usable correlation spectra for each target

Target	No. of spectra	Spectral Type (Hunter)
J0229-13	3 (but two less than 1 hour apart)	F7
J1430-40	2	F7
J2138-68	1	F6
J2233-23	2	G1

The MOLLY/`xcor` method requires a template star of a similar spectral type (Appendix E1) and the star chosen was HD 22484 (10 Tauri, spectral type F9V). The reasons for choosing this star were i) its spectrum is included in the ESO library of standard spectra (www.eso.org/sci/observing/tools/uvespop/ field_stars_uptonow.html) and
ii) it is a CORAVEL standard star (obswww.unige.ch?~udry/std,stdcor.dat), hence the radial velocity γ is well characterised ($\gamma = 27.9 \pm 0.3$ km s^{-1}). It was originally intended to use template spectra from stars observed during the run itself and spectra from standard stars HD 131977 (Proxima Librae, spectral type K4) and HD 187691 (Omicron Aquilae, spectral type F8) were obtained for this purpose. However cross-correlating the spectra of these two stars produced a cross-correlation spectrum which was doubled peaked and hence unsatisfactory for a reason which remains unknown. The hypothesis that the cause was the difference in the spectral types of these two stars was eliminated by cross-

correlating against other against ESO standard spectra. A further reason for observing standard stars during the run itself was that their spectra can in principle be used to determine the rotational velocities, since the method for this (Sect. 12.5.3) requires that instrumental factors should be the same for both the target and template spectra. Unfortunately an attempt to do this was unsuccessful because the spectra were not of sufficient quality.

The correlation spectra obtained by using the basic MOLLY `xcor` command showed broad wings about the peaks. These were partially suppressed by using the MOLLY `bfilt` command to filter out the low frequency components.

TODCOR

The exposures which could provide usable correlation spectra were also analysed by TODCOR to obtain radial velocities. Since this is a two-parameter correlation program, two templates are required. The templates used were the ESO library spectra for HD 22484 (10 Tauri, spectral type F9V) and HD 25069 (spectral type G9V), which were chosen so that the spectral types are significantly different from each other, but that each template spectrum is still comparable with its target star. The first template is thus the same as was used for the MOLLY/`xcor` analysis. It was not possible to use TODCOR with filtered spectra. An attempt to use TODCOR for exposures which could not be analysed by MOLLY/`xcor` was also unsuccessful.

12.4 Analytical methods for deriving radial velocity amplitudes and systemic velocities from observed radial velocities

Essentially the stellar parameters were derived by combining the `xcor`/TODCOR analysis of the correlation spectra with analysis of photometric light curves in the SuperWASP archives by JKTEBOP, and then applying Kepler's Laws. The first step is to determine the radial velocity amplitudes and systemic velocities.

Ideally an accurate solution for the orbital elements needs typically 30 pairs of good radial velocity measurements spread over an orbital period but concentrated towards the quadrature phases i.e. when the stars are moving directly towards or away from the observer and there is a large difference between the two velocities (Southworth, 2012). The radial velocity amplitude and systemic velocity (that of the centre of mass relative to the observer) are usually determined by fitting a radial velocity curve to the observed velocities. This is done by the program SBOP (Sect. 9.4.2), or one similar to it. A typical radial velocity curve is shown in Fig. 9.3. Helminiak et al. (2009) have published solutions for 18 eclipsing binaries, based on often three or four pairs but in some cases more. For the observations described here only two or effectively two pairs for two binaries could be obtained. (The phrase "effectively two" refers to J0229-13 for reasons explained later). Two pairs of radial velocities are too small a data set to use SBOP. Two pairs are nevertheless the bare minimum necessary to derive the orbital elements since the radial velocity equation can be written with two sets of variables and these can be solved as as simultaneous equations, although the uncertainty on the derived parameters is much larger. Obviously many more radial velocity measurements are desirable, and would be required to publish orbital elements to the accuracy expected in the literature.

The method used here to obtain orbital elements from just two pairs of radial velocity values is based on the following relation given by Hilditch (2001, Eqn. 2.45).

$$V_{rad} = K\,[\cos(\theta + \omega) + e\,\cos\omega] + \gamma \qquad 12.1$$

where

$$K = \frac{2\pi\, a\, \sin i}{P.(1 - e^2)^{½}} \qquad 12.2$$

and V_{rad} is the observed (i.e. projected) radial velocity

θ is the true anomaly (the angle between a) the focus of the elliptical orbit and point of periastron and b) the focus and the position of the star in its orbit)

The term "true anomaly", and the term "eccentric anomaly" used later on are illustrated below.

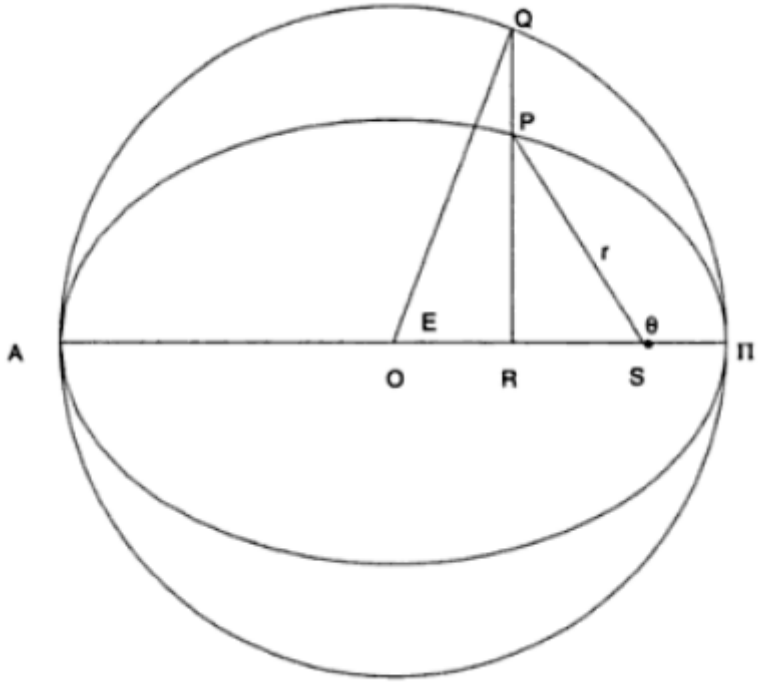

Fig. 12.1. Illustration of true and eccentric anomaly in an eccentric orbit. taken from Fig. 2.4 of Hilditch (2001).

In Figure 12.1 the ellipse has a focus at S, Π is the point of periastron and A the point of apastron (where the orbit is furthest from the focus S). The true anomaly is the

angle ΠSP. The eccentric anomaly is the angle ΠOQ, where Q lies on the auxiliary circle i.e. the circle which touches the ellipse at A and Π and has its common centre with the ellipse at O. The angle of periastron is shown in Fig. 12.2, taken from Fig. 4.2 of Hilditch (2001). It is the angle between the line joining the focus of the relative orbit and point of nearest approach, and the line of nodes which is the line joining the intersections of the projection of the orbit plane with the tangent plane of the sky.

In more detail Fig. 12.2 shows the orbit of the primary in an eclipsing binary relative to the secondary at the point O. The primary eclipse occurs when the primary is at the point P and the secondary eclipse when the primary is at point S. Orbits are shown for three different angles of periastron ω, solid line for $\omega = 45°$, dotted line for $\omega = 60°$, and dashed line for $\omega = 250°$. For the first case the orbit of the primary is along the ellipse PAS. The line of sight is along the line SOP, and the line of nodes is in a plane perpendicular to this i.e. tangential to the celestial sphere. The angle T is the angle in an anticlockwise direction between i) the line OΠ and ii) the line between O and the position of the primary.

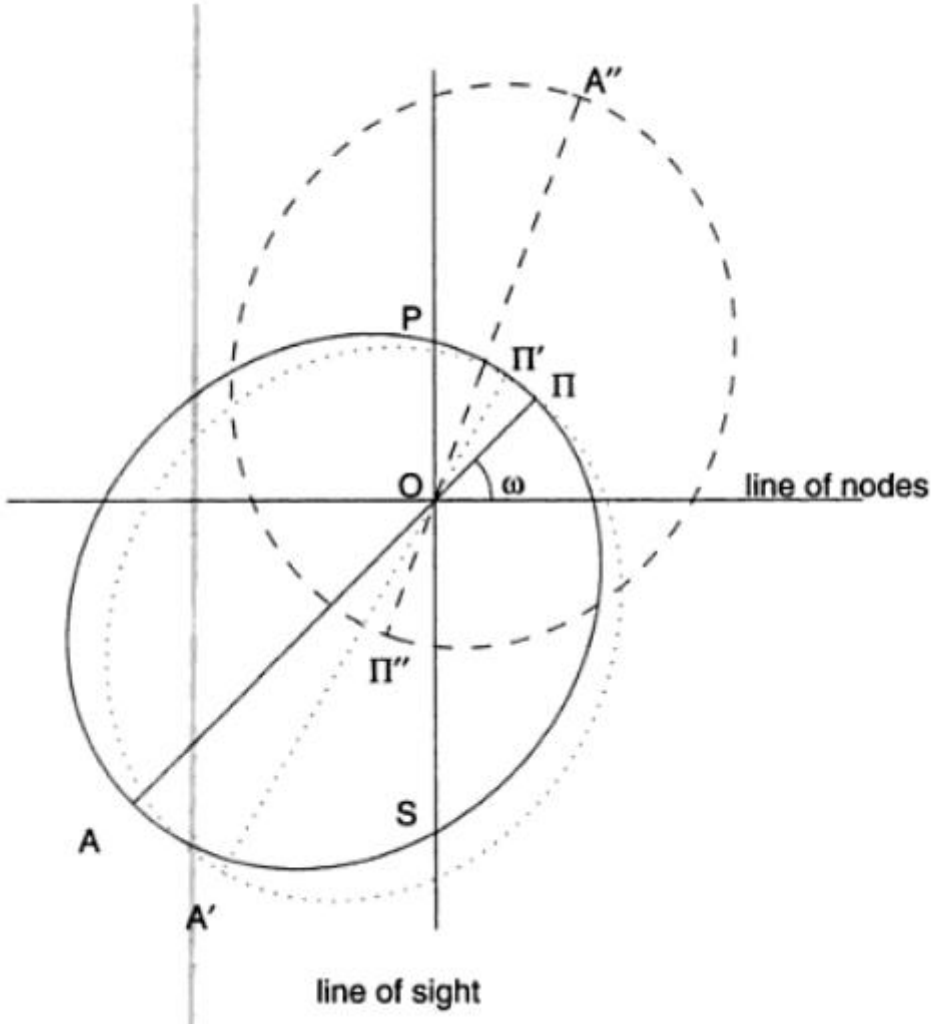

Fig. 12.2 Illustration of angle of periastron, taken from Fig. 4.2 of Hilditch (2001).

Method of solution

The two radial velocities available for each star in the target may be substituted into Eqn. 12.1 to provide a pair of simultaneous equations. Hence the unknowns K and γ may be derived.

Equation 12.1 requires values of θ and ω, which need to be calculated from the phase. The phase itself is known from previous observations since the light curves in the

SuperWASP archives give the period and times of eclipses. Thus the task required is to calculate θ, which is the true anomaly relative to periastron, from the phase relative to the primary eclipse. This requires calculating the phase, relative to periastron, at which the primary eclipse occurred. The value of the eccentricity e was determined by analysing the light curves with JKTEBOP. The procedure is as follows.

The value θ_p at the primary eclipse may be obtained from Eqn. 4.9 of Hilditch (2001) i.e.

$$\delta.\left(1 + e\ \cos\theta_p\right) = \ (1 - \ e^2).\left[1 - \ sin^2\ i\ .sin^2\left(\theta_p + \ e\right)\right]^{½} \qquad 12.3$$

This may be solved by minimising δ by trial and error, taking as a starting point the value $\theta_p = \pi/2 - \omega$ which would obtain for an inclination i = 90°. This relation is evident from Fig. 12.1, where it may also be seen that this relation is only approximate for i close to, but not equal to 90°.

The next step is to calculate the eccentric anomaly E_p at the time of primary eclipse by the relation (Hilditch, 2001, Table 2.1)

$$\tan\left(\frac{\theta_p}{2}\right) = \left[\frac{1+e}{1-e}\right]^{½} \tan\left(\frac{E_p}{2}\right) \qquad 12.4$$

where the angles θ and E are illustrated in Fig. 12.1,

The phase ϕ_p of the primary eclipse relative to periastron then follows from Kepler's Equation i.e.

$$\phi_p = \ E_p - \ e \sin E_p \qquad 12.5$$

where E_p is in radians.

The phase ϕ_{obs} at time of observation is simply ϕ_p plus the phase relative to primary eclipse.

12.5 Analytical methods to determine the fundamental stellar parameters

12.5.1 Stellar Masses

Since the radial velocity amplitudes are now known the masses can be calculated from the standard relation derived from Kepler's Laws (Hilditch, 2001, Eqn. 2.52)

$$M_{1,2}\,sin^3\,i = 1.0361\times\ 10^{-7}\ (1-\ e^2)^{\frac{3}{2}}.(K_1+\ K_2)^2.K_{2,1}\,P\ \times\ M_\odot \qquad 12.6$$

where the subscripts 1 and 2 refer to stars 1 and 2 respectively.

The semi-major axis *a* of the relative orbit can be derived from Kepler's Third Law as expressed by the first equation in Table 3 of Harmanec and Prša (2011), i.e.

$$\left(\frac{a}{R_\odot}\right)^3 = 74.5887.P(days).(M_1+\ M_2) \qquad 12.7$$

12.5.2 Stellar radii

The absolute radii can now in principle be obtained from the value of *a* and those of the relative radii from the JKTEBOP analysis. In practice these values can be refined by repeating the JKTEBOP analysis and this time also inputting the approximate luminosity ratio obtained as below by using the JKTEBOP command LRAT (Sect. 9.6). The output also provides refined values of the surface brightness ratio. The uncertainties in the relative radii were obtained from a specially written program which takes as input the luminosity ratio and the uncertainty on it, and then calculates the relative radii, ratio of the radii, inclination and uncertainties.

12.5.3 Rotational velocities

The rotational velocity can be determined from the width of the autocorrelation spectrum of the template with the target spectrum. The autocorrelation spectrum of the template with itself is artificially broadened by the MOLLY command `rbroad` to match the width of the peaks of the autocorrelation spectra of the target systems. This clearly requires values of the FWHM, which are obtained by the MOLLY command `mgfit`.

The width of a correlation spectrum peak is a convolution of instrumental broadening, the broadening due to the rotation of the template star, and the broadening due to the rotation of the target star. If the template and target were observed by the same spectrograph, the instrumental broadening can be made to cancel. The following analysis is based on the theoretical treatment of Tonry and Davis (1979) where all widths are FWHM's.

The width μ of the correlation peak is given by

$$\mu^2 = \sigma^2 + \tau^2 \qquad 12.8.$$

where

σ is the width of the template peak .

τ is the width induced by the instrumental broadening.

Hence by writing this equation for i) the template/target peak and ii) the template autocorrelation peak and subtracting we obtain

$$\mu^2 \text{ (target peak)} - \mu^2 \text{ (template peak)} = (v \sin i \text{ (target)})^2 - (v \sin i \text{ (template)})^2 \qquad 12.9$$

The *v sin i* value corresponding to $\delta\lambda$, the μ terms above when expressed in wavelengths, may be obtained from Eqn. 12 of Collins and Truax (1995) i.e.

$$v \sin i = \frac{\delta\lambda}{2\lambda} . \frac{c}{\chi} \qquad 12.10$$

where

λ is the base wavelength used in the correlation analysis (5000 A)

χ is a function of the limb darkening parameter. For the parameter 0.5 assumed in the analysis χ = 0.744 (Collins and Truax, Table 2).

The template star is HD187691, for which two definite values of *v sin i* are available i) Bernacca and Perinotto (1970), and ii) Takeda et al., 2005) who both give *v sin i* = 3 km/s. Thus all the terms needed to calculate v sin *i* (target)) are known.

12.6. Values obtained for orbital elements, stellar masses and radii, and for the luminosity ratios.

12.6.1 Orbital elements

It would appear that an orbital solution can be obtained for three systems for which two pairs of radial velocities are available i.e. J0229-13, J1430-40 and J2233-23 (Table 12.2). Closer inspection however shows that a solution could not be obtained for J2233-23. Relevant details are as follows.

J0229-13. Let the three spectra listed in Table 11.3 were taken for this system be labelled July 21, 4.28 SAST and 5.02 SAST as a) and b); and July 22, 6.17 SAST as c). The two pairs used to derive radial velocity amplitudes are (a/c) and (b/c). The pair (a/b) could not

be used since the spectra were taken just over half an hour apart and the difference between the radial velocities was too small to derive a velocity amplitude. For the purposes of curve fitting the pair (a/b) behaves as a single point. The phases of these observations reckoned from the primary minimum are (Table 11.4) 0.915 for spectrum b) and 0.066 for spectrum c) i.e a phase difference of just 0.151.

J1430-40. The two pairs of radial velocities could be used for analysis without major problems. For convenience times of observations are repeated here from Table 11.4 as July 20, 23.59 SAST, phase 0.476 and July 22, 21.06 SAST, phase 0.676 i.e. a phase difference of 0.200.

J2233-23. Analysis yielded the unphysical result of mass ratio ~ 5, but luminosity ratio ~ 1. This result is very unlikely to be genuine. If both stars are on the Main Sequence, the more massive star will be the more luminous, contrary to what is observed. If the two members of the binary are assumed to be formed at the same time, and one star has evolved off the Main Sequence, then the more massive one will have done so first and so would be even more luminous. The reason for this anomalous result is unknown, but may be (Maxted, private communication) that the radial velocity for the secondary star measured from the cross correlation function is inaccurate, i.e., measured from a spurious peak due to noise. This system is not considered further.

12.6.2 JKTEBOP analysis

Input data

The two binaries J0229-13 and J1340-40 were analysed by JKTEBOP in a manner similar to V1094 Tau. Much of the input data were obtained either by fitting by eye or from trial JKTEBOP runs. The remaining input data were obtained as follows.

Base minimum time	A specially written program *findecl* linked to the SuperWASP archives.
Period	From *findecl*.
Mass ratios	From the masses obtained from the RV's. These are very close to the values obtained from *jktabsdim* and listed below.
Gravity darkening coefficient	From the tables of Claret and Bloemen (2011) as for V1094 Tau
Limb darkening coefficient	From *jktld* as for V1094 Tau.

Since the SuperWASP light curves were obtained with an optical telescope array, it was judged that the most appropriate spectral band to use for the darkening coefficients is an average of the Johnson V- and R-bands. The tables and programs for the darkening coefficients need prior input data, namely:

Gravity darkening:	*Log g* (obtained from previous estimates of mass and radius) and T_{eff} (estimated from the spectral type). The required value was interpolated between the surrounding values in the table grid.
Limb darkening	T_{eff} as above.

The values adopted were:

Binary	Gravity darkening		Limb darkening	
	Primary	Secondary	Primary	Secondary
J0229-13	0.331	0.331	0.623	0.623
J1430-40	0.331	0.331	0.621	0.621

Luminosity ratios

As for the analysis of V1094 Tau a luminosity ratio is calculated by JKTEBOP, and the degeneracy in a JKTEBOP solution can be constrained by a luminosity ratio obtained independently. For the SAAO observations a very approximate independent ratio can be obtained from the area of the cross-correlation peaks calculated by the MOLLY/`xcor` software (Appendix C, Sect. C2) if the two stars are broadly of the same spectral type. The area was estimated from a simple triangular approximation i.e. (area $\propto$ height × FWHM). The justification for assuming that the luminosity ratio is approximately given by the area ratio is taken from the work of Howarth et al. (1997). These authors discussed how the area under the peak of a correlation spectrum depends on the spectral type (their Fig. 10) and also show in their Table 6 that if the two binary components are of the same spectral type the luminosity ratio is approximately equal to the ratio of the areas of the peaks of the correlation spectrum. Details are as follows.

J0229-13. A MOLLY/`xcor` luminosity ratio could be obtained for only the last of the three spectra itemised in the last subsection, namely $L_2/L_1 = 0.76 \pm 0.15$ for spectrum c) on July 22, 6.17 SAST. It is not possible to make any firm statement about agreement with the JKTEBOP ratio derived below because the latter is so uncertain. The peaks on the first two correlation spectra are only partially resolved and so cannot provide a luminosity ratio. They are nevertheless sufficiently distinct to determine radial velocities.

J1340-40 The MOLLY/`xcor` luminosity ratios are as follows.

Exposure	Ratio	Uncertainty
Jul. 20 23.59 SAST	0.83	0.22
Jul. 22 21.06 SAST	0.80	0.05
Weighted average	0.81	0.04

The weighted average ratio is in almost perfect agreement with the ratio 0.80 ± 0.17 obtained from JKTEBOP.

Derived stellar parameters

The results for the orbital parameters and the output from JKTEBOP were inputted into jktabsdim as for V1094 Tau. The stellar parameters finally obtained are listed in Table 12.3.

Table 12.3. Stellar parameters of J0229-13 and J1430-40

Parameter	Value	Value	Source
Object	J0229-13	J1430-40	
$P_{sid}/days$	7.1035303 (228)	9.3821249 (87)	findecl (see above)
$M_1/M_\odot$	1.08 ± 0.10	1.30 ± 0.25	jktabsdim
$M_2/M_\odot$	1.10 ± 0.10	1.14 ± 0.22	jktabsdim
$R_1/R_\odot$	1.4 ± 0.4 (Note a))	1.5 ± 0.1	jktabsdim
$R_2/R_\odot$	1.7 ± 0.52(Note a))	1.4 ± 0.1	jktabsdim
$a/R_\odot$	20.2 ± 0.6	25.2 ± 1.5	jktabsdim
$log\ g_{,1}$	4.2 ± 0.3	4.18 ± 0.04	jktabsdim
$log\ g_{,2}$	4.0 ± 0.3	4.22 ± 0.04	jktabsdim
e	0.070 ± 0.002	0.024 ± 0.013	JKTEBOP
$\omega\ (deg)$	90.0 (Note b))	89.6	JKTEBOP
i (deg)	85.35 ± 0.49	87.200 ± 0.018	JKTEBOP
$K_1\ (km\ s^{-1})$	72.0 ± 2.9	63.8 ± 5.5	Two R.V's
$K_2\ (km\ s^{-1})$	71.2 ± 3.0	72.4 ± 6.3	Two R.V's
γ	48.1 ± 3.0	-12.7 ± 6.3	Two R.V's
$T_{eff,1}/K$	6275 ± 140	6265 ± 150	Note c)
$T_{eff,2}/K$	6265 ± 140	6110 ± 150	
$L_1/L_\odot$	3.0 -1.5,+2.1	3.2 ± 0.5	jktabsdim
$L_2/L_\odot$	3.7 -1.8,+3.3	2.6 ± 0.4	jktabsdim
L_2/L_1	See Note d)	0.80 ± 0.17	Derived from above.
Distance (pc)	141 ± 31	251 ± 16	jktabsdim

Note a) The error bars on R_2/R_1 calculated by the residual shift method in jktebop.in.3 are 1.176 + 0.006 – 0.537. The wide negative error bar feeds through into the large uncertainty which jktabsdim calculates for R_2 and R_1. (The value $R_1 + R_2 = 0.1554 \pm 0.0060$ has much tighter error bars).

Note b) The routine jktebop.in.3 returns $e \cos \omega \sim 0.00017 \pm 0.00040$. Thus the normal method of estimating the uncertainty in ω through that in $\tan \omega$ breaks down.

Note c) Estimated by using Eqns. 2 and 3 of Coughlin et al. (2011)

Note d): The error bars on this luminosity ratio are so wide as to make the value of the ratio itself almost meaningless.

It will be seen that the stars in both systems are slightly evolved. In order to assess how valuable these systems are for future study the following table shows how much larger the radii are from what would be expected from the relation $R \propto M^{0.8}$ and adopting the Sun as a base. The results are shown in Table 12.4.

Table 12.4 Percentage degree to which radii exceed empirical main sequence relation

System	Primary	Secondary
J0229-13	35 ± 43 %	57 ± 50 %
J1430-40	24 ± 26 %	24 ± 25 %

The parameters of rotational velocities and spectral type were also investigated but few definite conclusions could be reached, as explained in the next two subsections.

It was not possible to investigate the kinematics of these binaries, as was done in Part I and for V1094 Tau, since the proper motions are not known.

12.7 Rotational velocities and periods.

The demands on the accuracy of rotational velocity measurements needed to draw significant conclusions are severe. For a binary where the orbital period is 8 days and each star has a mass of $1M_{\odot}$, the rotational period is predicted by Zahn (1994) to be about 10 days (Appendix R, Fig. R2). For this 10 day period the quantity *v sin i* is about 5.1 km s^{-1} (Eqn. 10.2), whereas if the rotational period were synchronised to the orbital period of 8 days the value of *v* sin *i* would be about 6.3 km s^{-1}. Thus rotation velocities should be measured to an accuracy to much better than the ~ 1.3 km s^{-1} difference between the two. In fact the currently achievable precision is somewhat less than 0.5 km s^{-1}. Note that as for the radial velocity method for detecting exoplanets, the use of correlation spectra makes it possible to measure much smaller Doppler shifts than those implied by the spectral resolution of the spectrometer.

Only one meaningful result could be obtained, for the more luminous star in the system J1430-40. Many of the correlation spectra showed obvious inconsistencies e.g. the fitted spectrum to the correlation spectrum being slightly narrower than the autocorrelation spectrum. For some spectra the difference in spectral half widths (template/target) – (template/template) was less than the uncertainties and for one spectrum the template/target correlation peak was slightly narrower than the template/template autocorrelation spectrum. For J1430-40 the analysis method in Appendix P gives *v sin i* ~ 12 ± 3 km s^{-1}. Combining this with the absolute radius gives a rotation period of ~ 5.7 ± 1.3 days. The orbital period is ~ 9.38 days. This does not agree well with the prediction of Zahn (1994) that the rotational and orbital periods synchronise for orbital periods shorter than about 8 days. It is inconsistent with a further prediction of Zahn, that for orbital periods longer than ~ 8 days the rotational period stabilises shortly after the stars reach the

Main Sequence at a value longer than the orbital period. This contradiction could be resolved only if the stars are very young and the rotational velocities have not stabilised. Apart from this somewhat contrived explanation this result is not understood.

12.8 Spectral Type

An attempt was made to derive a spectral type from the intensity ratio of prominent spectral lines (Ca I (4226.74Å), Fe I (4045.82Å), Fe I (4250.79Å) and Hδ (4101.75Å) to the Ca II K line (3968.49Å)) by comparing observed ratio with those in the spectral atlas of Gray (www.ned.ipac.caltech.edu/level5/Gray/Gray_contents.html). This was unsuccessful. The spectral types derived from each ratio were very inconsistent; this was ascribed to contamination from telluric lines in the second order from first-order light not effectively excluded in the instrument configuration chosen.

12.9 Conclusion

The conclusions from the telescope run are necessarily very limited, and are be evident from Tables 12.3 and 12.4. The stars in both the systems J0229-13 and J1430-40 are both slightly more massive than the Sun unless they lie at the edge of, or just over the error bars. The stars in J0229-13 appear to be slightly evolved. Table 12.4 shows that the stars in J1430-40 could be very slightly evolved but this is not certain due to the width of the error bars. The luminosities of the J0229-13 stars are roughly $3L_{\odot}$, albeit with very wide error bars, which is larger than what would be expected from masses of about $1.1\pm0.1M_{\odot}$ and the commonly quoted simple empirical relation $L \propto M^4$. This again suggests that the stars are slightly evolved. For J1430-40 the error bars on the masses and luminosities admit either that the values for these parameters are consistent with this relation or they are not. The question “are these systems good candidates for follow-up

observations?" depends on i) whether binaries with periods around 8 days and closer to the Main Sequence are discovered and ii) the importance of testing tidal interaction theory for somewhat evolved stars. The orbital periods of both systems are close to the 8 day cut-off for synchronisation of the rotational period with the orbital period.

Even though only two pairs of radial velocities could be measured for each binary it was still possible to make a preliminary decision on whether the stars in a binary were main sequence or evolved. If the telescope run had not been curtailed by bad weather it is likely that masses could have been determined more accurately. Thus this work supports the proof in principle of the method; that observations on a 2 metre class telescope can validate the choice of eclipsing binaries for definitive observations on 3 to 4 metre class telescope.

It may be asked whether observations should have been confined to just J0229-13 and J1430-40. A basic constraint underlying the choice of targets during the run was that the ultimate aim of this study determines that periods of the targets are comparable to 8 days. It was intended to observe the targets at times chosen to provide a broadly even spread of points across radial velocity curves similar to those in Fig. 9.4. This would have been achieved by observing several targets on one night and then observing them again a number of times during the one week allocated to the run, but the bad weather prevented this. Restricting observations to two targets during the three consecutive nights when observations were possible would have confined radial velocity values to a phase coverage of order only a quarter and so the radial velocity curves would not have been well defined.

Even if targets turn out to be unsuitable for studying the tidal evolution of main sequence stars, they may be very good targets for studying other stellar astrophysics problems. For example Torres et al. (2014) have described a detailed study of the dEB AQ Serpentis to investigate problems with convective overshooting (mixing above the convective core) for stars evolving off the main sequence.

Lists of potential targets for future studies of the type have been drawn up and prioritised.

TECHNICAL ACKNOWLEDGMENTS

Parts I and III of this project made use of data from the SuperWASP project. This is is funded and operated by Queen's University Belfast, the Universities of Keele, St Andrews and Leicester, the Open University, the Isaac Newton Group, the Instituto de Astrofisica de Canarias, the South African Astronomical Observatory and by the United Kingdom Science and Technology Funding Council.

The author would like to thank the following colleagues and collaborators, cited in alphabetical order, for providing him with programs and data.

Professor S.Aarseth of the Institute of Astronomy at Cambridge for providing the author with his (Prof. Aarseth's) program to calculate values of Z_{max} from stellar positions and velocities.

Professor C.H.S. Lacy of the Department of Physics, University of Arkansas for light curves from the NFO and URSA telescopes.

Professor K. Pavlovski for spectral disentangling and spectral fitting software. (This was not used in the definitive analysis).

Professor G.Torres of the Harvard-Smithsonian Centre for Astrophysics for a set of radial velocity measurements, and for collaboration in preparing a paper on the subject of this thesis.

Dr. K.T. Wraight of the Department of Physics and Astronomy, The Open University, Milton Keynes for light curves obtained from the STEREO mission. (These however were not used for the definitive analysis).

This thesis has also used data and light curves discovered in the files of Professor Clausen of the Niels Bohr Institute, Copenhagen University after his death. The first use of this data (Table 8.2) is referenced as (Clausen, private commumication, see Acknowledgements), the remainder are referenced simply as (Clausen, private communication).

The author would like to thank the support staff at the South African Astronomical Observatory at Sutherland for the technical assistance necessary for the week's observing run there.

This thesis has made use of the following data bases.

- SIMBAD and VizieR (Ochsenbein et al. 2000), maintained at the Centre pour Données Astronomiques de Strasbourg (CDS), University of Strasbourg, France.

- The Extrasolar Planets Encyclopaedia (www.exoplanet.eu) maintained by J.Schneider at the Observatory of Paris.

- The NASA Astrophysics Data System and the arXiv scientific paper preprint service operated by Cornell University.

- Data products from the Two Micron All Sky Survey (Cutri et al. 2003), which is a joint project of the University of Massachusetts and the Infrared Processing and Analysis Center/California Institute of Technology, funded by the National Aeronautics and Space Administration and the National Science Foundation.

This thesis has also used the Veusz scientific plotting package developed by J.Sanders (www.home.gna.org/veusz/docs/manual.html).

Acknowledgements for the star charts used in Appendix L are given there.

REFERENCES

Aerts, C., Christensen-Dalsgaard, J and Kurtz, D.W.
Asteroseismology, Astronomy and Astrophysics Library. ISBN 978-1-4020-5178-4.
Springer Science+Business Media B.V., 2010.

Albrecht, S., Reffert, S., Snellen, I., Quirrenbach, A. and Mitchell, J.N.
Astron. and Astrophys, 474, 565-573, (2007).

Albrecht, S., Reffert, S., Snellen, I.A.G. and Winn, J.N.
Nature, 461, 373-376, (2009).

Albrecht, S., Setiawan, J., Torres, G., Fabrycky, D.C. and Winn, J.N.
Astrophys. J., 767, id32, 9 pp, (2013).

Alonso, R. and 11 coauthors.
Astrophys. J. Lett, 613, L153-L156, (2004a).

Ammler-von Eiff, M., Santos, N.C., Sousa, S.G., Fernandes, J., Guillot, T., G. Israelian,G., Mayor,M. and Melo, C.
Astron. and Astrophys, 507, 523-530, (2009).

Andersen, J and Vaz, L.P.R.
Astron. and Astrophys., 130, 102-110, (1984).

Andersen, J., Garcia, J.M., Gimenez, A. and Nordström, B.
Astron. and Astrophys., 174, 107-115, (1987).

Andersen, J., Clausen, J.V., Nordström, B., Tomkin, J. and Mayor, M.
Astron. and Astrophys., 246, 99-117, (1991).

Argelander, F. W. A.
Eds. Marcus and Weber's Verlag, Bonn, (1903).

Aumer, M. and Binney, J.J.
Mon. Not. R. Astron. Soc. 397, 1286-1301, (2009).

Auvergne, M. and 109 coauthors.
Astron. and Astrophys., 506, 411-424, (2009).

Baines, E.K., McAlister, H.A., ten Brummelaar, T.A., Sturmann, J., Sturmann, L., Turner, N.H., and Ridgway, S.T.
Astrophys. J., 701, 154-162, (2009).

Bakos, G.A. and 18 coauthors.
Astrophys. J., 656 (1), 552-559, (2007).

Baldwin, R.B.,
Popular Astronomy, 52, 186-190, (1944).

Baraffe, I., Chabrier, G., Allard, F., & Hauschildt, P. H.
Astron. and Astrophys., 337, 403-412, (1998).

Baranne, A., Mayor, M. and Poncet, J.L.
Vistas in Astronomy, 23, 279-316, (1979).

Baranne, A., Queloz, D., Mayor, M., Adrianzyk, G., Knispel, G., Kohler, D., Lacroix, D., Meunier, J-P., Rimbaud, G. and Vin, A.
Astron. and Astrophys. Suppl. Ser. 119, 373-390, (1996).

Barge, P. and 37 coauthors.
Astron. and Astrophys., 482, L17–L20, (2008).

Barney, I.
Trans. Astron. Obs. Yale Univ., 25, (1954).

Basri, G., Borucki, W. J., and Koch, D.
New Astr. Rev., 49, 478-485, (2005).

Bethe, H.A.
Phys. Rev. 55, 434-456, (1939)

Bernacca, P.L. and Perinotto, M. (1970), Contr. Oss. Astrof. Padova in Asiago, 239

Berger, D.H., Gies, D.R., McAlister, H.A., ten Brummelaar, T.A., Henry, T.J., Sturmann, J., Sturmann, L., Turner. N.H. and Mérand, A.
Astrophys. J., 644, 475–483, (2006).

Bessell, M.S
Publ. Astron. Soc. Pacific, 102, 1181-1199, (1990).

Bessell, M.S
Publ. Astron. Soc. Pacific, 112, 961-965, (2000).

Bessell, M.
Ann. Rev. Astron. Astrophys., 43, 293-336, (2005).

Bilir, S., Karaali, S., Ak, S., Önal, Ö., Dagtekin, N.D., Yontan, T., Gilmore, G. and Seabroke, G.M.
Mon. Not. R. Astr. Soc.,421, 3362-3388, (2012)

Binnendijk, L., "Properties of Double Stars", p.163, (1960). Publisher not known.

Binney, J. and Merrifield, M.
Princeton University Press, 1998, ISBN 0-691-00402-1 (hardback) or 0-691-02565-7 (paperback).

Bodenheimer, P., D'Angelo, G., Lissauer, J.J.,Fortney, J.J. and Saumon, D.
Astrophys. J., 770, id. 120, (2013).

Böhm-Vitense, E.
Zeit. für Astr., 46, 108-143, (1958).

Bordé, P., Rouan, D. and Léger, A.
Astron. and Astrophys., 405, 1137-1144, (2003).

Borucki, W.J. and 27 coauthors.
American Astronomical Society Meeting 215, Session 101.01. (2010a).

A more accessible publication, giving some first results is:
Borucki, W.J., and 18 coauthors.
Astrophys. J. Lett., 713, Issue 2, L126-L130, (2010).

Boss, A. P. (1992). "Formation of Binary Stars".
In. *The Realm of Interacting Binary Stars*. P.355,
(Eds.) Sahade, J., McCluskey G.E. and Kondo, Y.
Dordrecht: Kluwer Academic Press, ISBN 0-7923-1675-4.

Bressan, A., Fagotto, F., Bertelli, G. and Chiosi, C.
Astron. and Astrophys. Supp. Ser., 100, 647-664, (1993).

Brown, T.M. and Christensen-Dalsgaard, J.
Astrophys. J. Lett., 500, L195–L198, (1998).

Burke, C.J., and 17 coauthors.
Astrophys. J., 671 (1), 2115-2128, (2007).

Butler, R.P., Marcy, G.W., Williams, E., McCarthy, C., Dosanjh, P. and Vogt, S.S.
Publ. Astron. Soc. Pacific, 108, 500-509, (1996).

Cannon, A.J. and Mayall, M.W.
Ann. Astron. Obs. Harvard Coll., 112, 1-295 (1949)

Cannon, A.J. and Pickering, E.C.
"The Henry Draper Catalogue", Annals of the Harvard College Observatory 91-99,
(1918 – 1924).
The nine issues of the Annals cover Right Ascensions as:
0- 3 hr, 91 (1918); 4- 6 hr, 92 (1918); 7- 8 hr, 93 (1919);
9-11 hr, 94 (1919); 12-14 hr, 95 (1920); 15-16 hr, 96 (1921)
17-18 hr, 97 (1922); 19-20 hr, 98 (1923); 21-23 hr, 99 (1924).

Carroll, B.W. and Ostlie, D.A.
"An Introduction to Modern Astrophysics". Addison-Wesley. (2007).

Chabrier, G., and Baraffe, I.
Astron. and Astrophys., 327, 1039-1053, (1997).

Chabrier, G., Gallardo, J. and Baraffe, I.
Astron. and Astrophys., 472, L17-L20, (2007).

Charbonneau, D., Brown, T.M., Latham, D.W. and Mayor, M.
Astrophys. J. Lett., 529, L45 – L48, (2000).

Charbonneau, D., Brown, T.M., Noyes, R.W. and Gilliland, R.L.
Astrophys. J, 568, 377–384, (2002).

Charbonneau, D., Allen, L.E., Megeath, S.T., Torres, G., Alonso, R., Brown, T.M., Gilliland, R.L., Latham, D.W., Mandushev, G., O'Donovan, F.T. and Sozzetti, A.
Astrophys. J., 626, 523–529, (2005).

Claret, A. and Gimenez, A.
Astron. and Astrophys. Suppl. Ser., 96, 255-267, (1992).

Claret, A. and Gimenez, A.
Astron. and Astrophys., 277, 487-502, (1993).

Claret, A.
Astron. and Astrophys., 363, 1081-1190, (2000) .

Claret, A. and Bloemen, S.
Astron. and Astrophys., 529, A75, (2011).

Claret, A and Hauschildt, P.H.
Astron. and Astrophys., 412, 241-248, (2003).

Claret, A.,
Astron. and Astrophys., 467, 1389-1396, (2007).
Claret, A., Torres, G. and Wolf, M.
Astron. and Astrophys., 515, id.A4, 6 pp, (2010).

Clausen, J.V,
Astron. and Astrophys., 246, 397-406, (1991).

Clausen, J. V., 1998, in Kjeldsen, H., Bedding, T. R., eds.,
"The First MONS Workshop: Science with a Small Space Telescope" p. 105.

Clausen, J.V., Bruntt, H., Claret, A., Larsen, A., Andersen, J., Nordström, B. and Giménez, A.
Astron. and Astrophys., 502, 253–265, (2009).

Clausen, J.V., Frandsen, S., Bruntt, H., Olsen, E.H., Helt, B.E., Gregersen, K., Juncher, D. and Krogstrup, P.
Astron. and Astrophys., 516, A42, 14 pp, (2010).

Collier Cameron, A. and 38 coauthors.
Mon. Not. R. Astr. Soc., 375, 951-957, (2007).

Collier Cameron, A. and 31 coauthors.
Mon. Not. R. Astr. Soc., 380, 1230-1244, (2007b).

Collier Cameron, A. and 25 coauthors.
Mon. Not. R. Astr. Soc., 400, 451-462, (2009).

Collins, G.W. and Truax, R.J.
Astrophys. J., 439, 860-874, (1995).

Coughlin, J.L., Lopez-Morales, M., Harrison, T.E., Ule, N. and Hoffman, D.I.
Astron. J., 141, id. 78, (2011).

Cowling, T.G.,
Mon. Not. R. Astr. Soc., 98, 734-743, (1938).

Crawford, D. L.,
Astrophys. J., 128 , 185–206, (1958).

Crawford, D.L.,
Astronom. J., 80, 955-971, (1975a).

Crawford, D.L.,
Publ. Astron. Soc. Pacific, 87, 481-494, (1975b)

Cutri R.M. and 24 coauthors.
University of Massachusetts and Infrared Processing and Analysis Center
(IPAC/California Institute of Technology), (2003).
VizieR catalogue II/246, CDS, Strasbourg, France. www.vizier. u-strasbg.fr

Daemgen,S., Hormuth, F., Brandner, W., Bergfors, C., Janson, M., Hippler, S. and Henning, T.
Astron. and Astrophys., 498, 567-574, (2009).

Debosscher, J., Aerts, C., Tkachenko, A., Pavlovski, K., Macaroni, C., Kurtz, D., Beck, P.G., Bloemen, S., Degroote, P., Lombaert, R. and Southworth, J.
Astron. and Astrophys., 556, A56, 11 pp, (2013).

Dehnen, W. and Binney, J.J.
Mon. Not. R. Astr. Soc., 298, 387-394, (1998).

Delfosse, X.; Beuzit, J.-L.; Marchal, L.; Bonfils, X.; Perrier, C.; Ségransan, D.; Udry, S.; Mayor, M.; Forveille, T.
In "Spectroscopically and Spatially Resolving the Components of the Close Binary Stars" ASP Conf. Ser. 318, 166 (2004), Edited by R. W. Hilditch, H. Hensberge and K. Pavlovski.

Deming, D., Seager, S., Richardson, L. J., and Harrington, J.
Nature, 434, Issue 7034, 740-743, (2005).

Devor, J. and Charbonneau, D.
Astrophys. J., 653, 647-656, (2006a).

Diaz-Cordoves, J., Claret, A. and Gimenez, A.
Astron. and Astrophys. Supp., 110, 329-350 (1995).

Diethelm, R.
Inf. Bull. Var. Stars, No. 6011, (2012a).
Konkoly Observatory, Budapest.

Diethelm, R.
Inf. Bull. Var. Stars, No. 6029, (2012b).
Konkoly Observatory, Budapest.
Dobbs-Dixon, I., Lin, D.N.C. and Mardling, R.A.
Astrophys. J., 610, 464–476, (2004).

Dommanget J. and Nys O.
"Catalogue of the components of double and multiple stars (CCDM), first edition".
Com. de l'Observ. Royal de Belgique, 115, 1 (1994).

Duquennoy, A., & Mayor, M.
Astron. and Astrophys., 248, 485-524, (1991).

Eggleton, P.P.
Astrophys. J., 268, 368, (1983)

Enoch, B., Collier Cameron, A., Parley, N.R. and Hebb, L.
Astron. and Astrophys., 516, id.A33, (2010).

Etzel, P.B.
Masters Thesis, San Diego State University. (1975).

Eyer, L. and 13 coauthors.
From Interacting Binaries to Exoplanets: Essential Modeling Tools, Proceedings of the International Astronomical Union. Edited by M. T. Richards and I. Hubeny,
IAU Symposium, Volume 282, p. 33-40, (2012).

Eyles, C.J. and 17 coauthors.
Solar Phys., 254, 387–445, (2009).

Feiden, G.A.
Ph. D thesis, Dertmouth College (Hanover, New Hampshire),(2013)

Feiden, G.A. and Chaboyer, B.
Astrophys. J., 761, id. 30, (2012).

Feiden, G.A. and Chaboyer, B.
Astrophys. J., 779, id. 183, (2013).

Fischer, D.A. and Valenti, J.
Astrophys. J., 622, 1102–1117, (2005).

Florentin-Nielsen, R.,
Chapter 5 of "Stellar photometry - Current techniques and future developments".
Proceedings of the IAU Colloquium No. 136 held in Dublin; Ireland; 4-7 August 1992;
Cambridge: Cambridge University Press, (1993); edited by C.J. Butler and I. Elliott, p.213.

Fitzpatrick, E.L.
Publ. Astron. Soc. Pacific., 111, 63-75, (1999).
Fontenla, J.M., Curdt, W., Haberreiter, M., Harder, J. and Tian, H.
Astrophys. J., 707, 482–502, (2009).

Fortney, J. J., Marley M. S., and Barnes J. W.
Astrophys. J., 659, 1661-1672, (2007).
Freytag, B., Steffen, M. and Dorch, B.
Astron. Nachrichten, 323, 213-219, (2002).

Gaudi, B.S., Seager S., Mallen-Ornelas G.,
Astrophys. J., 623, 472-481, (2005).

Gaudi B.S. and Winn, J.N.
Astrophys. J., 655, 550-563, (2007).

Gimenez, A.
Astrophys. J., 297, 405-412, (1985).

Griffin, R.F. and Boffin, H.M.J.
The Observatory, August 2003.

Guillot T., Santos N. C., Pont F., Iro N., Melo C., Ribas, I.,
Astron. and Astrophys., 453, L21-24, (2006).

Hadrava, P.
Astron. and Astrophys. Suppl. Ser., 114, 393-396, (1995).

Harmanec, P. and Prša, A.
Publ. Astron. Soc. Pacific, 123, 976-980, (2011).

Hartmann, J.
Astrophys. J., 27, 254-259, (1908).

Hayashi, C.
Publ. Astron. Soc. Japan, 13, 450-452, (1961).

Hebb, L. and 34 coauthors.
Astrophys. J., 693, 1920–1928, (2009).

Heckmann, O.
Hamburg-Bergedorf: Hamburger Sternwarte, edited by Dieckvoss, W. (1975).

Hellier, C. and 22 coauthors.
Nature, 460, 1098-1100, (2009).

Hełminiak, K.G., Konacki, M., Ratajczak, M. and Muterspaugh, M.W.
Mon. Not. R. Astr. Soc., 400, 969-983, (2009).
Hełminiak, K.G. and Konacki, M.
Astron. and Astrophys., 526, id.A29 (2011).

Hełminiak, K. G.; Konacki, M.; Złoczewski, K.; Ratajczak, M.; Reichart, D. E.; Ivarsen, K. M.; Haislip, J. B.; Crain, J. A.; Foster, A. C.; Nysewander, M. C.; Lacluyze, A. P.
Astron. and Astrophys., 527, id.A14, (2011).

Henry, G.W., Fekel, F.C., Sowell, J.R and Gearhart, J.S
Astron. J., 132, 2489-2495, (2006).

Henyey, L.G., Lelevier, R. and Levée, R.D
Publ. Astron. Soc. Pacific, 67, 154-160, (1955).

Hilditch, R.W.,
Cambridge University Press, 2001, ISBN 0 521 79800 0 (paperback).

Høg, E., Fabricius, C., Makarov, V.V., Urban, S., Corbin, T., Wycoff, G., Bastian, U., Schwekendiek, P. and Wicenec, A.
Available as Catalogue I/259 in the VizieR service.

Holman, M.J., Winn, J.N., Latham, D.W., O'Donovan, F.T., Charbonneau, D., Torres, G., Sozzetti, A., Fernandez, J., and Everett, M.E.
Astrophys. J., 664, 1185-1189, (2007).

Holmberg J., Nordström B., Andersen J.,
Astron. Astrophys. 475, 519-537, (2007). (H07)

Holmberg J., Nordstrom B. and Andersen J.
Astron. Astrophys. 501, 941-947, (2009). (Vizier Catalogue V/130).

Horne, K.
Publ. Opt. Soc. Pacific, 98, 609-617, (1986).

Howard A.W and 63 coauthors
Astrophys. J. Supp. Series, 201, id15, 20 pp, 2012.

Howarth, I.D., Siebert, K.J., Hussain, G.A.J. and Prinja, R.K.
Mon. Not. R. Astron. Soc., 284, 265-285, (1997).

Hoxie, D.T.,
Astron. and Astrophys., 26, 437-441, (1973).

Huber, D. and 29 coauthors
Astrophys. J., 760, id.32, 17 pp, (2012).

Huber, D. and 33 coauthors
Astrophys. J., 767, id.127, 17 pp, (2013).

Hübscher, J.
Inf. Bull. Var. Stars, No. 5643, (2005).
Konkoly Observatory, Budapest.

Hübscher, J., Paschke, A. and Walter, F.
Inf. Bull. Var. Stars, No. 5657, (2005).
Konkoly Observatory, Budapest.

Hübscher, J. and Lehmann, P.B.
Inf. Bull. Var. Stars, No. 6070, (2013).
Konkoly Observatory, Budapest.

Hut, P.,
Astron. and Astrophys., 99, 126-140, (1981).

Ida, S. and Lin, D.N.C.,
Astrophys. J., 616, 567-572, (2004).

Iglesias, C.A. and Rogers, F.J.
Astrophys. J., 464, 943-953, (1996).

Ilijić, S.
M.Sc thesis submitted to the University of Zagreb, Croatia, 2003.

Ilijić, S., Hensberge, H., Pavlovski, K. and Freyhammer, L.M.
In "Spectroscopically and Spatially Resolving the Components of the Close Binary Stars", Proceedings of the Workshop held 20-24 October 2003 in Dubrovnik, Croatia.
Edited by R. W. Hilditch, H. Hensberge and K. Pavlovski. ASP Conference Series, Vol. 318. San Francisco:
Astronomical Society of the Pacific, 2004, p. 111-113

Imbert, M. and Prévot, L.
The Messenger, No.25, 6-7, (1981).

International Astronomical Union
"Working Group on Extrasolar Planets: Definition of a "Planet" "
Position Statement, 28 February 2003.

Irwin, J.M. and 16 coauthors
Astrophys. J., 742, id. 123, 21 pp, (2011).

Ivezić, Ž. and 25 coauthors.
Serb. Astron. J., 176, 1-13, (2008).

Jackson B., Barnes R., Greenberg R.,
Astrophys. J., 698, 1357-1366, (2009).

Jeffers, H.M., van der Bos, W.H. and Greeby, F.M.
Publications of the Lick Observatory, Mount Hamilton: University of California, Lick Observatory, 1963.

Jenkner, H., Lasker, B.M., Sturch, C.R., McLean, B.J., Shara, M.M. and Russell, J.L.,
Astron. J., 99, 2082-2154, (1990).

Johnson D.R.H., Soderblom D.R.,
Astron. J., 93, 864-867, (1987).

Johnson, J.A., Marcy, G.W., Fischer, D.A., Laughlin, G., Butler, R.P., Henry, G.W.,
Valenti, J.A., Ford, E.B., Vogt, S.S. and Wright, J.T.
Astrophys, J., 647, 600-611, (2006).

Johnson, H. L., and Morgan, W. W.
Astrophys. J., 117, 313–352, (1953).

Joshi, Y.C.
Mon. Not. R. Astron. Soc. 378, 768-776, (2007).

Just, A. and Jahreiss, H.
Mon. Not. R. Astron. Soc. 402, 461-478, (2010).
Kaiser, D.H.
Inf. Bull. Var. Stars, No. 4119, (1994).
Konkoly Observatory, Budapest.

Kaiser, D.H., Terrell, D., Baldwin, M.E., Gunn, J., Stephan, C., and Hakes, B.,
Inf. Bull. Var. Stars, No. 4168, (1995).
Konkoly Observatory, Budapest.

Kaiser, D.H. and Frey, G.
Inf. Bull. Var. Stars, No. 4544, (1998).
Konkoly Observatory, Budapest.

Kaiser, M.L., Kucera, T.L., Davila, J.M., St. Cyr, O.C., Guhathakurta, M., and
Christian, E.
Space Sci Rev., 136: 5–16, (2008).

Kalas,P., Graham, J.R., Chiang, E., Fitzgerald, M.P., Clampin, M., Kite, E.S.,
Stapelfeldt, K., Marois, C. and Krist, J.
Science. 322, 1345-1348, (2008).

Kaluzny, J., Thompson, I.B., Rozyczka, M., Dotter, A. Krzeminsky, W., Pych, W.,
Rucinski, S.M., Burley, G.S. and Shectman. S.A.
Astron. J., 145, id43, 13 pp, (2013).

Kaluzny, J., Thompson, I.B., Dotter, A.,Rozyczka, M., Pych, W., Rucinski, S.M.,
Burley, G.S.
Acta Astronomica, 64, 11-26, (2014).

Kervella, P., Thévenin, F., Di Folco, E. and Ségransan, D.
Astron. and Astrophys. 426, 297-307, (2004).

Kharchenko N.V., Scholz R.-D., Piskunov A.E., Roeser S. and Schilbach E.
Astron. Nachr., 328, 889-896, (2007).

Kopal, Z., “Close Binary Systems”, Chapman and Hall, London, U.K. (1959).

Kordopatis, G, and 50 coauthors,
Astron. J., 146, id134 , 36 pp, (2013).

Kraus, A.L., Tucker, R.A., Thompson, M.L., Craine, E.R. and Hillenbrand, L.A.
Astrophys, J., 728, id48 ,18 pp, (2011).

Kroupa, P.,
Mon. Not. R. Astron. Soc., 322, 231-246, (2001).

Kurtz, M.J., Mink, D.J., Wyatt, W.F., Fabricant, D.G., Torres, G., Kriss, G.A. and Tonry, J.L. (1992).
A.S.P. Conference Series, Vol. 25, 1992, Page 432,
Eds. Worrall, D.M., Biemesderfer, C. and Barnes, J.

Kurucz, R.L., CD-ROM 13, Smithsonian Astrophysical Laboratory, (1993).

Lacy, C.H.,
Astrophys. J. Supp. Ser., 34, 479-492, (1977).

Lacy, C.H.S, Hood, B. and Straughn, A.
Inf. Bull. Var. Stars, No. 5067, (2001).
Konkoly Observatory, Budapest.

Lacy, C.H.S.,
Inf. Bull. Var. Stars, No. 5357, (2002).
Konkoly Observatory, Budapest.

Lacy, C.H.S.,
Inf. Bull. Var. Stars, No. 5487, (2003).
Konkoly Observatory, Budapest.

Lacy, C.H.S., Claret, A., Sabby, J.A., Hood, B. and Secosan, F.
Astron. J., 128, 3005-3011, (2004).

Lacy, C.H.S., Torres, G., Claret. A. and Vaz, L.P.R.
Astron. J., 130, 2838-2846, (2005).

Lacy, C.H.S., Torres, G., Claret, A. and Menke, J.L.
Astron. J., 131, 2664-2672, (2006).

Lacy, C.H.S.,
Inf. Bull. Var. Stars, No. 5910, (2009).
Konkoly Observatory, Budapest.

Lacy, C.H.S, Torres, G., Claret, A., Charbonneau, D., O’Donovan, F.T. and Mandushev, G.
Astron. J., 139, 2347-2359, (2010).

Lacy, C.H.S.,
Inf. Bull. Var. Stars, No. 5972, (2011).
Konkoly Observatory, Budapest.

Lacy, C.H.S. and Fekel, F.C.
Astron. J., 142, id. 185, (2011).

Lacy, C.H.S.,
Inf. Bull. Var. Stars, No. 6014, (2012).
Konkoly Observatory, Budapest.

Lacy, C.H.S., Torres, G., Fekel, F.C., Sabby, J.A. and Claret, A.
Astron. J., 143, id. 129, 18 pp, (2012).

Lastennet, E., Fernandes, J., Valls-Gabaud, D and Oblak,J.
Astron. and Astrophys. 409, 611-618, (2003).

Latham, D.W.
IAU Colloquium No. 88, P.21, (1985).

Latham, D.W., Nordström, B., Andersen, J., Torres, G., Stefanik, R.P., Thaller, M. and Bester, M.J.
Astron. and Astrophys. 314, 864-870, (1996).

Latham, D.W. and 18 coauthors.
Astrophys. J., 704, 1107-1119, (2009).

Lehmann-Filhes, R.
Astronomische Nachrichten., 136, 17-30, (1894).

Levrard, B., Winisdoerffer, C. and Chabrier, G.
Astrophys. J. Lett., 692, L9-L13, (2009).

Lindegren, L. and Dravins, D.
Astron. and Astrophys., 401, 1185–1201, (2003).

Lopez-Morales, M
Astrophys. J., 660, 732– 739, (2007).

Lovis, C. and Mayor, M.
Astron. and Astrophys., 472, 657–664, (2007).

McCullough, P.R. and 13 coauthors.
Astrophys. J., 648, 1228-1238, (2006).

Majewski, S.R.
A Giant Step: from Milli- to Micro-arcsecond Astrometry, Proceedings of the International Astronomical Union, IAU Symposium, Vol. 248, 450-457 (2008).

Mandel, K. and Agol, E.
Astrophys. J. Lett., 580, L171-L175, (2002).

Marsh, T.
Publ. Opt. Soc. Pacific, 101, 1032-1037, (1989).

Mason, B.D., Wycoff, G.L., Hartkopf, W.I., Douglass, G.G. and Worley, C.E.
"The 2001 US Naval Observatory Double Star CD-Rom.
Astron. J., 122, 3466-3471, (2001).

Maxted, P.F.L., Heber, L., Marsh, T.R. and North, R.C.
Mon. Not. R. Astron. Soc., 326, 1391- 1402, (2001).

Maxted, P.F.L., Hutcheon, R.J., Torres, G., Lacy, C.H.S., Southworth, J., Smalley, B., Pavlovski, K., Marschall, L.A. and Clausen, J.V.
Accepted by Astron. and Astrophys. (2015).

Mayor, M. and Queloz, D.
Nature, 378, 355 – 359, (1995).

Mayor, M and 13 coauthors
arXiv:1109.2497v1 (2011).

Mazeh, T.
Proceedings IAU Symposium No. 253, 11-19 (2009).

Meibom, S., Grundahl, F., Clausen, J.V., Mathieu, R.D., Frandsen, S., Pigulski, A., Narvid, A., Steslicki,M. and Lefever, K.
Astron. J., 137, 5086-5098, (2009).

Milone, E.F., Kurpinsky-Winiarska, M. and Oblak, E.
Astron. J., 140, 129-137, (2010).

Miyamoto, M. and Nagai, R.
Publ. Astron. Soc. Japan, 27, 533-543, (1975).

Momany Y., Zaggia S., Gilmore G., Piotto G., Carraro G., Bedin, L.R., De Angeli F.,
Astron. and Astrophys., 451, 515–538, (2006).

Morales, J.C., Ribas, I. and Jordi, C.
Astron. and Astrophys., 478, 507–512, (2008).

Morales, J.C. and 14 coauthors.
Astrophys. J., 691, 1400–1411, (2009a).

Morales, J.C., Torres, G., Marschall, L.A. and Brehm, W.
Astrophys. J., 707, 671–685, (2009b).

Morales, J.C., Gallardo, J., Ribas, I., Jordi, C., Baraffe, I. and Chabrier, G.
Astrophys. J., 718, 502–512, (2010).

Moutou, C. and 12 coauthors.
Astron. and Astrophys. 527, id.A63, 11 pp, (2011).

Munari, U., Tomov, T., Zwitter, T., Milone, E.F., Kallrath, J., Marrese, P.M., Boschi, F., Prša, A., Tomasella, L. and Moro, D.
Astron. and Astrophys. 378, 477-486, (2001).

Nelson, B. and Davis, W.D.
Astrophys. J., 174, 617-628, (1972).

Nichols, R.W.
J. Quant. Spectr. Rad. Trans., 40, 275-289, (1988).

Ochsenbein F., Bauer P., Marcout J., 2000,
Astron. and Astrophys. Supp., 143, p.23-32

Ohta, Y., Taruya, A. and Suto, Y.
Astrophys. J., 622, 1118-1135, (2005).

Olsen, E.H.
Astron. and Astrophys. 189, 173-178, (1988).

Paczyński, B., Szczygiel, D., B. Pilecki, B. and Pojmański, G.
Mon. Not. Royal Astr. Soc., 368, 1311-1318, (2006).

Pavlovski, K. and Hensberge, H.
ASP Conference Series Proceedings of 'Binaries - Key to Comprehension of the Universe". (Brno, Czech Republic, 2009).

Perryman, M.A.C. and 19 coauthors.
Astron. Astrophys. 323, L49–L52 (1997).

Pfeiffer, M.J., Frank, C., Baumüller, D., Fuhrmann, K. and T. Gehren, T.
Astron. Astrophys. Suppl. Ser. 130, 381 – 393, (1998).

Pojmanski, G. urvey
Acta Astronomica, 47, 467-481, (1997).

Pollacco, D.L. and 27 coauthors.
Proc. Astron. Soc. Pacific, 118, 1407-1418, (2006).

Popper, D.M. and Etzel. P.B.
Astronom. J., 86, 102-120, (1981).

Popper, D.M.
Astrophys. J., 254, 203-213, (1982).

Popper, D.M., Lacy, C.H., Frueh, M.L. and Turner, A.E.
Astronom. J., 91, 383-404, (1986).

Popper, D.M.
Astronom. J., 114, 1195-1205, (1997).

Pourbaix D., Tokovinin, A.A., Batten, A.H., Fekel, F.C., Hartkopf, W.I., Levato, H., Morell, N.I., Torres, G. and Udry S.
Astron. Astrophys. 424, 727-732, (2004).

Press, W.H., Teukolsky, S.A., Vetterling, W.T. and Flannery, B.P.
Third Edition, Cambridge University Press, ISBN-1-: 0521880688, (2007).

Prša, A., Pepper, J. and Stassun K.G.
Astronom. J., 142, id52, 8pp, (2011).

Queloz, D., Eggenberger, A., Mayor, M., Perrier, C., Beuzit. J.L., Naef, D., Sivan, J.P. and Udry, S.
Astron. and Astrophys. 359, L13–L17 (2000).

Queloz, D., Henry, G. W., Sivan, J. P., Baliunas, S. L., Beuzit, J. L., Donahue, R. A., Mayor, M., Naef, D., Perrier, C. and Udry, S.
Astron.and Astrophys., 379, 279-287, (2001).

Raghavan, D., McAlister, H.A., Henry, T.J., Latham, D.W., Marcy, G.W., Mason, B.D., Gies, D.R., White, R.J. and ten Brummelar, T.A.
Astrophys. J. Supp, 190, 1-42, (2010).

Rauer, H and 160 coauthors
Eprint arXiv:1310.0696.

Reid, M.J.
Ann. Rev. Astron. and Astrophys., 31, 345-372, (1993).

Ribas, I.
Astron.and Astrophys., 398, 239–251, (2003).

Ribas, I.
Astrophys. and Space Sci., 304, 89-92, (2006).

Roeser S., Bastian U.
Astron. Astrophys. Suppl. Ser. 74, 449 (1988)

Russell, H.N.,
Astrophys..J., 15, 252-260, (1902).

Russell, H.N.,
In "Astronomy", Vol. 2, by H.N. Russell, R.S. Dugan and J.Q. Stewart, Ginn and Co., Boston, p. 910, (1927).

Russell, H.N.,
Mon. Not. Royal Astr. Soc., 88, 641-643, (1928).

Ressell, H.N.,
Mon. Not. Royal Astr. Soc., 91, 951-966, (1931).

SAO staff.
Smithsonian Astrophysical Observatory Staff, Publications of the Smithsonian Institution of Washington, D.C., no. 4652, 4 vols., 1966, (Reprinted 1971).

Sabby, J.A. and Lacy, C.H.S.
Astronom. J., 125, 1448-1457, (2003).

Salpeter, E.E.
Astrophys..J., 121, 161-167, (1955).

Samus, V.V., Durlevich, O.V., Kazarovets E V., Kireeva N.N., Pastukhova E.N., Zharova A.V., et al.
General Catalog of Variable Stars (GCVS database, Version 2012 Jan).

Santos, N. C., Mayor, M., Naef, D., Pepe, F., Queloz, D., Udry, S., Burnet, M., Clausen, J. V., Helt, B. E., Olsen, E. H. and Pritchard, J. D.
Astron. and Astrophys., 392, 215-229, (2002).

Santos N.C., Israelian G., Mayor M., 2004, A&A, 415, 1153
Astron. and Astrophys., 415, 1153-1166, (2004). (Sant04)

Sato, B. and 20 coauthors.
Astrophys. J., 633, 465-473, (2005).

Scalo, J.,
ASP Conferenced Series, "The Stellar Initial Mass Function", 142, 201-236, (1998).

Schlaufman K.C., Laughlin G.,
Astrophys. J., 738, Art. id. 177, (2011).

Seagar, S. and Mallén-Ornelas, G.
Astrophys. J. 585, 1038-1055, (2003).

Serenelli, A.
AIP Conf. Proc., 1594, 137-145, (2014).

Setiawan, J., Weise, P., Henning, Th., Launhardt, R. and Müller, A.
Astrophys. J., 660, L145–L148, (2007).

Shakura, N.I.
Sov. Astron.Lett. 11, 224-226, (1985).

Shporer, A. and Brown, T.
Astrophys. J., 733, id.30, 5 pp, (2011).

Siess, L., Forestini, M. and Bertout, C.
Astron. and Astrophys., 326, 1001-1012, (1997).

Simkin, S.M.
Astron. and Astrophys., 31, 129-136, (1974).

Simon, K.P. and Sturm, E.
Astron. and Astrophys., 281, 286-291, (1994).

Skrutskie, M.F. and 30 coauthors.
Astron.J, 131, 1163-1183, (2006).
Available as Catalogue II/246 in the VizieR service

Smalley, B., Smith, K. C., & Dworetsky, M. M. 2001, UCLSYN Userguide (unpublished).

Smart, W.M., 1953, "Celestial Mechanics", Longmans, London.

Smith, K. C., 1992, Ph.D. Thesis, University of London.

Southworth, J., Maxted, P. F. L. and Smalley, B.
Mon. Not. R. Astron. Soc., 349, 547-559, (2004a).

Southworth, J., Maxted, P. F. L. and Smalley, B.
Mon. Not. R. Astron. Soc., 351, 1277-1289, (2004b).

Southworth, J., Zucker, S., Maxted, P. F. L. and Smalley, B.
Mon. Not. R. Astron. Soc., 355, 986-994, (2004c).

Southworth, J., Smalley, B., Maxted, P.F.L., Claret, A. and Etzel, P.B. (2005),
Mon. Not. R. Astron. Soc., 363, 529-542. (2005).

Southworth, J.
Thesis submitted under the name of J.K.Taylor to University of St. Andrews, (2006).

Southworth, J.
Mon. Not. R. Astron. Soc., 386, 1644-1666, (2008).
Southworth, J.
Mon. Not. R. Astron. Soc., 394, 272-294, (2009).

Southworth, J.
Mon. Not. R. Astron. Soc., 408, 1689-1713, (2010).

Southworth, J.
Mon. Not. R. Astron. Soc., 417, 2166-2196, (2011).

Southworth, J. and 31 coauthors.
Astron. and Astrophys., 527, id.A8, 5 pp, (2004).

Southworth, J., Pavlovski, K., Tamajo, E., Zucker, S., Smalley, B., West, R.G.
and Anderson, D.R.
Mon. Not. R. Astron. Soc., 414, 3740-3750, (2011).

Southworth, J.
Proceedings of the workshop "Orbital Couples: Pas de Deux in the Solar System and the Milky Way". Held at the Observatoire de Paris, 10-12 October 2011. Editors: F. Arenou, D. Hestroffer. ISBN 2-910015-64-5, p. 51-58, (2012).

Sozzetti, A., Torres, G., Charbonneau, D., Latham, D.W., Holman, M.J., Winn, J.N., Laird, J.B. and O'Donovan, F.T.
Astrophys. J. 664, 1190-1198, (2007).

Sterne, T.E.,
Mon. Not. Royal Astr. Soc., 99, 451-462, (1939).

Strömgren, B.,
Vistas in Astronomy, 2 , Issue 1, 1336–1346, (1956).

Takeda, Y. and 15 coauthors.
Publ. Astron. Soc. Japan 57, 13–25, (2005).

Tomkin, J. and Fekel. F.C
Astron. J., 131, 2652-2663, (2006).

Tonry, J. and Davis, M.
Astron. J., 84, 1511-1525, (1979).

Torres, G., Stefanik, R.P., Andersen, J., Nordström, B., Latham, D.W. and Clausen, J.V.
Astron. J., 114, 2764-2777, (1997).

Torres, G., Lacy, C.H.S., Claret, A., Zakirov, M.M., Arzumanyants, N., Bayramov, N., Hojaev, A.S., Stefanik, R.P., Latham, D.W. and Sabby, J.A.
Astron. J., 118, 1831-1844, (1999).

Torres, G., Lacy, C.H.S., Claret, A. and Sabby, J.A.
Astron. J., 120, 3226-3243, (2000).

Torres, G., and Ribas, I.
Astrophys. J. 567, 1140-1165, (2002).

Torres, G., Lacy, C.H., Marschall, L.A., Sheets, H.A. and Mader, J.A.
Astrophys. J., 640, 1018–1038, (2006).

Torres, G., Winn, J.N. and Holman, M.J.
Astrophys. J., 677, 1324–1342, (2008).

Torres, G., Andersen. J. and Giménez, A.
Astron. and Astrophys. Rev., 18, 67–126, (2010).

Torres, G., Vaz, L.P.R., Sandberg Lacy, C.H. and Claret, A.
Astron. J., 147, id.36, 11 pp. (2014).

Torres, G., Lacy, C.H.S., Pavlovski, K., Feiden, G.A., Sabby, J.A., Bruntt, H. and Clausen, J.V.
Astrophys. J., 797, id.31, 16 pp, (2014).

Triaud, A.H.M.J and 16 coauthors
Astron. and Astrophys., id. A25, 22 pp, (2010).

Turner, D.G.
Astrophys. and Space Science, 326, 219–231, (2010).

Udalski, A., Paczynski, B., Zebrun, K., Szymanski, M., Kubiak, M., Soszynski, I., Szewczyk, O., Wyrzykowski, L. and Pietrzynski, G. (2002).
Acta Astronomica, 52, 1-27, (2002).

Udalski, A.
Transiting Extrapolar Planets Workshop ASP Conference Series, Vol. 366
Astronomical Society of the Pacific, 2007, p.51.

Underhill, A.B., "The Early Type Stars", p.127, (1966). Publisher not known.

Valenti, J. A. and Piskunov, N.
Astron. and Astrophys. Supp., 118, 595 – 603, (1996).

Valenti J.A., and Fischer D.A.
Astrophys. J. Supp. Series, 159, 141-166. (2005). (VF05)

VandenBerg, D.A., Bergbusch, P.A. and Dowler, P.D.
Astrophys. J. Supp. Series, 162, 375-387, (2006).

Van Hamme, W
Astron. J., 106, 2096-2117, (1993).

van Leeuwen, F.
Astron. and Astrophys., 474, 653-664, (2007).

Voges, W. and 19 coauthors
Astron. and Astrophys., 349, 389-405, (1999).

Vogt, H.
Astron. Nachr., 226, 301-304, (1926).

Vogt, S.S., Butler, R.P., Marcy, G.W., Fischer, D.A., Pourbaix, D., Apps, K. and Laughlin, G.
Astrophys. J., 568, 352–362, (2002).

von Weizsäcker, C.F.
Physikalische Zeitschrift, 39, 633-646, (1938).

Westera, P., Lejeune, T., Buser, R., Cuisinier, F. and Bruzual, G.
The models themselves are available at www.astro.unibas.ch/BaSeL_corr.html

White, N.M.,
Vistas in Astronomy, Vol. 30, 13-25, (1987).

Wilsing, J.,
Astronomische Nachrichten, 134, 89-92, (1893).

Winn, J.N.
The Astrophysics of Planetary Systems: Formation, Structure, and Dynamical Evolution, Proceedings of the International Astronomical Union, IAU Symposium, Volume 276, 230-237, (2006).

Winn, J.N. and 33 coauthors
Astrophys. J. Lett., 741, id. L1, 6 pp., (2011).

Wolf, M., Claret, A., L. Kotková, L., Kučáková, H., Kocián, R., Brát, L., Svoboda, P., and Šmelcer, L.
Astron. and Astrophys., 509, A18, (2010).

Wolfe, R.H., Horak, H.G., and Storer, N.W. in Hack M., ed., Modern Astrophysics: A memorial to Otto Struve, Gordon and Breach, New York, p. 251, (1967).

Wolszczan, A. and Frail, D.A.
Nature, 355, 145 – 147, (1992).

Woltjer, R.
Bulletin Astron. Institutes Netherlands, 1, 95, (1922).

Wraight, K.T., White, G.J., Bewsher, D. and Norton, A.J.
Mon. Not. Royal Astr. Soc., 416, 2477-2493, (2011).
Wright J.T.,
Publ. Astron. Soc. Pacific, 117, 657-664, (2005).

Yakut, K., Aerts, C. and Morel, T.
Astron. and Astrophys., 467, 647-655, (2007).

Zacharias, N., Monet, D. G., Levine, S. E., Urban, S. E., Gaume, R. and Wycoff, G. L.
American Astronomical Society Meeting 205, #48.15; Bulletin of the American Astronomical Society, Vol. 36, 1418, (2004).
Available as Catalogue I/297 in the VizieR service.

Zahn, J-P.
Astron. and Astrophys., 57, 383-394, (1977).

Zahn, J-P.
Astron. and Astrophys., 67, 162, (1978).

Zahn, J-P.
Astron. and Astrophys., 288, 829-841, (1994).

Zahn, J-P. and Bouchet, L.,
Astron. and Astrophys., 223, 112-118, (1989).

Zahn, J-P.
EAS Publications Series, 29, 67-90, (2008).

Zasche, P. and Wolf, M.
Astron. and Astrophys., 558, id.A51, (2013).

Zucker S. and Mazeh T.,
Astrophys. J., 420, 806-810, (1994).

.

Website Reference List

Aerts (lecture notes): www.ster.kuleven.be/ ~zima/helasna5/Downloads/ astero2007.pdf

ASAS: www.astrouw.edu.pl/asas/

BaSeL stellar flux models: www.astro.unibas.ch/BaSeL_corr.html

CORAVEL standard stars: obswww.unige.ch?~udry/std,stdcor.dat

Dartmouth Stellar Evolution Database : www.stellar.dartmouth.edu?~models/isolf.html
Also www.adsabs.harvard.edu/abs/2008ApJS..178...89D

DEBCat (Southworth): www.astro.keele.ac.uk/jkt/debcat

European Extremely Large Telescope (E-ELT): www.eso.org/sci/facilities/eelt

Extrasolar Planets Encyclopaedia : www.exoplanet.eu

Gaia mission : www.sci.esa.int/gaia

Gray, Spectral Atlas: www.ned.ipac.caltech.edu/level5/Gray/Gray_contents.html

HARPS facility: www.eso.org/eci/facilities/lasills/instruments.harps.html

Hertzsprung-Russell diagram (1):
www.atnf.csiro.au/outreach/education/senior/astrophysics/
stellarevolution_hrintro.html

Hertzsprung- Russell diagram (2):
www.sci.esa.int/education/35774-stellar-radiation-stellar-types/?fbodylongid=1703

IBVS: Information Bulletin on Variable Stars, published by the Konkoly Observatory, Budapest, Hungary. www.konkoly.hu/IBVS.

INT STARALT: www.catserver.ing.iac.es/staralt/index.php.

jktabsdim (Southworth): www.astro.keele.ac.uk/jkt/codes/jktabsdim

JWST (James Webb Space Telescope):

Kolmogorov-Smirnov (KS) test: www.physics.csbsju.edu/stats/KS-test.html

LSST (Large Synoptic Survey Telescope): www.lsst.org/lsst/news

Mamajek (absolute bolometric magnituide of the Sun):
www. sites.google.com/site/mamajeksstarnotes/bc-scale

MOLLY: www2.warwick.ac.uk/fac/sci/physics/research/astro/people/marsh/software

NFO: www.webscope.nfo.edu

NOMAD : VizieR catalogue I/297, accessed via vizier.u-strasbg.fr/viz-bin/VizieR

Roche lobes: www.hemel.waarnemen.com/Informatie/Sterren/hoofdstuk6.html#mtr

Rough mass/radius relation: www.astronomy.ohio-state.edu/~dhw/Intro/lec6.html

SBOP: www.mintaka.sdsu.edu/faculty/etzel/

SIMBAD :SIMBAD.u-strasbg.fr/SIMBAD

Southworth (PAMELA software):
www.astro.keele.ac.uk/jkt/GrSpInstructions/GrSpInstructions.html

Southworth (Thesis): www.astro.keele.ac.uk/jkt/pubs.html

Standard ESO spectra:
www.eso.org/sci/observing/tools/uvespop/field_stars_uptonow.html

SuperWASP: www.superwasp.org

TESS mission: www.tess.gsfd.nasa.gov

TOPCAT: www.star.bristol.ac.uk/~mbt/topcat and www.starlink.ac.uk/topcat

uvbysplit routine (Southworth): webpage at www.astro.keele.ac.uk

Veusz scientific plotting package: www.home.gna.org/veusz/docs/manual.html

VizieR catalogue service: www.vizier. u-strasbg.fr

Vogt-Russell theorem**:** www.mpagarching.mpg.de/~weiss/Cox_Vol_II_CD/ch18.pdf.

APPENDIX A. OBSERVING LOG FOR THE INT OBSERVATIONS OF V1094 TAU

The times when the INT spectra provided by Maxted and Southworth (private communication) were taken are listed below.

Spectrum Number	Run No.	Day Oct.02	Time Hour	Min.	Sec.	Heliocentric Julian Date	Phase
1	323574	14	1	58	43	52561.5865	0.16974
2	323575	14	2	4	3	52561.5902	0.17015
3	323576	14	2	9	23	52561.5940	0.17056
4	323577	14	2	14	43	52561.5977	0.17098
5	323578	14	2	20	3	52561.6014	0.17139
6	323631	14	5	55	3	52561.7507	0.18800
7	323632	14	6	0	23	52561.7544	0.18841
8	323633	14	6	5	43	52561.7581	0.18882
9	323634	14	6	11	3	52561.7618	0.18924
10	323635	14	6	16	23	52561.7655	0.18965
11	323645	14	6	35	41	52561.7789	0.19114
12	323646	14	6	41	1	52561.7826	0.19155
13	323763	15	1	24	23	52562.5627	0.27834
14	323764	15	1	29	44	52562.5664	0.27876
15	323765	15	1	35	4	52562.5701	0.27917
16	323783	15	4	5	10	52562.6744	0.29076
17	323784	15	4	10	30	52562.6781	0.29118
18	323785	15	4	15	50	52562.6818	0.29159
19	323822	15	6	20	42	52562.7685	0.30123
20	323823	15	6	26	2	52562.7722	0.30165
21	323824	15	6	31	22	52562.7759	0.30206
22	323917	16	2	40	49	52563.6158	0.39550
23	323918	16	2	46	9	52563.6195	0.39591
24	323919	16	2	51	29	52563.6232	0.39632
25	323953	16	6	12	58	52563.7631	0.41189
26	323954	16	6	18	18	52563.7668	0.41230
27	323955	16	6	23	38	52563.7705	0.41271
28	324330	18	3	44	3	52565.6597	0.62289
29	324331	18	3	49	23	52565.6634	0.62330

30	324332	18	3	54	43	52565.6671	0.62371
31	324369	18	4	53	33	52565.7080	0.62826
32	324370	18	4	58	53	52565.7117	0.62867
33	324371	18	5	4	14	52565.7154	0.62909
34	324408	18	6	5	31	52565.7579	0.63382
35	324409	18	6	10	52	52565.7617	0.63423
36	324410	18	6	16	12	52565.7654	0.63465
37	324411	18	6	21	33	52565.7691	0.63506
38	324412	18	6	26	53	52565.7728	0.63547
39	324528	19	5	8	40	52566.7185	0.74068
40	324529	19	5	14	3	52566.7222	0.74110
41	324530	19	5	19	25	52566.7259	0.74151
42	324531	19	5	24	47	52566.7297	0.74193
43	324532	19	5	30	9	52566.7334	0.74234
44	324543	19	6	10	5	52566.7611	0.74543
45	324544	19	6	15	27	52566.7648	0.74584
46	324545	19	6	20	50	52566.7686	0.74626
47	324546	19	6	26	12	52566.7723	0.74667
48	324547	19	6	31	34	52566.7760	0.74709
49	324548	19	6	38	7	52566.7806	0.74759
50	324549	19	6	43	30	52566.7843	0.74801
51	324550	19	6	46	57	52566.7867	0.74827
52	324612	21	2	54	23	52568.6252	0.95281
53	324613	21	2	59	39	52568.6289	0.95322
54	324614	21	3	4	56	52568.6325	0.95363
55	324651	21	5	40	39	52568.7407	0.96566
56	324652	21	5	45	55	52568.7443	0.96606
57	324653	21	5	51	11	52568.7480	0.96647
58	324965	22	6	20	57	52569.7687	0.08002
59	324966	22	6	26	14	52569.7723	0.08043
60	324967	22	6	31	30	52569.7760	0.08084
61	324968	22	6	36	47	52569.7797	0.08125
62	324969	22	6	42	4	52569.7833	0.08165
63	324970	22	6	47	24	52569.7870	0.08207
64	325296	23	5	54	21	52570.7502	0.18922
65	325297	23	5	59	38	52570.7539	0.18963

The phase is given relative to the primary minimum.

All exposures were taken in the wavelength range 4227-4499Å with an exposure time of 300 seconds.

Some exposures were not analysed by TODCOR since the two peaks of the correlation spectrum could not be resolved. These were Exposures 28-38 (near the secondary minimum at phase ~ 0.652) and 58-63 (near the primary minimum)

APPENDIX B STANDARD SYMBOLS FOR STUDIES OF BINARY STARS

The standard symbols used throughout this thesis for binary star parameters are listed below.

M_1,M_2	Masses of the two stars
q	Mass ratio m_2/m_1
R_1, R_2	Radii of the stars relative to the semi-major axis of the relative orbit.
a_1, a_2	Semi-major axes of the orbits of each star, also $a = a_1 + a_2$.
e	Eccentricity.
ω	Angle of periastron
i	Inclination of the orbit.
K_1, K_2	Amplitude of the radial velocities of each star.
γ	Systemic velocity
$S_2/S_1 = J$	Surface brightness ratio of the secondary to the primary.
$L_2/L_1 = k$	Luminosity ratio of the secondary to the primary.
U	Period of apsidal motion.

APPENDIX C DETERMINATION OF RADIAL VELOCITIES BY MOLLY/`xcor` CROSS-CORRELATION SOFTWARE

C.1 Introduction

A spectrum of a binary is a blend of the spectra from each of these two stars where the spectral profile depends on the relative radial velocity at the time of observation. The radial velocity of each star can be extracted from this blended spectrum by analysing the correlation between the observed spectrum and a template spectrum of a standard single star. When this method was first introduced the same template was used for both stars. The two spectra are plotted by logarithmic wavelength so that a given step on the wavelength axis always corresponds to the same Doppler shift, and the template spectrum is Doppler shifted to give the best fit to the observed spectrum. The basic concept is that the template spectrum is dragged across the target spectrum until the greatest degree of overlap is obtained; this shows that the template should be from a star of a similar spectral type as the target system. This concept may be expressed in precise mathematical form as a cross-correlation function, as was done first by Simkin (1974) and later by Tonry and Davis (1979). In the formalism of Tonry and Davis, a spectrum is treated as in *n* discrete bins. The bins are defined as logarithmic functions of wavelength i.e. the spectrum is expressed as *f(n)* where $f(n) = A \ln \lambda + B$ so that a Doppler shift corresponds to a uniform shift of the spectrum. The cross-correlation function may be written:

$$C_{f,g}(s) = \frac{\sum_n f(n) g(n-s)}{N \sigma_f \sigma_g} \qquad \text{C.1}$$

In this expression

$C_{f,g}(s)$	is the cross-correlation function
g (n)	is the template spectrum
g (n – s)	is the template spectrum shifted through s bins
N	is the number of bins in each spectrum
σ_f and σ_g	are the r.m.s values of the spectra such that

$$\sigma_f^2 = \frac{1}{N}\sum_n f(n)^2$$

and similarly for σ_g

The cross-correlation spectrum is therefore a plot of $C_{f,g}(s)$ against radial velocity expressed here as "s." The equation C.1 is defined so that if the template spectrum $g(n)$ is exactly the same as the observed spectrum $f(n)$, but shifted by d bins, $C_{f,g}(s)$ has a peak of 1 for $n = d$. In practice $C_{f,g}(s)$ is evaluated by fast Fourier techniques.

Since each star at any given time will have different radial velocities the cross-correlation spectrum of a binary system will have two peaks. This introduces an inherent source of error: the double peak spectrum may be considered as a blend of two single peak spectra and hence the peaks themselves will not correspond exactly to the true radial velocities. When the cross-correlation technique is applied to a single star the cross-correlation spectrum will of course contain only one peak.

The use of cross-correlation techniques to study eclipsing binaries has been described by Latham et al. (1996) in their analysis of DM Virginis. Latham et al. first discuss one-dimensional correlation and do this with the code they themselves used, the XCSAO code developed by Kurtz et al. (1992), which implements the theoretical

framework of Tonry and Davis. They point out two sources of systematic error. First, strong lines in the observed spectrum happen to coincide with other strong lines in the template spectrum. This leads to side lobes to the main peak of the correlation spectrum, and can also happen when correlation techniques are used to determine the radial velocity of a single star. The second source is a result of the shift in the peak position due to blending as explained above. If the spectral region used is wide, this source of systematic error is expected to be small.

C.2 MOLLY/`xcor`

Description of Method

MOLLY is a software suite to process 1D spectroscopic data, written by Marsh (http://www2.warwick.ac.uk/fac/sci/physics/research/astro/people/marsh/software also Marsh (1989) for background concepts). Spectra are stored in a single long 1 D array and the software can handle many tasks. Cross-correlation is carried out in the MOLLY software by the command `xcor`. This requires as input the target spectrum and a template spectrum from a standard star. The complete procedure is as follows.

- Read both target and template spectra into MOLLY.
- Smooth the template spectra so that they have approximately the same pixel resolution as the target spectra. This is done by the MOLLY `gsm` command.
- Plot both spectra on to a common log(wavelength) scale, so that a given Doppler shift corresponds to the same number of pixels over the whole spectrum, This is done with the MOLLY `vbin` command. The input parameters for `vbin` are given at the appropriate places in the main text.
- Normalise the spectra to unity with the MOLLY `pfit` (polynomial fit) and `div` (divide) commands. This typically requires a polynomial of order 3 or 4; order 4 was used throughout here.

- Subtract a constant of unity from the normalized spectra by the `csub` command, as required by the `xcor` command.

- Use the MOLLY command `xcor` to generate the correlation spectra themselves.

MOLLY has provision to mask spectral regions by the `mask` subroutines. In principle this may be used to mask strong absorption lines. This is necessary because such lines are wide; thus the cross-correlation peaks are wider and the resolution of the cross-correlation spectra degraded. For the SAAO spectra the region below 3990Å was masked out.

The INT spectra include the Hγ line at 4341 Å, but this was not masked because it is not significantly stronger than other lines in the same spectrum.

The output from `xcor` is a plot of correlation strength against velocity. When the software is used to determine the radial velocity of a single star there is a single peak. The position of the peak gives the radial velocity, and the FWHM is related to the rotational velocity. For a binary there are two peaks. The position, height and FWHM of the correlation peaks were determined by the MOLLY command `mgfit` (Multiple Gaussian fit), where "multiple" means that the correlation peak can be fitted to the sum of more than one Gaussian. The FWHM and height together provide an estimate of the area under the correlation peak, which provides further information because the ratio of the areas is roughly equal to the luminosity ratio if the two stars are of approximately the same spectral type. The uncertainties returned by `mgfit` are only fitting uncertainties, and do not include instrumental scatter. For example, when the `mgfit` command was applied to determine radial velocities from the INT spectra of V1094Tau, the fitting uncertainty was frequently less than 0.1 km/sec, whereas scatter in the radial velocity values was frequently of order 1 – 2 km s^{-1}. The degree of scatter is normal, as discussed by Maxted et al. (2001, Sect. 3.2). Note that this does not invalidate the use above of `mgfit` to obtain the

wavelength resolution. The method of estimating the rotational velocity from the FWHM is described in Sect. C.4.

C3. Input parameters

Standard wavelength binning parameters (MOLLY command `vbin`)

All operations with MOLLY for a given set of spectra were carried out with standardised parameters for wavelength binning by the `vbin` command. The binning parameters used for the SAAO and INT spectra appear below.

Table C1 Standard `vbin` parameters for the INT and SAAO spectra.

	INT	SAAO	
		Short λ	Long λ
Number of pixels	2580	1750	1750
Number of km s^{-1} $pixel^{-1}$	7.239	13.685	8.494
Central wavelength (Å)	4361.0	4091.0	5058.0
Wavelength range (Å)	4227.35 to 4499.10	3930.82 to 4257.71	4934.15 to 5184.96

C4. Choice and smoothing of templates

Choice. The choice of templates is explained at the description of each set of spectra in the main text. The two requirements are that the template star should be of a similar spectral type as the target star and that the radial velocity should be accurately known, since the raw radial velocities returned by the cross-correlation routines must be corrected for the radial velocity of the template. High quality template spectra are available from the library of field star spectra held on the ESO Paranal website (http://www.eso.org/sci/observing/tools/uvespop/field_stars_uptonow.html).
Some of these stars host exoplanets detected by the radial velocity method and so the radial velocity of these template stars is in principle known very precisely (e.g. Wittenmyer et al., 2011).

Smoothing. The ESO spectra used as templates have a much finer spectral resolution than any of the observational spectra described in this thesis. The MOLLY/`xcor` routine requires that the resolution of the template and observational spectra should be comparable. This is achieved by smoothing the template spectra by the MOLLY command `gsm` where the key argument is the FWHM of the smoothed spectrum in pixels. The value used for this parameter is the ratio of the spectral resolutions of the two spectra.

The spectral resolution of the ESO spectra is taken to be the dispersion in pixels. This can be obtained from the output of the MOLLY/vbin command when the ESO spectra are loaded in. The resolution of the observational spectra was taken to be twice the pixel dispersion. The measured resolution is between a factor 1 and 2 coarser than this, so Nyquist sampling implies a resolution of twice the pixel dispersion.

APPENDIX D DETERMINATION OF RADIAL VELOCITIES BY TODCOR CROSS-CORRELATION SOFTWARE

D.1 Description

The TODCOR software was developed by Zucker and Mazeh (1994) and was explicitly written to analyse composite spectra which are blends of the spectra from each member of an EB. It is a "two-dimensional" cross-correlation algorithm and is a generalisation of the cross-correlation method described in the previous Appendix in that it obtains the Doppler shift of the two components of an EB *simultaneously* by using a different template for each star, instead of the same template as before. Each template can thus be matched more closely to each star. The cross-correlation output is now a two-dimensional plot where the peak of the one dimensional plot is replaced by two bands parallel to each axis. Thus with two stars there are four bands, two main peaks defining the radial velocities and two cross-peaks. The cross-correlation function $R_{f,g1,g2}\ (s_1,s_2,\alpha)$ is now a two-dimensional extension of Eqn. C.1 i.e.

$$R_{f,g_1,g_2}(s_1,s_2,\alpha) = \frac{\sum_n f(n)[g_1(n-\ s_1)+\ \alpha g_2(n-\ s_2)]}{N\sigma_f\sigma_g(s_1.s_2)} \qquad \text{D.1}$$

Thus the cross-correlation function is a function of the two shifts s_1 and s_2

In this expression α is the intensity ratio of the two stars which is defined to maximise the cross-correlation function and

$$\sigma_g(s_1,s_2)^2 = \frac{1}{N}\sum_n [g_1(n-\ s_1)+\ \alpha g_2(n-\ s_2)]^2 \qquad \text{D.2}$$

A typical TODCOR correlation spectrum, for the INT spectrum 43 (Appendix A) is shown below. This shows the correlation function in terms of the radial velocities s_1 and s_2 (marked as v_1 and v_2 on the graph). The value of the correlation function increases as the shading becomes darker. The radial velocity is defined by the maximum of the function $\sigma_g(s_1,s_2)^2$ at the intersection of the bands; the precise value of this velocity was obtained from a program written by Maxted (private communication). This exposure is the same as was used earlier to illustrate an INT spectrum and was chosen because of the large difference between the radial velocities of the two stars. TODCOR provides a much higher accuracy and finer resolution than the standard cross-correlation technique. If the velocity difference between the two components is comparable to the width of the correlation peak, the standard method cannot resolve the peaks and so cannot derive the velocity of the secondary whereas this is no problem for TODCOR. Zucker and Mazeh demonstrate this with simulated spectra of two stars with a radial velocity difference of 20 km s^{-1} This is beyond the capabilities of the standard cross-correlation technique but is easy for TODCOR. In fact for a real case of two stars with a radial velocity difference of 20.5 ± 0.7 km s^{-1} each velocity could be determined to within 1 km s^{-1} (Latham et al., 1996).

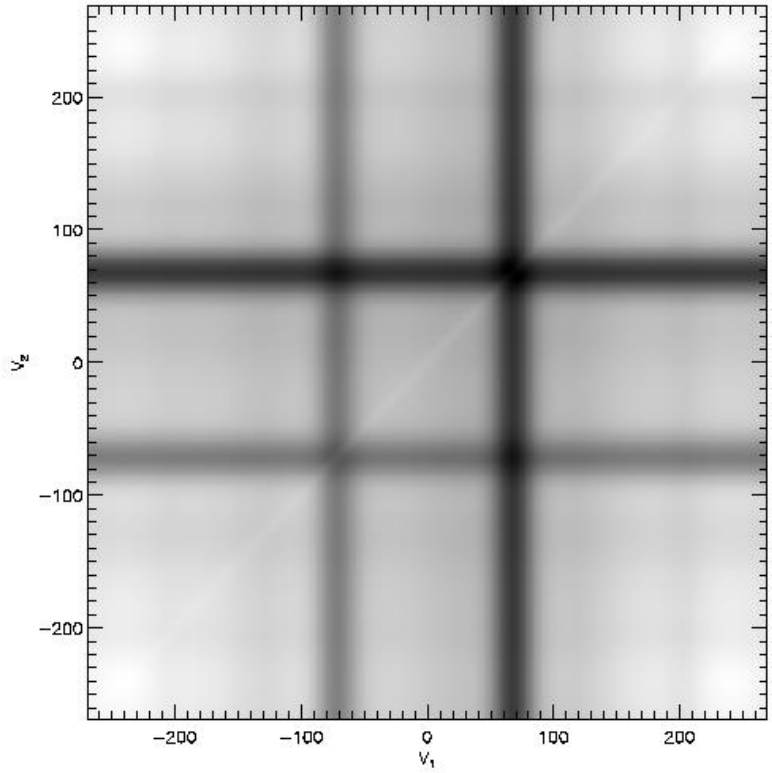

Fig. D1 TODCOR two-dimensional spectrum for INT exposure 43.

D.2 Correction for systematic errors

Experience with TODCOR shows that the systematic errors arising in MOLLY/`xcor` are also present in TODCOR but are smaller. The sources of the errors are the same as MOLLY/`xcor` namely a) the main correlation peak from one star can blend with the side lobe of the correlation peak from the other star and b) a spectral line from one star can blend with another spectral line from the other star (Latham et al. 1996). These authors report, in their investigation of the eclipsing binary DM Virginis, that when they analysed a corresponding template spectrum the systematic error with TODCOR was an order of magnitude smaller than with the one-dimensional cross-correlation code XCSAO (Kurtz et al., 1992). Systematic errors in TODCOR have also been investigated by Torres et al. (1997) and Torres and Ribas (2002). A correction for this systematic error was

applied in the present work by following the procedure in these two last papers. The principle is to build a synthetic spectrum by introducing what are thought to be the radial velocities, use TODCOR to obtain radial velocities from that and adopt the difference as the correction. The steps are as follows.

- Load ESO spectra for both template stars (MOLLY/`lasc`)
- Broaden template spectra to match INT resolution (MOLLY/`gsm`)
- Rebin to INT wavelength (MOLLY/`vbin`)
- Shift by radial velocities from uncorrected TODCOR spectra (MOLLY/`move`)
- Multiply each template spectrum by flux ratio (MOLLY/`cmul`)
- Add the template spectra (MOLLY/`add`)
- Obtain new radial velocities from TODCOR

This procedure was not implemented for the SAAO spectra since the spectra were not of sufficient quality to warrant it. For the INT spectra it was implemented for a representative selection of spectra for each observing night. In general the corrections for a given night were averaged and this average was applied to all the exposures for that night. This was done because the scatter in the corrections was too great to discern a trend. For just one night a clear linear trend could be discerned and was applied.

TODCOR was accessed by a program written by Maxted (private communication).

APPENDIX E TABLE OF RADIAL VELOCITIES USED FOR ANALYSIS OF V1094 TAU.

Details of all the radial velocity data sets used to analyse the orbital elements of V1094 Tau are listed below. Further details appear at the foot of the Table.

Time HJD - 2400 000	Primary Velocity km s^{-1}	Uncert	O-C	Secondary Velocity km s^{-1}	Uncert	O-C	Systemic velocity Omdot	Source
50080.540	-21.77	0.48	-0.06	30.23	0.78	-0.44	3.43	CFA
50081.556	-38.88	0.48	0.58	50.37	0.78	0.46	3.43	CFA
50090.675	-41.24	0.48	-0.28	51.83	0.78	0.30	3.43	CFA
50094.618	56.09	0.48	0.52	-54.37	0.78	-1.30	3.43	CFA
50098.587	-23.78	0.48	-0.50	32.35	0.78	-0.03	3.43	CFA
50108.542	-39.91	0.48	-0.20	49.58	0.78	-0.60	3.43	CFA
50114.642	41.48	0.48	-0.55	-38.23	0.78	0.16	3.43	CFA
50115.471	7.67	0.48	-0.38	-1.65	0.78	-0.08	3.43	CFA
50118.484	-46.88	0.48	-0.64	56.71	0.78	-0.54	3.43	CFA
50120.518	-9.73	0.48	0.07	18.57	0.78	0.80	3.43	CFA
50121.542	52.50	0.48	-0.40	-50.95	0.78	-0.77	3.43	CFA
50126.630	-41.45	0.48	-0.47	50.17	0.78	-1.38	3.43	CFA
50127.536	-46.27	0.48	0.03	57.95	0.78	0.64	3.43	CFA
50140.529	83.50	0.48	0.37	-81.36	0.78	1.57	3.43	CFA
50143.508	-22.23	0.48	0.56	32.83	0.78	0.99	3.43	CFA
50144.506	-40.20	0.48	-0.37	51.83	0.78	1.53	3.43	CFA
50146.502	-38.70	0.48	0.49	49.77	0.78	0.16	3.43	CFA
50147.584	-4.42	0.48	0.58	12.51	0.78	-0.05	3.43	CFA
50152.500	-22.38	0.48	0.49	33.50	0.78	1.57	3.43	CFA
50153.503	-40.59	0.48	-0.67	51.56	0.78	0.76	3.43	CFA
50154.531	-46.06	0.48	0.25	57.99	0.78	0.67	3.43	CFA
50155.486	-38.99	0.48	0.27	48.56	0.78	-1.12	3.43	CFA
50156.497	-8.02	0.48	0.67	17.00	0.78	0.44	3.43	CFA
50170.504	-22.83	0.48	0.64	33.48	0.78	0.90	3.43	CFA
50173.511	-38.10	0.48	0.35	48.50	0.78	-0.32	3.43	CFA
50176.511	83.07	0.48	0.40	-82.65	0.78	-0.21	3.43	CFA
50179.525	-24.65	0.48	-0.48	34.28	0.78	0.94	3.43	CFA
50336.874	25.90	0.48	-0.34	-22.14	0.78	-0.85	3.43	CFA
50346.821	81.46	0.48	0.51	-80.36	0.78	0.22	3.43	CFA
50348.766	23.79	0.48	0.08	-17.74	0.78	0.81	3.43	CFA
50350.806	-34.24	0.48	-0.59	44.53	0.78	0.92	3.43	CFA
50352.811	-45.12	0.48	-0.81	54.89	0.78	-0.28	3.43	CFA
50356.829	64.64	0.48	-0.10	-62.91	0.78	0.10	3.43	CFA
50360.787	-45.05	0.48	-0.24	55.20	0.78	-0.51	3.43	CFA

50363.834	26.12	0.48	0.25	-21.08	0.78	-0.19	3.43	CFA
50443.683	-26.88	0.48	-0.81	36.36	0.78	0.97	3.43	CFA
50449.593	-32.54	0.48	-0.36	41.64	0.78	-0.38	3.43	CFA
50456.569	26.26	0.48	0.07	-20.35	0.78	0.89	3.43	CFA
50460.575	-45.61	0.48	-0.60	56.77	0.78	0.85	3.43	CFA
50462.498	13.01	0.48	0.60	-5.31	0.78	0.99	3.43	CFA
50464.615	67.53	0.48	-0.45	-66.14	0.78	0.38	3.43	CFA
50466.698	-13.92	0.48	-0.93	21.62	0.78	0.39	3.43	CFA
50472.545	77.68	0.48	0.43	-76.37	0.78	0.19	3.43	CFA
50474.691	20.79	0.48	0.54	-15.29	0.78	-0.50	3.43	CFA
50477.577	-44.26	0.48	0.16	55.50	0.78	0.21	3.43	CFA
50478.522	-45.18	0.48	0.01	56.59	0.78	0.47	3.43	CFA
50481.688	81.34	0.48	-0.57	-82.83	0.78	-1.21	3.43	CFA
50493.512	-8.84	0.48	-0.09	16.81	0.78	-0.90	3.43	CFA
50495.491	-43.39	0.48	0.60	55.05	0.78	0.24	3.43	CFA
50503.542	-33.01	0.48	-0.53	43.68	0.78	1.34	3.43	CFA
50505.525	-44.95	0.48	0.02	55.92	0.78	0.04	3.43	CFA
50516.576	21.92	0.48	0.23	-18.16	0.78	-1.80	3.43	CFA
50523.505	-44.90	0.48	0.05	56.22	0.78	0.36	3.43	CFA
50527.518	68.51	0.48	-0.15	-66.81	0.78	0.44	3.43	CFA
50531.540	-45.05	0.48	-0.42	54.84	0.78	-0.67	3.43	CFA
50535.499	77.99	0.48	-0.46	-76.93	0.78	0.94	3.43	CFA
50536.504	68.83	0.48	0.08	-67.54	0.78	-0.19	3.43	CFA
50538.502	-11.08	0.48	-0.96	18.03	0.78	-0.08	3.43	CFA
50540.529	-45.25	0.48	-0.62	55.61	0.78	0.10	3.43	CFA
52545.596	-44.90	0.53	0.17	57.80	0.91	-0.61	4.59	GB
52561.587	-28.94	1.51	0.80	32.28	1.63	0.25	-0.09	INT
52561.590	-27.30	1.51	2.51	33.68	1.63	1.56	-0.09	INT
52561.594	-26.60	1.51	3.29	34.94	1.63	2.74	-0.09	INT
52561.598	-29.11	1.51	0.85	32.46	1.63	0.17	-0.09	INT
52561.601	-28.97	1.51	1.07	32.56	1.63	0.20	-0.09	INT
52561.751	-31.40	1.51	1.58	35.83	1.63	0.29	-0.09	INT
52561.754	-36.43	1.51	-3.38	31.43	1.63	-4.19	-0.09	INT
52561.758	-33.42	1.51	-0.31	34.26	1.63	-1.43	-0.09	INT
52561.762	-37.48	1.51	-4.29	30.59	1.63	-5.18	-0.09	INT
52561.765	-37.51	1.51	-4.26	30.45	1.63	-5.39	-0.09	INT
52561.779	-32.93	1.51	0.57	35.66	1.63	-0.46	-0.09	INT
52561.783	-35.62	1.51	-2.05	32.86	1.63	-3.33	-0.09	INT
52562.563	-43.50	1.51	1.37	49.21	1.63	0.77	-0.09	INT
52562.566	-44.83	1.51	0.09	47.26	1.63	-1.23	-0.09	INT
52562.570	-45.01	1.51	-0.05	47.22	1.63	-1.31	-0.09	INT
52562.674	-44.66	1.51	1.33	50.30	1.63	0.66	-0.09	INT
52562.678	-44.90	1.51	1.12	50.23	1.63	0.55	-0.09	INT
52562.682	-44.38	1.51	1.67	51.03	1.63	1.31	-0.09	INT
52562.768	-46.72	1.51	0.09	50.16	1.63	-0.38	-0.09	INT
52562.772	-48.43	1.51	-1.59	48.51	1.63	-2.06	-0.09	INT

52562.776	-46.51	1.51	0.36	50.33	1.63	-0.27	-0.09	INT
52563.616	-49.68	1.51	0.00	53.96	1.63	0.31	-0.09	INT
52563.619	-49.58	1.51	0.10	54.07	1.63	0.43	-0.09	INT
52563.623	-49.51	1.51	0.16	53.58	1.63	-0.05	-0.09	INT
52563.763	-48.04	1.51	1.19	54.07	1.63	0.91	-0.09	INT
52563.767	-48.84	1.51	0.37	52.88	1.63	-0.26	-0.09	INT
52563.771	-48.88	1.51	0.32	52.98	1.63	-0.14	-0.09	INT
52566.597	64.80	0.53	-0.16	-61.28	0.91	-0.84	4.59	GB
52566.718	67.66	1.51	0.69	-71.19	1.63	0.96	-0.09	INT
52566.722	66.88	1.51	-0.28	-72.05	1.63	0.31	-0.09	INT
52566.726	66.96	1.51	-0.38	-72.84	1.63	-0.28	-0.09	INT
52566.730	67.19	1.51	-0.34	-72.72	1.63	0.04	-0.09	INT
52566.733	67.76	1.51	0.05	-72.67	1.63	0.29	-0.09	INT
52566.761	69.18	1.51	0.11	-74.22	1.63	0.21	-0.09	INT
52566.765	69.41	1.51	0.16	-74.14	1.63	0.48	-0.09	INT
52566.769	70.05	1.51	0.63	-73.39	1.63	1.42	-0.09	INT
52566.772	70.28	1.51	0.68	-74.14	1.63	0.85	-0.09	INT
52566.776	70.54	1.51	0.77	-74.16	1.63	1.02	-0.09	INT
52566.781	70.42	1.51	0.44	-74.19	1.63	1.22	-0.09	INT
52566.784	69.21	1.51	-0.94	-76.27	1.63	-0.67	-0.09	INT
52566.787	70.69	1.51	0.43	-77.47	1.63	-1.75	-0.09	INT
52568.625	33.26	1.51	-0.61	-35.50	1.63	0.79	-0.09	INT
52568.629	33.09	1.51	-0.62	-34.80	1.63	1.31	-0.09	INT
52568.633	32.77	1.51	-0.77	-34.66	1.63	1.27	-0.09	INT
52568.741	28.53	1.51	-0.27	-30.12	1.63	0.67	-0.09	INT
52568.744	27.30	1.51	-1.33	-31.13	1.63	-0.51	-0.09	INT
52568.748	26.81	1.51	-1.66	-31.41	1.63	-0.96	-0.09	INT
52570.750	-32.28	1.51	0.61	35.55	1.63	-0.51	-0.09	INT
52570.754	-33.54	1.51	-0.58	34.33	1.63	-1.81	-0.09	INT
52571.585	-40.20	0.53	0.35	53.90	0.91	0.40	4.59	GB
52575.644	68.00	0.53	-0.02	-64.40	0.91	-0.26	4.59	GB
52580.627	-40.10	0.53	0.97	54.90	0.91	0.83	4.59	GB
52585.570	80.70	0.53	-0.31	-78.20	0.91	0.02	4.59	GB
52589.535	-40.50	0.53	-0.23	53.10	0.91	-0.10	4.59	GB
52613.474	41.90	0.53	-0.57	-34.50	0.91	1.96	4.59	GB
52618.383	-38.20	0.53	-0.69	49.30	0.91	-0.91	4.59	GB
52644.500	-45.30	0.53	-0.28	58.40	0.91	0.05	4.59	GB
52645.478	-35.60	0.53	-0.49	47.80	0.91	0.19	4.59	GB
52647.353	56.40	0.53	0.46	-51.20	0.91	-0.14	4.59	GB
52649.523	37.60	0.53	-0.62	-31.30	0.91	0.55	4.59	GB
52651.266	-21.80	0.53	-1.22	32.00	0.91	0.14	4.59	GB
52651.390	-22.90	0.53	0.43	34.20	0.91	-0.64	4.59	GB
52655.257	-9.40	0.53	0.69	21.00	0.91	0.50	4.59	GB
52656.276	51.50	0.53	-0.12	-45.90	0.91	0.48	4.59	GB
52657.292	84.40	0.53	-0.32	-83.30	0.91	-1.06	4.59	GB
52660.346	-22.10	0.53	0.52	34.40	0.91	0.32	4.59	GB

52663.253	-38.30	0.53	0.40	52.70	0.91	1.20	4.59	GB
52665.260	51.70	0.53	0.38	-47.70	0.91	-1.65	4.59	GB
52666.440	81.40	0.53	-0.29	-77.60	0.91	1.36	4.59	GB
52667.336	45.10	0.53	-0.51	-38.50	0.91	1.36	4.59	GB
52672.316	-37.10	0.53	0.38	50.10	0.91	-0.08	4.59	GB
52684.401	82.00	0.53	-0.08	-79.30	0.91	0.08	4.59	GB
52685.376	43.30	0.53	0.54	-35.10	0.91	1.67	4.59	GB
52688.338	-39.30	0.53	0.20	52.10	0.91	-0.27	4.59	GB
52689.334	-45.00	0.53	0.14	59.90	0.91	1.42	4.59	GB
52690.298	-36.90	0.53	0.50	49.40	0.91	-0.69	4.59	GB
52691.359	-2.30	0.53	0.76	13.10	0.91	0.22	4.59	GB
52692.370	60.90	0.53	0.24	-58.90	0.91	-2.73	4.59	GB
52693.340	82.70	0.53	-0.47	-80.60	0.91	-0.04	4.59	GB
52714.315	-23.30	0.53	0.14	34.30	0.91	-0.66	4.59	GB
52715.319	-39.80	0.53	-0.13	52.70	0.91	0.15	4.59	GB
52718.323	-3.80	0.53	-0.66	10.90	0.91	-2.07	4.59	GB
52732.331	-24.40	0.53	-0.13	36.50	0.91	0.64	4.59	GB
		Avg.	-0.03		Avg.	-0.01		
		Std.dev	0.91		Std.dev	1.18		

In this table the uncertainties are those from SBOP. The sources are indicated as follows.

CfA: Centre for Astrophysics, Harvard (Torres, private communication).

GB: Griffin and Boffin (2003).

INT: Run at the Isaac Newton Telescope (Southworth, private communication).

The (Observed – Calculated) residuals can in principle be obtained in at least two ways. First, they can be taken directly from the SBOP output. Alternatively the calculated velocities can be obtained from the orbital elements by solving the equations for elliptical orbits. Thus Kepler's equation (Eqn. 12.4) is solved iteratively as explained by Hilditch (2001, paragraph after Eqn. 2.35), and the radial velocity then obtained from Eqns 12.1 and 12.2. This calculation used the value of radial velocity amplitudes from *Omdot*, and values

for the eccentricity and angle of periastron which are weighted averages of the values from *Omdot* and JKTEBOP. This method was used here because the average residual, shown at the bottom of the Table, is closer to zero. The SBOP average residuals were -0.11 ±0.90 and -0.08 ± 1.18 km s^{-1} respectively.

The different values for the systemic velocity for each source are explained in the text (Sect.9.4).

APPENDIX F THE ECLIPSING BINARY CODE JKTEBOP

A standard program suite for modelling photometric light curves from eclipsing binaries is the JKTEBOP suite developed by Dr. J. Southworth at Keele University (EBOP stands for Eclipsing Binary Orbit Program) and described in detail by Southworth (2010, 2011). It is a descendant of the EBOP program written by Etzel (1975) via the EBOP code of Popper and Etzel (1981), and originally derives from the model for calculating the intensity curve from eclipsing binaries in eccentric orbits developed by Nelson and Davis (1972). The JKTEBOP suite calculates theoretical light curves from trial parameters, and then calculates improved values by minimizing the difference between the observed and calculated curves. Issues surrounding the use of JKTEBOP have been discussed in detail by Southworth (2006, thesis). The input parameters include amongst others trial relative radii (actual radii divided by the semi-major orbital axis), observed period, and light curves. As explained by Southworth the input parameters are chosen to be those which define the light curve profile most directly and which have the lowest possible correlation. The JKTEBOP suite assumes that the stars are spherical in the main part of the calculation but at a later stage a correction is applied which treats the stars are biaxial ellipsoids i.e. ellipsoids in which the two perpendicular horizontal (i.e. in the orbital plane) axes are equal, but still close to spherical. The condition of being close to spherical will be met for the long period EB's considered here because the stars are relatively far apart and tidal interaction is relatively weak. The output parameters include the relative radii, ratio of the surface brightnesses, inclination of the orbits to the line of sight, eccentricity of the orbit and the angle of periastron. The radius is defined as the radius of a sphere with the same volume as the biaxial ellipsoid actually treated. JKTEBOP does not provide absolute radii, so these can be obtained only by combining it with other observations. Software which analyses a light curve profile due to one star eclipsing another clearly has to allow for the

mechanisms through which the apparent surface brightness varies over the surface of a star i.e. gravity and limb darkening.

Limb darkening. A star is observed to an optical depth of about unity all over its surface. When a star is observed at the centre of its disk it is seen to a certain depth into the star. When however the star is observed at its edge, at a highly oblique angle, the same optical depth corresponds to a much higher layer of the atmosphere. This layer is cooler and less luminous one so the star appears fainter. The variation of surface brightness over the projected surface disc can be approximated by a cosine law (Sect. 9.6.2).

Gravity darkening. Some stars are oblate. For single stars this can result from rapid rotation for example α Leonis (Regulus). In binary stars this may also occur if the stars are close enough for tidal interactions to distort them. Thus the emergent intensity at each point varies over the stellar surface; the poles are brighter than the equator. According to the original treatment by Von Zeipel (1924), the emergent flux F is proportional to the surface gravity g i.e. $F \propto g$, and since $F \propto T^4$ where T is the local temperature, we have $T \propto g^{0.25}$. It is now standard practice to write $F \propto g^{\beta}$ or $T \propto g^{\beta}$ where β is known as the gravity darkening coefficient. Later treatments allow for whether the stellar envelope is radiative or convective and generally predict lower values of β.

JKTEBOP can allow for both sources of darkening.

If limb and gravity darkening, and departures from the stars being spherical, are taken into account it is not possible to calculate the total brightness of the system analytically. The brightness must then be evaluated by treating the stars as large arrays of small elements of annuli and summing over the elements.

The JKTEBOP suite was used here by following procedure.

- Use the input file jktebop.in.0 to calculate a theoretical light curve from trial stellar parameters. Display this with observed light curve.

- Adjust stellar parameters in jktebop.in.0 to obtain a good fit by eye between theoretical and observed curve. This provides fair values for the sum and ratio of the relative radii, the orbital inclination and the functions $e\ cos\omega$ and $e\ sin\omega$ of the eccentricity e and angle of periastron ω (Sect. 12.4).

- Use the input file jktebop.in.1 with control parameters set to adjust the orbital elements and chosen stellar parameters. This refines the solution.

- Use the input file jktebop.in.2 with control parameters to refine the orbital and stellar parameters further and to determine the uncertainty in the period and time base for the minima.

- Use the input file jktebop.in.3 with control parameters to refine the orbital and stellar parameters further and to determine the uncertainty in these parameters.

The uncertainties given by jktebop.in.3 are calculated by the residual shift method. In this method a best fit is first found to the whole set of data points and the residuals to the best fit calculated. For each parameter the residual for each point is then shifted to the next point and another best fit calculated (the residual for the last data point is now applied to the first one i.e. residuals are wrapped round the data points). This therefore generates as many best fits as data points. The uncertainty is taken as the 1 sigma standard deviation.

The degeneracies between the parameters outputted by JKTEBOP are described in the main text (Sect. 9.6).

APPENDIX G THE STRÖMGREN *uvbyβ* COLOUR INDEX SYSTEM

Description

The Strömgren *uvbyβ* system was introduced by Strömgren (1956) and extended by Crawford (1958). It is designed to cover bands where the colour index differences are sensitive to stellar temperature, gravities and metallicity. It is an intermediate width band system which has the merit that the wavelength bands are narrower than for the widely used Johnson UBV system (Johnson and Morgan, 1953), and so the detector response will not change significantly over the pass band. Further, the narrower bands and hence finer spectral resolution greatly increases the diagnostic power, in spite of the reduced signal strength. These wavelength bands are shown in Table G.1 below and are taken from Bessell (2005):

Table G.1 Wavelength bands in Strömgren uvbyβ colour index system

Band	Maximum (Å)	50% transmission (approx) (Å)
u	3560	3365 - 3675
v	4120	4025 - 4195
b	4660	4605 - 4780
y	5420	5360 - 5590
	Band centre	Band width
Narrow *β*	4861 (Hβ)	4846 - 4876
Wide *β*	4861 (Hβ)	4811 - 4911

The “narrow” and “wide” *β* bands are included to avoid problems due to interstellar reddening (absorption of light by interstellar dust and gas). The absorption becomes stronger towards bluer wavelengths, hence the term “reddening”. Since the two *β* bands are

both relatively narrow their intensities are affected by reddening by approximately the same relative amount and hence the intensity ratio can be used as a temperature diagnostic.

It is convenient for the purposes of this thesis to add at this point the particulars of the Johnson V band i.e.

Band	Maximum (Å)	50% transmission (approx) (Å)
V-band	5448	5030 – 5870

The central wavelengths of the Strömgren *y*-band and Johnson V-band are sufficiently close (according to some literature sources equal) that transformation equations can be derived between the magnitudes in the two bands. The wavelengths of the Strömgren and Johnson bands are shown in Fig. G.1. This Figure also shows the variation of interstellar extinction with wavelength as a solid black line.

Index differences are defined to take account of the Balmer discontinuity at 3646Å and blanketing (any effect on the emitted flux due to differences in chemical composition from star to star).

The following three index differences are frequently used.

(b-y) This is reasonably free of blanketing (Crawford,1975), measures the slope of the continuum in the blue to yellow region (Hilditch, 2001, Sect. 5.3.3) and so is sensitive to temperature OB to G spectral type range.

$c_1 = (u-v) – (v-b)$ This is a measure of the Balmer discontinuity index and is sensitive to luminosity for A and F-type stars (Hilditch, 2001). This index is broadly free of blanketing since at 3500Å this is roughly twice than at 4100Å (Crawford, 1975), and this index is a “difference of a difference”.

$m_1 = (v-b) – (b-y)$ This index is a measure of blanketing, by a similar type of argument.

The index β is defined as $\beta = -2.5\ log_{10}[f_n/f_w]$, where f_n and f_w are the flux densities in the narrow and wide β bands. Thus f_n is a measure of the strength of the Hβ line and f_w of the local continuum flux density.

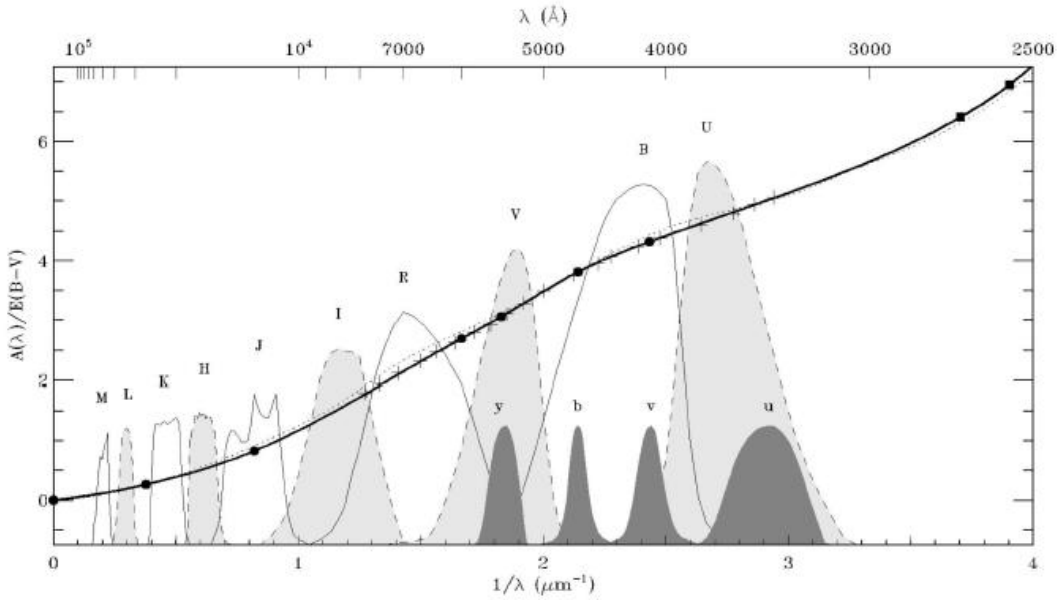

Fig. G.1 Wavelengths of the Strömgren and Johnson-Cousins spectral bands, and variation of the interstellar extinction with wavelength. This figure is taken from Fig. 6 of Fitzpatrick (1999).

APPENDIX H REDUCTION OF CCD TRACES TO ONE DIMENSIONAL SPECTRA (*PAMELA* software)

This purpose of this stage in the data reduction is to extract the true one-dimensional spectrum from the two-dimensional image recorded by the CCD i.e. the raw count per pixel. This is accomplished by the PAMELA software. The general principles of this have been explained by Horne (1986) and Marsh (1989) although neither of these papers refer to PAMELA by name. A detailed explanation of this process with specific reference to PAMELA commands has been given by Southworth (website reference www.astro.keele.ac.uk/jkt/GrSpInstructions/GrSpInstructions.html).

The main steps in this stage are i) the readout of the CCD image, ii) correction of the two-dimensional image for instrumental factors and iii) "optimal extraction" i.e. minimising the statistical noise in the corrected image.

H1. Correction for instrumental factors

The three corrections for the instrumental factors are

a) The CCD has a positive bias. This must be subtracted from the signal.

b) Each pixel has a slightly different response. This must be calibrated by a "flat field" spectrum from a laboratory source; it is also necessary to calibrate against the spectral profile of this source itself.

c) The intensity contribution from the sky must then be subtracted from the image.

The positive bias referred to in step a) is supplied to the CCD to prevent difficulties arising when the mean pixel signal is subtracted from the signal from each pixel. Otherwise the subtractions from the pixels with less than the average signal would generate negative numbers in the read out process. The method to determine the bias relies on the

mode of operation of the CCD. The bias is supplied by the controller linked to an ADC (analogue to digital) converter, which not only provides a digital readout from the pixels of the CCD but also a digital map of the bias, known as the bias strip. The clipped mean value in the bias strip is subtracted from all the pixels in the image.

Step b) is to correct the image for i) the different sensitivity of each pixel, and ii) for slowly varying responses of the detector sensitivity due to e.g. the jaws of the slit not being exactly parallel. This correction was made by using a tungsten lamp to create a "master flat" field image where the count for each pixel is the median count for all the exposures . However this "masterflat" image is still convolved with the spectral response of the tungsten lamp itself. Since the dispersion direction is approximately parallel to the image columns this spectral response is removed by dividing each column of the image by a low-degree polynomial fit by least-squares to the sum of the image rows. The spatial variations in the sensitivity are removed by dividing each image row by the sum of the corresponding image columns. The image is then divided by a constant so that the mean pixel value is approximately 1. This corrected "master-flat" image can then be used to calibrate the different response of each pixel.

Step c) is to subtract the light from the sky from the image. The method here is to fit, for each row, a polynomial to those pixels illuminated by the sky alone. This fitted polynomial is then used to subtract the sky contribution.

H2. Optimal extraction of spectrum

. The second stage is to reduce statistical noise in the extracted spectrum to a minimum by finding a self-consistent solution, a procedure known as "optimal extraction" (Horne, 1986) where the signal from each pixel is weighted by its variance.

. The detailed description of this procedure closely follows that of Horne. Following Horne we use the word *spectrum* to denote the light from the star, and the word *image* to denote the signal on the CCD.

The optimal extraction technique is applied to obtain the true one-dimensional spectrum from the calibrated two-dimensional image. It minimises the statistical noise in the spectrum while at the same time preserving its spectrophotometric accuracy. The main features of this can be understood by considering a simple case where the spectrum covers n_c columns without curvature. For a given wavelength, i.e. CCD pixel row, let the probability that a photon is registered in pixel n be P_n, thus $\Sigma_n P_n = 1$. Let us, following Horne, write the data value for pixel n of the corrected image as D_n and the sky background image as S_n. In the absence of noise a value the object spectrum f for this wavelength could be obtained from each pixel i.e. $f_n = (D_n - S_n)/P_n$. The values f_n obtained from each pixel would all be the same. In fact statistical noise is inevitably present, and hence the values of f_n have different variances. The object spectrum f may then be written

$$f = \frac{\sum_n W_n (D_n - S_n)/P_n}{\sum_n W_n} \qquad \text{H.1}$$

where W_n is the weighting factor for pixel n.

The variance of f can be minimised by assigning weights which are inversely proportional to the variances of the individual components $(D_n - S_n)/P_n$ i.e.

$$\frac{1}{W_n} = var\left[\frac{(D_n - S_n)}{P_n}\right] = \frac{V_n}{{P_n}^2} \qquad \text{H.2}$$

where V_n is the variance of pixel n.

The kernel of the optimal extraction method is an iterative procedure to find self-consistent values of the image profile P_n, the variance image V_n and the object spectrum f_n. The iteration for V_n starts from the noise properties of the detector and the spectral image D_n. These are used to find a first estimate of the variance of the spectrum and the latter are then used iteratively to find better values of V_n. Values of P_n are found in two stages. First, for each row values of P_n are estimated from the fraction $(D_n - S_n)/f$. However these values are noisy and the second stage is to smooth the profiles of P_n in the wavelength direction. Horne describes at this point a further iterative procedure to eliminate rogue pixel counts due to cosmic ray hits, a procedure which continues until the number of rejected outlier pixels is the same in successive iterations.

APPENDIX J WAVELENGTH CALIBRATION AND DETERMINATION OF SPECTRAL RESOLUTION OF THE ONE DIMENSIONAL (SAAO) SPECTRA BY *MOLLY* SOFTWARE

The output from the data reduction so far is an optimally extracted 1-D spectrum over pixels. So far there has been no wavelength calibration. This is provided by a copper/argon arc lamp where it is the argon lines used for the calibration. Because of flexure of the telescope when moved to different positions, a wavelength calibration must be interpolated from arc spectra taken before and after each exposure.

The process is in two stages

Stage 1) Create an arc line map, i.e. identify the lines in the arc spectrum, and obtain a dispersion curve (wavelength in terms of pixel number) from it.

Stage 2) Apply the dispersion curve to each stellar spectrum.

The process again closely follows that described in the website of Southworth, referenced in the last subsection.

Creation of arc line map

The steps in this are as follows.

1. Several arc spectra are averaged to form a basis arc spectrum for identification.

2. About four or five strong lines in the averaged spectra were identified by visual comparison with laboratory spectra available from the La Palma ING (Isaac Newton Group of Telescopes) website

   http://www.ing.iac.es/astronomy/instruments/isis/calib/arcRCA.html.

3. The spectra are loaded into arc and fitted to a second order polynomial by the command fit, by following the detailed instructions given by Southworth. The process is repeated by including more lines and increasing the order of polynomials until further steps do not reduce the fitting residuals significantly.
   This leads to typically a fourth or fifth order polynomial. Residuals of typically 0.05Å are satisfactory.

4. On leaving the arc submenu an arc spectrum with a wavelength calibration can be seen.

Determination of wavelength resolution

The wavelength resolution can be obtained from the lines of the arc calibration spectrum. These are narrow enough that their width can be ignored compared with instrumental broadening. Thus the FWHM of these lines on the observed calibration spectrum is due effectively wholly to the instrumental broadening and can be taken to be the spectral resolution. This FWHM can be determined from a least-squares fit of a Gaussian function to a reasonably strong, isolated arc line.

APPENDIX K THEORY OF TIDAL INTERACTION

K1 Basic concepts.

The two stars in a binary system will follow circular or elliptical orbits about their common centre of mass according to Kepler's Third Law.

For a sufficiently close binary, each star raises tides upon the other and is deformed into an axially symmetric ellipsoid. The distortions are known as tidal bulges. Due to friction within the stellar material the rotation tends to carry the bulges with it and hence if the rotational period is shorter than the orbital period the bulges are ahead of the axis joining the centres of the two stars. If the rotational period is longer than the orbital period the bulges lag behind this axis. The gravitational force on the nearer bulge is stronger than that on the further bulge and this produces a torque upon them which tends to synchronise the rotational period with the orbital period. Further arguments show that the interchange between orbital and rotational momentum tends to circularise the orbits. The time scales for synchronisation and circularisation depend strongly on the initial binary parameters and on the physical processes responsible for the dissipation of energy.

A dimensional analysis shows that the strength of the tidal interaction depends sharply on the relative radii of the stars (absolute radii divided by the semi-major axis of the relative orbit). The two main dependences are:

- The mass of the bulge, relative to the stellar mass. This varies $\propto (R/a)^3$, arising from the balance between the differential acceleration exerted on the bulges to the surface gravity.

- The tidal force $\propto (R/a^3)$, the differential of the gravitational force.

Both of these terms have an $1/a^3$ dependence. A proper analysis shows that the strength of the tidal interaction varies as $(R/a)^6$. Because of the sixth power dependence, there is a sharp cutoff in the (R/a) values for tidal interactions to be significant. The dependence on relative separation overwhelms dependence on mass. This cutoff corresponds to an orbital period of roughly 8 days for a wide range of masses. A corollary is that systems with periods shorter than about 8 days have circular orbits and systems with longer periods have elliptical orbits.

K2 Sketch of detailed theory

The detailed theory of the evolution of the orbital and rotational periods of binaries, starting from the initial protostar stage, has been investigated in detail by Zahn in a series of papers including Zahn (1977, 1978, 1994), and Zahn and Bouchet (1989). The main points relevant to this thesis are briefly described below.

K2.1 Tidal friction on the main sequence

The detailed theoretical study by Zahn (1977), with numerical errors corrected by Zahn (1978) examines tidal interactions within binaries on the Main Sequence. The gravitational field from Star 1 applies a torque on the tidal bulges of Star 2 and vice versa. The perturbing potential due to the tidal bulges on each star can be expressed in terms of Legendre polynomials. The eccentricities of the orbits can be treated by a potential varying periodically with time, and hence the polynomials are decomposed further into Fourier components. By following standard treatments Zahn derives equations for the secular evolution of the orbital elements i.e.for da/dt, de/dt and $d(I\Omega)/dt$, the time evolution of respectively a the stellar separation, e the eccentricity and $I\Omega$, the product of the moment of inertia I and rotational momentum Ω. These expressions lead naturally to expressions

for the synchronisation time t_{sync} between orbital and rotational velocities and the circularisation time t_{circ}. Numerical errors in this paper were corrected shortly afterwards by Zahn (1978). Simple approximations for t_{sync} and t_{circ} are derived in Eqns 6.1 and 6.2 of Zahn (1977) and been given wider publicity by Hilditch (2001, Eqns. 4.42 and 4.43). They are as follows.

Synchronisation time

$$t_{sync} \sim q^{-2}\left(\frac{a}{R}\right)^{6} \sim 10^{4}\left(\frac{(1+q)}{2q}\right)^{2} P^{4} \quad \text{years} \qquad \text{K.1}$$

Circularisation time

$$t_{circ} \sim \left(\frac{q(1+q)}{2}\right)^{-1}\left(\frac{a}{R}\right)^{8} \sim \frac{10^{6}}{q}\left(\frac{(1+q)}{2}\right)^{\frac{5}{3}} P^{\frac{16}{3}} \quad \text{years} \qquad \text{K.2}$$

where symbols have their usual meaning.

For mass ratio q = 1 and period 7.80 days, values chosen to correspond with the more detailed treatment described below, these expressions give t_{sync} ~ 37 Myr and t_{circ} ~ 57 Gyr.

An improved treatment with amended secular equations was later given by Zahn (1989).

K.2.2 Approach to, and arrival on to the Main Sequence.

Zahn and Bouchet (1989) extended the treatment of Zahn (1989) to include the earlier stages of the evolution of a binary system, starting from protostars as they move along the Hayashi track towards the Main Sequence. Thus their treatment takes account of conservation of angular momentum when the stars contract. They solved the secular

equations by numerical integration to the point where the stars are on the Main Sequence and the rotational velocity has stabilised, and present results diagrammatically for two particular cases. One solution is shown in Fig. K.1, which is for a system where both stars have a mass $M_1 = M_2 = M_\odot$, the final orbital period is 7.80 days, and the initial eccentricity and period have particular values as explained in the caption. The symbols Ω and ω denote the rotational and orbital velocities. The point at which the stars reach the Main Sequence is shown by the thick black arrow. Zahn and Bouchet discuss this figure in detail in their Sect. 5. The main features of this Figure are as follows.

- The orbits are circularised on a time scale of order 10^5 years, before the stars reach the Main Sequence, and remain circularised while on it. The rotation speeds up before the stars reach the Main Sequence since the stars are contracting and have to conserve angular momentum. This also weakens the tidal torque.
- When the stars reach the Main Sequence they stop contracting and the rotational velocity stops increasing.
- The rotation synchronises with the orbital period relatively shortly after the stars reach the Main Sequence, on a time scale of order 10^8 to 10^9 years.

It may be noticed that Fig. K1 predicts a circularisation time of 10^5 years, whereas Eqn. K2 predicts 57 Gyr for the same period amd mass ratio! The complete resolution of this apparent contradiction is not fully understood, but the following two points can be made.

a) The calculated circularisation time is extremely sensitive to the period. If the calculations represented in Fig. K1 had been made for only the slightly longer period of 7.98 days instead of 7.80 days, the circularisation time would have been 10 Gyr (Zahn and Bouchet, Sect. 5) instead of 10^5 years.

b) Equation K1 for the circularisation time is only an approximation.

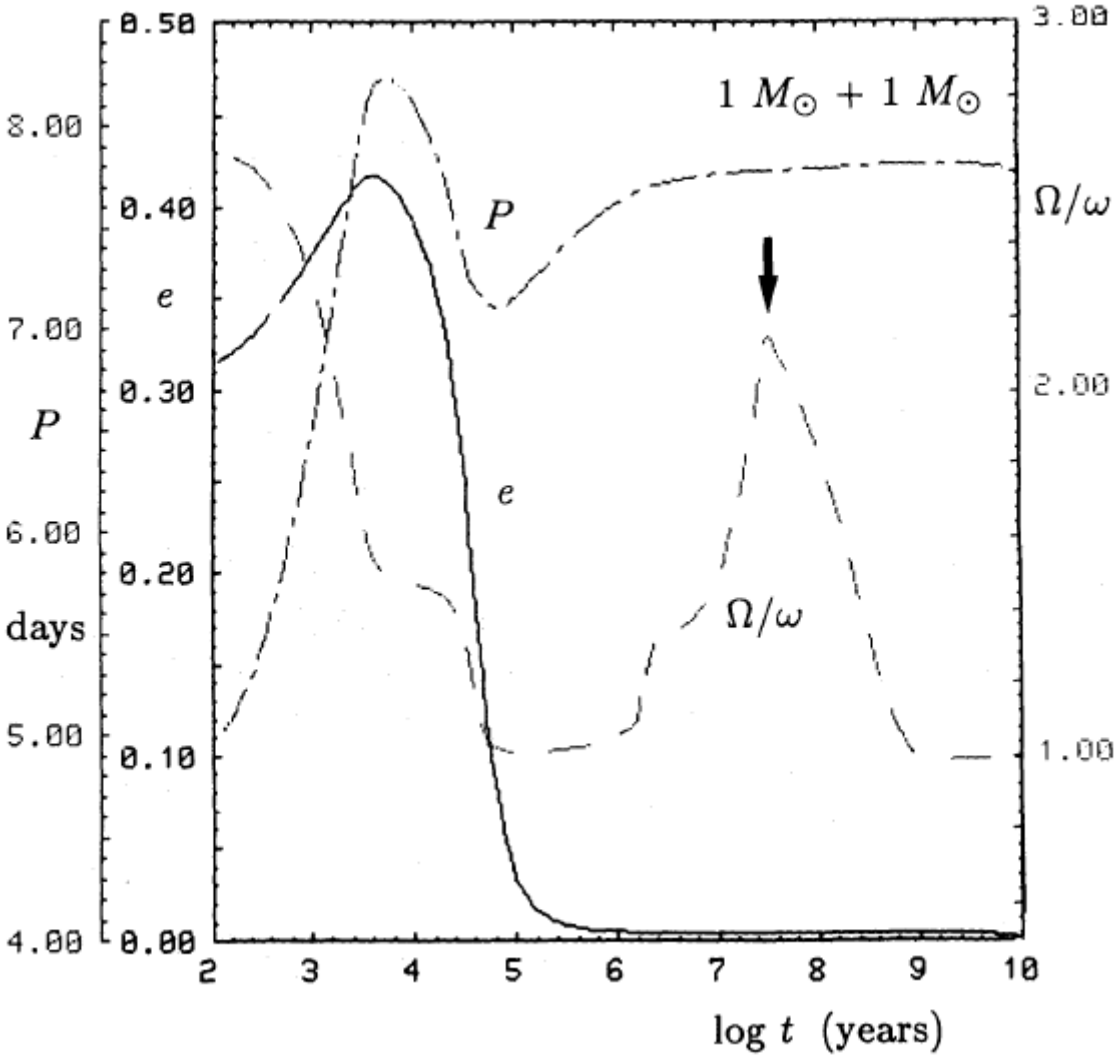

Fig. K1 Evolution of system parameters due to tidal interaction for both stars with masses $1M_\odot$. Taken from Fig. 1 of Zahn and Bouchet (1989).

K2.3 Equilibrium on the Main Sequence

Zahn (1994) has extended this treatment in several ways, in particular to to include spin down i.e. rotational braking due to the torque between the stellar wind and the magnetic field.

The time evolution of the rotational velocity is described by Eqn. 3.6 of Zahn (1994), which is a descendant of the secular equation for $d(I\Omega)/dt$ (Eqn. 4.5 of Zahn (1977), as corrected by Zahn (1978)), through Eqn. 11 of Zahn (1989). It is:

$$\frac{d\Omega}{dt} = \frac{6}{t_f}\frac{q^2}{k^2}\lambda_2\left(\frac{R}{a}\right)^6(\omega - \Omega) - \frac{\Omega}{t_{sd}} \qquad \text{K.3}$$

In this equation the first R.H.S. term represents the torque due to the tidal interactions, and the second the spin down. The symbols Ω and ω are defined earlier; the other symbols are as follows.

t_f the turbulent friction time $T_f = (MR^2/L)^{1/3}$, where M,R and L are the stellar mass, radius and luminosity.

q is the mass ratio of the secondary star to the primary.

k the reduced moment of inertia I/MR^2, where I is defined as

$$I_b\Omega_s = \int_0^{r_b} 4\pi\rho r^4\Omega(r)dr \qquad \text{K.4}$$

λ_2 is a tidal torque coefficient discussed by Zahn (1994)

a is the separation of the stars

t_{sd} is the spin-down time due to magnetic braking from the stellar wind and is defined as

$$-\frac{d\ln\Omega}{dt} = \frac{1}{t_{sd}} \qquad \text{K.5}$$

Solutions of Eqn. K3, together with other equations of Zahn (1994) not reproduced here, are shown in Fig. K3. The main results are as follows.

- If the orbital period is less than about 8 days, the orbital and rotational periods are already synchronised when the stars reach the Main Sequence. These two periods then gradually shorten in step.

- For orbital periods longer than 8 days, and if the orbital period does not lengthen to more than a factor $2^{1/4}$ times the period when the stars reach the Main Sequence, the rotational period is determined by a balance between angular momentum exchange due tidal interactions and spin down and settles to an equilibrium value somewhat longer than the orbital period. The relation between the two periods may be obtained by setting $d\Omega/dt = 0$ in Eqn. K.3.

Zahn shows that if the orbital period lengthens to more than a factor $2^{1/4}$ times the value when the stars reach the Main Sequence, the tidal torques become too weak to brake the rotational motion significantly, and the stars behave as single stars.

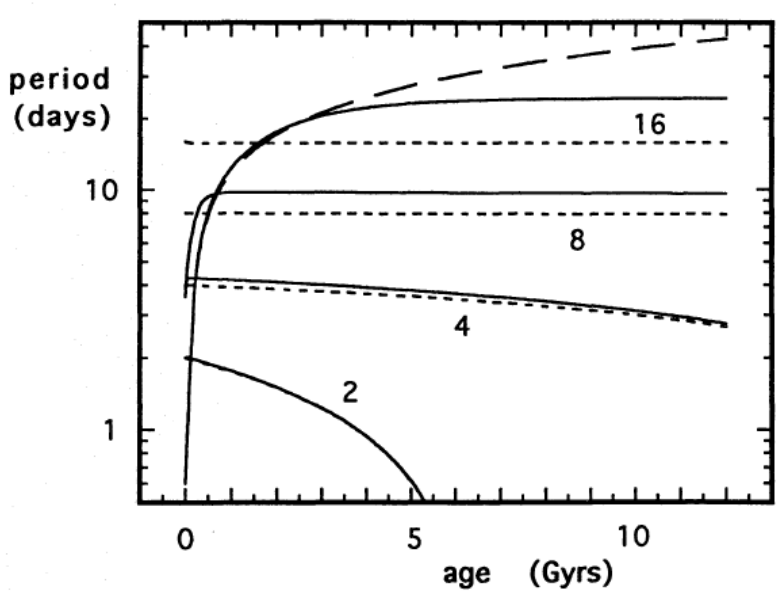

Fig. K2. Evolution of rotational and orbital periods for binary where both stars have masses $1M_{\odot}$, with initial ZAMS periods of 2,4,8 and 16 days. the rotational and orbital periods are shown as continuous and short-dashed lines. The spin down period of a single star is shown as the long dashed line. Taken from Fig. 3 of Zahn (1994).

K.3 Further relevance to exoplanet studies

The theoretical framework for tidal interactions between stars in eclipsing binaries is similar to that for interactions between a star and its exoplanet. The difference between the orbital and rotational periods can in principle yield a value for the tidal interaction parameter *Q*. This is a measure how effectively a star dissipates tidal energy in its envelope, and is a key parameter in the theory of tidal interaction between a star and a planet. Short period exoplanets raise tides on their host stars. The tides exert a torque which drains angular momentum from the orbit of the planet, causing the planet to spiral inwards into the star. The value of *Q* determines the lifetime of Hot Jupiters (Levrard et al., 2009). These authors quote a critical value of the total angular momentum of an exoplanet system. If the total angular momentum is less than this critical value the exoplanet will eventually spiral into its host star, as was predicted for all but one of the 26 exoplanets these authors consider. Regrettably the value of *Q* is uncertain to orders of magnitude (Levrard et al.); further it may depend on the nature of the star, and even the question of the dominant processes which determine its value remains unresolved (Dobbs-Dixon et al. 2004). For an exoplanet like the “Very Hot Jupiter" WASP-18b (Hellier et al. 2009), with its extreme combination of an unusually massive planet and close orbital radius the strength of tidal interactions between the planet and the star is comparable with that between EBs of periods of order 10 days. For such systems.the tides raised on the host star even by the planet can in principle affect the evolution of the star’s angular momentum, and hence tend to synchronise the rotation of the host star with the orbital motion of the planet.

APPENDIX L. STAR CHARTS FOR V1094 TAU.

The position of V1094 Tau in the sky is shown on the three following charts. The first one is a general chart covering R.A. 23h. 20 to 4h. 40. The box shown in the top left hand corner, with Aldebaran at the bottom left is expanded on the second chart. On this chart the coordinates of V1094Tau are listed at the foot of the page, and the star itself is circled. The third chart was obtained from the website of the Space Telescope Science Institute (www.archive.stsci.edu/cgi-bin/dss_form). It coves a 30′ × 30′ area of the sky, thus each side is half the length of an (approximate) square on the second chart. The two stars approximately 3 mm. to the right of V1094 Tau on the second chart are clearly visible towards the right hand side of the third chart.

The first chart is taken from "The Cambridge Sky Atlas" published by the Cambridge University Press.

The second chart is taken from Uranometria, by kind permission of the publishers Willmann-Bell. They have asked me to provide the following credit.

"Chart 133 from Uranometria 2000.0, Volume 1, The Northern Hemisphere to -6° by Wil Tirion, Barry Rappaport and George Lovi. Copyright ©1987 by Willmann-Bell, Inc. Used with Permission".

The Space Science Institute have asked for the following acknowledgement for the third chart.

"The Digitized Sky Surveys were produced at the Space Telescope Science Institute under U.S. Government grant NAG W-2166. The images of these surveys are based on photographic data obtained using the Oschin Schmidt Telescope on Palomar Mountain and the UK Schmidt Telescope. The plates were processed into the present compressed digital form with the permission of these institutions".

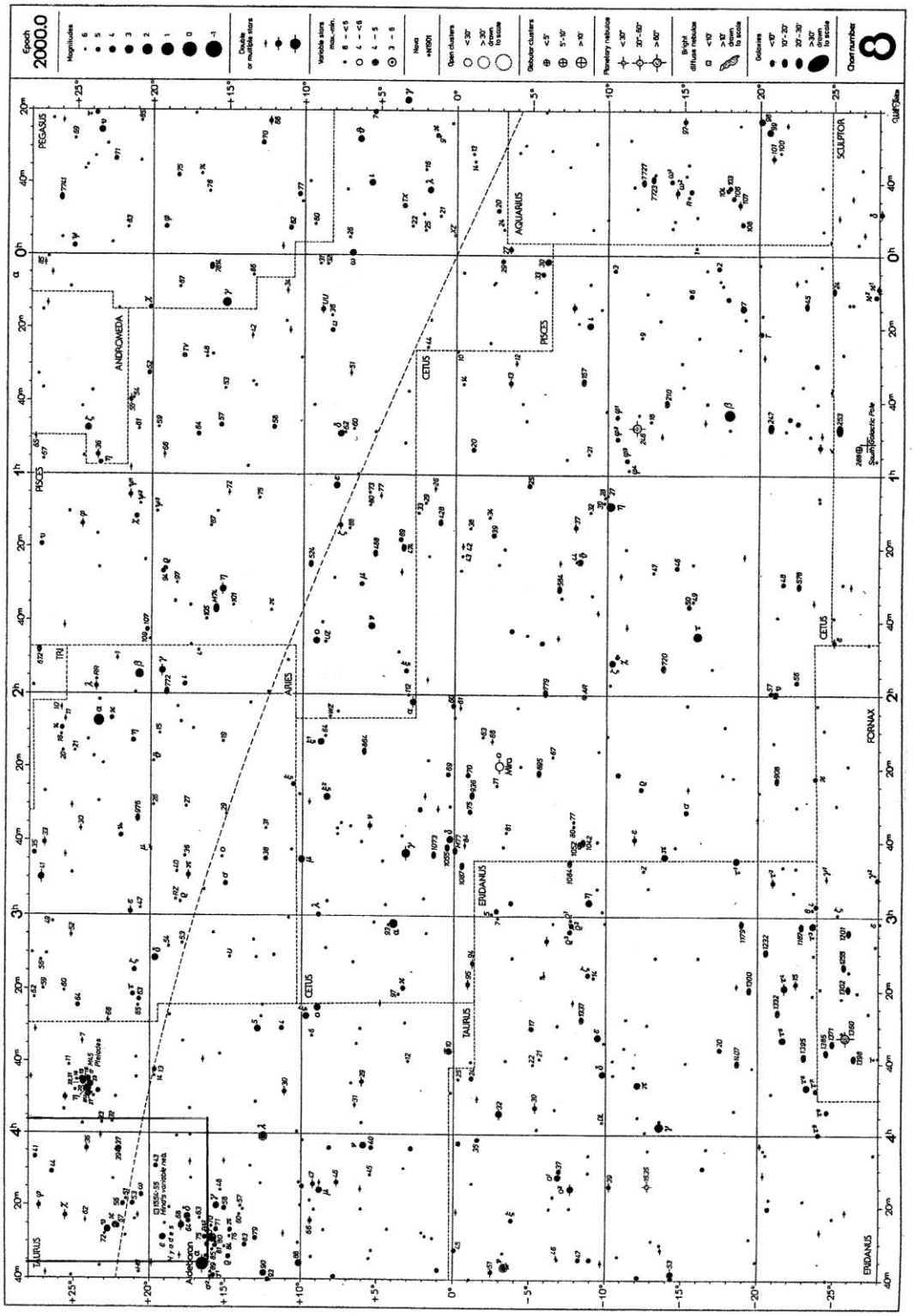

Fig. L1 General finder chart for V1094 Tau.

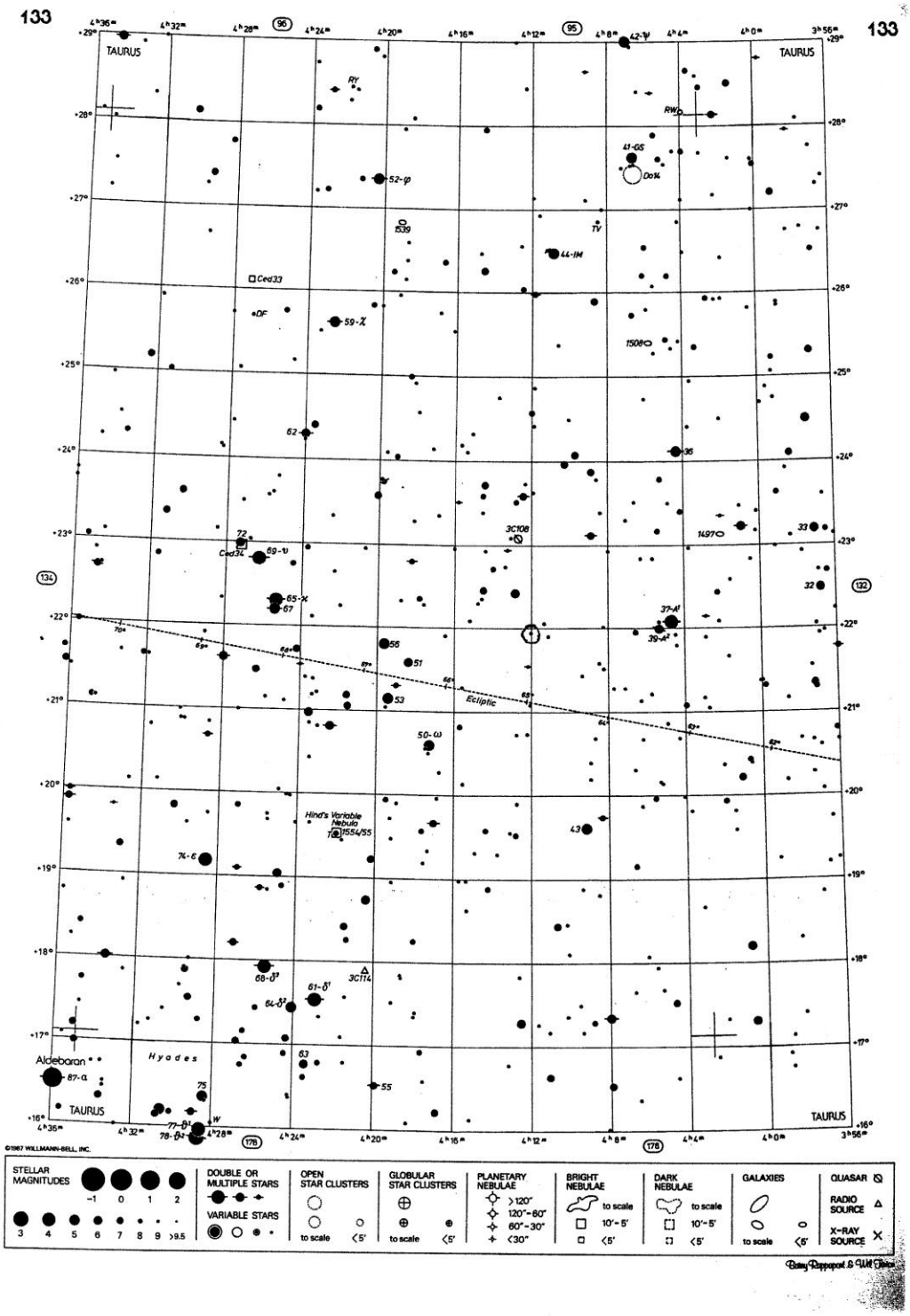

R.A. **4h 12′ 3.5926″**

Dec. **+21° 56′ 50.551″**

Fig L2. Uranometria finder chart for V1094 Tau.

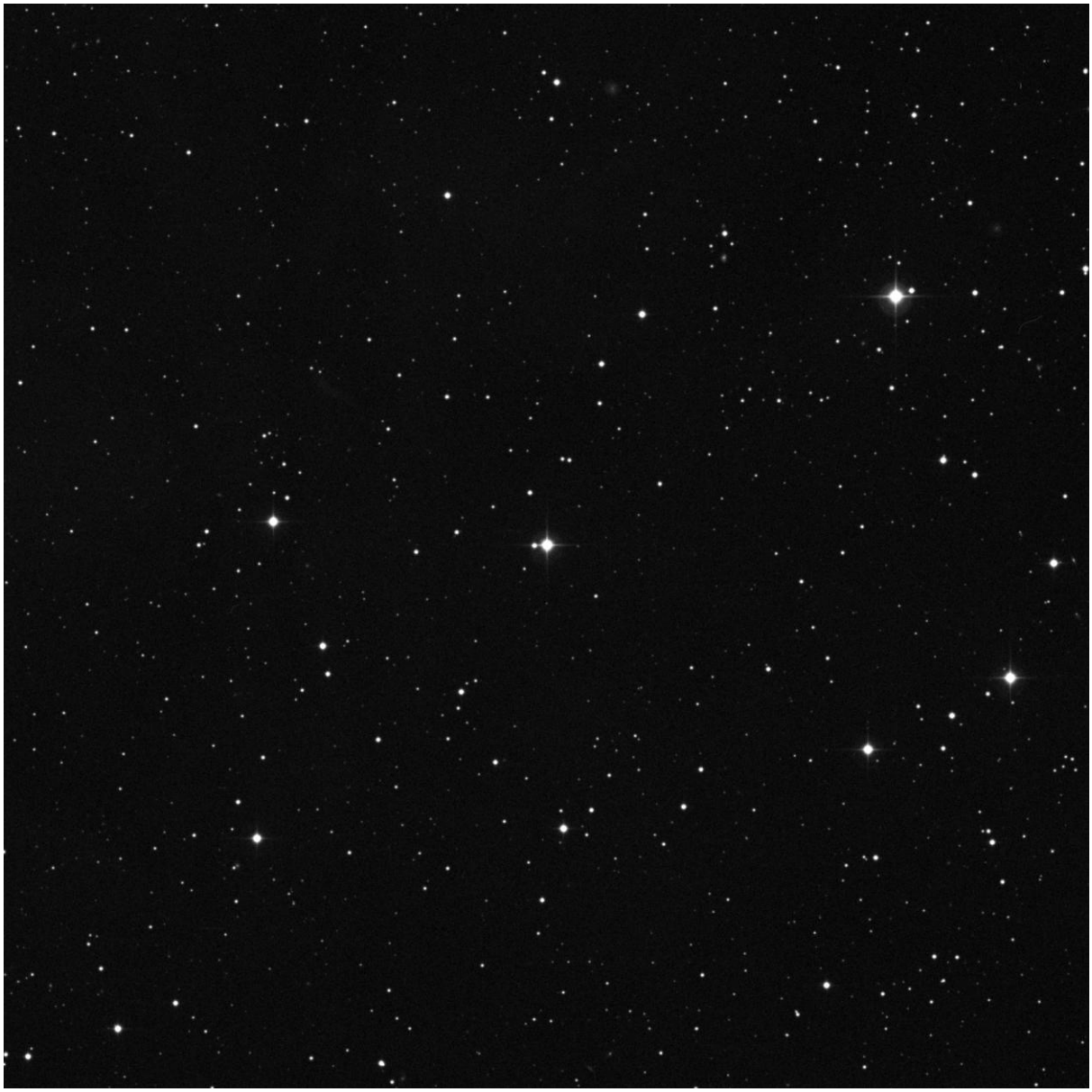

Fig. L3. Space Telescope Science Institute chart of 30′ × 30′ region centred on V1094 Tau.

The comparison stars HD 284196 and HD 284197 are the relatively bright stars on the right hand side and about 2 to 3 cm. below HD 284195; HD 284196 is the upper one.